DISS. ETH NO. 19664

Hybrid Imaging: Combining Fluorescence Molecular Tomography with Magnetic Resonance Imaging

A dissertation submitted to the

ETH Zurich

for the degree of

Doctor of Sciences

presented by

Florian Stuker
M. Sc., University of Bern
born January 16th, 1980
from Eriswil (Bern)

accepted on the recommendation of

Prof. Dr. Markus Rudin, examiner
Prof. Dr. Jorge Ripoll, co-examiner
Prof. Dr. Wilhelm Krek, co-examiner
PD Dr. Martin Wolf, co-examiner

2011

Contents

1 Introduction **1**
- 1.1 Optical Imaging . . . 3
  - 1.1.1 Planar Imaging . . . 3
  - 1.1.2 Tomography Imaging . . . 4
- 1.2 Hybrid Imaging . . . 8
- 1.3 Fluorescent Probes . . . 11
- 1.4 Aim of the Thesis . . . 13

2 From Radiative Transfer Equation to the Diffusion Equation **15**
- 2.1 Basic Quantities Used to Describe Radiative Transfer . . . 16
- 2.2 The Radiative Transfer Equation . . . 17
- 2.3 Derivation of the Diffusion Equation . . . 20
  - 2.3.1 Diffusion Approximation . . . 20
  - 2.3.2 Diffusion Equation . . . 21

3 Solution of the Diffusion Equation for Infinite Homogeneous Media **23**
- 3.1 Solution for the Excitation Source Term . . . 23
- 3.2 Solution for the Fluorescent Source Term . . . 25
  - 3.2.1 The Fluorescent Source Term . . . 25
  - 3.2.2 The Born Approximation . . . 28
  - 3.2.3 Propagation of the Fluorescent Light . . . 28

4 Solution of the Diffusion Equation for Bounded Media **31**
- 4.1 Light Propagation in Arbitrary Shaped Media . . . 31
  - 4.1.1 Boundary Conditions . . . 32
  - 4.1.2 Intensity and Flux at the Boundary . . . 33
  - 4.1.3 Solving the Surface Integral: Kirchhoff Approximation . . . 35
- 4.2 Free Space Propagation of Diffuse Light . . . 36
- 4.3 The Concept of Boundary Removal . . . 38
- 4.4 Incorporation of the Source Intensity Profile . . . 40

5 Inverse Problem **43**
5.1 Measurement Normalization . . . 43
5.2 Discretization and Weight Matrix . . . 44
5.3 Inversion Technique . . . 46

6 FMT **49**
6.1 Aims and Objectives . . . 49
6.2 Material and Methods . . . 50
6.2.1 Instrumentation . . . 50
6.2.2 Fluorescence Data Acquisition . . . 51
6.2.3 Fluorescence Data Reconstruction . . . 53
6.2.4 Phantom Preparation . . . 53
6.3 *In vivo* Applications . . . 55
6.3.1 Tail Vertebra Imaging . . . 55
6.3.2 Lymph Node Imaging . . . 58
6.3.3 Alzheimer's Disease . . . 61

7 Hybrid Imaging: Non-contact FMT/MRI **65**
7.1 1st Generation Non-contact FMT/MRI Setup . . . 66
7.1.1 Aims and Objectives . . . 66
7.1.2 Material and Methods . . . 66
7.1.3 Results . . . 72
7.1.4 Discussion . . . 78
7.2 2nd Generation FMT/MRI Setup . . . 80
7.2.1 Aims and Objectives . . . 80
7.2.2 Material and Methods . . . 81
7.2.3 Results . . . 87
7.2.4 Discussion . . . 92

8 Conclusions and Outlook **97**
8.1 FMT . . . 97
8.2 FMT/MRI . . . 99
8.3 Outlook . . . 100

A Photon Transport Theory **105**
A.1 Transport Equations . . . 105
A.1.1 Wave Propagation and Scattering in Random Media . . . 105
A.1.2 Linear Transport Theory . . . 107
A.1.3 Neutron Transport Theory . . . 107
A.2 P_N Approximation . . . 108
A.3 P_1 Approximation . . . 115
A.4 Diffusion Equation . . . 119

B Coil Design **121**

C A Setup to derive the optical properties of samples 123
C.1 Introduction . . . 123
C.2 Theory . . . 124
C.2.1 Measurement of Optical Properties . . . 124
C.2.2 Indirect Measurements of Optical Properties . . . 125
C.2.3 Adding-Doubling Method . . . 126
C.3 Material and Methods . . . 127
C.3.1 Measurement Setup . . . 127
C.3.2 Sample Preparation . . . 128
C.3.3 Measurement Procedures . . . 128
C.4 Results . . . 132
C.4.1 Intersample Reproducibility . . . 133
C.4.2 Measurement Reproducibility . . . 133
C.4.3 Unscattered Transmittance . . . 135
C.4.4 Calculation of the Optical Properties . . . 135
C.5 Discussion . . . 135
C.6 Outlook . . . 137

Bibliography 153

List of Symbols

Notation	Description	Units
$N_{v,s,d}$	Total number of voxels, sources, detectors	
$N_{x,y,z}$	Number of voxels in all directions in space	
T_1, T_2, T_2^*	Different MR relaxation times	ms
$L(\mathbf{r}, \hat{\mathbf{s}}, t)$	Radiance or specific intensity	W cm^{-2} sr^{-1}
$\hat{\mathbf{s}}$	Unit vector	
$\mathbf{r}$	Position vector	
$d\Omega$	Unit solid angle	sr
$du(\mathbf{r}, t)$	Energy density within $d\Omega$	J cm^{-3} s^{-1}
$u(\mathbf{r}, t)$	Energy density	J cm^{-3}
dE	Differential energy	J
dS	Differential area	cm^2
dV	Differential volume	cm^3
dt	Time intervall	s
$U(\mathbf{r}, t)$	Average intensity	W cm^{-2}
$\mathbf{J}(\mathbf{r}, t)$	Total flux density	W cm^{-2}
$J_{tot}(\mathbf{r}, t)$	Total normal flux density	W cm^{-2}
$J_{in,out}(\mathbf{r}, t)$	Inward/outward flux	W cm^{-2}
$\mathbf{n}$	Outward normal vector	
υ	Speed of light in the medium	cm s^{-1}
$p(\hat{\mathbf{s}}, \hat{\mathbf{s}}')$	Phase function	
$\sigma_{a,s}$	Absorption/scattering cross-section	cm^2
μ_t	Total attenuation coefficient	cm^{-1}
$\mu_{a,s}$	Absorption/scattering coefficient	cm^{-1}
μ_s'	Reduced scattering coefficient	cm^{-1}
l_{sc}	Scattering mean free path	cm
l_a	Absorption length	cm
l_{tr}	Transport mean free path	cm
g	Anisotropy factor/average cosine	
D	Diffusion coefficient	cm
S	Photon source term	
$\lambda_{exc,fl}$	Excitation/fluorescence wavelength	nm
k	Complex wave number	cm^{-1}
η	Fluorescence quantum yield	
Γ	Total decay rate	
$C(n)$	Interface coefficient	
$QE^{\lambda_{exc,fl}}$	Detector quantum efficiency at λ_{exc} and λ_{fl}	
$\Theta_d(\mathbf{r}_d)$	Detector gain	
$\Theta_s(\mathbf{r}_s)$	Source gain	
Θ_f^{fl}	Fluorescence filter attenuation	
Θ_f^{exc}	Excitation filter attenauation	
$Y_{l,m}$	Spherical harmonic of the order l and degree m	
P_l	Legendre polynom	
ω	Modulation frequency	Hz

Abstract

Optical imaging techniques, in particular fluorescence imaging is nowadays widely used in biomedical research. Among those optical imaging approaches, fluorescence microscopy is one of the most established and routinely used techniques in daily research. Unfortunately microscopy techniques are only applicable to study molecular and cellular processes in cell culture or tissue samples. Therefore an imaging strategy which would allow to apply the wealth of tools that have been developed for optical microscopy to intact organisms such as mice would be very attractive. Fluorescence molecular tomography (FMT) is such a promising and powerful macroscopic imaging technique. Due to significant technological progress during the last years FMT has emerged as interesting molecular imaging solution for various fields in biomedical research. FMT allows a three-dimensional reconstruction of fluorophore distribution *in vivo* by scanning an excitation source pattern on the sample surface and collecting the diffuse light by an array detector. In contrast to first contact setup implementations where the animal is place vertically in a liquid filled imaging chamber connected to a limited number of source and detector fibers, recent setups provide a more convenient horizontal non-contact measurement geometry. These setups are more flexible and have a large number of source/detector pairs which leads to improved reconstructed image resolution. Compared to straightforward implementations of planar imaging techniques where quantitative measurements are impossible to achieve, FMT allows depth resolved information and therefore the quantification of fluorophore distributions which is important for biological investigations.

The major advantage of optical imaging techniques are the high sensitivity which makes it suitable to detect low concentration of target molecules in tissue. Furthermore, optical reporter systems such as fluorescent dyes or bioluminescent and fluorescent reporter proteins are stable molecules and can be easily targeted to report on specific molecular processes *in vivo*. Additionally, the techniques are relatively inexpensive, which facilitates their protrusion into the biomedical research community.

The development and construction of a non-contact FMT setup was the first goal of this thesis. In a preliminary step the theoretical background of FMT and especially the concepts allowing for non-contact FMT were discussed in details. A second section describes the technical realization of the setup including further improvements compared to already published examples such as an integrated filter switch mechanism and preparative steps for multispectral imaging. Different *in vivo* applications demonstrated a proper function of the implemented method: In a first experiment load induced changes in bone osteoblast and osteoclast activity responsible for bone formation and resorption were evaluated in mouse tail vertebrae using a commercial available molecular fluorescence probe targeting hydroxyapatite. Clear changes in the reconstructed fluorescence intensity were observed for different loading forces and furthermore the FMT readouts was shown to correlate well with a X-ray computed tomography (CT) readout. A further proof demonstrating the feasibility of quantitative FMT imaging was performed on a second experiment where the objective was

to image cervical lymph nodes with an indocyanine green (ICG) labeled antibody in an inflamed mouse model. In this study the localization of the inflamed and healthy lymph node was shown with help of reconstructed ICG distribution. Interestingly even signals from the lymph nodes in control animals could be observed at the specific wavelength used. Finally, FMT was applied in a mouse model of Alzheimer's disease where the time course of fluorescence intensity elicited by an oxazine derived dye, which has been shown to specifically bind to aggregated beta-amyloid in the brain cortex, was compared in transgenic animals developing amyloid plaques to wild type litter mates. The fluorophore concentration could be clearly localized in the cortical region of both animals: the slower dye clearance in the brain of transgenic animals indicated an enhanced dye binding to the Alzheimer's plaques.

In summary, a successful operation of the designed FMT method could be shown by means of various *in vivo* applications resulting in well resolved reconstructed fluorophore distributions and its quantification under *in vivo* conditions.

A major limitation of FMT, which is characterized by high sensitivity sufficient for providing molecular and functional information, is the relatively poor spatial resolution in comparison to structural/anatomical imaging modalities which may render the allocation of molecular data to a specific anatomic structure difficult. This lead to the second major goal of this project where the elimination of this constraint was intensively studied. The result was a novel hybrid multimodal imaging concept where a combination of non-contact FMT and high field MRI was used for simultaneous measurements. Preclinical MRI is an attractive counterpart to FMT as it provides high resolution images of structures due to excellent soft tissue contrast. This complementary anatomical information would help to better localize and furthermore improve the reconstructed fluorophore distribution.

With a non-contact free space FMT design principle restrictions of recently published setups such as low numbers of source/detector pairs in a rigid configuration, fiber based bulky construction, small field of view coverage and related limited diffusive light collection could be eliminated. The here presented newly developed setup is working in non-contact fiber-free reflection geometry where the optical detector array is placed in close proximity to the sample in the isocenter of a 9.4T animal MRI scanner. The sample illumination is provided from outside the bore of the MR scanner and is freely adjustable to the geometry of the sample. First performance tests of the setup in tissue mimicking silicone phantoms using a 32×32 single photon avalanche diode (SPAD) array yielded adequate spatial resolution both in plane and in depth, which correlated well with simulation results. The proof of principle of this first generation setup was demonstrated in a tumor bearing mouse where the distribution of a fluorescent protease probe could be three dimensionally represented and localized with help of an anatomical reference provided by the MR.

Based on experiences of the first generation FMT/MRI setup a further improved completely redesigned second generation setup was implemented. The second setup is primed to be used in transmission or reflection mode and the limited detector resolution was extended by using newly developed detector technologies having higher

number of pixels available. A specially designed 256×256 CMOS detector array could be attached to the system. The small field of view limiting the optical imaging in the first setup was widened with an improved objective lens and a larger detector size. A further gain in field of view was achieved by increasing the focal distance which was achieved by scanning the sample surface from the side and not as in the previous version from the top. Moreover simplifications for the handling were achieved by attaching the platform to a rigid rail system consisting of two carbon rods fixed to the MR scanner compared to the less stable fixation used in the first version. First tests on tissue mimicking silicone phantoms demonstrated the proper function of both the MR and the optical part during simultaneous acquisitions. Furthermore it was found that the spatial resolution and the sensitivity is comparable to stand alone FMT setups working with the same principle. *In vivo* experiments in an Alzheimer's disease mouse model performed simultaneously with the FMT/MRI setup showed comparable results to the presented study with the stand alone FMT system.
Summing up, based on a new idea of combining FMT and MRI imaging a first generation and improved second generation dual-modality setup allowing simultaneous measurements was designed and characterized. Performance tests on tissue phantoms and *in vivo* experiments in mice demonstrated a correct functioning of both modalities and showed the potential of such hybrid setups in providing complementary information required for a comprehensive understanding of the processes investigated.

Zusammenfassung

Optische Bildgebung, insbesondere Fluoreszenz-Bildgebung, ist heutzutage in der biomedizinischen Forschung weit verbreitet. Unter den optischen Bildgebungsverfahren ist Fluoreszenz-Mikroskopie eine der meist verwendeten und routinemässig eingesetzten Techniken, welche in der täglichen Forschungsarbeit zum Einsatz kommen. Leider sind Mikroskopie-Techniken zur Untersuchung von molekularen und zellulären Prozessen nur in Zellkulturen oder Gewebeproben anwendbar. Aus diesem Grund wäre eine bildgebende Technik, welche man auf lebende Gesamtorganismen, wie zum Beispiel einer Maus, anwenden könnte wünschenswert. Die molekulare Fluoreszenz-Tomograpie (FMT) ist ein solches vielversprechendes makroskopisches Bildgebungsverfahren, welches in den letzten Jahren durch intensive Forschungs- und Entwicklungsarbeit einen interessante Lösungsansatz für die molekulare Bildgebung in verschiedensten Gebieten der biomedizinischen Forschung bietet. FMT bietet die Möglichkeit einer drei-dimensionalen Rekonstruktion einer Fluorophorverteilung *in vivo*, bei der man eine Anregungspunktquelle über ein vordefiniertes Punktraster auf der Oberfläche eines Objekts führt und das dabei erzeugte diffuse Licht mit einem Detektor aufnimmt. Im Vergleich zu früheren Systemen, bei denen die Tiere vertikal in einem mit Flüssigkeit gefüllten Tank platziert wurden, welcher in Kontakt zu den Detektor- und Anregungslichtleitungsfasern stand, bieten heutige kontaktfreie Aufbauten eine anatomisch korrekte horizontale Positionierung der Tiere. Diese Messgeometrien sind

flexibler und haben eine grosse Anzahl an Quellen/Detektor-Paaren, welche zu einer verbesserten Bildauflösung der rekonstruierten Daten führen. Im Vergleich zu den einfacheren planaren Systemen, bei denen eine Quantifizierung des Fluoreszenzsignals nicht möglich ist, erlaubt die FMT-Technik eine Tiefenauflösung, welche die Quantifizierung einer Fluorophorverteilung möglich macht. Die Quantifizierbarkeit der gewonnenen Informationen ist für biologische Untersuchungen von grosser Bedeutung.
Einer der grössten Vorteile von optischen bildgebenden Verfahren ist die hohe Sensitivität, welche es erst ermöglicht, geringe Konzentrationen eines Moleküls im Gewebe nachzuweisen. Weiter sind optische Reportersysteme, wie zum Beispiel fluoreszierende Farbstoffe oder Biolumineszenz- und Fluoreszenz-Proteine meistens stabile Moleküle, welche dazu dienen einen spezifischen molekularen Prozess *in vivo* sichtbar zu machen. Zudem sind die Techniken sehr preiswert was dazu führt, dass diese in der biomedizinischen Forschung oft angewendet werden und daher weit verbreitet sind.
Das erste Ziel dieser Dissertation war die Entwicklung und Konstruktion eines kontaktfreien FMT-Systems. In einem vorhergehenden Schritt wurde die Theorie, welche hinter dieser bildgebenden Technik steht erläutert, wobei der Schwerpunkt auf die kontaktfreie FMT-Technik gelegt wurde. In einem zweiten Abschnitt wurde die technische Umsetzung des Aufbaus genauer erklärt, wobei Verbesserungen im Vergleich zu bestehenden Systemen, wie das integrierte Filterrad und die vorbereiteten Schritte für multispektrale Bildgebung erläutert wurden. Das System wurde mit verschiedenen *in vivo* Anwendungen auf die korrekte Funktionsfähigkeit hin getestet: In einem ersten Experiment wurde der Knochenaufbau und -abbau, welcher Aufschlüsse über die Osteoblasten und Osteoclasten Aktivität gibt, mit einem kommerziellen Fluoreszenzfarbstoff, welcher an Hydroxyapatite bindet, untersucht. Dazu wird der zu untersuchende Schwanzwirbel in eine Vorrichtung eingespannt, welche es erlaubt verschiedene Stärken von Kräften auf diesen einwirken zu lassen. Eine Abhängigkeit der angelegten Kraft und des rekonstruierten Fluoreszenzsignals konnte gezeigt werden. Weiter wurde gezeigt, dass die strukturelle Untersuchung der Knochen mit einem micro Computer Tomographie (CT) System sehr gut mit den optischen Daten übereinstimmt. Ein weiterer Nachweis, dass FMT quantitatives Arbeiten ermöglicht, wurde in einem zweiten Versuch gezeigt, wobei man cervicale Lymphknoten mit Hilfe eines mit indocyanine green (ICG) gekenntzeichneten Antikörpers untersucht hat. Das gewählte Mausmodell erlaubte die Erzeugung einer Entzündung, welche dazu führte dass die Lymphknoten anschwellten. In der Studie wurde gezeigt, dass durch die rekonstruierte ICG-Konzentration die entzündeten und gesunden Lymphknoten auf beiden Seiten des Halses lokalisierbar sind. Interessanterweise konnten bei den verwendeten Wellenlängen auch schwache Signale der gesunden Lymphknoten in gesunden Kontrolltieren beidseitig nachgewiesen werden. Zum Schluss wurde FMT auf ein Mausmodell zur Untersuchung der Alzheimer Krankheit angewendet. Dabei wurde ein Zeitverlauf des Fluoreszenzsignals nach der Injektion eines Oxazin-Fluoreszenzfarbstoffs untersucht, welcher sich spezifisch an β-amyloid plaques binden sollte. Der Zeitverlauf einer transgenen Maus, welche Alzheimer-Plaques in der Hirnrinde entwickelt,

wurde mit einem Kontrolltier verglichen, wobei herausgefunden wurde, dass der Farbstoff beim Kontrolltier schneller ausgewaschen wurde als beim verglichenen transgenen Tier. Dies zeigte, dass der Farbstoff an die Alzheimer-Plaques gebunden wurde. Weiter war es möglich, das Fluoreszenzsignal in der Region der Hirnrinde zu lokalisieren. Es konnte somit in verschiedenen Mausmodellen gezeigt werden, dass der Aufbau und die angewendete Methode funktionieren, dass das rekonstruierte Fluoreszenzsignal lokalisiert und zudem noch quantifiziert werden kann.
Die Haupteinschränkung in der FMT-Technik welche zwar eine hohe Sensitivität aufweist, um molekulare und funktionale Informationen zu erhalten, ist die beschränkte örtliche Auflösung im Vergleich zu Modalitäten, welche strukturelle und anatomische Informationen bieten. Daher ist es kaum möglich, die molekulare Information von optischen Systemen einer anatomischen Struktur zu zuordnen, ohne die Miteinbeziehung von weiteren Informationen anderer bildgebenden Verfahren.
Eine Möglichkeit zur Behebung dieses Problems wurde im zweiten Teil dieses Projekts intensiv untersucht. Das Resultat war ein neuartiges hybrides bildgebendes Konzept, welches aus einer Kombination von einem kontakt-freien FMT- und einem Magnetresonanz-System (MRI) besteht. Das entwickelte System erlaubt eine simultane optische wie auch eine MR-Messung. Ein präklinisches Kleintier-MR bietet einen hohen Weichgewebe-Kontrast und eine sehr hohe örtliche Auflösung und ist somit das ideale Gegenstück zur optischen FMT-Technik. Die ergänzenden strukturellen Informationen würden helfen, die rekonstruierten Fluoreszenzsignale besser im anatomischen Kontext des umgebenden Gewebes zu lokalisieren und die Rekonstruktion zu verbessern.
Mit einem kontakt- und glasfaserlosem FMT Konzept könnten die Einschränkungen der kürzlich publizierten glasfaserbasierten Aufbauten eliminiert werden. Die limitierenden Faktoren von Glasfasersystems sind die geringe Anzahl an Quellen/Detektor-Paaren, die platzraubenden Fibern, die feste Geometrie, das limitierte effektive Bildfeld und die miteinhergende geringe Lichtausbeute. Der hier präsentierte neuentwickelte Aufbau ist kontakt- und glasfaserfrei und erlaubt die simultane Bildgebung in einer Reflektionsgeometrie mit Hilfe eines optischen Detektorarrays in der Nähe des Versuchskörpers im Iso-Zentrum eines MR-Systems mit einer Feldstärke von 9.4T. Das Licht zur Untersuchung des Objekts im Magneten wird von ausserhalb der Magnetöffnung eingestrahlt und kann je nach Geometrie des Objekts frei angepasst werden. Erste Tests an Gewebephantomen aus Silikon haben gezeigt, dass der hier verwendete optische 32×32 Bildsensor basierend auf einem Array von single photon avalanche diodes (SPAD) eine hinreichende örtliche Auflösung in allen Raumrichtungen bietet. Die experimentellen Resultate wurden mit Simulationen verifiziert und ergaben eine gute Übereinstimmung. Dass das hier angewendete Prinzip auch bei der Untersuchung von Tiermodellen angewendet werden kann, wurde mit einem Tumormodell gezeigt. Das Fluoreszenzsignal einer durch Protease aktivierte Probe eines Tumors in der Flanke einer Nacktmaus konnte erfolgreich detektiert und mit Hilfe der parallel aufgenommenen strukturellen Bilder anatomisch zugeordnet werden.
Die Erfahrungen dieser ersten Generation eines solchen FMT/MRI-Setups flossen

in eine weiterentwickelte und verbesserte zweite Generation. Dieser zweite Aufbau ermöglicht nun Messungen in der Transmissions- und Reflektionsgeometrie und bietet zudem eine verbesserte Detektorauflösung aufgrund der Verwendung eines neuentwickelten und eigens für diese Anwendung angepassten 256×256 CMOS Arraydetektors. Das kleine Bildfeld des ersten Detektors konnte mit Hilfe der grösseren Detektorfläche und einer verbesserten Objektivlinse aufgeweitet werden. Zur Bildfeldaufweitung hat auch die vergrösserte Fokusdistanz beigetragen, welche durch eine abgeänderte nun an der Seite angebrachte Ablenkung des Laserstrahls erreicht wurde. Im Vergleich zum ersten Setup wird das Punktraster des Laserstrahls auf dem Objekt nun von der Seite abgefahren und nicht mehr von oben herab. Weiter wurde die Handhabung des ganzen Aufbaus vereinfacht und stabilisiert, was durch die Fixierung der Plattform auf einem Schienensystem aus zwei Karbonrohren, welches am MR-Gerät fest angebracht wird, erreicht werden konnte. Erste Tests an Gewebephantomen aus Silikon ergaben eine örtliche Auflösung, welche derjenigen Systemen entspricht die mit charge-coupled device (CCD) Kameras ausgerüstet sind. Die ersten simultanen Messungen an einer Alzheimer-Maus haben gezeigt, dass die Resultate vergleichbar sind mit der im ersten Teil erwähnten Studie.
In zweiten Teil dieser Dissertation wurde ein neuentwickeltes Konzept der Kombinierung von FMT und MRI zur gleichzeitigen Bildaufnahme in einem Setup der ersten Generation und einer verbesserten zweiten Ausführung demonstriert und charakterisiert. Die Resultate der Phantommessungen und der anschliessend ausgeführten *in vivo* Messungen konnten zudem das Potential dieser neuartigen hybriden Technologie aufzeigen, indem komplementäre Informationen gewonnen werden können, welche dazu dienen sollten, die untersuchten biologischen Prozesse besser zu verstehen.

Chapter 1

Introduction

Parts of this chapter are adapted from:

F. Stuker, J. Ripoll and Markus Rudin. Fluorescence molecular tomography: principles and potential for pharmaceutical research. *Pharmaceutics*, 3(2): 229-274, April 2011.

Optical imaging techniques, especially optical tomography has made significant progress over the past few years and is nowadays an established tool in the field of molecular imaging [1]. The term molecular imaging can be defined as the characterization and measurement of biological processes in an intact organism on a cellular and subcellular scale [2]. The field is rapidly growing and is mainly driven by fast advances in molecular biology and biotechnology providing tools to visualize molecular processes *in vivo* [3, 4] e.g. in the field of oncology [5]. Among the different molecular imaging probes, optical probes forced the implementation of optical imaging techniques for molecular imaging studies [6]. Therefore molecular imaging plays its role at the interface where technical and biological disciplines meet to deliver meaningful readouts [7]. Furthermore molecular imaging is an attractive and indispensable tool for basic research and in the field of drug discovery and development [8, 9].
Before optical imaging was used as a molecular imaging modality it showed the potential to uncover deep seated tissue abnormalities in clinics by simple transillumination approaches of female breasts. With the formulation of the theoretical framework how light propagates within highly scattering and absorbing media such as tissue the development of sophisticated optical imaging methods started. Based on this new understanding of light interaction with different tissue components, optical imaging techniques were successfully applied on different fields in clinics e.g. to measure hemodynamic changes, detecting tumors and providing functional brain images and were further developed for pre-clinical research. All these applications visualize changes in the absorption and scattering properties of tissue which are inherent sources of contrast and strongly related to morphological and pathological changes in tissue.
As these processes occur on the molecular level a direct visualization of these biological events would be of interest. In biomedical research fluorescence microscopy is widely

used to study molecular and cellular processes in cell culture or tissue samples. This is motivated by the high inherent sensitivity of fluorescence techniques, the stability of the fluorescent labels used and the sophisticated labeling strategies that have been developed for selectively labeling target molecules [10]. Theses fluorescence contrast agents such as fluorescent dyes, quantum dots, fluorescent proteins and bioluminescent proteins were adapted for optical imaging studies tagging specific cells or proteins to probe molecular events and pathways in intact organisms.
In general optical imaging techniques suffer from the limited penetration depth of light, which ranges from a few millimeters for wavelengths shorter than 500nm (green,blue) to several centimeters for wavelengths longer than 650nm (red, near-infrared). Therefore, fluorescence imaging is mainly used in combination with probes absorbing and fluorescing in the red to near infrared (NIR) spectral range [11, 12], for which the light penetration depth is sufficient for pre-clinical imaging using small animals [13, 14] and even humans [15]. The optimal wavelength can be found by considering the absorption spectra of the main components in tissue (blood and water) as shown in Fig. 1.1. As seen, there exists a spectral window in the range of 650 to 900nm where minimal absorption values are present. Another concern related to modalities providing molecular and functional information such as optical imaging techniques is the relatively poor spatial resolution in comparison to structural/anatomical imaging modalities such as X-ray computed tomography (CT) and magnetic resonance imaging (MRI), which may render allocation of molecular data to a specific anatomical structure difficult.

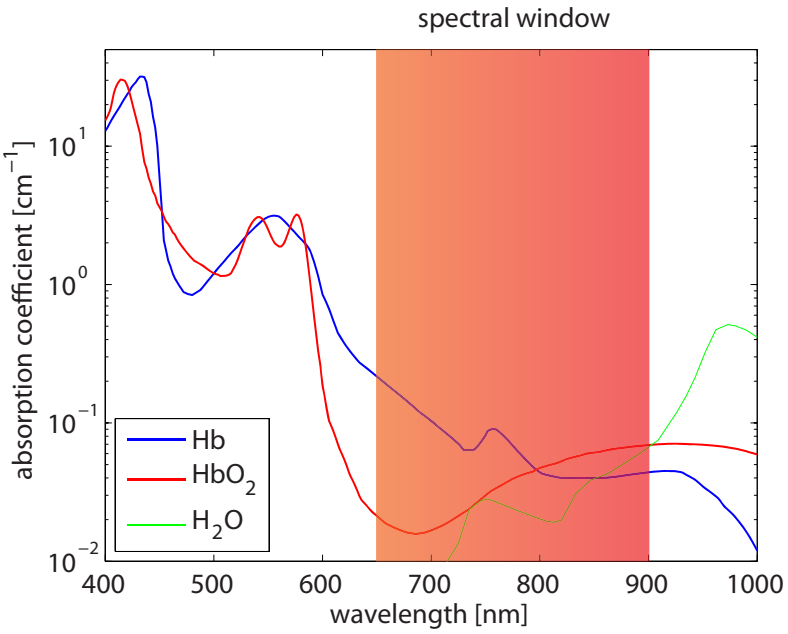

Figure 1.1: Absorption spectra of the main components of tissue, namely the blood components oxyhemoglobin (red) and deoxyhemoglobin (blue) and water (green)

A solution for this issue was addressed in the concept of multimodality or hybrid imaging where two or more modalities are combined to provided a complementary imaging readout. The integration of the strength of two modalities and probably eliminate the weaknesses of an individual readout offers improved diagnostic and therapeutic monitoring in clinical and preclinical applications [16]. In terms of optical imaging it is mainly the combination with CT which is dominating but also MRI [17] is an attractive partner due to the high soft tissue contrast which is superior to that achieved with CT. Nowadays it is well known that complementary information of a structural, functional and/or molecular read out is necessary to get a comprehensive understanding of the investigated processes and therefore the applications and developments in the field of multimodality imaging and especially in the field of pre-clinical optical multimodality imaging is large and constantly growing.

1.1 Optical Imaging

1.1.1 Planar Imaging

The simplest approach for imaging the distribution of a fluorophore *in vivo* is planar imaging, also called fluorescence reflectance imaging (FRI). In this case the signal detected is heavily surface weighted, i.e. is dominated by the contribution of dye molecules at or close to the surface. The instrumental design is such that large parts of the animal or the whole animal is simultaneously illuminated, e.g. using an optically expanded laser beam at the excitation wavelength, light emitting diodes or a white light source using appropriate bandpass filters. The fluorescent light from the tissue surface is detected using a high sensitive charge-coupled device (CCD) camera (Fig. 1.2 left column). The noise requirement (e.g. electronic noise which could potentially influence the imaging performance) of the camera for planar imaging is not as stringent since in general the detection sensitivity limit is governed by the background tissue fluorescence (autofluorescence). The use of bandpass filters with high transmission efficiency for a narrow wavelength range is essential to prevent bleed-through of excitation light into the fluorescent images. The use of lenses with a low f-number, i.e. large aperture, warrants a high light collection efficiency. For anatomical registration the fluorescence images are superimposed on mouse images typically obtained with white light illumination. FRI approaches were first described in 1999 [18] and then successfully used to study epidermal growth factor receptor labeled with Cy5.5 in breast tumors [19] tumor protease activity of breast carcinoma [18, 20], protease activity in arthritis [21], osteoblast activity in vertebra [22] and GFP expressing tumors [23] in mice.
Fluorescence intensity measured at the detector depends on the length of the total light path (excitation and fluorescence light) through tissue. For FRI fluorescent sources close to the surface contribute much more than deeply embedded ones. In particular autofluorescence of superficial structures will limit the depth field of view of FRI. In

comparison, when using transillumination, the total path length is approximately constant irrespective of the location of the fluorescence source within the sample, which enhances the detection probability for deeply embedded fluorescent sources. Fluorescence transillumination was used in various research fields [10] and can be considered as an extension of the transillumination approach used in 1929 by Cutler [24] to resolve absorbing lesions in breast tissue. This method produced shadows attributed to vascular structure (shadowgrams) and has been further developed for breast imaging. Normalization fluorescence planar imaging in reflectance and transillumination mode has been shown to further improve image quality, depth sensitivity and imaging accuracy compared to non-normalized data [25]. An extension of this imaging approach is the use of spectral information in the image to discriminate the contributions by different fluorochromes or to reduce the contribution of tissue autofluorescence (non-specific background fluorescence) [26, 27]. Even though these suggested image improvements makes planar imaging a reliable tool for researchers it still suffers from a lack in depth resolution and difficult quantification.
In summary planar optical imaging is attractive for qualitative high-throughput measurements demonstrating the presence of a fluorescent probe *in vivo* or in excised tissues. The method provides no depth resolution and correspondingly quantification of the data is difficult. Technical simplicity and easy handling makes it an attractive screening modality in biology laboratories. In addition planar optical imaging instrumentation is relatively inexpensive.

1.1.2 Tomography Imaging

In order to reconstruct a three-dimensional data set containing $N_v = N_x \times N_y \times N_z$ voxels N independent measurements (each corresponding to an individual source/detector pair) are required. As already stated, planar imaging is mathematically equivalent to having a high number of point sources illuminating simultaneously, which implies that each source/detector pair cannot be distinguished (deconvolved) individually. By using sequential illumination of the individual sources this problem can be circumvented. This is the basic principle of DOT and FMT: Tissue is sequentially illuminated with an array of light sources and the emanating light is captured with an array of detectors (Fig. 1.2 right column). For each source location, of a total N_s sources being sampled, the light distribution on the sample surface is recorded with each detector of the N_d detector array. A light propagation model for the specific sample is developed and parameterized in terms of unknown scattering and absorption coefficient as a function of position in the tissue. By comparing the model prediction with the experimental intensity measurements of all $N_s \times N_d$ source/detector pairs, optimized values for the distribution of scattering and absorption parameters are obtained.
The theory was further extended to not only deal with intrinsic contrast but to also account for fluorescence contrast, termed as fluorescence diffuse optical tomography (fDOT). Fluorescence measurements can be obtained using appropriate filters in front of the detectors. Similar generic tomography principles are used for reconstructing the

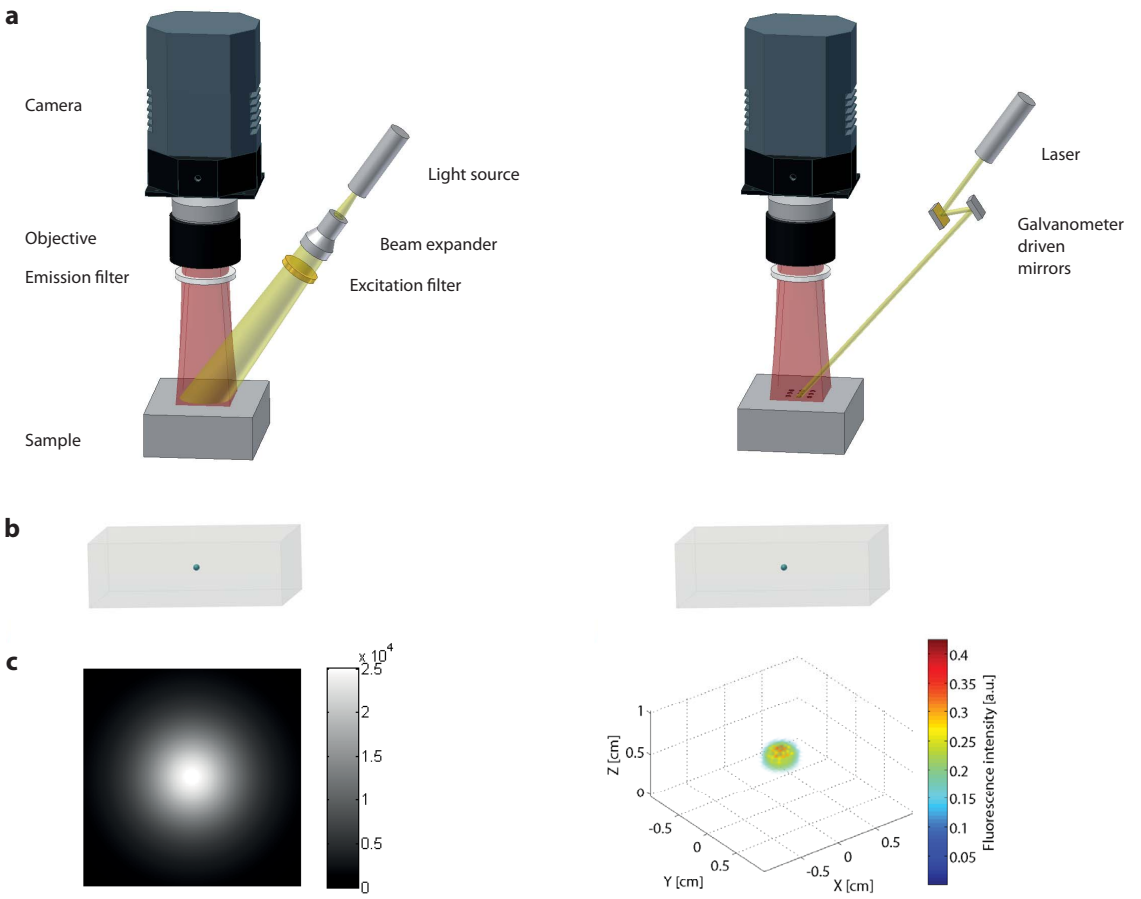

Figure 1.2: Planar and FMT imaging. **a** Setup. Schematic of a planar (left) and an FMT (right) measurement setup and its components in reflection geometry. Transmission geometry (not shown) can be easily achieved by installing either the camera or the source on the other side of the sample. **b** Schematic of an embedded fluorophore (turquoise) in depth of a cubic sample (gray). **c** (left) Imaging result of the planar setup showing the light distribution at the surface of the sample. Only qualitative information is obtained. (right) Reconstructed fluorophore of an FMT data set allowing the depth resolution and therefore quantification.

distribution of a fluorescence agent in the tissue. The use of targeted probes in DOT is what finally granted the access of optical tomography into the molecular imaging world. This technique was originally termed Fluorescence-mediated Molecular Tomography, but is currently referred to simply as Fluorescence Molecular Tomography (FMT) [28]. It represents a novel concept and a complete change of mindset and application targets when compared with DOT and fDOT, even though the physics behind them is equivalent. The main goal of FMT is to obtain molecular information on intact biological organisms.

There exist three basic illumination-detection technology schemes for optical tomography imaging [1, 13]: (a) the continuous wave (CW) domain using light of constant

intensity; (b) the frequency domain (FD) using light of modulated intensity (typically 100MHz-1GHz) and (c) the time-domain (TD) using ultrafast laser pulses (femtosecond to picosecond) [7]. The CW approach is attractive, as low cost illumination sources can be used and an optimal signal-to-noise performance is achieved due to the high stability and low noise characteristic of the light sources and detectors. Nevertheless the major drawback of the method is the difficulty of separating the contributions of absorption and scattering from the signal attenuation and the inability to image fluorescence lifetime. Time domain methods resolve the arrival of light from the laser pulse as a function of time at different positions on the tissue. Information from early arriving photons can be used to improve resolution since they have suffered less scattering events [29, 30]. Highly diffusive and thus delayed photons are rejected. TD methods are less sensitive (they record a smaller number of photons) and the instrumentation is noisier than CW systems due to time and intensity fluctuations associated with fast switching electronics and pulsing lasers. In FD technologies the laser intensity is frequency modulated, which allows the analysis of the emanating wave with regard to amplitude and phase shift. This allows measuring the tissue optical properties and the fluorochrome distribution. FD methods are less affected by ambient light than CW and TD methods. To improve the resolution compared to CW a modulation of several hundred MHz or higher is required. FD methods are less robust than CW methods because of the reduced signal-to-noise detection involved in sensing high frequencies. Therefore, for molecular imaging applications, where the signals are in general weak, CW technologies are advantageous because of better signal-to-noise performance [1]. This is comparable to DOT, where mainly endogenous absorption changes (e.g. blood oxygenation changes) and scattering properties of tissue are measured. For DOT application the imaging systems are based on TD or FD methods.
One of the first optical tomography scanners was developed for breast imaging in clinics. The DOT measurement setup worked in TD and was based on a parallel plate geometry [31] where the breast was slightly compressed and could therefore considered as a homogeneous slab during reconstruction. Additionally this development was also the first hybrid approach as in the parallel plates MR coils with fiducial markers were implemented to acquire simultaneous data sets. The first ICG enhanced breast images were in good correlation with the acquired contrast agent enhanced MR images in terms of lesion localization [32]. Some years later, driven by the fast development of fluorescent reporter systems in preclinical research and further theoretical understandings in the field of light propagation the first FMT scanner based on CW techniques and designed for cylindrical geometry for preclinical application was reported by Ntziachristos et. al [33]. Optical fibers were arranged in rings around a cylindrical cavity and connecting either detectors or light sources with the imaging chamber. The sample is placed vertically in the chamber, which was filled with a fluid matching the average optical properties of living tissue. A respectable spatial resolution of 3mm (resolved gap between two capillary tubes) and a detection limit of 1nM of Cy5.5 contained in 100μl was found in cylindrical phantoms [33] and revealed the potential of using optical tomography techniques to detect fluorescent probes in small animals which was

demonstrated by resolving enzymatic activity in brain tumors in mice [28]. This index matching fluid was on one hand used to increase signal-to-noise ratio and on the other hand to simplify theoretical constraints associated with boundary modeling: for the reconstruction the irregular object was assumed having quasi-cylindrical geometry.
Cylindrical fiber based systems using matching liquid based methods suffer from several limitations: due to geometrical constraints only a limited number of fibers can be used, reducing the number of source/detector pairs sampled. Other limitations are light loss due to coupling between tissue and fibers and restrictions with regard to body regions that can be sampled. It was shown in simulation analysis of a plane parallel geometry that an increased field of view and smaller distances between the detector fibers could improve the resolution [34]. Based on this knowledge a vertical parallel plate imager was developed for clinical breast imaging, where the breast is suspended in a tank filled with matching fluid and one plate was movable to compress tissue [35, 36]. The source fiber grid was attached on one side of the imaging chamber and the light was acquired on the other side of the chamber by using a CCD camera focused onto the glass window using a set of imaging lenses. With that, the fiber-optic detector could be replaced and the number of detector locations could be enormously increased allowing a higher resolution.
This vertical imaging geometry was then also used for preclinical applications in small animals [37]. These systems offer a higher number of source/detector pairs but still suffer from the limitation of fixed geometries, tissue compression and matching fluid. Using such a device a superiority of FMT over FRI could be demonstrated: in a mouse tumor study protease activity in the tumor could only be accurately visualized in the FMT data [37]. A further modification of a parallel plate imager was shown by Zacharakis et al. where the plates were horizontally installed and instead of fiber source illumination a free beam illumination was used in combination with a galvanometric driven mirror scanner for the point grid scanning [38].
A major conceptual step was the introduction of non-contact excitation/detection concepts for irregular geometries in FMT, for which there is no geometrical constraint due to optical fibers and no additional light dispersion due to the use of a fluid filled chamber [39]. This required the development of a theory for solving the problem of light propagation from diffuse media (tissue) into free-space (surrounding air) assuming detectors at positions away from the diffuse medium [40]. Experimental feasibility was demonstrated both in phantom studies [41] and *in vivo* [39]. It was successfully shown that a non-contact setup can be built for sample placements in a more natural horizontal position for lymph nodes [42] and lung tumor [43] imaging instead of the previously mentioned upright sample positioning setups. All of the so far mentioned setups have the limitation that due to a fixed positioning only parts of the animal can be imaged. Therefore a concept based on the rotating gantry principle used in CT was implemented to image the animal 360°. In such systems the sample is placed vertically in a rotating cylinder and can be transilluminated for 360° [44, 45]. A further advantage of these systems is the straight forward implementation of the surface capture by white light projection illumination [46]. Yet another interesting setup used to

image tumor bearing mice was proposed by Li et al. and is based on a conical mirror design [47]. The sample is place horizontally and is surrounded by the conical mirror allowing on one hand a sample surface extraction and on the other hand a non-contact detection and a free-beam illumination covering the animals surface in a half space.

1.2 Hybrid Imaging

Combining two or more imaging modalities that provide complementary information on tissue morphology and tissue-specific molecular processes is an attractive concept for improving diagnostic specificity and patient care. For example, the combination of positron emission tomography (PET) and CT has emerged as a sensitive tool in cancer diagnostics [48]. More recent developments relate to hybrid PET/MRI systems as clinical and preclinical imaging devices [49].
In the last decade the role of optics in multimodality imaging or hybrid imaging to generate complementary read-outs has become an attractive research area. Multimodal *in vivo* imaging systems enable visualization and quantitative assessment of anatomical, physiological, metabolic and cellular properties of an organism as well as its molecular constituents and/or pathways by exploiting different mechanisms generating an imaging signal. Due to economy of scale and technical complexity research today is focused on combining two individual techniques typically combining structural information with an additional readout. Examples are the combination of an anatomical method such as CT, MRI or ultrasound scanning with optical imaging methods providing cellular and molecular insight. Alternatively, optical imaging could be combined with positron emission tomography (PET) or single photon emission computer tomography (SPECT) both providing functional and/or molecular information.
Combinations with MRI are attractive due to the high quality structural information provided as a result of high soft-tissue contrast. MR images represent a weighted distribution of hydrogen nuclei (protons) in the body, the principal signal contributors being the protons of water and adipose tissue. Nuclei with odd proton and/or neutron number such as the proton possess a magnetic moment, i.e. behave as tiny magnets. In a strong magnetic field magnetic moments align either parallel or opposed (anti-parallel) to the field direction, with slight excess in the parallel orientation leading to a net macroscopic magnetization. Irradiation with electromagnetic waves of a certain frequency (the Larmor frequency, which corresponds to the difference in energy between the parallel and anti-parallel state) will excite the spin system and generate observable non-equilibrium magnetization that is measured using an MRI receiver coil. The MRI signals decay by relaxation processes (T_1,T_2,T_2*) that are tissue specific and constitute the source of the high soft-tissue contrast of the method. Dedicated MRI methods also yield accurate information on tissue physiology that might be intimately linked to the underlying molecular processes. Moreover, MRI does not involve ionizing radiation like CT.
Mapping of molecular processes *in vivo* demands for high sensitivity of the imaging

modality as provided e.g. by PET. However, applications of PET may be limited by the short half-life of commonly used positron emitting isotopes, which requires on-site synthesis of PET tracers and correspondingly access to a cyclotron and radiochemistry facility. In contrast, fluorescence markers are in general stable and, when emitting in the near-infrared range, suited for imaging structures deeply embedded in tissue. Therefore, fluorescence imaging has emerged as an alternative to PET for small animal imaging yielding comparable molecular sensitivity. In view of the strengths of the two modalities the combination of MRI and fluorescence imaging constitutes an attractive concept for preclinical research [17].
In designing a hybrid FMT/MRI instrument, two strategies can be pursued for merging information generated by different imaging techniques: 1) measurements can be carried out sequentially using a sample support that is compatible with several modalities. Proper alignment of images (registration) is carried out by data post-processing using anatomical landmarks of fiducial markers based on either rigid body transformation ignoring any deformation or more advanced non-rigid registration algorithms compensating for movement/deformation of the subject. Such an approach benefits from the full performance of the individual imaging modalities. Its obvious disadvantage is that it precludes the simultaneous study of biological processes and that sample motion during the transfer cannot be excluded. 2) By integrating more than one type of imaging technology into one functional unit these issues are inherently addressed. Such a system would allow for simultaneous data acquisition under identical physiological conditions and also eliminates the registration problem. The technical challenge for an integrated solution is to maintain the performance level of the individual techniques in the combined system, i.e. avoiding or at least minimizing any potential interference between the systems. The high magnetic field strengths (>1.5T) and the restricted access to the sample render a hybrid design involving the incorporation of the FMT into an MRI scanner, rather challenging. Non magnetic optical components have been developed for this purpose. For biomedical research such devices would be highly attractive as they would allow for multiplexed time-correlated measurements of biological system in the same physiological or diseased state.
A prerequisite for combining two (or more) functional/molecular imaging approaches is availability of multimodal probes targeting the same biological process but using different reporter moieties that can then be visualized by different modalities.
Instrumentation and theoretical development for combining MRI with optical imaging e.g. integrated DOT/MRI systems was driven by the need of an efficient detection for early stage breast tumor in women. Breast tissue is relatively weakly absorbing and therefore lend itself for optical imaging studies. As discussed in the previous section the structural and dynamic contrast enhanced MRI imaging method was complemented by optical imaging targeting tumor angiogenesis. The sensitivity of the optical readout for assessing the tumor vasculature was increased by using the fluorescent dye indocyanine green (ICG), an intravascular agent approved for clinical use [32]. An overview about technologies for breast cancer management with optical and combined optical and MR systems is given in [50]. FMT may become a powerful tool in breast imaging

once target-specific fluorescent agents capable of highlighting physiological processes associated with cancer pathology become available for diagnostic applications. It is not surprising that breast studies are in the focus of FMT/DOT method development. Experiments using "breast-like" phantoms with fluorescent inclusions [51] or simulations based on MR images of breast tissue [52] should demonstrate the potential of these combined techniques.
Another clinical application using hybrid imaging was focussing on brain imaging and has been used to compare the functional MRI (fMRI) signal evoked by an external stimulus with hemodynamic changes assessed by DOT. Consistency in spatial localizations of fMRI and DOT signals in activated brain regions was demonstrated. Structural MRI information has been used to generate a patient specific head model [53] or to fuse fMRI and DOT information into one model to generate a joint estimate of the underlying physiological contrast [54].
Nevertheless, the focus of studies addressing hybrid FMT/MRI systems relate to preclinical applications. The first presented approaches combining FMT with MRI were sequentially acquired and were carried out by Ntziachristos et al. [28] who analyzed cathepsin B activation in 9L gliosarcoma in nude mice. By superposition of the reconstructed fluorescence intensity distribution indicating protease activity and the gadolinium enhanced MR image the correct localization of the optical signal in the corresponding MR brain slice could be revealed. A related study of a mouse brain glioma model was recently performed by McCann et al. where FMT was applied to image protease activity in the tumor using a commercial FMT system while the subsequently recorded MRI data provided the anatomical reference [55]. The authors claim that only the combined analysis of FMT and MRI data correctly predicted the effects of chemotherapeutic intervention. By having a MR sample platform which is compatible with a bioluminescence system, it has been shown that the accurate knowledge of tissue layers segmented from an MR image can improve the bioluminescence imaging [56].
All integrated solutions for preclinical combinations of FMT/MRI found in literature uses a fiber based FMT as an insert into either a clinical MRI magnet or a preclinical MR scanner. For this setup the fibers have to be brought in physical contact with the sample. Such design constitutes a compromise in terms of imaging performance for both modalities. Space requirements of fiber bundles may not be compatible with dimensions of high-field small animal MRI scanners [57]. Therefore the animals were measured using a human scanner with a large bore compared to animal scanners. This will compromise spatial resolution and thus the quality of structural information. On the other hand performance is affected by light loss due to inevitable loss in coupling to the fibers guiding the light to the detectors located outside the MRI magnet and that these fibers recover light only from a small part of the surface. Moreover such systems are bulky and restricted with regard to the relatively low number of source/detector pairs [58] and also with regard to the flexibility in potential excitation schemes. Nevertheless such a system was successfully implemented and proof of concept was demonstrated for mouse brain where human glioma tumor cells were im-

planted intracranially [57, 59]. The tumor area was segmented according to the MRI image and an improvement in tumor localization could be shown by applying the prior knowledge. Recently the setup has been used to assess the epidermal growth factor receptor (EGFR) status in an animal model of brain tumor. Tissue regions segmented on the basis of the MR image were used to guide the reconstruction of fluorescence distribution of the NIR fluorescent dye conjugated to the EGF ligand [60]. The setup comprises a single ring of fibers connected to light sources and detectors and therefore allows the fluorescence reconstruction of one single slice. The corresponding slice in the MRI data is identified on the basis of fiducial markers mounted at the fiber tip in contact with the animal. Similar systems has been developed for DOT imaging to measure changes to study rat cerebral oxygen consumption [61] or to visualize increased blood volume in rodent breast tumor models [62]. In all cases, structural information was used for the reconstruction of optical data.

1.3 Fluorescent Probes

Target specific probes that report on cellular and molecular processes in the living organism are the key to molecular imaging. There are two strategies for probe design: exogenous synthetic and genetically encoded reporter systems. The design of exogenous probes comprise a targeting moiety (e.g. a receptor binding ligand) and a reporter moiety that will generate a signal detected by the respective imaging modality. It is important that the reporter group has no or only a minimal effect on the target interaction of the probe, i.e. it should not interfere with the pharmacophor of the targeting moiety responsible for the receptor binding. Molecular targets typically occur at low concentration increasing the demands on the sensitivity of the reporter principle. Optical and in particular fluorescence techniques provide excellent sensitivity and are therefore highly attractive for such applications. Each fluorescent probe has a specific characteristic in terms of an absorption and emission spectrum (Fig. 1.3) which is needed to select appropriate spectral excitation and emission ranges.
Optical reporters can be divided into three main groups: small synthetic, organic dyes such as cyanine-, oxazine-compounds (e.g. Cy5.5 or AOI987), genetically encoded fluorescent proteins such as green fluorescence protein (GFP) or tdTomato and semiconductor solid-state nanoparticles such as quantum dots. Dye molecules and fluorescent proteins contain a structure with delocalized π-electrons, the dimension of which determines the absorption/excitation spectrum. As a rule of thumb we may state that the longer the π-system the more red-shifted the spectrum. This property has been used for the design of red and near-infrared dyes as well as for the genetical engineering of red-shifted fluorescent proteins [63, 64].
An attractive feature of fluorescence is that it can be modulated by the environment (this, of course, if not taken into account also represents an uncontrolled variable in an imaging experiment). Chemical reactions may modify the structure of the fluorophore and thereby the absorption/emission spectrum of fluorescent dyes may interact with

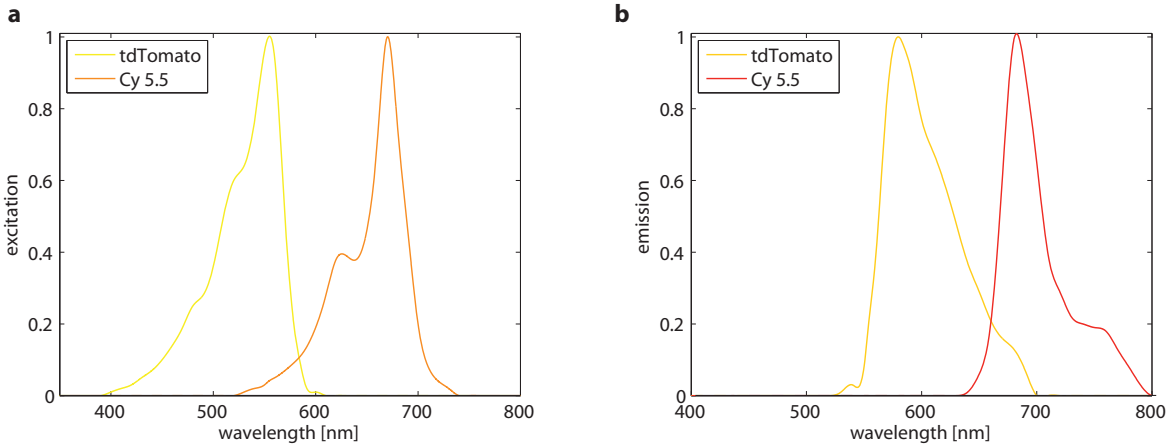

Figure 1.3: Fluorophore spectra: **a** Excitation spectra of the canine dye Cy5.5 and the fluorescent protein tdTomato and the corresponding emission spectra **b**.

nearby molecules leading to fluorescence quenching or resonance energy transfer. These properties have prompted the development of so-called smart or activatable probes, the fluorescence intensity of which is altered upon interaction with their molecular target, e.g. switched 'on' and 'off' when the dye is interacting with a nearby quenching molecule [65]. Such probe designs are advantageous since an unbound probe would not give rise to a fluorescence signal, which results in a high target-to-background ratio (TBR). Similar designs are not feasible for radiotracer probe, which are always 'on', i.e. the radionuclide decays with a certain probability; correspondingly TBR may be compromised.

Quantum dots display a broad excitation but a narrow emission spectrum, the central frequency of which depends on the physical dimension of the quantum dot (as long it does not exceed the Bohr radius of the electron-hole pair). As a consequence different quantum dots can be excited with a single excitation wavelength, a property that lends itself for multiplexing studies, i.e. simultaneous probing of multiple processes. The drawback of this class of probes is the challenging spectral unmixing procedure to assign the different fluorescent wavelength to the studied multiple processes. Another interesting class of nanoparticles are phosphor nanoparticles consisting of a crystalline matrix doped with lanthanide ions. They display lower toxicity than quantum dots and offer the possibility of upconversion, which means that emission is observed at a shorter wavelength (i.e. corresponding to a higher energy difference) than the excitation wavelength. The main advantage of these probes is the complete removal of autofluorescence and therefore better imaging performance. The mechanism underlying upconversion is based on multiple photon absorption and shows advantages of sharp emission lines, long lifetimes and superior photostability [66, 67, 68]. Phosphor nanoparticles have also been used for X-ray luminescence CT [69, 70] which is based on the conversion of X-ray into visible light.

1.4 Aim of the Thesis

In the first part of this thesis the theory of fluorescence optical tomography imaging is discussed starting from the radiative transfer equation and closing with the applied inversion technique.
In chapter two it is described which mathematical steps and assumptions are needed to derive the diffusion equation from a radiative transfer model. As the radiative transfer equation, which precisely describes the processes involved in light propagation in a medium is rather complex, it is nowadays common to use the diffusion equation to describe the processes of light propagation in tissue or in general in a turbid medium.
Chapter three deals with the simplest solution of the diffusion equation for an infinite homogeneous medium for an excitation and a fluorescence source term. It is obvious that the fluorescence light which is produced internally by the excited fluorophores needs an other treatment to derive the solution to the diffusion equation compared to the excitation term.
However, for real experiments we deal with a bounded sample and therefore this case needs to be specially treated to derive a solution which is outlined in chapter four. A first part is dedicated to the boundary conditions and how the light intensity and flux can be described at the surface of a sample. Since in a non-contact setup the detector is placed at some distance from the sample a description of the light propagation from the surface of the sample to the detector is described. To complete this forward modeling procedures new ideas to simplify the problem are shown such as the boundary removal and the source intensity profile concept.
The last chapter of the theoretical part is devoted to the inverse problem which deals with inverting the forward model and retrieving the distribution of the fluorophore concentration within the sample. It is shown that the measurement normalization reduces the amount of hardly definable parameters without impairing the results. By using another simplification where the volume of interest is discretized into a number of voxels, the concept of the weight matrix which is a measure for the contribution of each voxel to the whole volume is explained. To close the part concerning the inverse problem an iterative technique to invert the set of linear equations, the so called algebraic reconstruction technique is described.
Chapter six focusses in the first part on the technical realization and implementation of a non-contact FMT imager operating at multiple-wavelength and working either in reflection or transmission mode. The system was further validated *in vivo* to extract the fluorophore concentration by investigating oxazine dye labeled plaques in the brain of mice developing Alzheimer's disease, imaging inflamed lymph nodes with a labeled antibody approach and providing a molecular readout in processes involved in bone resorption and formation.
Finally, in chapter seven, a newly developed hybrid FMT/MRI system based on a non-contact FMT is presented. A new concept of combining the two imaging modalities could be shown based on a 32×32 single photon avalanche diode array. It was demonstrated that the miniaturized optical detection insert was working properly in

a small animal MRI scanner operating at a magnetic field strength of 9.4T. Phantom performance tests and an *in vivo* proof of principle study in tumor bearing mice showed a proper setup functioning. As the first generation system bears some limitations in terms of the chosen reflection geometry, the small size of the detector array and the cumbersome handling a second generation setup was developed enabling either reflection or transmission illumination and using a 256×256 CMOS array based on a rigidly fixed rail system. Again performance tests were carried out as well as a proof of principle study in Alzheimer's disease animals was demonstrated.

Chapter 2

From Radiative Transfer Equation to the Diffusion Equation

Two theories can be distinguished when modeling light propagation in a highly scattering media where multiple scattering events dominates the fluctuation and characteristics of a wave: One is the analytical theory or multiple scattering theory and the other one is the radiative transport theory.
The analytical theory starts with the differential equation of the Maxwell equations or the wave equation. This method is mathematically complete and accounts for all effects (absorption, scattering, diffraction, interference,...) involved in multiple scattering problems but is impractical to use.
The radiative transport theory on the other hand is based on the radiative transfer equation (RTE) which describes the transport of energy through a medium containing particles. The theory is heuristic and mathematically not as rigorous as the analytical theory but is nowadays widely used to describe highly scattering problems as they occur for example in tissue samples.
The solution of the RTE is computational expensive and no general analytical (closed-form) solutions are available and therefore simple approximation models are usually applied. An approximation which is often and successfully used to model light propagation dominated by multiple scattering is the so-called diffusion approximation. This approach yields to the diffusion equation (DE) which is used to describe the problem for steady-state and time-dependent sources.
In this chapter we first introduce the quantities describing the radiative transfer which leads to the RTE. Moreover the derivation of the diffusion equation from RTE is shown and the different forms in frequency and time domain for time dependent or steady state conditions are listed.

2.1 Basic Quantities Used to Describe Radiative Transfer

A radiometric quantity to characterize the light passing through a medium and its interaction is described by the **radiance** or the **specific intensity** $L(\mathbf{r}, \hat{\mathbf{s}}, t)$ [W cm^{-2} sr^{-1}]. It describes the amount of monochromatic light passing through a particular area oriented in the direction of the unit vector $\hat{\mathbf{s}}$ at position $\mathbf{r}$ and falling within a given solid angle at time t.
The radiance $L(\mathbf{r}, \hat{\mathbf{s}}, t)$ is related to the energy density $u(\mathbf{r}, t)$ at position $\mathbf{r}$ at time t as follows: The energy dE crossing an area dS in the time interval dt in a direction $\hat{\mathbf{s}}$ normal to it within a solid angle $d\Omega$ is described by $dE = L(\mathbf{r}, \hat{\mathbf{s}}, t)\, dS\, d\Omega\, dt$ and occupies the volume $dV = dS\, \upsilon\, dt$ where υ is the speed of light in a medium. The energy density du is therefore

$$du = \frac{dE}{dV} = \frac{L(\mathbf{r}, \hat{\mathbf{s}}, t)\, dS\, d\Omega\, dt}{dS\, \upsilon\, dt} = \frac{L(\mathbf{r}, \hat{\mathbf{s}}, t)\, d\Omega}{\upsilon} \tag{2.1}$$

with units [J cm^{-3} sr^{-1}]. By taking the radiation in all directions into account the energy density is given by

$$u(\mathbf{r}, t) = \frac{1}{\upsilon} \int_{4\pi} L(\mathbf{r}, \hat{\mathbf{s}}, t)\, d\Omega \tag{2.2}$$

which has units [J cm^{-3}].
The energy density $u(\mathbf{r}, t)$ is related to the average intensity $U(\mathbf{r}, t)$ by $u{=}U/\upsilon$ and can be written as

$$U(\mathbf{r}, t) = \int_{4\pi} L(\mathbf{r}, \hat{\mathbf{s}}, t)\, d\Omega \tag{2.3}$$

and similarly the flux density $\mathbf{J}$ is defined as

$$\mathbf{J}(\mathbf{r}, t) = \int_{4\pi} L(\mathbf{r}, \hat{\mathbf{s}}, t)\, \hat{\mathbf{s}}\; d\Omega \tag{2.4}$$

both with units [W cm^{-2}].
The total normal flux density J_{tot} that traverses a differential area dA is given by

$$J_{tot} = \mathbf{J}(\mathbf{r}, t) \cdot \mathbf{n} = J_{out}(\mathbf{r}, \mathbf{n}, t) - J_{in}(\mathbf{r}, \mathbf{n}, t) = \int_{4\pi} L(\mathbf{r}, \hat{\mathbf{s}}, t)\, \hat{\mathbf{s}} \cdot \mathbf{n}\, d\Omega \tag{2.5}$$

where $\mathbf{n}$ is the surface normal of a certain differential area dA, J_{out} the outward and J_{in} the inward flux density into the corresponding half space given in terms of L as

$$J_{out}(\mathbf{r},\mathbf{n},t) = \int_{(2\pi)^+} L(\mathbf{r},\hat{\mathbf{s}},t)\,\hat{\mathbf{s}}\cdot\mathbf{n}\,d\Omega \tag{2.6}$$

$$J_{in}(\mathbf{r},\mathbf{n},t) = \int_{(2\pi)^-} L(\mathbf{r},\hat{\mathbf{s}},t)\,\hat{\mathbf{s}}\cdot(-\mathbf{n})\,d\Omega\ . \tag{2.7}$$

If the light is treated as an ensemble of photons which is a common description in particle physics we can convert any of the radiometric quantities into quantities related to particles by substituting the unit J by photons/$h\nu$ where $h = 6.626\cdot 10^{-34}$Js is the Plank's constant and ν [1/s] is the photon frequency. The energy density $u(\mathbf{r},t)$ [J cm^{-3}] becomes the photon density $\Phi(\mathbf{r},t) = u(\mathbf{r},t)/h\nu$ [#photons cm^{-3}].
So far the introduced quantities describe the light propagation through a turbid media in a general case of a time-dependent source. These quantities are well suited to describe a time resolved response for a source emitting energy with a function of time. In most cases the tissue is illuminated with a steady state CW source emitting a constant power. In these cases the responses of the radiance, the fluence, and the flux are time independent an can be written as $L(\mathbf{r},\hat{\mathbf{s}})$, $U(\mathbf{r})$, $\mathbf{J}(\mathbf{r})$ and $\Phi(\mathbf{r})$.

2.2 The Radiative Transfer Equation

The principle of wave energy conservation for light propagating through a volume element of an absorbing and scattering turbid medium can be formulated in a differential equation. It describes the different mechanisms by which the radiance can increase or decrease inside an arbitrary volume. The equation is derived from the Boltzman equation used in neutron transport theory [71, 72] and is called equation of transfer in radiative transfer theory [73, 74, 75] or radiative transfer equation (RTE).
The RTE can be written in case of **time-dependent sources** as

$$\begin{aligned}\frac{1}{\upsilon}\frac{\partial L(\mathbf{r},\hat{\mathbf{s}},t)}{\partial t} &+ \hat{\mathbf{s}}\cdot\nabla L(\mathbf{r},\hat{\mathbf{s}},t) + \mu_t\,L(\mathbf{r},\hat{\mathbf{s}},t)\\ &= \mu_s\int_{4\pi} L(\mathbf{r},\hat{\mathbf{s}}',t)\,p(\hat{\mathbf{s}},\hat{\mathbf{s}}')\,d\Omega' + S(\mathbf{r},\hat{\mathbf{s}},t)\end{aligned} \tag{2.8}$$

where μ_t [cm^{-1}] is the total attenuation coefficient defined as

$$\mu_t = \rho\,\sigma_t = \rho\,(\sigma_a + \sigma_s)\ . \tag{2.9}$$

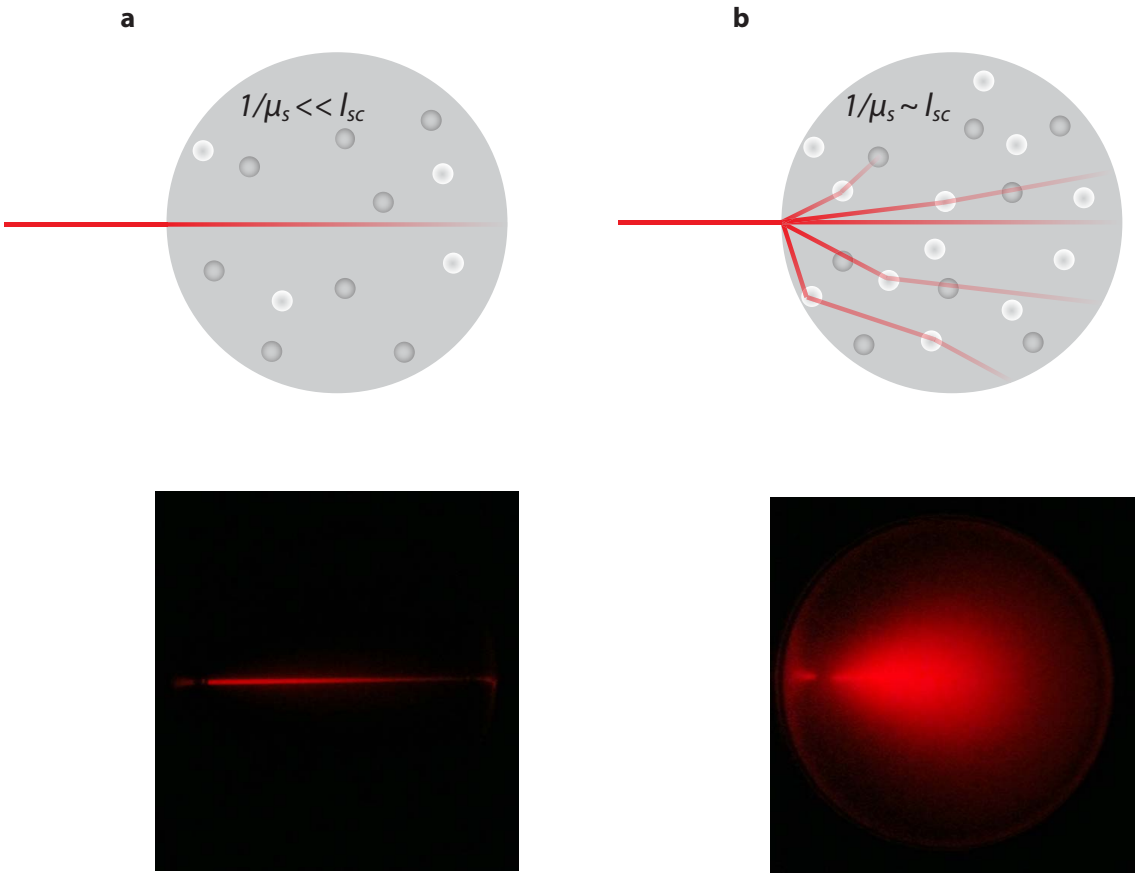

Figure 2.1: Light propagation in tissue. **a** Highly absorbing medium where the mean free path l_{sc} defining the distance between two scattering events is large compared to $1/\mu_s$, μ_s being the scattering coefficient. In this case the light intensity decreases with the distance d according to $I \propto I_0 \exp(-\mu_t d)$ where $\mu_t = \mu_s + \mu_a$. **b** Highly scattering medium where l_{sc} is approximately $1/\mu_s$. This case represents the situation in tissue where light propagation can be modeled with diffusion theory.

In Eq. (2.9) ρ [1/cm^3] is the density of scatterers, σ_a the absorption cross-section and σ_s the scattering cross-section. Therefore μ_t can be written as $\mu_t = \mu_a + \mu_s$, where μ_a and μ_s ar the scattering and absorption coefficients, respectively.
In terms of μ_s the mean free path l_{sc} (scattering mean free path) can be defined as

$$l_{sc} = \frac{1}{\mu_s} \tag{2.10}$$

which is defining the distance between two scattering events. The mean free path is not influenced by the absorption since the mean time between two scattering events $t_{sc} = l_{sc}/v$ is not changed by the absorption.

The absorption reduces only the intensity and therefore the absorption length l_a can be defined in terms of the absorption coefficient μ_a as

$$l_a = \frac{1}{\mu_a} \tag{2.11}$$

which defines the distance at which the light intensity decreases by a factor of e following an exponential law, i.e. $L \propto \exp(-\mu_a\, d)$.
The term $p(\hat{\mathbf{s}}, \hat{\mathbf{s}}')$ denotes the normalized scattering phase function which represents the probability of scattering from direction $\hat{\mathbf{s}}$ into direction $\hat{\mathbf{s}}'$.

In the following the meaning of the different terms in Eq. (2.8) is described:

$\frac{1}{\upsilon}\frac{\partial L(\mathbf{r},\hat{\mathbf{s}},t)}{\partial t}$: the temporal change in number of photons entering and leaving at position $\mathbf{r}$ in direction $\hat{\mathbf{s}}$ at time t.

$\hat{\mathbf{s}} \cdot \nabla L(\mathbf{r},\hat{\mathbf{s}},t)$: transport of photons (flux of photons) from position $\mathbf{r}$ in direction $\hat{\mathbf{s}}$.

$\mu_t\, L(\mathbf{r},\hat{\mathbf{s}},t)$: change in number of photons (loss) at position $\mathbf{r}$ that move in the direction $\hat{\mathbf{s}}$ due to attenuation (scattering and absorption).

$\mu_s \int_{4\pi} L(\mathbf{r},\hat{\mathbf{s}}',t)\, p(\hat{\mathbf{s}},\hat{\mathbf{s}}')\, d\Omega'$: scattering from all directions $\hat{\mathbf{s}}'$ into direction $\hat{\mathbf{s}}$ at position $\mathbf{r}$ at time t. This corresponds to a net increase in L and thus represents a pseudo source term.

$S(\mathbf{r},\hat{\mathbf{s}},t)$: photon source term, i.e. the number of photons per unit volume and time at position $\mathbf{r}$ with velocity υ in direction of $\hat{\mathbf{s}}$ at time t with units of [W m^{-3} sr^{-1}]

For **steady-state sources** such as CW sources the RTE can be written as

$$\hat{\mathbf{s}} \cdot \nabla L(\mathbf{r},\hat{\mathbf{s}}) + \mu_t\, L(\mathbf{r},\hat{\mathbf{s}}) = \mu_s \int_{4\pi} L(\mathbf{r},\hat{\mathbf{s}}')\, p(\hat{\mathbf{s}},\hat{\mathbf{s}}')\, d\Omega' + S(\mathbf{r},\hat{\mathbf{s}})\ . \tag{2.12}$$

2.3 Derivation of the Diffusion Equation

Given that no analytic solutions for the RTE exists solutions are usually based on numerical methods. These methods are in general computationally very expensive and therefore much simpler approximate models are used as a closed solution to the RTE. One of this widely used and successful model is the diffusion approximation [76, 77, 78] which can be derived for steady-state and time-dependent sources. This approximation leads then to the diffusion equation [79] which is nowadays widely used to describe diffuse light propagation.

2.3.1 Diffusion Approximation

For the diffusion approximation the radiance, the phase function and the source term are expanded in a series of spherical harmonics $Y_{l,m}$ which can be stopped at $l = N$. A complete derivation of the spherical harmonics expansion of the RTE can be found in Appendix A.2.
In order to derive the diffusion approximation it is enough to truncate the spherical harmonics expansion after the second term which is then denoted as the P_1 approximation [1] where $l = 1$ and only the isotropic and linearly anisotropic terms are retained. The result is a pair of coupled differential equations

$$\frac{1}{\upsilon}\frac{\partial}{\partial t}U(\mathbf{r},t) + \mu_a\, U(\mathbf{r},t) + \nabla\,\mathbf{J}(\mathbf{r},t) = S_0(\mathbf{r},t) \tag{2.13}$$

$$\frac{1}{\upsilon}\frac{\partial}{\partial t}\mathbf{J}(\mathbf{r},t) + \frac{1}{3D}\,\mathbf{J}(\mathbf{r},t) + \frac{1}{3}\,\nabla U(\mathbf{r},t) = \mathbf{S}_1(\mathbf{r},t)\ . \tag{2.14}$$

In addition to the P_1 approximation the following assumptions are made:

- The temporal variation in the flux density is much smaller than the average time between scattering events affecting the average intensity of a highly scattering media, such as tissue. Therefore we can write

$$\frac{\partial}{\partial t}\mathbf{J}(\mathbf{r},t) << \frac{\upsilon}{3}\,\mu_s'\,\mathbf{J}(\mathbf{r},t) \tag{2.15}$$

  and assume that $\frac{\partial}{\partial t}\mathbf{J}(\mathbf{r},t)$ is negligible[2].

[1] A complete derivation of the P_1 approximation can be found in Appendix A.3

[2] Expression 2.15 can be found by analyzing Eq. (2.14):
$\nabla U(\mathbf{r},t) = 3\,\mathbf{S}_1(\mathbf{r},t) - 3\,\frac{1}{\upsilon}\left(\frac{\partial}{\partial t} + \frac{\upsilon}{3}\,\mu_s' + \frac{\upsilon}{3}\,\mu_a\right)\mathbf{J}(\mathbf{r},t)$

- We assume that the photon sources are isotropic and therefore

$$\mathbf{S}_1(\mathbf{r}, t) = 0 \ . \tag{2.16}$$

Taking the assumption in Eqs. (2.15) and (2.16) into account, Eq. (2.14) reduces to

$$\frac{1}{3D}\,\mathbf{J}(\mathbf{r}, t) + \frac{1}{3}\,\nabla\, U(\mathbf{r}, t) \;\; = \;\; 0 \tag{2.17}$$

resulting in Fick's law of diffusion for the average intensity

$$\mathbf{J}(\mathbf{r}, t) = -D\,\nabla\, U(\mathbf{r}, t) \ . \tag{2.18}$$

By replacing $\mathbf{J}(\mathbf{r}, t)$ in Eq. (2.13) by the expression derived in Eq. (2.18) we obtain the diffusion equation for a homogeneous media.

2.3.2 Diffusion Equation

The above mentioned approximations and assumptions lead to the **diffusion equation for a homogeneous media in time domain**[3]

$$\frac{1}{\upsilon}\,\frac{\partial}{\partial t}\,U(\mathbf{r}, t) - D\,\nabla^2\, U(\mathbf{r}, t) + \mu_a\, U(\mathbf{r}, t) \;\; = \;\; S_0(\mathbf{r}, t) \tag{2.19}$$

where the diffusion coefficient D [cm] can be written in a general form as [80]

$$D \;\; = \;\; \frac{1}{3\,(\mu_s' + \alpha\,\mu_a)} \tag{2.20}$$

accounting for the absorption effects[4]. In our analysis we only consider homogeneous media where μ_a and μ_s are constant throughout the media and therefore do not depend on the position $\mathbf{r}$. Even though in a complex and anisotropic medium such as

[3] Expressions for the frequency domain and heterogeneous media are given in Appendix A.4

[4] Another definition of D is given by $D = \upsilon/3\,(\mu_s' + \alpha\,\mu_a)$, where υ is the speed of light in the medium. This is commonly used when the diffusion approximation is derived in terms of energy density instead of the here listed average intensity since they are related by $u = U/\upsilon$

biological tissue constant optical properties seems to be invalid. Nevertheless it was proven in the past that the light propagation in tissue described by the diffusion equation and assumed constant optical properties leads to accurate results.
The so-called reduced scattering coefficient μ_s' is defined as

$$\mu_s' = \mu_s \left(1 - g\right) \tag{2.21}$$

where g is the anisotropy factor accounting for the direction of scattering (g values close to 1 represents strong forward scattering). Therefore we can define the transport mean free path l_{tr}

$$l_{tr} = \frac{1}{\mu_s'} = \frac{l_{sc}}{1 - g} \ . \tag{2.22}$$

If we consider the case of fully isotropic scattering ($g = 0$) where no preferred scattering direction is dominant one obtains $l_{tr} = l_{sc}$. This states that after one scattering mean free path the radiation can be scattered to any direction. Considering a highly anisotropic medium, such as tissue then $g \approx 1$ (typical values of g in tissue range from 0.7 to 0.95 [81]) and $l_{tr} \approx \infty$ which means that radiation can propagate large distances without changing its direction. This leads furthermore to the conclusion that the transport mean free path describes the distance which lights travels before the propagation direction is completely randomized due to several scattering events. This leads to the statement that $1/\mu_s'$ defines the distance where the scattering can be regarded as isotropic.
The factor α depends on the absorption, scattering and anisotropy of the medium and was derived by J. Ripoll et al. [82] as

$$a = 1 - \frac{4}{5} \frac{\mu_s' + \mu_a}{\mu_s' \left(1 + g\right) + \mu_a} \ . \tag{2.23}$$

In the wavelength range of 600-900nm, the so called diagnostic window for optical imaging where the tissue absorption is minimal either the special case of $\alpha = 1$ or $\alpha = 0$ is used for calculating the value of D.

Chapter 3

Solution of the Diffusion Equation for Infinite Homogeneous Media

Although most objects are bounded by a surface we will derive first a solution for the case of an infinite homogeneous medium. For all following calculations we assume a constant CW illumination, therefore all time dependent terms vanish and the diffusion equation for a homogeneous media turns into a steady state equation

$$-D\,\nabla^2 U(\mathbf{r}) + \mu_a\,U(\mathbf{r}) \;=\; S_0(\mathbf{r})\;. \tag{3.1}$$

If we consider an experiment, we realize that we have to deal with two sources of light: one source is the laser excitation at a wavelength λ_{exc} that illuminates the medium and the embedded fluorescent probes and the other source is the emitted light at wavelength λ_{fl} of the excited fluorescent probes.
In this chapter we first derive a solution for the diffusion equation Eq. (3.1) for a steady state excitation source term which will describe the propagation of the excitation light. Second we derive an expression for the fluorescence source term and apply that on the diffusion equation Eq. (3.1) to derive a solution for the emitted fluorescence light propagating in the medium.

3.1 Solution for the Excitation Source Term

As already mentioned we consider a CW laser source illuminating the sample and exciting the embedded fluorophores. A common approach to model the illumination source is to define a point source located at $z \sim l_{tr}$ (l_{tr} is the transport mean free path length) inside the scattering medium. To get the excitation source term a common approach has been applied: The source is defined in the scattering media as a point source located at $z \sim l_{tr}$ (l_{tr} is the transport mean free path length) inside the medium. It has been shown, that this simple approach provides good results even

for small source/detector separations in phantoms and *in vivo* experiments [83]. The excitation point source can be modeled by a delta function which implies an isotropic light distribution. Therefore the excitation source term can be written as

$$S_0(\mathbf{r}, \mathbf{r}_s) \;=\; S_{dc}\,\delta(\mathbf{r} - \mathbf{r}_s) \tag{3.2}$$

where S_{dc} is the source strength.

Using now the source term defined in Eq. (3.2) with Eq. (3.1) we obtain

$$-\,D\,\nabla^2\,U(\mathbf{r}) + \mu_a\,U(\mathbf{r}) \;=\; S_{dc}\,\delta(\mathbf{r} - \mathbf{r}_s)\;. \tag{3.3}$$

Eq. (3.3) can be transformed into a Helmholtz equation

$$\left(\nabla^2 + k_{dc}^2\right)\,U(\mathbf{r}, \mathbf{r}_s) \;=\; -\,\frac{S_{dc}\,\delta(\mathbf{r} - \mathbf{r_s})}{D} \tag{3.4}$$

where the diffusion wave number k_{dc} results in

$$k_{dc} \;=\; i\,\sqrt{\frac{\mu_a}{D}}\;. \tag{3.5}$$

A Helmholtz equation can be solved in general by use of Green's functions

$$\left(\nabla^2 + k^2\right)\,G(k \mid \mathbf{r} - \mathbf{r}' \mid) \;=\; -\delta(\mathbf{r} - \mathbf{r}') \tag{3.6}$$

where $G(k \mid \mathbf{r} - \mathbf{r}' \mid)$ is the solution function which can be written in case of an infinite homogeneous medium in a closed form as

$$G(k \mid \mathbf{r} - \mathbf{r}' \mid) \;=\; \frac{e^{ik|\mathbf{r}-\mathbf{r}'|}}{4\pi \mid \mathbf{r} - \mathbf{r}' \mid}\;. \tag{3.7}$$

According to the solution of a Helmholtz equation Eq. (3.7) we can write as a solution for the average intensity of an excitation point source with source strength S_{dc} in an

infinite homogeneous medium the following term [84]

$$\begin{aligned} U_{exc}(\mathbf{r},\mathbf{r}_s) &= \frac{S_{dc}}{D_{exc}} \frac{e^{ik_{dc}|\mathbf{r}-\mathbf{r}_s|}}{4\pi \mid \mathbf{r}-\mathbf{r}_s \mid} \\ &= \frac{S_{dc}}{D_{exc}} \frac{e^{-k_{exc}|\mathbf{r}-\mathbf{r}_s|}}{4\pi \mid \mathbf{r}-\mathbf{r}_s \mid} \end{aligned} \tag{3.8}$$

where $k_{exc} = \sqrt{\frac{\mu_a}{D}}$.
Considering a more general case of a spatially distributed source term $S(\mathbf{r},\mathbf{r}_s) = S_{dc}(\mathbf{r})\,\delta(\mathbf{r}-\mathbf{r}_s)$ the solution of the diffusion equation is written as follows

$$\begin{aligned} U_{exc}(\mathbf{r},\mathbf{r}_s) &= \frac{1}{4\pi\, D_{exc}} \int_V dV' \, \frac{S_{dc}(\mathbf{r}')\, e^{-k_{exc}|\mathbf{r}'-\mathbf{r}_s|}}{\mid \mathbf{r}'-\mathbf{r}_s \mid} \\ &= \frac{1}{D_{exc}} \int_V dV' \, S_{dc}(\mathbf{r}')\, g(k_{exc} \mid \mathbf{r}'-\mathbf{r}_s \mid) \end{aligned} \tag{3.9}$$

where g denotes the Green's function for an infinite homogeneous medium.

3.2 Solution for the Fluorescent Source Term

The fluorescence process is triggered by the absorption of excitation light by the fluorescent probe. Therefore the excitation light propagates diffusive in the medium and reaches a fluorescent probe which is excited and emits light at a slightly red shifted (Stoke's shift) wavelength (as previously seen in Fig. 1.3) compared to the original excitation wavelength. Each fluorophore has a specific absorption and emission spectrum which helps to select the appropriate excitation wavelength and the corresponding emission bandpass filters. Again, the fluorescent light propagates diffusive in the medium and therefore first an expression for the fluorescent source and second an expression for the average intensity of the fluorescent light is needed as a solution of the diffusion equation.

3.2.1 The Fluorescent Source Term

The excited fluorophore acts as a secondary source of fluorescence light which is approximated as a two-level system where $N_e(\mathbf{r},t)$ is the number density of fluorescent molecules in the excited state and $N_g(\mathbf{r},t)$ is the number density of fluorescent molecules in the ground state. To describe this system the distribution of the excited fluorophores can be described by a rate equation. To get the rate equation we start formulating the transition rates of the processes in a two-level system. The losses in both levels can be written as:

For the absorption we can write

$$\frac{dN_e(\mathbf{r},t)}{dt} = B_{ge}\, N_g(\mathbf{r},t)\, U_{exc}(\mathbf{r},\mathbf{r}_s) \tag{3.10}$$

where B_{ge} is a constant and $U_{exc}(\mathbf{r},\mathbf{r}_s)$ the average intensity of the excitation light.

For the stimulated emission we can write

$$\frac{dN_e(\mathbf{r},t)}{dt} = -\,B_{eg}\, N_e(\mathbf{r},t)\, U_{exc}(\mathbf{r},\mathbf{r}_s) \tag{3.11}$$

where B_{eg} is a constant and $U_{exc}(\mathbf{r},\mathbf{r}_s)$ the excitation average intensity.

For the spontaneous emission we can write

$$\frac{dN_e(\mathbf{r},t)}{dt} = -\Gamma\, N_e(\mathbf{r},t) \tag{3.12}$$

where Γ is the total decay rate from the excited state to the ground state.

If we add up the three equations it leads to

$$\frac{dN_e(\mathbf{r},t)}{dt} = B_{ge}\, N_g(\mathbf{r},t)\, U_{exc}(\mathbf{r},\mathbf{r}_s) - B_{eg}\, N_e(\mathbf{r},t)\, U_{exc}(\mathbf{r},\mathbf{r}_s) - \Gamma\, N_e(\mathbf{r},t)\ . \tag{3.13}$$

Since the absorption and stimulated emission are inverse processes it can be written

$$B_{ge} = B_{eg} = \eta\, \sigma_{fl} \tag{3.14}$$

where η is the fluorescence quantum yield and σ_{fl} is the absorption cross section of the molecule at the excitation wavelength λ_{exc}.

Therefore Eq. (3.13) can be written as

$$\frac{dN_e(\mathbf{r},t)}{dt} = \eta\, \sigma_{fl} \Big[N_g(\mathbf{r},t) - N_e(\mathbf{r},t)\Big]\, U_{exc}(\mathbf{r},\mathbf{r}_s) - \Gamma\, N_e(\mathbf{r},t)\ . \tag{3.15}$$

The number of excited molecules per unit volume is then given by

$$\frac{dN_e(\mathbf{r},t)}{dt} = \eta\,\sigma_{fl}\left[N_t(\mathbf{r},t) - N_e(\mathbf{r},t) - N_e(\mathbf{r},t)\right] U_{exc}(\mathbf{r},\mathbf{r}_s) - \Gamma\, N_e(\mathbf{r},t) \tag{3.16}$$

where $N_t(\mathbf{r},t)$ is the total number density of the fluorescent molecules (the sum of N_e and N_g: $N_t = N_e + N_g$) as reported in [85].

In our case of CW laser excitation a steady state ($\frac{dN_e}{dt} = 0$) is reached and Eq. (3.16) becomes

$$\begin{aligned} 0 &= \eta\,\sigma_{fl}\left[N_t(\mathbf{r}) - 2N_e(\mathbf{r})\right] U_{exc}(\mathbf{r},\mathbf{r}_s) - \Gamma\, N_e(\mathbf{r}) \\ &= \eta\,\sigma_{fl}\, N_t(\mathbf{r})\, U_{exc}(\mathbf{r},\mathbf{r}_s) - \left[\Gamma + 2\,\eta\,\sigma_{fl}\, U_{exc}(\mathbf{r},\mathbf{r}_s)\right] N_e(\mathbf{r}) \\ N_e(\mathbf{r}) &= \frac{\eta\,\sigma_{fl}\, N_t(\mathbf{r})}{\Gamma + 2\,\eta\,\sigma_{fl}\, U_{exc}(\mathbf{r},\mathbf{r}_s)}\, U_{exc}(\mathbf{r},\mathbf{r}_s)\ . \end{aligned} \tag{3.17}$$

The absorption cross section is in the order of $\sigma_{fl} \sim 10^{-6}\mathrm{cm}^2$ and the fluorescent lifetime of the fluorophores is in the order of nanoseconds ($\Gamma \sim 10^9$).
For intensities of some mW/cm^2 used in our experiments $\Gamma \gg 2\,\eta\,\sigma_{fl}\, U_{exc}(\mathbf{r},\mathbf{r}_s)$ and Eq. (3.17) becomes

$$N_e(\mathbf{r}) = \frac{\eta\,\sigma_{fl}\, N_t(\mathbf{r})}{\Gamma}\, U_{exc}(\mathbf{r},\mathbf{r}_s) \tag{3.18}$$

and the production rate of fluorescent photons is then [86, 87]

$$\Gamma N_e(\mathbf{r}) = \eta\,\sigma_{fl}\, N_t(\mathbf{r})\, U_{exc}(\mathbf{r},\mathbf{r}_s)\ . \tag{3.19}$$

The term $\Gamma\, N_e(\mathbf{r})$ is now a source of fluorescent photons emitted per unit volume per time.
The **source term of the fluorescent light in case of a CW excitation** at position $\mathbf{r}$ is therefore

$$S_{fl}(\mathbf{r},\mathbf{r}_s) = \Gamma\, N_e(\mathbf{r}) = \eta\,\sigma_{fl}\, N_t(\mathbf{r})\, U_{exc}(\mathbf{r},\mathbf{r}_s)\ . \tag{3.20}$$

3.2.2 The Born Approximation

To derive an expression for all fluorescence light sources inside a volume we assume to have a first order scattering interaction between the excitation light intensity and the fluorescent sources which are treated as absorbers with σ_{fl} being the absorption cross section of the fluorophore.
The excitation intensity from a source at position $\mathbf{r}_s$ exciting a molecule at a position $\mathbf{r}$, can be written as the sum of the incident intensity $U_{inc}(\mathbf{r}, \mathbf{r}_s)$ (intensity that reaches the fluorophore directly) and the scattered intensity $U_{sc}(\mathbf{r}, \mathbf{r}_s)$ (intensity that reaches the fluorophore after being scattered by an other absorber)

$$U_{exc}(\mathbf{r}, \mathbf{r}_s) = U_{inc}(\mathbf{r}, \mathbf{r}_s) + U_{sc}(\mathbf{r}, \mathbf{r}_s) \ . \tag{3.21}$$

We assume that the non-linear effect of the presence of other absorbers are very small and thus

$$U_{inc}(\mathbf{r}, \mathbf{r}_s) \gg U_{sc}(\mathbf{r}, \mathbf{r}_s) \tag{3.22}$$

which is the so-called Born approximation stating that the scattering wave from the fluorophores can be neglected when calculating the intensity inside the fluorophores.

This assumption results in

$$U_{exc}(\mathbf{r}, \mathbf{r}_s) \approx U_{inc}(\mathbf{r}, \mathbf{r}_s) \tag{3.23}$$

which is valid for a weakly absorbing distribution of absorbers. This approximation has been used successfully in biological medium where fluorescence molecules are present and lead to reliable results.

3.2.3 Propagation of the Fluorescent Light

The diffusion equation describes how the fluorescent light at the wavelength λ_{fl} is propagating within the tissue. The integration over all contributions from the fluorophores describes then the solution of the diffusion equation for the fluorescent light [88, 86]

$$U_{fl}(\mathbf{r}_s, \mathbf{r}) \ = \ \int_V dV' \, S_{fl}(\mathbf{r}', \mathbf{r}_s) \, \frac{1}{D_{fl}} \, \frac{e^{-k_{fl}|\mathbf{r}'-\mathbf{r}|}}{4\pi \mid \mathbf{r}' - \mathbf{r} \mid} \ . \tag{3.24}$$

Replacing $S_{fl}(\mathbf{r}, \mathbf{r}_s)$ in Eq. (3.24) with the expression of Eq. (3.20) and applying the Born approximation it results in

$$U_{fl}(\mathbf{r}_s, \mathbf{r}) = \int_V dV' \, \eta \, \sigma_{fl} \, N_t(\mathbf{r}') \, U_{inc}(\mathbf{r}', \mathbf{r}_s) \, \frac{1}{D_{fl}} \, \frac{e^{-k_{fl}|\mathbf{r}'-\mathbf{r}|}}{4\pi \mid \mathbf{r}' - \mathbf{r} \mid} \, . \tag{3.25}$$

By applying Eq. (3.8) to Eq. (3.24) we get

$$U_{fl}(\mathbf{r}_s, \mathbf{r}) = \frac{\eta \, \sigma_{fl} \, S_{dc}}{16 \, \pi^2 \, D_{fl} \, D_{inc}} \int_V dV' \, \frac{e^{-k_{inc}|\mathbf{r}'-\mathbf{r}_s|}}{\mid \mathbf{r}' - \mathbf{r}_s \mid} \, N_t(\mathbf{r}') \, \frac{e^{-k_{fl}|\mathbf{r}'-\mathbf{r}|}}{\mid \mathbf{r}' - \mathbf{r} \mid} \, . \tag{3.26}$$

Eq. (3.26) shows that the fluorescent field is a superposition of two fields with different wave numbers for the excitation wavelength k_{inc} and for the emission (fluorescence) wavelength k_{fl}. $N_t(\mathbf{r})$ is the spatial distribution of the density of fluorescent molecules which is in the end the quantity obtained from the tomographic reconstruction.
Eq. (3.26) can be written in a general form in terms of Green's functions as

$$U_{fl}(\mathbf{r}_s, \mathbf{r}) = \frac{\eta \, \sigma_{fl} \, S_{dc}}{D_{fl} \, D_{inc}} \int_V dV' \, g_{inc}(\mathbf{r}', \mathbf{r}_s) \, N_t(\mathbf{r}') \, g_{fl}(\mathbf{r}', \mathbf{r}) \tag{3.27}$$

where $g_{inc}(\mathbf{r}', \mathbf{r}_s)$ and $g_{fl}(\mathbf{r}', \mathbf{r})$ denotes the infinite homogeneous Green's function for the excitation and fluorescence, respectively.

Chapter 4

Solution of the Diffusion Equation for Bounded Media

Until now the forward problem was modeled as light propagation in an infinite homogeneous medium. The derived solutions of light propagation for an incident excitation wavelength and for an emitted fluorescent wavelength are only valid within that framework.
However, in real situations the subject has an irregular surface and a finite volume and the solutions have to account for the contribution of the surface to the light propagation.
In this chapter the steps towards non-contact FMT is outlined and starts with the expression for light distribution at any position inside an irregular shaped object and its corresponding boundary conditions. As in a non-contact FMT system the camera is placed at a distance from the sample, the light at the surface needs to be related to the images on the detector which is in our case a CCD detector. The modeling of this free space propagation of the diffusive light towards the camera is further described. To complete we describe a method to transform the intensity information of the CCD camera from the surface of the bounded medium into an infinite case (Boundary Removal) which effectively simplifies the forward model computation procedure.

4.1 Light Propagation in Arbitrary Shaped Media

A model of light propagation inside a diffusive media of irregular shape was expressed in terms of a surface integral which was derived from Green's Theorem describing the relationship between a line integral around a closed curve and the bounded area by this curve. By taking the surface S into account, Ripoll et al. [89, 90] derived the average intensity $U(\mathbf{r}_s, \mathbf{r})$ generated by a light source $S(\mathbf{r})$, inside a homogeneous diffusive volume V with diffusion coefficient D and absorption coefficient μ_a as

$$U(\mathbf{r}_s, \mathbf{r}) = U_{inc}(\mathbf{r}, \mathbf{r}_s) - \frac{1}{4\pi} \int_S dS' \qquad \left[U(\mathbf{r}_s, \mathbf{r}') \, \frac{\partial g(k \mid \mathbf{r}' - \mathbf{r}_s \mid)}{\partial \hat{\mathbf{n}}'} \right.$$
$$\left. - \quad g(k \mid \mathbf{r}' - \mathbf{r} \mid) \, \frac{\partial U(\mathbf{r}_s, \mathbf{r}')}{\partial \hat{\mathbf{n}}'} \right], \; \mathbf{r} \in V \quad (4.1)$$

where $\hat{\mathbf{n}}'$ is the surface unit outward normal pointing into the non-diffusive medium, g is the Green's function for an infinite homogeneous medium and $U_{inc}(\mathbf{r})$ is the average intensity obtained in an unbounded homogeneous media

$$U_{inc}(\mathbf{r}, \mathbf{r}_s) \;=\; \frac{1}{4\pi \, D} \int_V dV' \, \frac{S(\mathbf{r}') \, e^{-k|\mathbf{r}' - \mathbf{r}_s|}}{\mid \mathbf{r}' - \mathbf{r}_s \mid} \; . \quad (4.2)$$

Eq. (4.1) describes the general case of a spatially distributed light source $S(\mathbf{r})$. The sources of light in the forward model are the laser source illuminating the sample and exciting the second light source namely the fluorescent molecules emitting light at a red shifted wavelength compared to the illumination wavelength. By inserting the corresponding source terms for the excitation and the fluorescence as derived in the previous chapter we get the expressions for the diffusive light in the presence of boundaries.

4.1.1 Boundary Conditions

A well known phenomena in transport problems but also in a number of other fields is the fact that diffusion is not valid close to a boundary region. Therefore boundary conditions are needed in order to find a solution at the surface of a medium e.g. in biological problems the air/tissue interface has to be considered.
There exist three commonly used boundary conditions: i) In the partial current boundary condition it is assumed that the light leaving the scattering medium through an air/tissue interface does not return into the medium which means that the photon flux $\mathbf{J}$ from the non-scattering medium into the tissue is set to zero. ii) In the zero boundary condition the fluence rate U directly at the air/tissue interface is set to zero. iii) For the extrapolated boundary condition the fluence rate U is extrapolated into the air by a straight line with an equal slope as the air/tissue boundary and vanishes at a some distance. A detailed description of the above mentioned boundary conditions can be found in [91, 92].
The so far mentioned boundary conditions describe the problem only in an approximative way which was derived from the theory of particles. An exact solution for boundary conditions for light based on the extrapolated approach was presented by Aronson [93] and is used and described in the following.
Within the diffusion approximation the boundary condition of index mismatched

boundaries between a diffusive and a non-diffusive medium is obtained by assuming that all flux traversing the interface is directed outwards into the non-diffusive medium [93]. This is valid as long as all sources are located inside the diffusive medium.
Due to the fact that the refractive index in tissue of $n_{in} \approx 1.333$ (approximated with that of water) is significantly different from the index of refraction of the surrounding air ($n_{out} \approx 1$) all possible Fresnel reflection at the boundary need to be considered. The boundary condition is then expressed as [93, 94]

$$U(\mathbf{r}_s, \mathbf{r}') = -\,C(n)\,D\,\frac{\partial U(\mathbf{r}_s, \mathbf{r}')}{\partial \hat{\mathbf{n}}'},\ \mathbf{r}' \in S \tag{4.3}$$

where $C(n)$ is the so called interface coefficient taking the refractive index mismatch of both media into account i.e. $n_{in} = n_{out}$, $C(n) = 2$ and for typical tissue/air interfaces and the corresponding index values we obtain $C(n) \approx 5$.

Fick's Law at the boundary writes as

$$J_{tot}(\mathbf{r}_s, \mathbf{r}') = -D\,\frac{\partial U(\mathbf{r}_s, \mathbf{r}')}{\partial \hat{\mathbf{n}}'} \tag{4.4}$$

and therefore we can derive an equation relating the average intensity $U(\mathbf{r}_s, \mathbf{r}')$ with the total flux density $J_{tot}(\mathbf{r}_s, \mathbf{r}')$ as

$$U(\mathbf{r}_s, \mathbf{r}') = C(n)\,J_{tot}(\mathbf{r}_s, \mathbf{r}')\ . \tag{4.5}$$

4.1.2 Intensity and Flux at the Boundary

Making use of Eqs. (4.4) and (4.5) in Eq. (4.1) we obtain an expression for the average intensity inside the volume V which only depends on the total flux density J_{tot}

$$U(\mathbf{r}_s, \mathbf{r}) = U_{inc}(\mathbf{r}_s, \mathbf{r}) - \frac{1}{4\pi\,D}\int_S dS' \quad \left[C(n)\,D\,\frac{\partial g(k \mid \mathbf{r}' - \mathbf{r}\mid)}{\partial \hat{\mathbf{n}}'} + g(k \mid \mathbf{r}' - \mathbf{r}\mid)\right] \times J_{tot}(\mathbf{r}_s, \mathbf{r}'),\ \mathbf{r} \in V\ . \tag{4.6}$$

Instead of having a spatially distributed light source $S(\mathbf{r})$ inside a volume V we have in state of the art non-contact measurement setups normally a generic source outside V, a fiber or a laser beam of a certain aperture and direction, which is incident onto the surface S producing an inward flux $J_{in}^{src}(\mathbf{r})$ propagating within V.

Therefore an expression for the incident average intensity $U_{inc}(\mathbf{r})$ is found directly from Eq. (4.6) as

$$U_{inc}(\mathbf{r}_s, \mathbf{r}) = \frac{1}{4\pi\, D} \int_S dS' \quad \left[C(n)\, D\, \frac{\partial g(k \mid \mathbf{r}' - \mathbf{r} \mid)}{\partial \hat{\mathbf{n}}'} + g(k \mid \mathbf{r}' - \mathbf{r} \mid) \right] \times J_{in}^{src}(\mathbf{r}_s, \mathbf{r}'),\ \mathbf{r} \in V\ . \tag{4.7}$$

Concerning the source producing an inward flux $J_{in}^{src}(\mathbf{r})$, the complete solution of the total average intensity U at any point inside the volume V is given as [40]

$$U(\mathbf{r}_s, \mathbf{r}) = \frac{1}{4\pi\, D} \int_S dS' \quad \left[C(n)\, D\, \frac{\partial g(k \mid \mathbf{r}' - \mathbf{r} \mid)}{\partial \hat{\mathbf{n}}'} + g(k \mid \mathbf{r}' - \mathbf{r} \mid) \right] \times \left[J_{tot}(\mathbf{r}_s, \mathbf{r}') + J_{in}^{src}(\mathbf{r}_s, \mathbf{r}') \right],\ \mathbf{r} \in V\ . \tag{4.8}$$

Taking Eq. (4.5) into account we can derive the solution for the total flux density $J_{tot}(\mathbf{r}_s, \mathbf{r})$ [40]

$$J_{tot}(\mathbf{r}_s, \mathbf{r}) = \frac{1}{4\pi\, C(n)\, D} \int_S dS' \quad \left[C(n)\, D\, \frac{\partial g(k \mid \mathbf{r}' - \mathbf{r} \mid)}{\partial \hat{\mathbf{n}}'} + g(k \mid \mathbf{r}' - \mathbf{r} \mid) \right] \times \left[J_{tot}(\mathbf{r}_s, \mathbf{r}') + J_{in}^{src}(\mathbf{r}_s, \mathbf{r}') \right],\ \mathbf{r} \in S\ . \tag{4.9}$$

The incident average intensity $U_{inc}(\mathbf{r}_s, \mathbf{r})$ inside a volume V defined by the surface integral of $J_{in}^{src}(\mathbf{r}_s, \mathbf{r}')$ is often approximated by a point source located at position $\mathbf{r}_s$ one transport mean free path ($l_{tr} = 1/\mu_s'$) inside the diffusive medium [79] with respect to the surface normal where the beam impinges and can be written as

$$U_{inc}(\mathbf{r}, \mathbf{r}_s) \;=\; \frac{1}{4\pi\, D}\, \frac{e^{-k\,|\mathbf{r} - \mathbf{r}_s|}}{\mid \mathbf{r} - \mathbf{r}_s \mid},\ \mathbf{r}, \mathbf{r}_s \in V\ . \tag{4.10}$$

A solution to $U(\mathbf{r}_s, \mathbf{r})$ in Eq. (4.6) and $J_{tot}(\mathbf{r}_s, \mathbf{r})$ in Eq. (4.9) is found by explicitly solving the surface integral and therefore the surface needs to be known. To retrieve the surface geometry of the sample several surface recovery techniques were proposed among those the surface reconstruction of shadow projections of white light illuminated samples [95, 46, 44] and laser triangulation techniques [96, 97] are the most promising.

Furthermore techniques using photogrammetric cameras (3D-cameras) were implemented. [41, 39]. A detailed overview of optical methods to retrieve three-dimensional shapes is given by Chen et al. [98]. Recent advances in hybrid imaging by combining FMT with structural imaging modalities such as MRI or CT are a further solutions to obtain the sample surface.

4.1.3 Solving the Surface Integral: Kirchhoff Approximation

To solve the surface integral the boundary values at the surface S has to be found by means of numerical methods such as the Boundary Element Methods by discretizing the surface into a number of surface elements and inverting the resulting matrix [89, 99].

The numerical solution of the obtained system of equations is time consuming and computational intensive. Therefore the so-called Kirchhoff approximation which replaces the surface at each point by its tangent plane was proposed by Ripoll et al. [100] which results in

$$U^{KA}(\mathbf{r}_s, \mathbf{r}) = U_{inc}(\mathbf{r}) + \frac{1}{4\pi} \sum_{p=1}^{N} \left[C(n)\, D\, \frac{\partial g(k \mid \mathbf{r}_p - \mathbf{r} \mid)}{\partial \hat{\mathbf{n}}_p} + g(k \mid \mathbf{r}_p - \mathbf{r} \mid) \right] \times \Delta S(\mathbf{r}_p)\, \frac{\partial U^{KA}(\mathbf{r}_s, \mathbf{r}_p)}{\partial \hat{\mathbf{n}}_p} \tag{4.11}$$

where N is the number of tangential area elements ΔS, $\hat{\mathbf{n}}_\mathbf{p}$ being the surface normal unit vector at position $\mathbf{r}_p$ on the surface S and $U^{KA}(\mathbf{r}_s, \mathbf{r})$ expressing the fluence rate with respect to the Kirchhoff approximation.

The surface values $\partial U^{KA}(\mathbf{r}_s, \mathbf{r}_p)/\partial \hat{\mathbf{n}}_p$ are obtained by using the extrapolated boundary condition [101] by

$$\frac{\partial U^{KA}(\mathbf{r}_s, \mathbf{r}_p)}{\partial \hat{\mathbf{n}}_p} = -\frac{1}{C(n)\, D} \left[U_{inc}(\mathbf{R}, \bar{Z}) - U_{inc}(\mathbf{R}, \bar{Z} + C(n)\, D) \right] \tag{4.12}$$

where $(\bar{\mathbf{R}}, \bar{Z})$ are the coordinates of $(\mathbf{r}_s - \mathbf{r}_p)$ with respect to the plane defined by $\hat{\mathbf{n}}_p$ namely

$$\bar{Z} = (\mathbf{r}_s - \mathbf{r}_p) \cdot [-\hat{\mathbf{n}}_p] \tag{4.13}$$

$$\bar{\mathbf{R}} = \bar{Z} - (\mathbf{r}_s - \mathbf{r}_p) \tag{4.14}$$

Eq. (4.11) can therefore be written as

$$U^{KA}(\mathbf{r}_s, \mathbf{r}) = U_{inc}(\mathbf{r}) - \frac{1}{4\pi} \sum_{p=1}^{N} \left[\frac{\partial g(k \mid \mathbf{r}_p - \mathbf{r} \mid)}{\partial \hat{\mathbf{n}}_p} + \frac{g(k \mid \mathbf{r}_p - \mathbf{r} \mid)}{C(n)\, D} \right] \Delta S(\mathbf{r}_p) \times \left[U_{inc}(\mathbf{R}, \bar{Z}) - U_{inc}(\mathbf{R}, \bar{Z} + C(n)\, D) \right] . \quad (4.15)$$

It was shown that the Kirchhoff approximation can be used iteratively to increase the accuracy [102].
Other numerical methods to derive solutions are based on volume element methods such as the Finite Element Method (FEM) [103, 104].

4.2 Free Space Propagation of Diffuse Light

So far we described the light distribution at the surface of a diffusive media and we will derive next how this boundary values given by $J_{tot}(\mathbf{r}_s, \mathbf{r})$ can be connected to the actual power measured by the detector located at a distance from the sample surface. Therefore a model is needed describing the free space light propagation in air from the surface S towards the detector.
The power emitted from a differential area dS at position $\mathbf{r}$ in direction of the unit vector $\hat{\mathbf{s}}$ within a solid angle Ω is given by

$$dp(\mathbf{r}, \hat{\mathbf{s}}) = L(\mathbf{r}, \hat{\mathbf{s}})\, \mathbf{n}_p \cdot \hat{\mathbf{s}}\, dS\, d\Omega \; . \quad (4.16)$$

The total power is obtained by integrating over the solid angle Ω and we can therefore write

$$P(\mathbf{r}, \hat{\mathbf{s}}) = dS \int_{\Omega} L(\mathbf{r}, \hat{\mathbf{s}})\, \mathbf{n}_p \cdot \hat{\mathbf{s}}\, d\Omega \; . \quad (4.17)$$

We can now relate the differential angle $d\Omega$ to the differential area dA of the imaging system as

$$d\Omega = \frac{\mathbf{n}_d \cdot \mathbf{u}_{\mathbf{r}-\mathbf{r}_d}}{\mid \mathbf{r}_d - \mathbf{r} \mid^2}\, dA \quad (4.18)$$

where $\mathbf{n}_d$ is the surface normal to the aperture of the detector and

$$\mathbf{u}_{\mathbf{r}-\mathbf{r}_d} = \frac{\mathbf{r}_d - \mathbf{r}}{\mid \mathbf{r}_d - \mathbf{r} \mid} \quad (4.19)$$

describes the unit direction of the specific intensity in terms of the measurement position $\mathbf{r}$ on the surface S and the position $\mathbf{r}_d$ of the differential area dA in the aperture. By using Eqs. (4.18) and (4.19) we can derive the total power emitted by dS as

$$\begin{aligned} P(\mathbf{r}, \mathbf{u}_{\mathbf{r}-\mathbf{r}_d}) &= dS \int_A L(\mathbf{r}, \mathbf{u}_{\mathbf{r}-\mathbf{r}_d}) \, (\mathbf{n}_p \cdot \mathbf{u}_{\mathbf{r}-\mathbf{r}_d}) \, \frac{\mathbf{n}_d \cdot \mathbf{u}_{\mathbf{r}-\mathbf{r}_d}}{\mid \mathbf{r}_d - \mathbf{r} \mid^2} \, dA \\ &= dS \int_A L(\mathbf{r}, \mathbf{u}_{\mathbf{r}-\mathbf{r}_d}) \cos\theta_p \, \frac{\cos\theta_d}{\mid \mathbf{r}_d - \mathbf{r} \mid^2} \, dA \end{aligned} \tag{4.20}$$

where $\mathbf{n}_p \cdot \mathbf{u}_{\mathbf{r}-\mathbf{r}_d}$ and $\mathbf{n}_d \cdot \mathbf{u}_{\mathbf{r}-\mathbf{r}_d}$ were replace by $\cos\theta_p$ and $\cos\theta_d$, respectively.
A relation between the emitted power by the area dS at position $\mathbf{r}_p$ and the power measured a the differential area dA at position $\mathbf{r}_d$ in the imaging system is given as

$$P(\mathbf{r}_d, \mathbf{u}_{\mathbf{r}-\mathbf{r}_d}) = \int_S dS \int_A L(\mathbf{r}, \mathbf{u}_{\mathbf{r}-\mathbf{r}_d}) \cos\theta_p \, \frac{\cos\theta_d}{\mid \mathbf{r}_d - \mathbf{r} \mid^2} \, dA \ . \tag{4.21}$$

We make now the assumption that the distance from the surface to the camera is much bigger than the aperture of the camera and Eq. (4.22) can be approximated by

$$P(\mathbf{r}, \mathbf{u}_{\mathbf{r}-\mathbf{r}_d}) = dS L(\mathbf{r}, \mathbf{u}_{\mathbf{r}-\mathbf{r}_d}) \cos\theta_p \, \frac{\cos\theta_d}{\mid \mathbf{r}_d - \mathbf{r} \mid^2} \, dA \tag{4.22}$$

and therefore Eq. (4.21) becomes

$$P(\mathbf{r}_d, \mathbf{u}_{\mathbf{r}-\mathbf{r}_d}) = \int_S dS L(\mathbf{r}, \mathbf{u}_{\mathbf{r}-\mathbf{r}_d}) \cos\theta_p \, \frac{\cos\theta_d}{\mid \mathbf{r}_d - \mathbf{r} \mid^2} \, dA \ . \tag{4.23}$$

To derive a relation between the specific intensity L and the total surface flux density J_{tot} we assume that each differential area dS acts as a Lambertian source i.e. radiates isotropically into free space. We can therefore write for the outward flux density J_{out} into free space

$$J_{out}(\mathbf{r}) = \int_{(2\pi)^+} L(\mathbf{r}) \, \hat{\mathbf{s}} \cdot \mathbf{n} \, d\Omega = L(\mathbf{r}) \, \pi \ . \tag{4.24}$$

Using the boundary condition $J_{tot}(\mathbf{r}) = J_{out}(\mathbf{r})$ [93] we obtain the following expression

$$L(\mathbf{r}) \, \hat{\mathbf{s}} = \frac{1}{\pi} \, J_{tot}(\mathbf{r}) \tag{4.25}$$

which relates the specific intensity to the total flux density at the boundary.
By introducing Eq. (4.25) into Eq. (4.23) the total power measured at the detector is obtained as

$$P(\mathbf{r}_d, \mathbf{u}_{\mathbf{r}-\mathbf{r}_d}) = \frac{1}{\pi} \int_S dS J_{tot}(\mathbf{r}) \cos\theta_p \frac{\cos\theta_d}{\mid \mathbf{r}_d - \mathbf{r} \mid^2} dA \tag{4.26}$$

which can be rewritten as

$$P(\mathbf{r}_d, \mathbf{u}_{\mathbf{r}-\mathbf{r}_d}) = \frac{1}{\pi} \int_S dS J_{tot}(\mathbf{r}) \Gamma(\mathbf{r}, \mathbf{r}_d) \tag{4.27}$$

where Γ is a so-called transformation factor describing the contribution of the surface points onto a certain detector at position $\mathbf{r}_d$ with a detector normal $\mathbf{n}_d$ and an area A [40]

$$\Gamma(\mathbf{r}_d, \mathbf{r}_p) = \xi(\mathbf{r}_d, \mathbf{r}_p) \frac{f(NA - \sin\theta_d)}{\mid \mathbf{r}_d - \mathbf{r}_p \mid^2} \cos\theta_p \cos\theta_d \, dA \tag{4.28}$$

where $\xi \in \{0, 1\}$ is a factor discarding surface points not visible by the detector, NA is the numerical aperture which is modeled through a function f which describes a Gaussian of full width at half maximum of $2NA$.

4.3 The Concept of Boundary Removal

When imaging arbitrary shaped tissues as it is always the case in biological samples we have seen that the effects of the boundaries need to be explicitly modeled when measuring in non-contact mode. The obtained data sets are in the order of 10^8 measurements and dependent on the accuracy of the forward model and the inversion it can lead to a computationally expensive procedure. To simplify and speed up the modeling processes without loosing accuracy Ripoll et. [105] all proposed a method to transform surface measurements to measurements which would be obtained in the absence of the surface which means in an infinite homogeneous media. This approach would allow to use infinite Green's function for the forward model and therefore circumvent complex numerical method solutions for arbitrary geometries and would allow fast direct inversion techniques [106]. This allows data back-projection from a detector outside the volume to anywhere inside the volume.
We already derived the average intensity U of a diffusive medium with volume V bounded by a surface S and containing a fluorescence distribution $S(\mathbf{r})$. By accounting for the boundaries an expression for U was found for any surface point of the

medium which resulted in Eq. (4.6) and is rewritten here

$$J_{tot}(\mathbf{r}_s,\mathbf{r}) = \frac{U_{inc}(\mathbf{r}_s,\mathbf{r})}{C(n)} - \frac{1}{4\pi\, D\, C(n)} \int_S dS' \qquad \left[C(n)\, D\, \frac{\partial g(k \mid \mathbf{r}' - \mathbf{r} \mid)}{\partial \hat{\mathbf{n}}'} + g(k \mid \mathbf{r}' - \mathbf{r} \mid) \right] \times J_{tot}(\mathbf{r}_s,\mathbf{r}'),\ \mathbf{r} \in V \tag{4.29}$$

where we used Eq. (4.5) stating that $U(\mathbf{r}_s,\mathbf{r}') = C(n)\, J_{tot}(\mathbf{r}_s,\mathbf{r}')$.
We recall that U_{inc} is the average intensity obtained in a homogeneous media in absence of a surface which as given in Eq. (4.30) by

$$U_{inc}(\mathbf{r},\mathbf{r}_s) \;=\; \frac{1}{4\pi\, D} \int_V dV' \, \frac{S(\mathbf{r}')\, e^{-k|\mathbf{r}'-\mathbf{r}_s|}}{\mid \mathbf{r}' - \mathbf{r}_s \mid} \; . \tag{4.30}$$

We can rearrange Eq. (4.29) to derive an expression for the average intensity of an infinite homogeneous media as a function of J_{tot}

$$U_{inc}(\mathbf{r}_s,\mathbf{r}) = C(n)\, J_{tot}(\mathbf{r}_s,\mathbf{r}) + \frac{1}{4\pi\, D} \int_S dS' \qquad \left[C(n)\, D\, \frac{\partial g(k \mid \mathbf{r}' - \mathbf{r} \mid)}{\partial \hat{\mathbf{n}}'} + g(k \mid \mathbf{r}' - \mathbf{r} \mid) \right] \times J_{tot}(\mathbf{r}_s,\mathbf{r}'),\ \mathbf{r} \in V \; . \tag{4.31}$$

If we now consider a measurement setup which would allow to detect the light that emits from all points on the surface S, it would be possible to measure the total surface flux density J_{tot}. In this case the experimentally measured values for J_{tot} can be directly included into Eq. (4.31) resulting in an expression for U_{inc} which is the average intensity created by a fluorescence source distribution in the absence of the surface. This means that the volume V has become infinite and the medium has everywhere in space the same optical properties while preserving the position and the strength of the source distribution $S(\mathbf{r})$.
Having now a CCD camera focussing on the surface of the sample and recording the emitted light we can acquire the quantity J_{tot} on the surface. The so-called measured infinite case average intensity U_{inc}^{meas} at each detector position $\mathbf{r}_i$ (pixel position) for a total of N_d detectors (in our case $N_d = 512 \times 512 = 262144$) can be written as

$$U_{inc}^{meas}(\mathbf{r}_s,\mathbf{r}_i) = C(n)\, J_{tot}^{meas}(\mathbf{r}_s,\mathbf{r}_i) + \frac{1}{4\pi\, D} \sum_{j=1}^{N_d} \qquad \left[C(n)\, D\, \frac{\partial g(k \mid \mathbf{r}_j - \mathbf{r}_i \mid)}{\partial \hat{\mathbf{n}}_j} + g(k \mid \mathbf{r}_j - \mathbf{r}_i \mid) \right] \times J_{tot}^{meas}(\mathbf{r}_s,\mathbf{r}_j)\, dA_j,\ \mathbf{r}_i \in S \tag{4.32}$$

where the surface was discretized into a number of surface elements dA and each surface measurement of an area dA_j at $\mathbf{r}_j$ was represented as $J_{tot}^{meas}(\mathbf{r}_j)$. The notation label $meas$ was introduced to distinguish the measured parameters from $J_{tot}(\mathbf{r}_j)$ and dS which give the rigorous solution of Eq. (4.31). The values $J_{tot}^{meas}(\mathbf{r}_i)$ are given by the camera images meaning that the values $J_{tot}^{meas}(\mathbf{r}_j)$ are obtained by projecting the camera measurements to the medium surface which is the inverse of the proposed free space propagation formulation in section (4.2) where the outward flux measured at the interface was related to the measurements obtained with the CCD camera. Therefore, although the medium has been transformed to infinite the surface information is still necessary.
In order to get an equivalent solution of the surface integral in Eq. (4.31) by the summation in Eq. (4.32) we need to measure the outward flux values at all points on the surface. In our measurement setup where the sample is place horizontally on a imaging platform only parts of the surface flux density can by captured by the camera. It was shown by Ripoll et al. [105] on a numerical simulation study that this partial measurement of the surface flux is not a major limitation. It was found that by focussing the camera on a surface region where the targeted sample is expected to lay underneath even a partial measurement coverage of the surface can lead to good and fast results. In all experiments presented here we used the prior knowledge of knowing where we expect the fluorophore and therefore on which part of the body the camera has to be focused.
In conclusion the proposed boundary removal method allow the use of the previously derived infinite case expressions for the excitation light Eq. (3.9) and for the fluorescence light Eq. (3.27).

4.4 Incorporation of the Source Intensity Profile

Measuring in non-contact reflection geometry where a generic laser source illuminates the tissue and creates an intensity distribution on the tissue surface which is then directly measured by a detector placed at the same side as the laser source bears several problems: i) signal-to-noise ratio is limited by autofluorescence since the excited tissue is directly visible by the detector. ii) the exact location of the excitation sources and their intensity profiles on the arbitrary surface of the sample are not known.
The second problem is in general addressed by assuming an intensity profile or by performing an approximation of a point source [79]. Although the information about the intensity profile is critical for high resolution images a concept to directly account for this in reflection geometry was proposed by Sarasa-Renedo et al. [107] and outlined in the following.

The Equation 4.8 which is rewritten here for convenience

$$U(\mathbf{r}_s, \mathbf{r}) = \frac{1}{4\pi\, D} \int_S dS' \qquad \left[C(n)\, D\, \frac{\partial g(k \mid \mathbf{r}' - \mathbf{r} \mid)}{\partial \hat{\mathbf{n}}'} + g(k \mid \mathbf{r}' - \mathbf{r} \mid) \right] \times \left[J_{tot}(\mathbf{r}_s, \mathbf{r}') + J_{in}^{src}(\mathbf{r}_s, \mathbf{r}') \right],\ \mathbf{r} \in V\ . \tag{4.33}$$

defines the total average intensity at any point $\mathbf{r}$ inside a Volume V if a generic source such as a fiber or a laser beam is incident from outside the volume onto the surface S. As shown in section 4.3 we can take J_{tot} as the experimentally measured flux J_{tot}^{meas} and approximate J_{in}^{src} as a point source as described in subsection 4.1.2 and solve Eq. (4.33) for U. Instead of doing that it is assumed that the reflectance measurement at the same wavelength as the illumination source (at the excitation wavelength) is proportional to J_{in}^{src} resulting in the expression $J_{tot} = \alpha J_{in}^{src}$. This approximation is valid as it is well understood that almost all signal measured in reflection geometry has its contribution from the reflection of the surface and from regions in the order of several transport mean free path length below the illuminated surface in the area where the beam impinges.
When the measurements are used to generate the intensity distribution within V we can write $J_{tot}(\mathbf{r}_s, \mathbf{r}') + J_{in}^{src}(\mathbf{r}_s, \mathbf{r}') \simeq (\alpha + 1)\, J_{tot}^{meas}$ where J_{tot}^{meas} is the experimental measurement. We can therefore write

$$U^{meas}(\mathbf{r}_s, \mathbf{r}) = \frac{1}{4\pi\, D} \int_S dS' \qquad \left[C(n)\, D\, \frac{\partial g(k \mid \mathbf{r}' - \mathbf{r} \mid)}{\partial \hat{\mathbf{n}}'} + g(k \mid \mathbf{r}' - \mathbf{r} \mid) \right] \times (\alpha + 1)\, J_{tot}^{meas}(\mathbf{r}_s, \mathbf{r}'),\ \mathbf{r} \in V\ . \tag{4.34}$$

Chapter 5

Inverse Problem

The above mentioned forward problem allows to predict the distribution of the light at the surface of the object where the focal plane of the camera is located.
With the following equation it is possible to simulate the measured power by the CCD chip by taking into account the detector characteristics (gain and filter attenuation).

5.1 Measurement Normalization

Until now an ideal detector system was assumed to measure the power. In order to simulate a real detector system we have to account for the detector characteristics such as the detector quantum efficiency $QE^{\lambda_{fl}}$, the detector gain $\Theta_d(\mathbf{r}_d)$, the source gain $\Theta_s(\mathbf{r}_s)$ and the fluorescence filter attenuation of the applied bandpass filter matching the fluorescence wavelength Θ_f^{fl} which results in

$$P^{fl}(\mathbf{r}_s,\mathbf{r}_d) = \underbrace{QE^{\lambda_{fl}}\,\Theta_d(\mathbf{r}_d)\,\Theta_s(\mathbf{r}_s)\,\Theta_f^{fl}}_{b^{fl}}\,\frac{1}{\pi}\int_S J_{\mathrm{tot}}^{fl}(\mathbf{r},\mathbf{r}_s)\,\Gamma(\mathbf{r},\mathbf{r}_d)\,dS\ . \tag{5.1}$$

By applying the expression for J_{tot}^{fl} derived from Eq. (3.27) to Eq. (5.1) we get

$$\begin{aligned} P^{fl}(\mathbf{r}_s,\mathbf{r}_d) &= b^{fl}\,\frac{1}{\pi}\int_S \frac{\eta\,\sigma_{fl}\,S_0}{D_{fl}\,D\,C(n)}\int_{V'} g_{exc}(\mathbf{r}_s,\mathbf{r}')\,N_t(\mathbf{r}')\,g_{fl}(\mathbf{r}',\mathbf{r})\,dV'\,\Gamma(\mathbf{r},\mathbf{r}_d)\,dS \\ &= \frac{b^{fl}\,\eta\,\sigma_{fl}\,S_0}{\pi\,D_{fl}D\,C(n)}\int_{V'}\int_S g_{exc}(\mathbf{r}_s,\mathbf{r}')\,N_t(\mathbf{r}')\,g_{fl}(\mathbf{r}',\mathbf{r})\,\Gamma(\mathbf{r},\mathbf{r}_d)\,dS\,dV'\ . \end{aligned} \tag{5.2}$$

Finding a solution of Eq. (5.2) requires the determination of the gain factors $\Theta_d(\mathbf{r}_d)$ and $\Theta_s(\mathbf{r}_s)$ for each source/detector pair located at position $\mathbf{r}_s$ and $\mathbf{r}_d$, respectively.

To circumvent this inconvenience a normalization procedure was suggested by dividing Eq. (5.2) by a second measurement performed at the excitation wavelength. This intrinsic light measurement was performed with an appropriate filter accounting for the excitation wavelength λ_{exc} and can be expressed as

$$\begin{aligned} P^{exc}(\mathbf{r}_s,\mathbf{r}_d) &= \underbrace{QE^{\lambda_{exc}}\,\Theta_d(\mathbf{r}_d)\,\Theta_s(\mathbf{r}_s)\,\Theta_f^{exc}}_{b^{exc}}\,\frac{1}{\pi}\int_S J_{\text{tot}}^{exc}(\mathbf{r},\mathbf{r}_s)\,\Gamma(\mathbf{r},\mathbf{r}_d)\,dS \\ &= b^{exc}\,\frac{1}{\pi}\int_S \frac{S_0}{D\,C(n)} g_{exc}(\mathbf{r},\mathbf{r}_s)\,\Gamma(\mathbf{r},\mathbf{r}_d)\,dS \\ &= \frac{b^{exc}\,S_0}{\pi\,D\,C(n)}\int_S g_{exc}(\mathbf{r},\mathbf{r}_s)\,\Gamma(\mathbf{r},\mathbf{r}_d)\,dS\ . \end{aligned} \tag{5.3}$$

The normalization method accounting for the intrinsic properties of the medium can be written as [108]

$$\begin{aligned} P^{nB}(\mathbf{r}_s,\mathbf{r}_d) &= \frac{P^{fl}(\mathbf{r}_s,\mathbf{r}_d)}{P^{exc}(\mathbf{r}_s,\mathbf{r}_d)} \\ &= a\,\frac{\eta\,\sigma_{fl}}{D_{fl}}\,\frac{\int_{V'}\int_S g_{exc}(\mathbf{r}_s,\mathbf{r}')\,N_t(\mathbf{r}')\,g_{fl}(\mathbf{r}',\mathbf{r})\,\Gamma(\mathbf{r},\mathbf{r}_d)\,dS\,dV'}{\int_S g_{exc}(\mathbf{r},\mathbf{r}_s)\,\Gamma(\mathbf{r},\mathbf{r}_d)\,dS} \end{aligned} \tag{5.4}$$

where the factor

$$a = \frac{QE^{\lambda_{fl}}\,\Theta_f^{fl}}{QE^{\lambda_{exc}}\,\Theta_f^{exc}} \tag{5.5}$$

can be determined experimentally.
Eq. (5.4) is the so-called normalized Born expression which normalizes the fluorescent intensity to the tissue heterogeneities. A further advantage is that position dependent factors such as the gain factors are canceled out. As this normalized Born approximation assumes homogeneous optical properties it was extensively tested for heterogeneous media such as heterogeneous phantoms [109] and for *in vivo* measurements yielding in very robust results.

5.2 Discretization and Weight Matrix

In order to obtain a tomographic image we discretize the medium of interest into N volume elements so-called voxels. The size of the voxels is chosen dependent on the resolution which should be achieved with the reconstruction: The smaller the

voxels for a fixed volume the larger the amount of data elements, the longer the reconstruction time. Within the discretization, the volume integral in the expression for the normalized Born approximation in Eq. (5.4) is replaced by a summation of N_v discrete volume elements. The center of each voxel is represented by $\mathbf{r}_n$ and leads to

$$P^{nB}(\mathbf{r}_s, \mathbf{r}_d) \;=\; a\,\frac{\eta\,\sigma_{fl}}{D_{fl}} \sum_{n=1}^{N_v} \frac{\int_S g_{exc}(\mathbf{r}_s, \mathbf{r}_n)\, N_t(\mathbf{r}_n)\, g_{fl}(\mathbf{r}_n, \mathbf{r})\, \Gamma(\mathbf{r}, \mathbf{r}_d)\, dS}{\int_S g_{exc}(\mathbf{r}, \mathbf{r}_s)\, \Gamma(\mathbf{r}, \mathbf{r}_d)\, dS} \Delta V \;. \quad (5.6)$$

Eq. (5.6) is representing a single measurement of a source at position $\mathbf{r}_s$ and a detector at position $\mathbf{r}_d$. As we use in normal measurements multiple source detector positions e.g. a source grid of 10×10 sources and a detector with 512×512 pixels we obtain a pair of linear equations. If we now assume u different source positions and v different detector elements we end up with $m = u \times v$ measurements. These measurements build the set of linear equations which can be written in a form of a matrix equation

$$\begin{bmatrix} P^{nB}(\mathbf{r}_{s1}, \mathbf{r}_{d1}) \\ P^{nB}(\mathbf{r}_{s1}, \mathbf{r}_{d2}) \\ \vdots \\ P^{nB}(\mathbf{r}_{su}, \mathbf{r}_{dv}) \end{bmatrix} = \begin{bmatrix} W_{11} & W_{12} & \cdots & W_{1n} \\ W_{21} & W_{22} & \cdots & W_{2n} \\ \vdots & \vdots & \ddots & \vdots \\ W_{m1} & W_{m2} & \cdots & W_{mn} \end{bmatrix} \times \begin{bmatrix} N_t(\mathbf{r}_1) \\ N_t(\mathbf{r}_2) \\ \vdots \\ N_t(\mathbf{r}_n) \end{bmatrix} \quad (5.7)$$

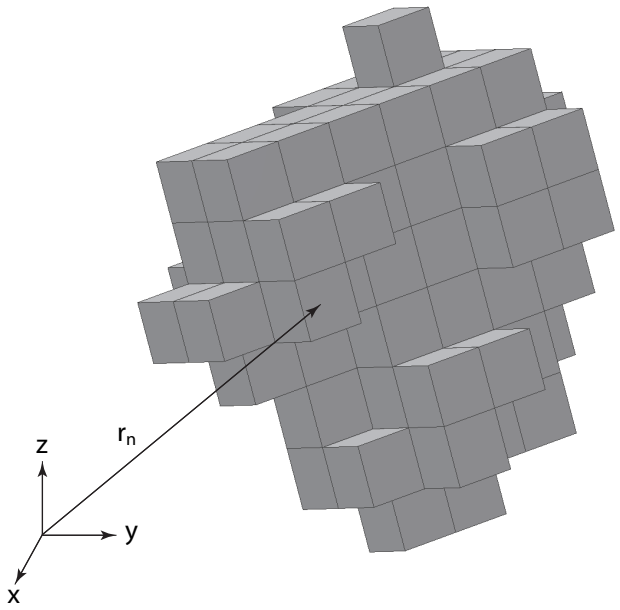

Figure 5.1: Discretized arbitrary volume

which can be written as $\mathbf{P}^{nB}_{M\times 1} = \mathbf{W}_{M\times N} \times \mathbf{N}_{t\,N\times 1}$ where W is the so-called weight matrix. A weight matrix element has the following form

$$W_{mn} = W_{u\times v\,n} = a\,\frac{\eta\,\sigma_{fl}}{D_{fl}}\,\Delta V\,\frac{\int_S g_{exc}(\mathbf{r}_{su},\mathbf{r}_n)\,g_{fl}(\mathbf{r}_n,\mathbf{r})\,\Gamma(\mathbf{r},\mathbf{r}_{dv})\,dS}{\int_S g_{exc}(\mathbf{r},\mathbf{r}_{su})\,\Gamma(\mathbf{r},\mathbf{r}_{dv})\,dS}\ . \tag{5.8}$$

Each matrix element represents the contribution of each voxel to the fluorescent concentration with respect to the source and detector position. To get the fluorescence concentration within the volume of interest we have to invert the above set of linear equation and solve it for $\mathbf{N}_t$ which leads to an inversion of the weight matrix W.

5.3 Inversion Technique

Inverting the weight matrix can be performed in different ways depending on the size of the matrix. For small data sets direct matrix inversion methods such as singular value decomposition can be used. In our case where we use a CCD camera we have a large number of detector elements in the order of 10^6 or smaller depending on the binning selected. This large number of equations can not directly inverted numerically due to the ill-posed (violation of at least one of the properties defined by Hadamard for well-posed problems: A solution exists, the solution is unique and the solution continuously depends on the data), ill-conditioned (a small error in P^{nB} may cause a large error in N_t) and underdetermined (more unknowns than equations) nature of the problem. Therefore standard linear reconstruction techniques such as algebraic methods can be used to solve the problem. Among those iterative techniques such as the algebraic reconstruction technique (ART) and the simultaneous iterative reconstruction technique (SIRT) [110] are the most common ones. For our datasets ART, which was originally developed for X-ray tomography, revealed as the best solution in terms of reconstruction speed and quality of the outcome.
To illustrate the ART algorithm we use a simple example of a system with two linear equations and two unknowns (adapted from [111]),

$$\begin{aligned} P_1 &= W_{11}\,N_1 + W_{12}\,N_2 \\ P_2 &= W_{21}\,N_1 + W_{22}\,N_2 \end{aligned} \tag{5.9}$$

where P_1 and P_2 are the measurements, N_1 and N_2 are the unknowns and the W's are the calculated weights.
The solution can be graphically represented as a two dimensional solution space spanned by N_1 and N_2 where the measurements are represented by two lines

$$\begin{aligned} N_2 &= -\frac{W_{11}}{W_{12}}N_1 + \frac{P_1}{W_{12}} \\ N_2 &= -\frac{W_{21}}{W_{22}}N_1 + \frac{P_2}{W_{22}}\ . \end{aligned} \tag{5.10}$$

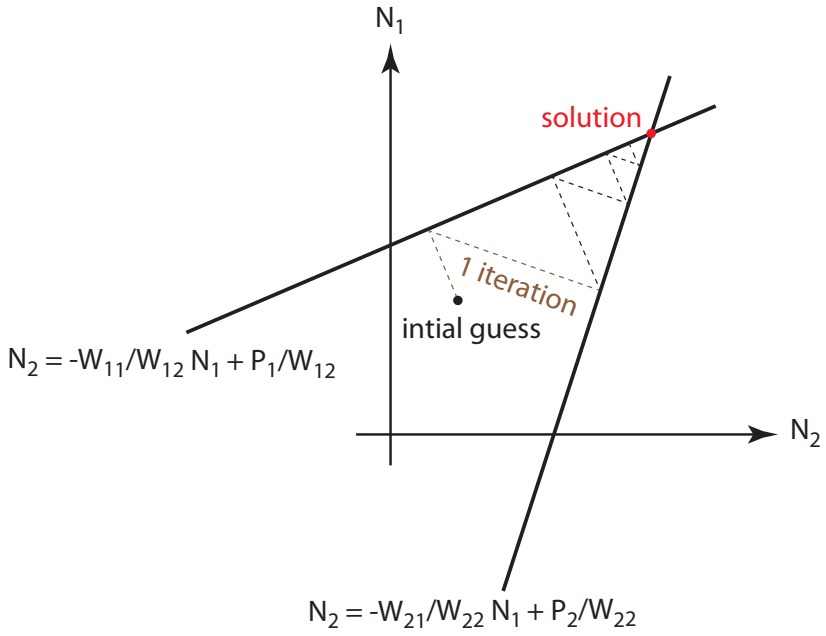

Figure 5.2: Graphical description of the ART in case of a unique solution.

The solution for the two-equation system is given at the intersection of the two lines. The function of the ART algorithm is now to find the intersection which starts with an initial guess at any point in space. This point is now rectangularly projected to the first line. Next, a similar move is made from the resulting point on the first line to the second line which completed the first iteration step. By consequently projecting the points from one to the other line the intersection and therefore the solution is reached and the algorithm converge after several iteration steps.
By applying this algorithm to a real situation where we have M equations and N unknowns, each equation represents a hyperplane in an N-dimensional space and the unique solution of the system is given by the point where M hyperplanes in the N dimensional space intersect. Basically three cases can be distinguished depending on the values of M and N:

$M = N$: the system has a unique solution (see Fig. 5.2).

$M > N$: the system is overdetermined i.e. more equations than unknowns. No unique solution exists and the final solution oscillates in an space formed by the intersection of the hyperplanes (in the example an area formed by the intersection of three lines) (see Fig. 5.3a).

$M < N$: the system is underdetermined i.e. fewer equations than unknowns. The algorithm converges to a space (in the example case a line) which contains the correct solution. Therefore the system can have an infinite number of solutions (see Fig. 5.3b).

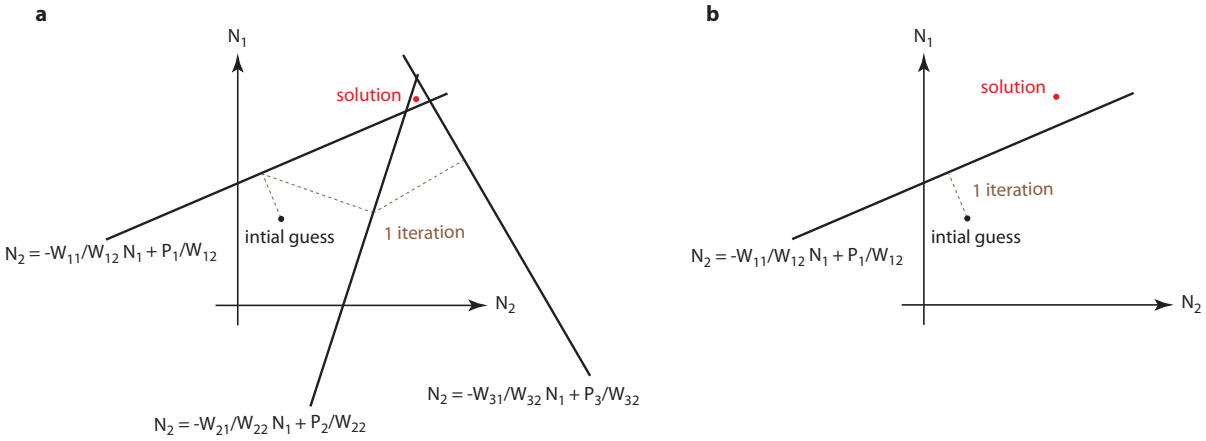

Figure 5.3: Graphical description of the ART for more equations than unknowns **a** and fewer equations than unknowns **b**.

In optical tomography experiments the number of equations is determined by the number of voxels N building the mesh volume. The number of voxels and therefore the resolution obtained in the reconstructed image is determined by the size of the voxel.
The number of equations M is determined by the number of source/detector pairs.

Chapter 6

FMT

The FMT technique is a fast developing research field where in the last decade multiple important instrumental and theoretical developments were undertaken to provide an attractive research tool mainly in preclinical biomedical research (see subsection 1.1.2). Among those the implementation of non-contact imaging strategies and the fast development of fluorescent probes were the most important steps in the field and raised the attention of researches in many fields.
However, the physical nature of light propagation in tissue, the unknown anatomical features of the sample, the uncertainty regarding optical parameters of tissue and the restricted number of independent source-detector measurements FMT allows only a limited and relatively poor spatial resolution. Nevertheless, non-contact FMT appears today as a fast, inexpensive and powerful technique for preclinical applications offering a high sensitivity comparable to PET readouts and makes FMT an attractive research tool.

6.1 Aims and Objectives

The first objective was the design and construction of a non-contact FMT system for multiple wavelengths based on a system reported by Martin et al. [42]. Automation of most of the hardware and therefore the integration of the components into the control software provided by J. Ripoll was a further issue. Within this we implemented a new concept for filter switching with help of an integrated filter wheel between the objective and the detector chip. Another setup requirement was the implementation of the two measurements geometries (transmission and reflection). Finally the system should be characterized with help of different biological *in vivo* applications in mice e.g. Alzheimer's disease measurement in mouse brain using the oxazine dye AOI987, lymph node imaging using a labeled antibody and to study bone growth induced by mechanical stimulation in tail bone vertebrae.

6.2 Material and Methods

6.2.1 Instrumentation

The setup consists of three different CW laser sources: i) a solid state laser at 670nm (B&W Tek, Newark, USA) with a maximum output power at the 100μm multimode fiber end of 300mW, ii) a free beam fiber laser at 592.5nm (MPB communications, Montreal, Canada) with an output power of 200mW and iii) a fiber coupled diode laser at 780nm (World Star Tech., Toronto, Canada) with an output power at the fiber end of 50mW. All lasers are coupled to a fiber switch (Piezosystems Jena, Jena, Germany) with multimode fibers of a core diameter of 200μm and an numerical aperture of 0.22 allowing automated selection of the appropriate wavelength delivered to the system. The fiber switch output fiber was connected to a numerical aperture matched achromatic collimation lens (Ocean Optics, Dunedin, USA) to the setup which is built in a custom-made black imaging box which ensures that no ambient light is disturbing the experiments. After the collimation lens the beam propagates freely through a thin glass slide splitting the beam where the output power is measured with a powermeter (Gentec-EO, Lake Oswego, USA) at 90° from the propagation direction and enters either a 100mm or a 50mm lens (Thorlabs, Munich, Germany) depending if the system is working in reflection or transmission mode, respectively. The lenses are used to focus the beam on the sample depending on the beam propagation distance. For the source scanning on the sample surface a scan head (ScanLab, Puchheim, Germany) was used containing two galvanometric driven mirrors. After the scan head the beam propagation direction is changed by 90° where it reaches a large (120×75mm) front surface mirror (mirror 1) deflecting the beam again by 90°. Depending on the position of mirror 1 the beam is directed towards the bottom surface of the sample for transmission measurements or towards a second mirror (mirror 2) allowing reflection measurements by deflecting the beam to the sample surface which is lying in the focal plane of the camera. The acquisition was performed with a 16 bit CCD camera (ANDOR Corporation, Belfast, Northern Ireland) water cooled down to -90°C for reduced dark and readout noise, with a chip size of 1024×1024 pixels and a 50mm f1.4 macro objective lens (Nikkor, Tokyo, Japan) resulting in a field of view (FOV) of 65×65mm. High quality standard 25.4mm diameter bandpass filters (Semrock, Rochester, USA) were used for excitation and emission light detection mounted in a filter wheel (DTA, Cascina, Italy) which is located in a housing between the objective and the CCD chip of the camera. The temperature controlled sample platform was connected to a water bath maintaining the temperature and allowing a horizontal sample placement and a flexible anesthesia mask fixation to place any part of the animal in the FOV of the imaging system. Two rectangular electroluminescent foils mounted in the roof of the imaging chamber were used for white light illumination for the acquisition of reference surface images.

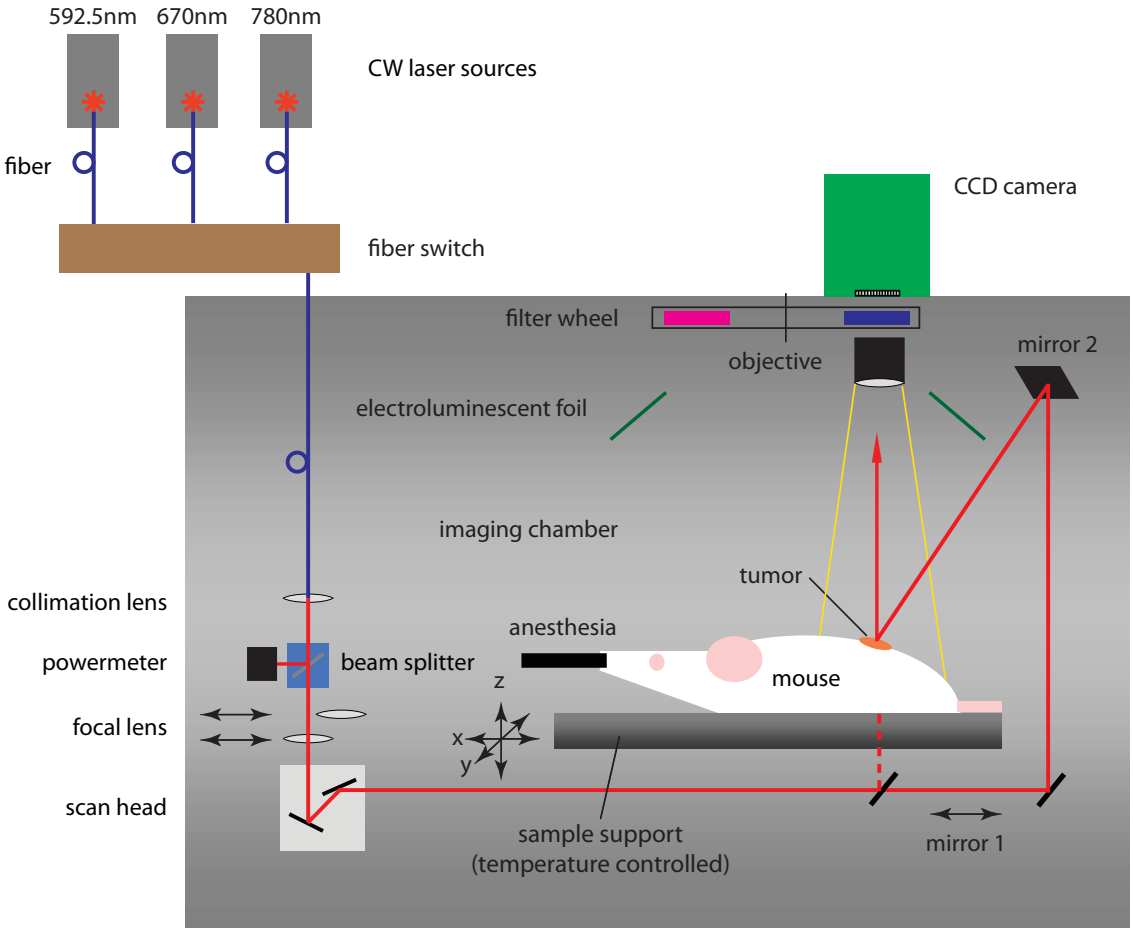

Figure 6.1: Schematic of the FMT instrumentation: The laser sources and fiber switch were located outside the imaging chamber. The light is guided into the system via an optical fiber which is connected to a collimation lens collimating the freely propagating beam. The power is measured with a powermeter and the beam is focussed with different focal lenses which could be slide into the optical path depending on the operation mode. The scan head allows the source scanning on the sample surface either in transmission or reflection geometry depending on the placement of mirror 1. Mirror 2 is only used in reflection geometry. The light is detected with a CCD camera with appropriate filters mounted in a filter wheel between the objective and the CCD chip. The sample platform allowing a horizontal animal placement can be illuminated with two electroluminescent panels for reference image acquirements.

6.2.2 Fluorescence Data Acquisition

The sample was placed on the temperature controlled imaging platform within the FOV of the optical system. Prior to each measurements two calibration steps were needed: First the coordinate systems of the camera and the scan head were related to

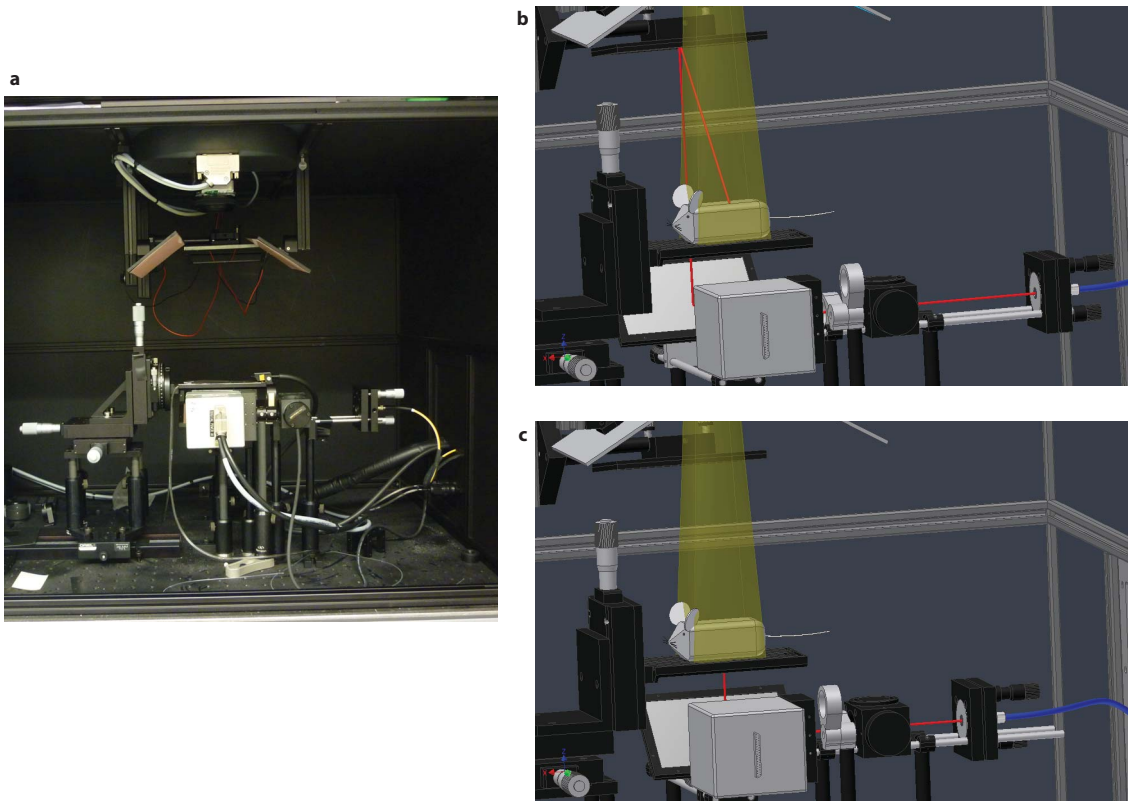

Figure 6.2: FMT instrumentation. **a** Side view of the imaging chamber. **b** Sketch of the measurement geometry in reflection mode. **c** Sketch of the measurement geometry in transmission mode.

each other to get the correct center position of the illumination sources. Second, the pixel dimension in centimeters was calculated with help of a millimeter paper in the focal plane of the camera. After that the position of the source grid and the number of sources was adjusted operator-interactively in order to match the region of interest (ROI) on the sample surface. An integration time has to be chosen which is depending on the fluorescence source strength and the applied laser power. Care must be taken to cover an adequate range of the 16bit resolution of the camera to have a high quality raw data set. The chosen integration time was applied to all illumination sources. After these adjustments the optical acquisition was started and the laser beam was scanned automatically across the defined grid of illumination spots. For each source position an image was recorded resulting in a $N_x \times N_y \times N_s$ array of images, where N_x and N_y are the number of pixels in x and y direction and N_s the number of sources. Overall two stacks of images were recorded with appropriate bandpass filters at two wavelengths regions corresponding to the excitation and emission maximum of the imaged fluorophore. Care has been taken that the leakage of the different spectra (excitation/emission spectra) is minimal. For all measurements a white light reference image of the sample and a dark background image accounting for the influence of

possible ambient light entering the black box were recorded. To complete the data set a text file was created containing all relevant information concerning the experiment.

6.2.3 Fluorescence Data Reconstruction

For image reconstruction the normalized Born approximation [108] was used, as described in the theoretical part of this thesis (see section 5.1). The values of this ratio were used in the forward model [112] accounting for the fluorescence signal on the sample surface. The reconstruction was performed by inverting this forward model using an ART method. This algorithm is an iterative method used in computed tomography [110] and adapted for imaging diffusive media with boundary restrictions [105]. An initial assumption for the fluorophore distribution is iteratively improved using a least square minimization procedure to minimize the difference between reconstructed and measured data. The reconstruction yielded a three dimensional map of the fluorescent source distribution within the subject.

6.2.4 Phantom Preparation

For the purpose of standardized system characterizations silicone based samples were used [113, 114, 115]. The phantoms were based on a transparent, two compound room temperature vulcanizing (RTV) silicone (Wacker Silicone, Munich, Germany). Compound A and B were mixed in a ratio of 9:1. Compound A solidifies by mixing with a hardener (compound B) after 24h at room temperature. The solidified rubber like material has an index of refraction of 1.4095 and a density of 1.02g/cm^3 at 23°C. To simulate optical tissue properties, TiO_2 particles (Alfa Aesar, Karlsruhe, Germany) with a size of <100nm and carbon black powder (Alfa Aesar, Karlsruhe, Germany) were added as scattering and absorbing agent, respectively. Both substances were first added to silicone compound A and mixed thoroughly for a few minutes before the hardener compound B was added. After another few minutes of mixing the silicone batch was put in a vacuum chamber to reduce air bubbles within the silicone material. After that the silicone batch is ready and can be poured into the prepared templates. One disadvantage of TiO_2 and carbon black powder is that it settles down and builds clusters when not stirred and therefore extended mixing is important to ensure that the particles are uniformly distributed. Another concern could be the limited achievable forward scattering ($g_{\max} = 0.7$) for TiO_2 which was observed in tissue mimicking phantoms made of resin [116] as tissue is known to be strongly forward scattering with $g > 0.7$.
The advantage of silicone phantoms is the long lifetime stability which makes it attractive for regularly standardized system performance tests. Furthermore silicone is simple to handle and can be used to model complex geometries with appropriate templates. A possible disadvantage is the broad range of autofluorescence which can be seen on the other hand as an advantage as it closely mimicks real tissue which is also autofluorescence. For phantom experiments we produced cuboid shape phantoms

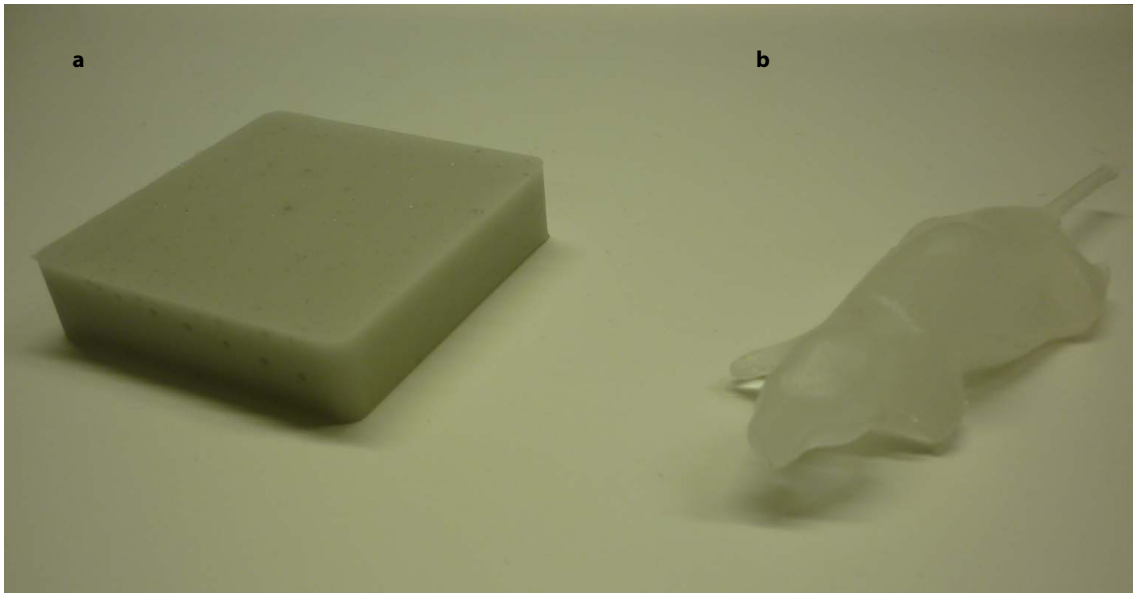

Figure 6.3: Silicone phantoms. **a** Cuboid shaped silicone phantom. **b** Mouse silicone phantom.

(see Fig. C.4a) with a thickness of ≈13mm containing holes of 1.5mm diameter in different depths and separations. The holes are used for fluorescent dye administration at a chosen position. The dye was filled into small glass capillaries (outer diameter: 1.5mm inner diameter: 0.6mm) and inserted into the holes. The optical properties of all the phantoms were matched to average tissue optical properties of μ_a=0.2cm^{-1} and μ_s'=10cm^{-1} which values are used throughout the thesis. To achieve these optical properties 0.1g of a 1:250 carbon black/TiO_2 mixture and 0.22g TiO_2 were added to a silicone batch of 76g. The resulting optical properties (μ_a and μ_s) were measured using a near infrared spectrometer (OxiplexTS, Illinois, USA) at a wavelength of 690nm. Unfortunately this measurement method is unable to provide information about the reduced scattering coefficient which is of main interest in optical imaging. Therefore a side project was started to design a measurement setup based on two integrating spheres accounting for all optical properties (μ_a, μ_s and μ_s') of a sample. A detailed description and first consistency experiments can be found in Appendix C.
As cuboid phantoms only mimick a simple ideal case we went further to model a mouse shaped template (see Fig. C.4b) which could be used as a further step for characterization experiments before going into *in vivo* applications. For this, a whole body structural MRI scan of a mouse was performed to obtain the animal's surface. After the surface rendering and smoothing process a negative image was generated, from which the mouse template was produced. The template could be separated into two parts for better handling and could be filled from the side of the tail. The template was produced layer by layer (thickness 0.016mm) with a 3D polymer printing

technique (irpd, St. Gallen, Switzerland) allowing an accurate surface recovery. Again the mouse shaped phantom can hold different holes in various parts and depths of the phantom body for dye administration allowing more realistic setup tests.

6.3 *In vivo* Applications

6.3.1 Tail Vertebra Imaging

This section is adapted from:

F. Lambers, F. Stuker, C. Weigt, G. Kuhn, K. Koch, F. A. Schulte, J. Ripoll, M. Rudin, R. Müller. Multimodality imaging of load-induced bone adaptation. In preparation and intended for submission to *Journal of Orthopedic Research*.

Introduction

One of the most common bone diseases is osteoporosis which is mainly occurring in the aged population. The balance of bone formation and resorption which is present in healthy individuals is shifted towards bone resorption lowering the bone density. This leads to fragility which may results in severe fractures leading to patient morbidity and mortality. The pathways underlying this disease involving the bone formation (mineralization of bone matrix) and resorption (demineralization of bone matrix) are not well understood. Therefore it would be highly attractive to visualize *in vivo* bone micro structure and molecular processes (Osteoblast and Osteoclast activity) which might help to improve the understanding of the biological processes involved in bone disease.

Aims and Objectives

The aim of the study was to measure load induced changes in the bone microstructure and osteoblast/osteoclast activity. To allow for this a multimodality sequential read out combining micro computed tomography (CT) and FMT was developed. CT was used to monitor changes in the bone microstructure and FMT to derive three dimensional molecular information of osteoblast activity. This was achieved by OsteoSense 680 (PerkinElmer, Boston, USA) injection which is a bisphosphonate fluorescent agent targeting hydroxyapatite and therefore osteoblast activity [22].

Material and Methods

To enable loading of the 6th caudal vertebrae stainless steel pins were surgically inserted in the 5th and 7th caudal vertebra of C57BL/6 mice. After a recovery time of 3 weeks the distal pin was mounted in an axial compression device [117] while the proximal pin was fixed, allowing a loading of either 0N (no-loaded group 1) or 8N

(loaded group 2) at a frequency of 10Hz. The loading was performed three times a week for a total duration of four weeks.
Each week the mice were scanned with CT (Scanco Medical, Brütisellen, Switzerland) before loading. The high resolution (10.5μm isotropic) structural scans of the vertebrae and appropriate post processing software tools allowed the extraction of relevant parameters to derive anatomical changes in the vertebrae. After rigid registration regions of bone formation and resorption could be visualized by the overlay of follow-up scans and dynamic morphometric parameters could be quantified such as bone resorption rate (BRR, volume of bone that is resorbed between the scans, divided by the total volume of bone at the first time point per day) and mineral resorption rate (MRR, mean thickness of the resorbed bone volume divided by the number of days between the measurements).
The FMT measurement and OsteoSense 680 injection protocol was as follows: 24h prior to the first FMT measurement (day 0) OsteoSense 680 was administered intraperitoneally. A second OsteoSense 680 injection was performed subsequently after the second FMT measurement at day 13. At day 14 and day 27 further FMT measurements were performed. Again, a third dosage of OsteoSense 680 was administered after the FMT measurement at day 27, with the last FMT measurement on day 28. To allow an appropriate illumination source placement and the application of diffusion theory for the reconstruction the mouse tails were embedded in a cubic shaped silicone phantom. Fiducial markers were used for a reproducible positioning of the phantom and for reproducibly placement of the vertebra. The fluorescence measurements were performed with a 671nm laser on a source grid of 7×8. The fluorescence signal was detected with a bandpass filter at 720nm. For the reconstruction we used 154 detectors and 0.05mm isotropic voxels. Due to resolution limits, the fluorescence readout, the mean fluorescence intensity, was derived from a ROI around the loaded vertebra incorporating also parts of the unloaded neighboring vertebrae. The measure of osteoblast activity was defined as the value at the first time point (day 0), the difference between day 14 and day 13 and the difference between day 28 and day 27 whereas the difference between day 13 and day 0 and day 27 and day 14 provided the measure of osteoclast activity. The mouse model and the CT measurements where provided by our collaborators (Group of R. Müller, Institute for Biomechanics, ETH Zurich, Switzerland)

Results

After each OsteoSense 680 injection an increased fluorescence intensity was observed in all mice whereas, a slight decrease between day 0 and 13 and day 14 and 27 was visible. By normalizing the mean values of all animals (of each group) to the first time point and deriving the percentage it was shown that after day 14 the values for the 8N group were always higher compared to the 0N group (Fig. 6.5a). By calculating the percentage differences between the time points it was shown that changes in bone formation and resorption rate as measured from difference in fluorescence intensity

were always greater for the 8N than 0N group (Fig. 6.5b). The bone formation was highest for both groups after two weeks whereas the bone resorption peaked for both groups in the third week compared to the other time points investigated.
The bivariate correlation analysis showed a significant correlation ($p<0.05$) between percentage difference in fluorescence intensities between day 0 and day 13 and corresponding BRR and the MRR values for both groups (Fig. 6.5c,d).

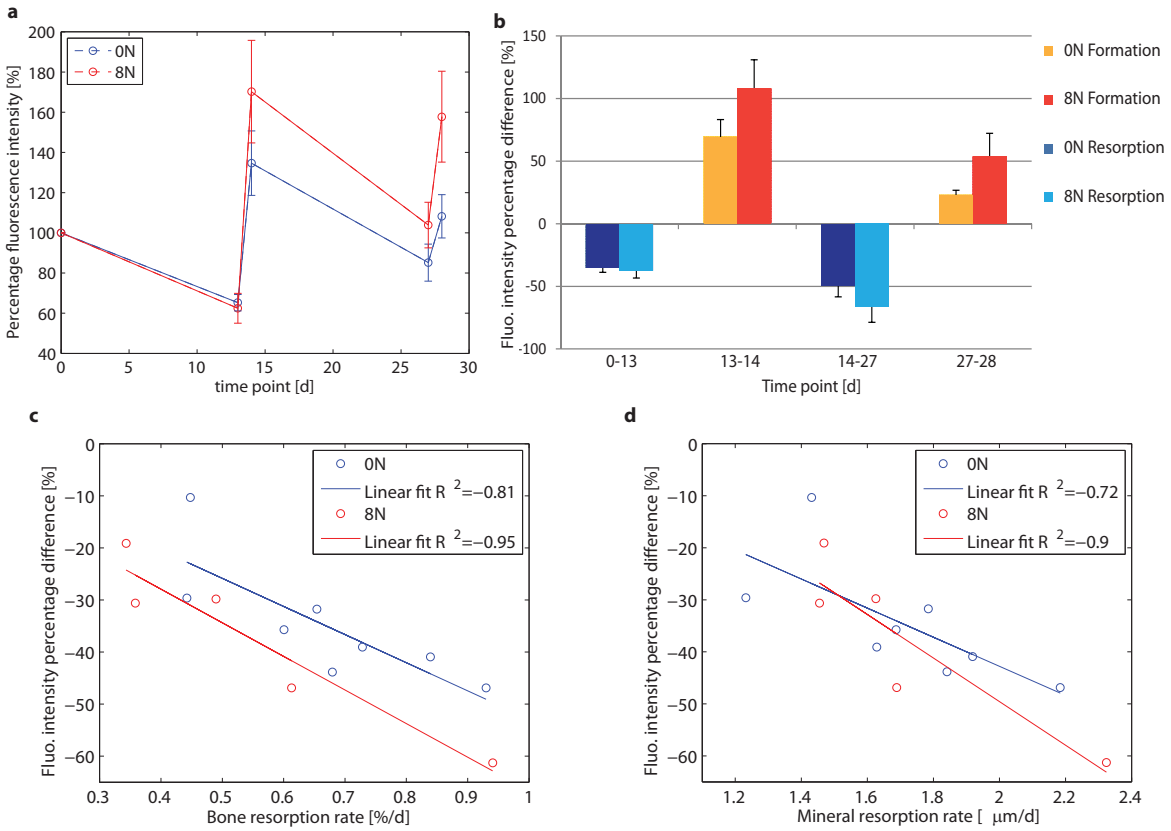

Figure 6.4: Quantification of FMT measurements in tail bone. **a** Normalized fluorescence intensity percentage at the different time points. **b** Fluorescence intensity percentage difference between the time points representing the bone formation and resorption. **c,d** Correlation between the percentage difference fluorescence intensity and BRR (**c**) and MRR (**d**) between day 0 and day 13. The values for the different groups (0N blue circles and 8N red circles) and its linear fit (blue and red line) is given.

Discussion

The result of the study showed the added value of monitoring load induced-adaptation in bone by two complementary readouts. Both modalities were able to give a specific insight to osteoblast and osteoclast activity: where FMT allowed to measure bone formation at a short time frame (∼1d), with CT a value could only be averaged over a week. With FMT an accurate measurement of osteoblast activity was achieved

by comparing the fluorescence intensities before and after OsteoSense 680 injection, while osteoclast activity could be shown by values which are similarly calculated as the BRR from CT data. Furthermore it could be shown that there is a significant correlation between these parameters. Finally the FMT readout confirmed the findings from the calculated bone formation rate from CT data which was higher in the 8N group compared to the 0N group. This was seen by the greater fluorescence signal after OsteoSense 680 injection. Taken together, these data show the feasibility of multimodal imaging, on one hand the ability to quantify molecular information in bone with FMT, and on the other hand structural information with CT.

6.3.2 Lymph Node Imaging

Introduction

The formation of metastasis was observed in most tumor types in humans and causes the majority of cancer deaths. A prognostic indicator of the disease progression is the metastasis to regional lymph nodes which is the first step of tumor dissemination in most cancer types. Therefore sensitive, non-invasive and preferentially simple methods to detect metastasis to lymph nodes in early stages of tumor dissemination would govern a great advantage compared to routine clinical approaches including the dissection of sentinel lymph nodes which can cause side effects such as lymphedema. It was recently shown in different mouse models of cancer metastasis that tumors induce the expansion of lymphatic vasculature (lymphangiogenesis) in tumor draining lymph nodes. Therefore lymph node lymphangiogenesis might serve as a novel target to image the very early stages of the metastatic process. Mumprecht et al. [118] visualized the first time with a non-invasive PET imaging approach the lymph node lymphangiogenesis using a ^{124}I labeled antibody against the lymphatic vessel endothelial hyaluronan receptor-1 (LYVE-1). To image lymphangiogenesis they decided to use a robust fast progressing inflammation induced transgenic mouse model (K14-VEGF-A) instead of a metastasis tumor model which has a large variability and discomfort for the animals.

Aims and Objectives

As most PET tracers suffer from a limited half life and high production costs due to an expensive infrastructure, a more stable and inexpensive approach was developed using a fluorescent labeled antibody. For the here presented proof-of-principle study an ICG labeled antibody against LYVE-1 was developed and used to image the auricular (also known as superficial cervical) lymph nodes in an inflamed mouse model which was all provided by our collaborator (Group of M. Detmar, Institute for Pharmaceutical Sciences, ETH Zurich, Switzerland).

Materials and Methods

For this study age matched K-14-VEGF-A mice were used which were shaved in the cervical region one day prior the experiments. Delayed-type hypersensitivity reactions were induced in the left ear skin which lead to lymph node lymphangiogenesis in the draining auricularly lymph node in the cervical region of the mice. The mice were therefore placed on the back on the imaging platform and the labeled antibody which was injected prior to the measurement was excited with a 780nm laser which was scanned across a grid of 56 source points. The fluorescence signal was detected with a bandpass filter at 820nm. For the reconstruction we used 192 detectors and a voxel size of 0.05mm^3.

Results

The reconstructed signals from the lymph nodes in the K-14-VEGF-A mice were clearly visible (Fig. 6.5a). The signal from the left side appears with a much larger spread compared to the right inflamed side. While quantifying the reconstructed intensities of the lymph nodes we noticed that the signal on the left non-treated side was 1.5 fold increased compared to the inflamed side. This was in contradiction to the expectations and the parallel acquired planar images where a 1.2 fold signal increased on the inflamed side was measured. To further investigate this discrepancy the ROI was dissected and it was observed that on the left side two nodes were lying behind each other and therefore both were contributing to the signal whereas on the right side only one lymph node was present. Unfortunately the distance (< 1mm) between the two lymph nodes was to small to be separated by FMT and lead therefore to a greater signal than on the right side. The analysis of the excised lymph nodes with the planar imaging readout where now both lymph nodes contribute to the signal resulted in similar values compared to the FMT readout.
Interestingly the control mouse where no antibody administration was performed showed a clearly distinguishable signal of both auricularly lymph nodes (Fig. 6.5b). Furthermore the depth localization showed a spherical fluorophore distribution according to the anatomy of the lymph nodes observed by dissecting them. Similar structures of the fluorphore distribution was also observed in other published FMT studies on different animal models [42, 119]. By having the depth information by hand it was possible to absolutely quantify the signals which was done by line profiles in the xz-projected image (Fig. 6.5c). The line profile confirmed the findings observed in Fig. 6.5a. The quantification of the control animal revealed in lower signal intensities on a same level for both lymph nodes compared to the unaffected right lymph node in the injected animal.

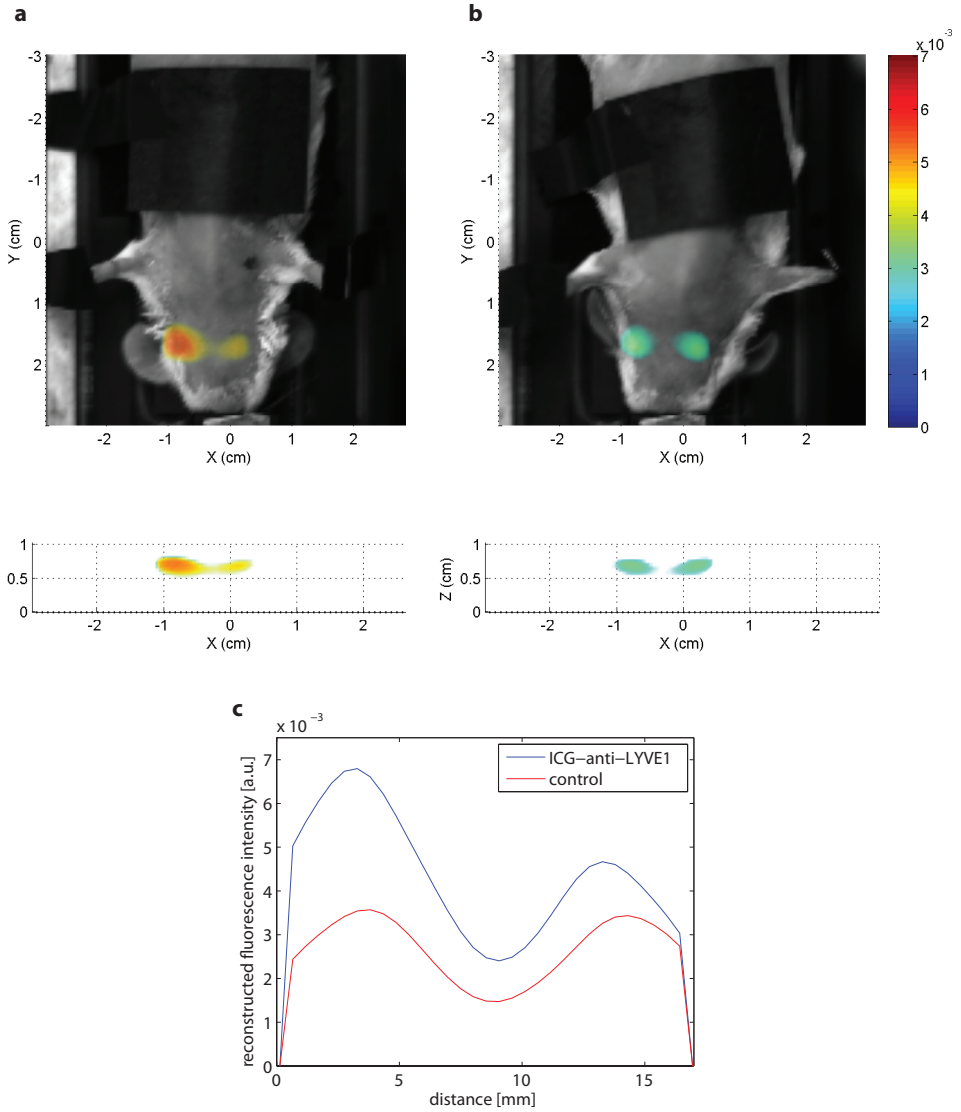

Figure 6.5: *In vivo* imaging of lymph node lymphangiogenesis. **a** Three dimensional reconstructed fluorophore distribution in a ICG-anti-LYVE1 injected mouse in xy-projection (upper image) and in xz-projection (bottom image). **b** Three dimensional reconstructed fluorophore distribution in a control mouse in xy-projection (upper image) and in xz-projection (bottom image). **c** Line profile of a cross-section in xz-projection of an ICG-anti-LYVE1 injected (blue) and a control mouse (red).

Discussion

Up to know it is unclear where the signal in the control animals originates from and further experiments on different animals with different excitation and emission wavelengths are needed to investigate this interesting finding. Even though the experimental outcome was different than expected it has been shown that in this specific experiment planar imaging quantification is difficult and need to be verified by other means. Furthermore the sensitivity of FMT was shown although its resolution limit to separate structures *in vivo* was clearly demonstrated.

6.3.3 Alzheimer's Disease

Introduction

Dementia, cognitive impairment such as memory loss are the most important clinical characteristics of Alzheimer's disease (AD). The pathogenesis is associated with the formation of insoluble aggregates of amyloid β-peptide, the amyloid plaques which are small, spherical aggregates (5-50 μm diameter) [120], which accumulate over time in the brain of Alzheimer's patients, primarily in the cortical region. Amyloid-β plaques and neurofibrillary tangles (another protein aggregate) are the principal histopathological hallmark of AD and therefore biomarkers of great interest. Approaches allowing the direct and non-invasive visualization of plaque growth *in vivo* would help to improve early diagnosis and contribute to accelerating drug developments. Furthermore, such tools would be attractive for basic research. There are great efforts on going in different imaging fields such as CT, MRI and optical imaging or in combined modalities [121] to detect amyloid plaque load in transgenic mouse models.

Aims and Objectives

It was shown that planar near infrared fluorescence imaging in combination with the fluorescent oxazine derivative dye AOI987 is suitable to visualized amyloid plaque depositions *in vivo* in the brain of APP23 mice [122]. The aim of this proof-of-principle study is to verify that with FMT the same information can be extracted and that furthermore it is possible to three-dimensionally localize and quantify the fluorophore distribution in the brain of a transgenic mouse (arcAβ) considered to be a model of AD and a control mouse. The dye was synthesized by our collaborators (K.-H. Altmann, Institute for Pharmaceutical Sciences ETH Zurich, Switzerland) according to previously established protocols [122].

Materials and Methods

For this FMT study we used a 17month old transgenic arcAβ mouse and its age matched control wild type littermate. The transgene arcAβ mice develop only vascular plaques compared to APP23 mice where vasculature and parenchymal plaques were

developed. Both animals were shaved in the head region one day prior the experiments to have no optical interference from the black fur. As a fluorescence probe AOI987 [122] was used which is known to have an excitation maximum at 670nm and binds to Aβ deposits in the brain. The dye was synthesized by our collaborators (K.-H. Altmann, Institute for Pharmaceutical Sciences ETH Zurich, Switzerland) according to previously established protocols [122].
For the experiment, the animals were cannulated and placed on the temperature controlled animal platform in the FMT scanner. After a intravenous bolus injection of 0.1mg/kg AOI987 the first measurement was taken 10min after the dye administration by sequentially scanning a 671nm laser across a 6×6 point grid on the animals head. To follow the time course, this procedure was repeated 60min and 120min after the dye administration. The fluorescence signal was detected with a bandpass filter at 720nm. For the reconstruction we used 140 detectors and a voxel size of 0.05mm^3.

Results

Immediately after the injection an intense fluorescence signal was detected. The disappearance of the signal was slightly slower in the transgenic arcAβ (Fig. 6.6a) compared to the control animal (Fig. 6.6b). On the reference image (Fig. 6.6c) anatomical landmarks are indicated for orientation purposes. The analysis of the time course using relative quantification (Fig. 6.6d) of the brain signals confirmed the findings of the reconstructed images where the brain signal of the arcAβ mouse decreased at a slower rate. The data points were fitted with an exponential function (dashed lines) which is usually applied to model the kinetic of a compound entering the blood pool. A comparison of the fluorescence intensities from arcAβ and control mice provides a measure for the specific binding of AOI987 (Fig. 6.6e) to amyloid plaques. The specific binding is defined according to [122] as the fluorescence signal of the transgenic mice minus the fluorescence signal of control mice divided by the fluorescence signal of the transgenic. This calculation accounts for the non-specifically bound dye fraction. The localization of the reconstructed fluorophore distribution in the brain region was found in the top layer of the reconstructed volume (insights in Fig. 6.6a,b) represented in an yz-projection.

Discussion

Our findings were in relation to a study performed by Hyde et al. [121] where a similar fluorophore distribution was observed with measurements on a hybrid FMT/CT modality. Furthermore, we could show that the reconstructed fluorescence intensity is prominent in the top layer of the reconstructed volume which indicates that the fluorescence signal originates from cortical brain regions. The depth information of FMT makes the quantification more reliable compared to the surface weighted readouts in planar methods where no information on the fluorophore distribution in deep tissue is

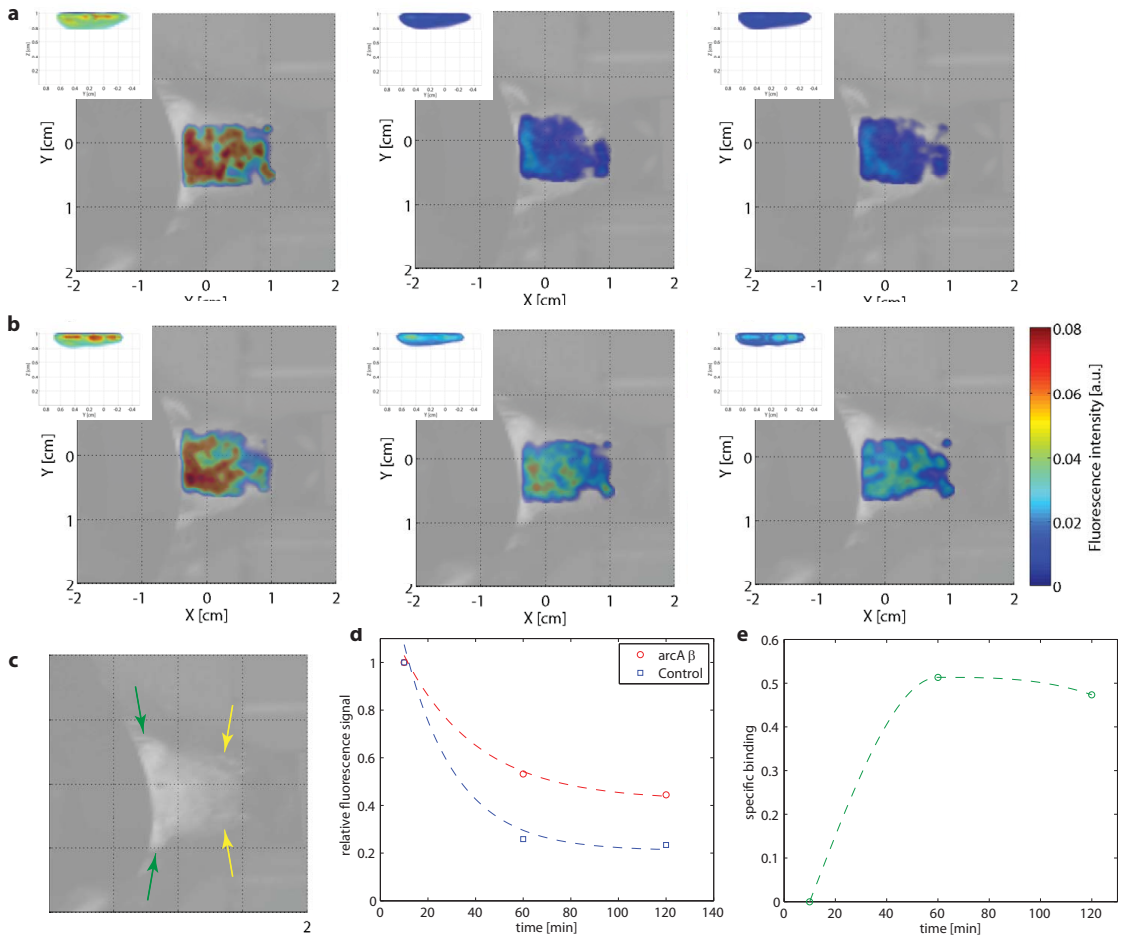

Figure 6.6: *In vivo* imaging of amyloid-β deposits. **a** Reconstructed fluorescence intensity in the xy-plane for a control animal measured at three different time points (10, 60 and 120min) left to right. The insights at each time point represents the fluorophore distribution in depth. **b** The same as in **a** but for a arcAβ mouse. **c** White light image where the yellow and green arrows point to the animals eyes and ears, respectively. **d** Time course of the relative fluorescent intensity of an arcAβ and a control mouse representing the binding affinity. **e** Specific binding of AOI9087 as a function of time after injection to an arcAβ mouse.

provided. Despite this limitations, it appeares that planar methods can provide quantifications, which are for this specific experiment comparable to FMT readouts. The sensitive FMT method might be the choice to resolve minor changes in plaque load where planar methods have its limitations. The slower fluorescence signal decrease in the transgenic animal compared to the wild type animal might be an indication for specific dye retention in cerebral tissue of transgenic mice which was also shown by the specific binding curve. Finally a good correspondence of the measured fluorescence intensity values at the different time points with the fitted exponential curve proofed that the FMT provides a quantitative, three-dimensional readout.

Chapter 7

Hybrid Imaging: Non-contact FMT/MRI

It was described in subsection 1.2 that all reported integrated FMT/MRI systems uses fibers for light delivery and detection. These fiber based concepts have some limitations such as the space requirements of the source/detector fiber bundle allowing only measurements using human MR scanners with a large bore (>500mm) which therefore compromise spatial resolution and thus the quality of structural information. Another concern is the limited optical spatial resolution due to only partially recovered light from the object surface and the inherently low number of source/detector fibers. A further issue might be the detector fiber coupling loss and the rigid geometry restricting the flexibility in potential excitation schemes.
However, small fluorescence detectors that operate in high magnetic fields of small animal MRI scanners would enable a fundamentally different solution. Detectors could be positioned in close proximity to the fluorescent source as an integral part of the radiofrequency (RF) antenna used for the detection of MRI signals. Such a detector concept would allow the implementation of a non-contact fluorescence light detection inside a small bore of a commercial small animal MRI scanner. A non-contact source scanning on the surface would further allow an implementation of fully contact free FMT system inside an MR scanner. This could be achieved via a free beam laser scanning from outside the bore as most probably scanning devices such as an xy-stage or a scan head would not work in high magnetic fields. This is the basic strategy which has been followed to design and characterize a first generation non-contact FMT/MRI setup which has been further improved in a second step.

7.1 1st Generation Non-contact FMT/MRI Setup

This section is adapted from:

F. Stuker, C. Baltes, K. Dikaiou, D. Vats, L. Carrara, E. Charbon, J. Ripoll and M. Rudin. Hybrid Small Animal Imaging System Combining Magnetic Resonance Imaging With Fluorescence Tomography Using Single Photon Avalanche Diode Detectors. *IEEE Transactions on Medical Imaging*, in press.

The instrumentation is further described in the following patents:

F. Stuker, K. Dikaiou, C. Baltes and M. Rudin. MRI Device With Fluorescence Molecular Tomography System. Pub. No.: EP 2 251 676 A1.

and

F. Stuker, K. Dikaiou, C. Baltes and M. Rudin. Optical MRI Device. Pub. No.: US 2010/0292563 A1.

7.1.1 Aims and Objectives

In the here presented first generation non-contact FMT/MRI setup we used avalanche photodiode detectors which are not susceptible to high magnetic fields as demonstrated in PET/MRI systems [123] and are often used in other biomedical applications [124]. We therefore describe a hybrid FMT/MRI system based on a non-contact FMT setup [40, 42] using single-photon avalanche diodes (SPAD) designed to fit inside the 120mm gradient bore of a small animal MRI scanner operating at a magnetic field strength of 9.4T. Devoid of optical fibers, the system offers maximal flexibility with regard to excitation schemes and sample placement. The performance of the hybrid FMT/MRI system was characterized using phantoms with optical parameters mimicking those of biological tissue that comprised one or several fluorescent sources. Aspects investigated were the accuracy of the spatial in-plane and depth information derived from FMT data as well as the sensitivity and linearity of the optical detectors. Feasibility for *in vivo* imaging was assessed by simultaneously studying protease activity and tumor morphology in a murine colon cancer model.

7.1.2 Material and Methods

Instrumentation

The experimental setup consisted of an illumination module located outside and a sample platform inside the magnet (Fig. 7.1). The illumination module consists of a fiber coupled 670nm continuous wave laser (B&W Tek, Newark, USA) for excitation. The multimode fiber (core diameter 100μm, NA=0.22) was connected to a numerical aperture matched collimation lens (Thorlabs, Munich, Germany). The pinhole

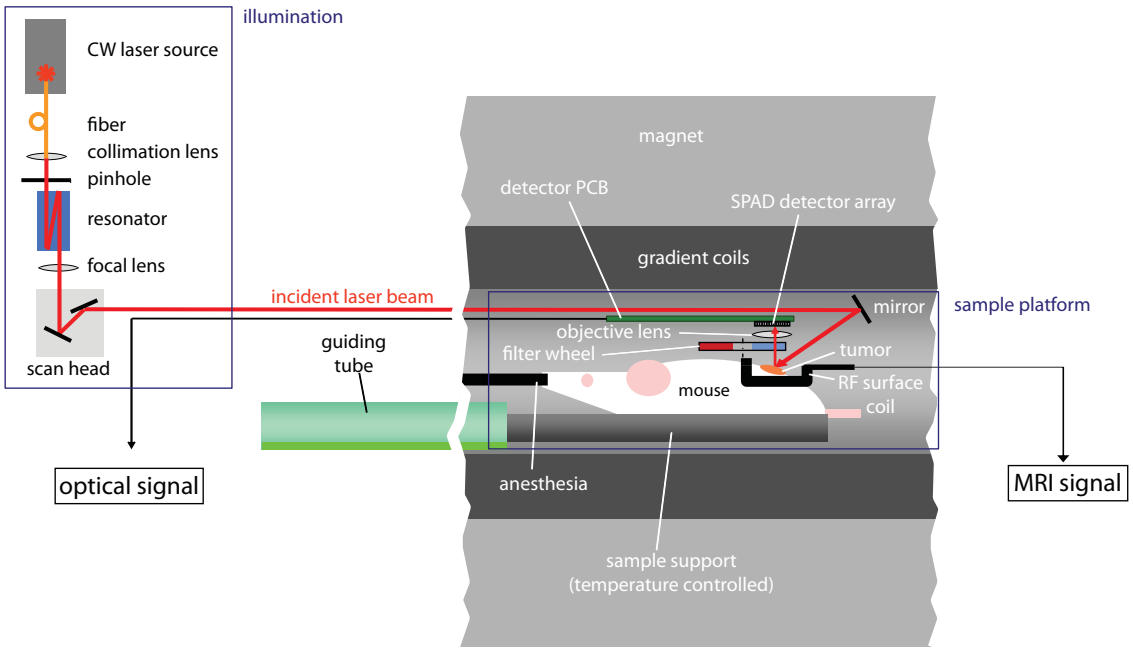

Figure 7.1: Experimental setup. Schematic of the FMT/MRI instrumentation. The illumination module comprises the laser source, a resonator and the scan head for deflecting the beam across the object. The sample platform comprises the SPAD detector, the focusing lens and the filter wheel used for selecting the wavelength for detection. A semi-cylindrical RF coil is used in transceiver mode. The laser beam is deflected to the sample surface using a mirror.

(diameter 0.5mm) behind the lens was mapped with an anti-reflectance coated spherical singlet lens (f=1000mm, Melles Griot, Bensheim, Germany) by a 2f image on the subject. To achieve a focal length of 2m (required due to the dimensions of the MR magnet) the laser beam was guided through an optical resonator mounted in-between pinhole and focusing lens. The resonator consisted of two coated economy front surface mirrors (Thorlabs, Munich Germany) placed 400mm apart and was traveled 5 times. The light was then guided to a scan head (Scanlab, Puchheim, Germany), where it was deflected by 2 galvanometric driven mirrors to allow scanning of sources on the sample surface. These mirrors deflected the beam by 90° from the input direction. The beam was then directed through an 1800mm long tempered epoxy resin tube of 72mm inner diameter, which could be separated at the center for better handling. All components were fixed on a movable home-built aluminum breadboard placed outside the bore of the magnet in a magnetic stray field <10mT to ensure the proper function of the components.

At distal end of the tube the sample platform was fixed. A coated front surface mirror (Edmund Optics, Karlsruhe, Germany) was placed at the back flange of the sample

platform (Fig. 7.2a) located in the isocenter of the MRI, to deflect the beam by an angle of approximately 70° on the surface of the object, passing through the rectangular window of the MRI transceiver surface coil. A reflection geometry setup was chosen, which allowed the use of source intensity profiles for image reconstruction [107]. Diffusive light patterns on the surface of the animal were recorded for each illumination point. Light is emanating from the surface were selected according to their wavelength using filters placed in the filter wheel. High quality bandpass filters (Semrock, Rochester, USA) with peak wavelengths of 660nm and 720nm for measurements at the excitation and fluorescence wavelength have been used. Filters were characterized by >90% transmission over a range of ±13nm. A small 4mm diameter fixed focus lens (Edmund Optics, Karlsruhe, Germany) was mounted to the printed circuit board (PCB) in front of the detector array, yielding a FOV of 8×8mm at a focal distance of 33mm (Fig. 7.2b). A custom made 32×32 array of single-photon avalanche diodes (SPAD) [125] bonded on the PCB was used as photon detector (Fig. 7.2c). A small LED stripe at the back flange was used for white light illumination during the acquisition of reference surface images. All parts used for the setup were made from materials compatible with operation in high magnetic fields. A detailed technical description of the here described hybrid imaging principle can be found in [126, 127].

Detector Details

A SPAD detector which is also know as Geiger-mode avalanche photodiode (APD) represents a class of solid-state photo detectors. These SPAD detectors can be arranged in an array form which enables to use this technology for imaging. The technology is based on a reverse biased pn-junction in which the impinging photons on the pixels can generate an avalanche current which is electronically measured. This is a reverse process which therefore allows to count the number of these events. This value is then transformed into gray values used for the image representation. Besides the events which occur when photons impinge on the detector surface there are thermally and tunnelling generated carriers. These carriers are induced by generation-recombination within the semiconductor and can start an avalanche process. Thus in complete darkness there exists the possibility to observe such signals. This effect is the major contribution to the detector noise and the characteristic parameter is called dark count rate (DCR) and is given as the average number of counts per seconds in [Hz].
The SPAD array used for this study was produced by our collaborators (Group of E. Charbon, AQUA Group, Lausanne, Switzerland) and has 32×32 pixels implemented in a 0.35μm CMOS technology [128]. Each pixel of dimension $30 \times 30\mu m^2$ comprised a SPAD, a quenching circuit, and a 1-bit counter, all implemented with ten NMOS and two PMOS transistors, resulting in a total pitch of only 30μm and a fill factor of 3.14% (area ratio). The SPAD is a pn-junction biased above a breakdown voltage (VBD=17.7V) in order to operate in time-uncorrelated photon counting mode. A cathode bias voltage VOP of 21V was applied to operate in Geiger mode yielding an excess bias voltage VE of 3.3V. At this excess value, a maximum photon detection

probability of 35% (fill factor not included) was measured with a sensitivity spectrum ranging from 350 to 850nm. Calculating the overall sensitivity (fill factor times photon detection probability) revealed that about one in one hundred photons is detected. The image sensor array operates according to the rolling shutter principle. Each row is selected via the row decoder and read independently for all the columns during one clock cycle. The row is subsequently reset for initiating a new integration period. A clock frequency of 48MHz was used due to firmware limitations, thus the minimum integration time in our experiment was 2.66μs. The total exposure time was set by the selected iterations to build a frame. Since each pixel produces single bit digital information, an external FPGA chip-set is used to reconstruct a multi-bit image by incrementing 1024 32-bit counters sequentially row-by-row. The chip-set was not designed to tolerate high magnetic fields and was thus placed outside the bore of the magnet along with the circuit needed for communication with the computer. The connection between the chip-set and PCB was achieved via conventional flat ribbon cables. The SPAD detector array was tested inside the MRI system to assess the potential interference of a high static magnetic field of 9.4T. The signal-to-noise ratio (SNR) of 45dB is dominated by Poisson noise, while the maximum dynamic range achieved at 12 frames per second was 90dB. The median of the noise DCR per pixel measured over the entire array is 140Hz at room temperature and can be reduced by cooling of the chip to -40°C to DCR a median of 98Hz. DCR was unaffected by the magnetic field.

MRI Details

All MR experiments were carried out on a Bruker BioSpec 94/30 (Bruker BioSpin MRI, Ettlingen, Germany) horizontal small animal MR system operating at 400MHz equipped with a gradient system capable of generating a maximum strength of 400mT/m with a minimum rise time of 80μs. A home-built rectangular surface coil (20×24mm) was used for RF signal transmission and reception. The coil made of a flexible PCB substrate with standard copper layer was designed for mouse imaging and therefore curved to a cylindrical radius of 15mm. A window of 13×20mm was cut out of this single loop coil to allow for optical measurement (illumination and detection) in reflectance mode from the top[1]. Three-dimensional MR imaging was performed using a gradient echo sequence with the parameters: Field of view FOV=40×40×16mm^3; matrix dimensions MTX=80×80×32; voxel dimension VOX=500×500×500μm^3; excitation pulse angle $\alpha = 25°$; echo time/repetition time TE/TR=3.9/90ms; number of averages NA=4 resulting in a scan time=15min22s. In addition separate acquisitions with zero excitation pulse angle were performed for estimation of noise levels. *In vivo* experiments were performed using a two-dimensional multislice MR sequence with the following parameters: 14 slices of 700μm thickness; FOV=30×20mm^2; MTX=200×133; pixel dimension PIX=150×150μm^2; TE/TR=5.0/250ms; NA=20, yielding a total acquisition time of 11min5s.

[1] A detailed description of the coil design can be found in Appendix B

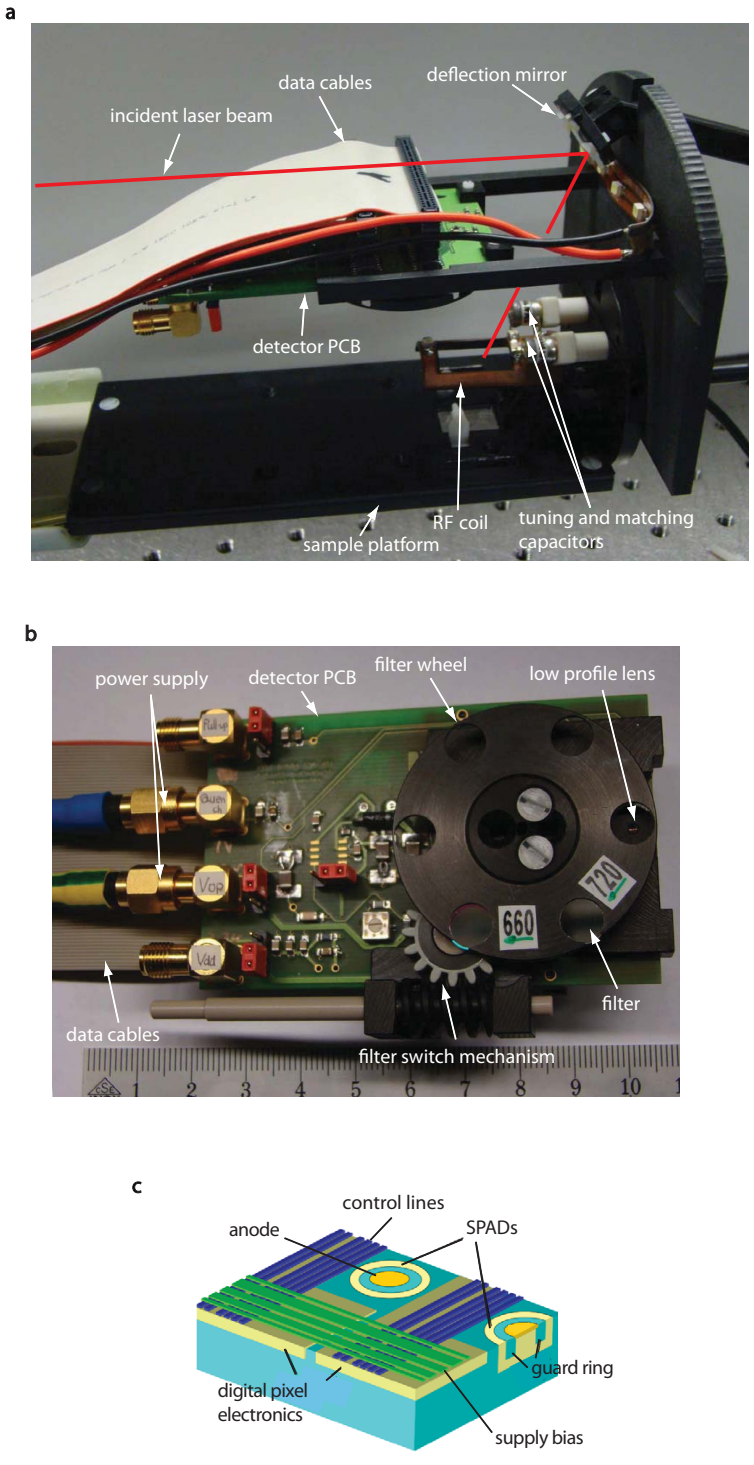

Figure 7.2: Setup components. **a** Side view of the sample platform. **b** Bottom view of the detector PCB. **c** Sketch of the SPAD architecture.

Phantom Preparation

For the phantom experiments two tissue-mimicking silicone-based phantoms were prepared (see section 6.2.4): Phantom (A) was used to characterize spatial resolution and concentration accuracy of the optical system and for the combined measurements with the MRI. It comprised holes for dye administration separated with center-to-center distances of 2, 3, 4 and 5mm in a plane parallel to the surface at a depth of 1mm.
Phantom (B) was used for depth analysis and comprised holes parallel to the surface at depths of 1, 2 and 3mm with respect to the surface with an in-plane separation of 5mm.

Subcutaneous Tumor Animal Model

Pathogen-free female BALB/C (CAnN.Cg-Foxn1<nu>/crl) nude mice (8-10 week old, weighing 20-25mg) were obtained from Charles River Laboratory (Sulzfeld, Germany) and housed in a controlled environment (23°C, 12h/12h light/dark cycle) with unlimited access to water and chlorophyll free food (Kliba Nafag, Kaiseraugst, Switzerland). All experiments were performed in accordance to the Swiss Veterinary law (License no. ZH 172-2008).
C51-cells, a colon cancer-derived secondary cell-line, were used to generate tumors. $1{\cdot}10^6$ cells were injected subcutaneously on the left thigh flank of the nude mice. The animals were monitored every second day for their body weight and tumor size. Animals with tumors of a size $3{\times}3\text{mm}^2$ and larger were selected for imaging experiments.

Fluorescent Agents

The commercially available cathepsin-activatable near infrared (NIR) fluorescent imaging agent ProSense 680 (VisEn Medical, Bedford, USA), a fluorophore conjugated graft polymer of polyethylene glycol (PEG) and poly-lysine, was administered intravenously via the tail vein in all *in vivo* imaging studies. A single dose of 13nmol was given followed by a second dose of 13nmol, 24h after the first injection. The FMT/MRI measurements were done 24h after the second dose of ProSense 680.
The near-infrared fluorescent oxazine dye AOI987 used in the phantom experiments was prepared according to published procedures [122].

Fluorescence Data Acquisition

The silicone-based phantoms were used for characterizing the performance of the FMT/MRI system. For each measurement, one or two fluorescent samples consisting of an aqueous solution of AOI987 [122] at various concentrations were included at defined depths and with variable spacing. Initially the sample was placed on the imaging platform within the FOV of the optical system and under the RF surface coil of the MRI system. For excitation, the laser beam was scanned across a grid with

7×7 illumination spots with dimensions and the exact location of the grid adjusted operator-interactively in order to match the ROI on the sample surface. We have chosen an integration time of 2 to 4s per source position depending on the fluorescent signal strength. This results in a total acquisition time between 5 and 9min. For each source position an image was recorded resulting in a $N_x \times N_y \times N_s$ array of images, where N_x and N_y are the number of pixels in x and y and N_s the number of sources. For calibration purposes the sources were measured on a white paper placed in the focal plane of the camera in order to get the center position of the sources and the pixel dimensions in centimeters. After that the optical acquisition was started and images were recorded at two wavelengths corresponding to the excitation (660nm) and emission maximum (720nm) of AOI987.
For *in vivo* measurements the illumination scheme and filter settings were kept the same.

Fluorescence Data Reconstruction

For image reconstruction the normalized Born approximation was used, which has been shown to yield robust data by considering the ratio of the measured emission and excitation images [108]. The values of this ratio were used in the forward model [112] accounting for the fluorescence signal on the sample surface. The reconstruction was performed by inverting this forward model using an algebraic reconstruction technique (ART). This algorithm is an iterative method used in computed tomography [110] and adapted for imaging diffusive media with boundary restrictions [105]. An initial assumption for the fluorophore distribution is iteratively improved using a least square minimization procedure to minimize the difference between reconstructed and measured data. The reconstruction yielded a three dimensional map of the fluorescent source distribution within the subject. Simulations were performed using the same forward model and reconstruction algorithm.

7.1.3 Results

Quantitative analyses have been carried out for assessing the crosstalk between modalities and the accuracy of in-plane and depth reconstruction. Moreover the linearity between the fluorescence intensity and the local dye concentration was investigated. Finally simultaneous hybrid measurements were performed with the combined system in a phantom experiment and in a first *in vivo* animal study.

Crosstalk

In hybrid systems potential crosstalk between the imaging modalities is an issue, i.e. sensitivity might be compromised as compared to the sensitivity of stand-alone devices. Also, interference might cause image artifacts or image distortions. We calculated the signal-to-noise ratio (SNR) of the FMT by dividing the signal of a ROI in fluorescent raw image by the standard deviation of noise value extracted from a ROI in a

background image, which was recorded in the absence of fluorescence excitation, and where only ambient light and detector noise contribute to the signal. The SNR was evaluated using the previously described phantom prior ($SNR_{opt} = 3.58 \pm 0.52$) and during the MR image acquisition ($SNR_{opt} = 3.67 \pm 0.39$) and we did not observe any degradation in SNR_{opt} within error limits due to insertion of the optical setup into the MRI system.
Similarly, the SNR of the MR measurements was evaluated with and without simultaneous optical measurement ($SNR_{MRI} = 64.41 \pm 2.51$ versus $SNR_{MRI} = 63.20 \pm 2.35$), which did not reveal an effect on the MRI sensitivity. For MRI SNR calculations the mean signal intensity in a sample ROI located at a fixed location within the FOV was divided by the standard deviation of the intensity in a ROI comprising only contributions from noise. Moreover, we did not observed any artifacts introduced by the optical detector in the MR images since the SPAD was positioned at at a distance of 40mm from the RF coil and outside the FOV of the MRI data acquisition. Correspondingly, potential artifacts caused by the SPAD were not visible in the MR images. All MR sequences can be run by the setup, the only limitation is the inhomogeneous excitation by the surface coil. We therefore conclude that crosstalk between modalities in FMT/MRI system is negligible.

Spatial Resolution

A critical parameter in imaging is spatial resolution. In MRI voxel dimensions are typically of the order of 150 to 500μm depending on the acquisition parameters, whereas resolution in FMT is inferior, typically 1-2mm isotropic. The FMT spatial resolution in our hybrid system was evaluated using phantom (A) comprising two identical fluorescent tubes with variable spacing (2-5mm). Simulations revealed that sources separated by more than 0.8mm could be clearly discriminated (Figs. 7.3a-c) by analyzing the line profile in x direction. To analyze the line profile the reconstructed volume was projected to the xz-plane. The line profile is drawn through the peak value of the embedded tubes. To determine the spatial separation a gauss fit was applied to each peak in the line profiles and the distance between the peak value of the two fitted Gaussian profiles was taken as the separation distance. If two clearly distinguishable peaks could be identified in the line profile the two signals were considered as spatially separable.
Experiments were limited by the diameter and the wall thickness of the capillaries used. The experimental dispersion of the fluorescence intensity was slightly larger than predicted by the simulations (Figs. 7.3d-e) and some artifacts were observed, which are a result of imperfect reconstruction due to deficiencies like the forward model (assuming a fluorescence point source embedded in an optically homogeneous medium), data collection (detector noise) and SNR which contributes to the uncertainty of the data lead therefore to these artifacts. Comparing the full widths at half maximum of the FMT/MRI setup for simulated and experimental data, we estimate the FMT in-plane spatial resolution of the FMT/MRI setup to be 0.9mm. A linear correlation has been

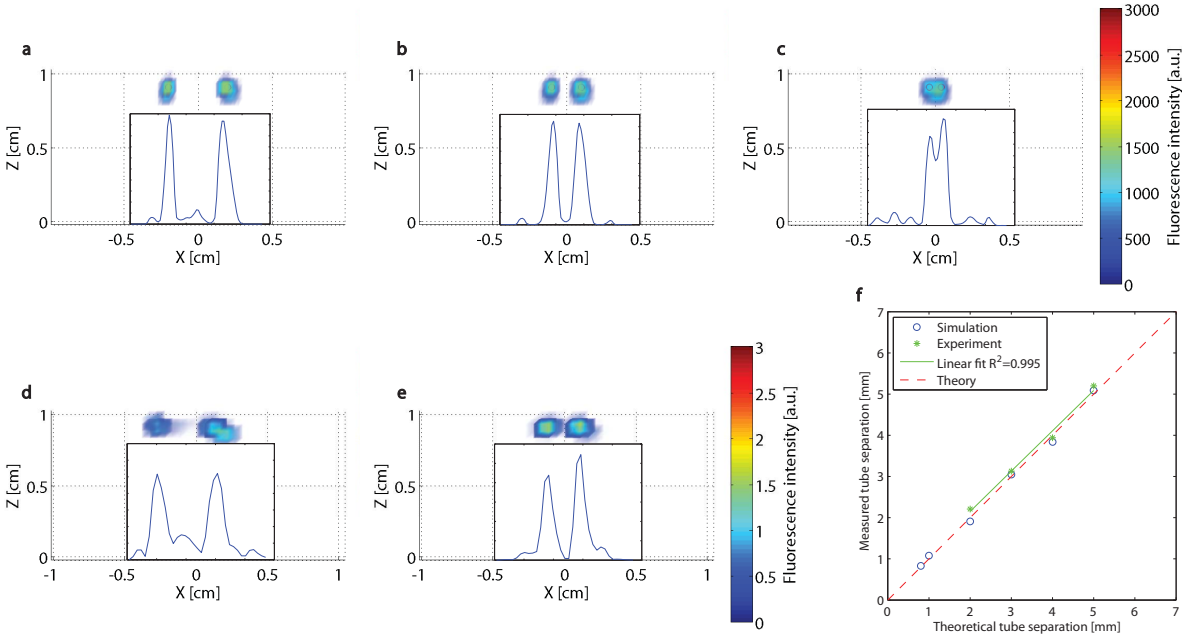

Figure 7.3: Spatial resolution in a phantom. **a-c** Reconstructed fluorescence intensity (arbitrary units) from simulated data in xz-projection for 4mm **a**, 2mm **b** and 0.8mm **c** center-to-center tube separation. The tubes are indicated as red circles. The insets show the line profiles at z=9mm. **d**, **e** Reconstructed fluorescence intensity (arbitrary units) from experimental data in xz-projection for 4mm **d** and 2mm **e** center-to-center distance. The inset show the line profiles at z=9mm. **f** Plot of the extracted tube separations for simulated data (blue circles) and experimental data (green stars) versus the theoretical separations (red dashed line).

found between reconstructed experimental data and true tube separation (R^2=0.995, slope=0.978; Fig. 7.3f) indicative of the accuracy of the in-plane spatial localization.

Depth Resolution

Quantitative analysis of dye concentrations depends on accurate reconstruction of the depth of the fluorescent source, which was analyzed for a depth range of 1 to 3mm using both simulations and experimental data. To analyze accuracy of depth information a line profile was drawn in z direction across the maximum intensity of the volume projected onto the xz-plane. The distance between the phantom surface and the peak value of a fitted Gaussian line was taken as a measure of depth. For this experiment phantom (B) was used comprising one fluorescent tube in the investigated depth. The dispersion of fluorescence intensity increases slightly with increasing depth (Figs. 7.4a-d), as photon scattering scales with their path length through tissue. The observed artifact in Fig. 7.4c is a result of imperfect reconstruction due to different

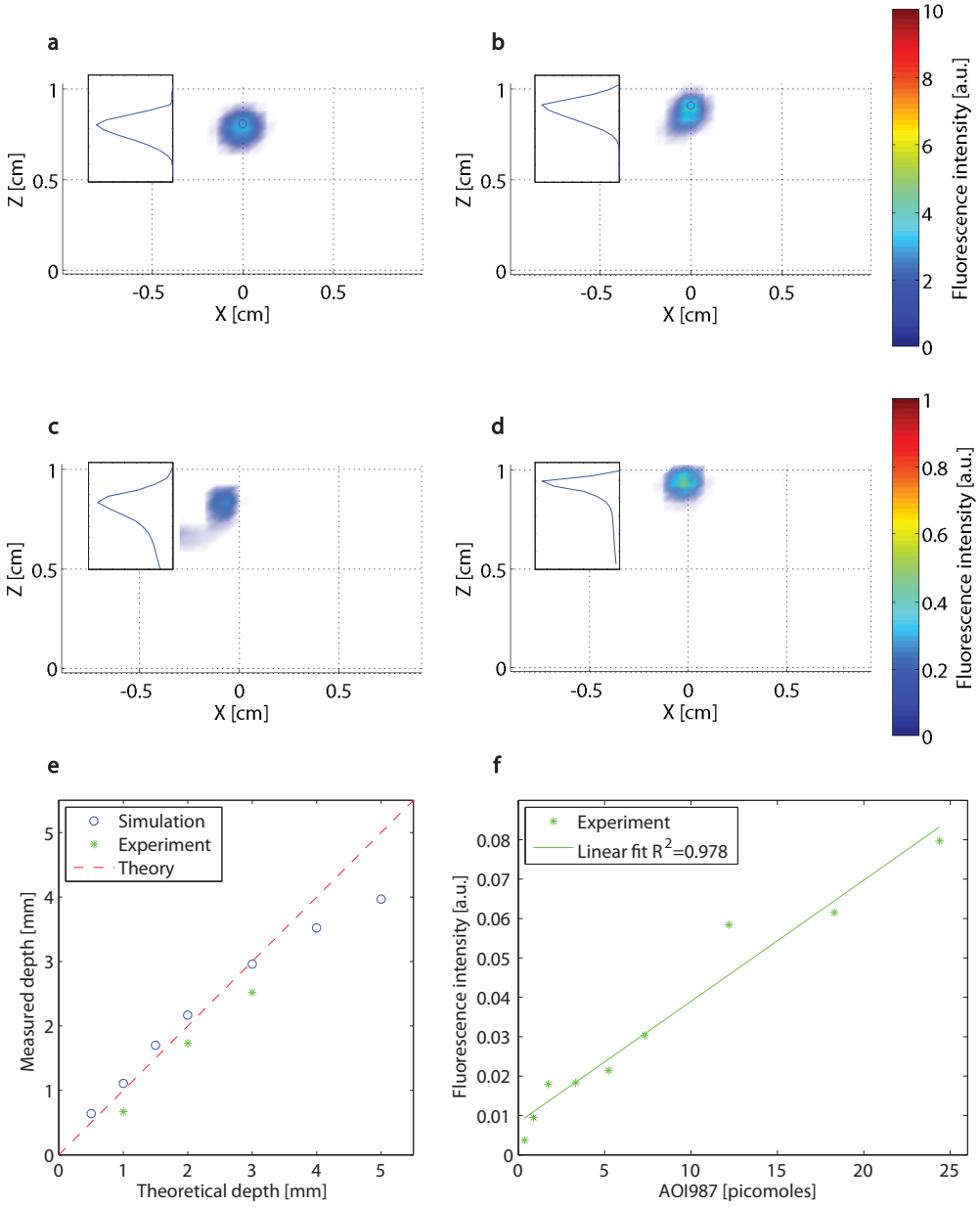

Figure 7.4: Depth resolution in a phantom. **a**, **b** Reconstructed fluorescence intensity (arbitrary units) from simulated data in xz-projection for 2mm **a** and 1mm **b** below the surface. The insets show the depth line profiles. The tubes are indicated as red circles. **c**, **d** Corresponding reconstructed fluorescence intensity (arbitrary units) from experimental data in xz-projection for 2mm **c** and 1mm **d** depth. The inset show the depth line profiles. **e** Plot of the extracted tube depth for simulated data (blue circles) and experimental data (green stars) versus theoretical depth (red dashed line). **f** Reconstructed mean fluorescence intensity versus AOI987 concentration in the tube of the phantom.

deficiencies like the forward model, data collection and SNR which contributes to the uncertainty of the data as already discussed. Comparing reconstructed with true depths demonstrated a good correlation up to depth values of about 3mm (Fig. 7.4e). If depth of the fluorescent source exceeds 3mm, the actual depth is underestimated in the reconstructed image data sets. This can be attributed to reflection geometry setup, which emphasizes contributions from superficial structures.
Simulated data reveal that the limited FOV in the current setup has only minor influences on the accuracy of depth localization: By keeping the imaging parameters constant and doubling the FOV the accuracy of the depth localization of the FMT setup only slightly increases by 2%.

Quantification Analysis

A principal motivation for using tomographic imaging is the ability to derive quantitative information on the local dye concentrations. Two aspects are of interest: a) the minimal dye concentration that can be detected (detection limit), and b) the linearity of the relationship fluorescence intensity versus dye concentration.
Experiments were carried out using a tissue phantom with a fluorescent source embedded at a depth of 1mm. The correlation between AOI987 concentration and fluorescence intensity reconstructed revealed a linear relationship (R^2=0.978; Fig. 7.4f) for a range from 0.36 to 25picomoles, with a detection limit of approximately 0.3picomoles of AOI987 dissolved in a volume of 1.5μl.

Hybrid Imaging

The feasibility of hybrid FMT/MRI was investigated using a tissue phantom (Figs. 7.5a-d) and *in vivo* using tumor bearing mice (Figs. 7.5e-j). Due to the fixed geometry of the two detector systems a phantom measurement using fluorescent tubes visible in both modalities enabled the definition of the affine transformation to register the FMT data using the MRI images as reference coordinate system. Voxel dimensions and the slice positions for the FMT data were adjusted accordingly. The same affine transformation could then be applied to *in vivo* data sets as the FMT/MRI geometrical arrangement was left unchanged.
For these experiments the acquisition time for both modalities for phantom and *in vivo* measurements were on the same time scale allowing to measure time dependent processes simultaneously. A sketch of the silicone slab used for phantom experiments is shown in Fig. 7.5a where one of four holes is filled with the fluorescent dye and the slice position is indicated. It was shown that the overlay image of MRI (Fig. 7.5b) and FMT (Fig. 7.5c) sections revealed an accurate localization of the reconstructed fluorescent tube from the FMT data (Fig. 7.5d). For *in vivo* proof-of-principle of simultaneous FMT/MRI measurements a murine tumor model was used. C51 cells (colon cancer-derived cell-line) were subcutaneously implanted in the flank of a nude BALB/C mouse. The majority of tumors are known to express high levels of pro-

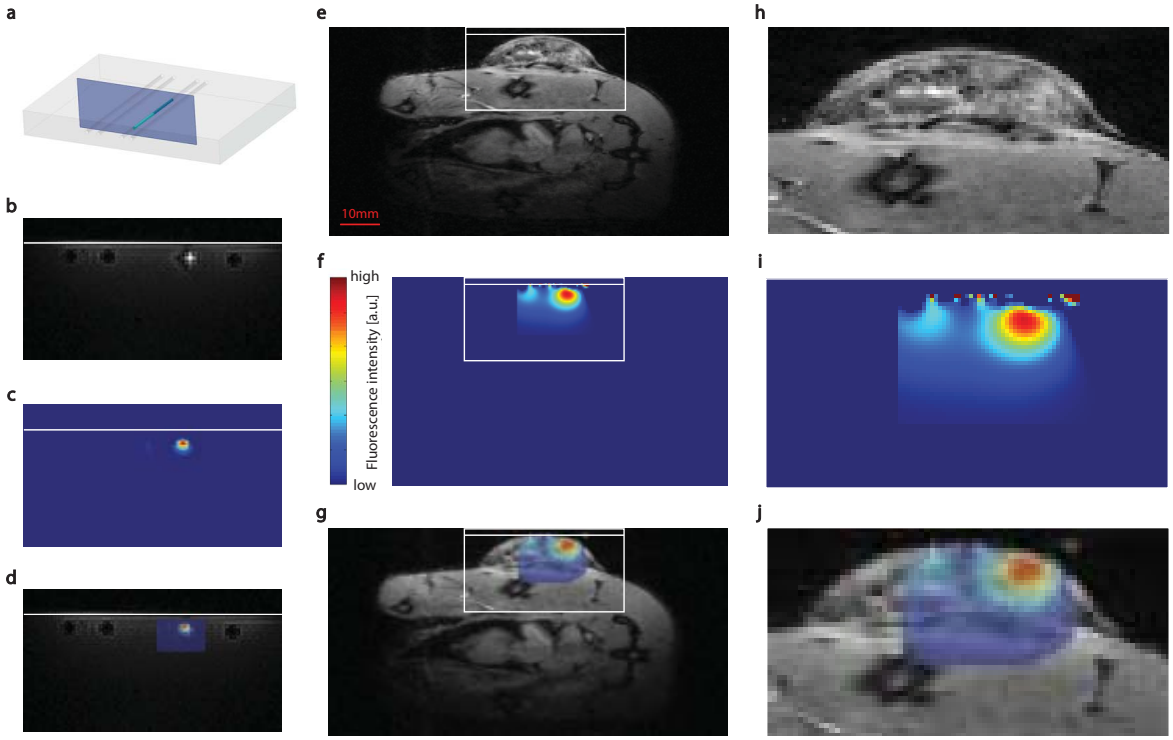

Figure 7.5: Simultaneous MRI and optical data acquisition. Phantom: **a** Schematic drawing of the phantom (A) (gray) with one whole filled with a fluorescent dye (green). The slice displayed in the FMT image is indicated in light blue). **b** MRI slice of the phantom. **c** Reconstructed slice (fluorescence intensity distribution) from the optical data set. **d** Overlay of MR image and reconstructed fluorescence intensity distribution. The white horizontal line indicates the top surface of the phantom. *In vivo*: **e** MRI slice of a tumor bearing mouse. **f** Corresponding reconstructed fluorescence intensity from the simultaneous measured optical signal. **g** Overlay of the two slices from the two different modalities. The white horizontal line indicates the topmost tangent plane to the tumor surface. **h-j** Detailed view of the tumor region.

teases (protein degrading enzymes), which are involved e.g. in the degradation of the extracellular matrix to enable tissue invasion and metastasis formation [129]. An activatable probe (ProSense 680) that generates fluorescent signals only upon cleavage by proteases [28, 18] was used to assess the level of protease activity by FMT. A representative MR image (Fig. 7.5e) and the corresponding FMT section displaying fluorescence intensity reflective of protease activity (Fig. 7.5f) have been registered (Fig. 7.5g). They show regions of high protease activity within the tumor tissue. The edge of the slab used for the FMT reconstruction corresponded to the tumor tangential plane in the MR image oriented parallel to the focal plane of the detector (indicated by the white horizontal line in Figs. 7.5e-g). An enlarged region of the registered FMT and MR image gives an insight into the fluorescence dye distribution (protease

activity) within the structural image provided by MR (Figs. 7.5h-j). Interestingly, protease activity measured in FMT was not homogeneous across the tumor. Histological analysis confirmed heterogeneity of protease activity throughout the tumor.

7.1.4 Discussion

Proper interpretation of molecular and/or cellular information derived from molecular imaging studies requires the registration to an anatomical reference that is commonly recorded using different imaging modalities. A straightforward solution is a sequential imaging strategy, which requires a sample support that is compatible with both modalities and that comprises fiducial markers as landmarks for the registration process. An advantage of this setup is that it provides optimal performance of each stand-alone system without compromising image quality. Disadvantages are that sequential measurements take inherently longer which puts demands regarding the maintenance of physiologically stable conditions throughout the measurement period. In addition, when studying fast concurrent processes with different modalities, sequential sampling is not feasible. Moreover, soft-tissue may move during the translocation between imaging modalities, which demands for non-rigid body registration procedures that are intrinsically difficult. Thus true hybrid systems are highly attractive for biomedical research applications, as they provide simultaneous multiplexed information in an inherently registered manner due to concurrent measurement with both modalities in a rigid configuration. Combinations with MRI, which provides a high soft-tissue contrast and has become a standard method both in preclinical and clinical structural and functional imaging, are challenging due to the hostile environment of a high magnetic field.

Hybrid optical imaging-MRI systems are typically fiber-based and used in combination with large bore clinical MRI with gradient systems of 50 to 60cm inner diameter to account for the space requirements by the source and detector fiber bundles. The use of a clinical scanner for studies in small rodents is suboptimal: lower field strength and weaker magnetic field gradients would compromise the spatial resolution achievable. This might be sufficient if MRI data are only used as reference indicating major anatomical structures; yet studies with MRI providing complementary information as independent imaging modality will suffer. Moreover, the rigid fiber geometry limits the flexibility of the optical imaging setup: the number of source/detector pairs is limited, definitely much smaller than for typical array detectors (with typically >1k pixels) and the excitation schemes/points are predefined by the position of excitation fibers. Fiber-based systems are typically operated with the light guiding fibers in direct contact with the sample. This renders the experimental procedure cumbersome requiring manual adjustments of individual fibers. The non-contact system presented in this work allows overcoming these limitations. Excitation can be varied by adjusting the parameters of the scanning device, while the fixed distance between the SPAD array detector and the MRI surface coil, which is directly placed over the animal's body surface, ensures maintenance of optical focus (apart from the surface curvature)

irrespective of the body region sampled. The focal plane was set according to a tangential plane on the animal surface perpendicular to the objective lens.
In a hybrid system combining two complementary imaging modalities, system performance of each modality should be not or only minimally degraded with regard to their stand-alone performance, though some performance loss as compared to optimized stand-alone systems, which might use different detector technologies, might be acceptable in view of the benefits of the multimodality readouts. In a combined FMT/MRI system, the MRI setup defines the design of the integrated FMT system: the detector must be functional at high magnetic fields and has to fit into the small bore of the gradient system (120mm inner diameter in our case). The use of an MRI-compatible SPAD array comprising 32×32 detectors led to some loss in performance as compared to stand-alone FMTs using cooled CCD cameras with regard to sensitivity, FOV and the number of source/detector pairs available. Nevertheless, the setup is still superior to fiber-based rigid geometry systems with regard to experimental flexibility and amount of independent data generated for reconstruction. Moreover, its performance is expected to improve with new generation SPAD arrays.
The spatial resolution provided by the FMT/MRI setup was found to be comparable to that of microPET systems [130, 131]: the in-plane spatial resolution derived from phantom experiments was at least 2mm, whereas simulations indicated that it should be possible to resolve two fluorescent sources of equal strength separated by 0.8mm. The linear dependence of measured and theoretical source separation for a range of 0.8 to 5mm center-to-center distance reflects the accuracy of the reconstruction algorithm. On the other hand, the estimation of the source depth from the sample surface was found to be systematically smaller than the theoretical depth both for simulated and experimentally found data for depth values exceeding 3mm. Two factors contribute to this: Due to diffusive light propagation the intensity is reduced to a level that makes detection difficult (in particular in view of autofluorescence contributions from surface structures) and secondly, the small FOV prevents accurate sampling of the intensity distribution of the surface which is critical for proper reconstruction of the source location and distribution. Though simulations have revealed that by increasing the FOV to 16×16mm, the accuracy of depth reconstruction can only be marginally improved.
The claim of molecular imaging is to provide non-invasive quantitative information on molecular processes in the intact organism. These events commonly occur at a low frequency; hence any molecular imaging modality should provide inherent high sensitivity. Calibration experiments revealed that the FMT/MRI system was capable of detecting sub-picomole amounts of dye. Moreover, fluorescence intensity depended linearly on the amount of fluorescent dye in the sample volume, an important prerequisite for quantitative studies. The amount of dye used covered the ranges typically reported for *in vivo* applications.
The true strength of a hybrid system is that high resolution structural images can be annotated with molecular information derived from an inherently registered data set. The *in vivo* study, which allowed identifying regions within a subcutaneous tumor that are high in protease activity, clearly illustrates the potential of the approach.

While the MRI signature clearly indicates tumor heterogeneity based on differences in MRI contrast (dominated by differences in T_1 relaxation times), the FMT information adds a molecular component to it: high protease activity is commonly associated with invasive (malignant) tumor behavior [65]. The heterogeneity of fluorescence activity confirmed by histological analysis reflects the sensitivity of our hybrid imaging system. Even more attractive FMT/MRI applications would be the correlations between physiological/functional MRI readouts (e.g. vascular permeability as a target for tumor angiogenesis [132]) with FMT derived molecular information which demand for simultaneous measurement. The prerequisite for such applications is that the time resolution of the slower of the two modalities is still sufficient to capture the biological process. Sequential measurements involving transfer of the sample from modality A to B might not be possible, as this would be too time consuming (including adjustments of individual modalities) so the sample state would be different.
Aside from collecting multiplexed data, hybrid systems can offer improved data reconstruction for the low-resolution modality, in our case for FMT. This has been used in PET/CT systems, where the CT map is used to compute the tissue attenuation correction required for reconstructing PET data [133]. Correspondingly, in an FMT/MRI system, the anatomical information provided by MR can be fed into both the forward and the backward model of the FMT reconstruction [134], which should render the FMT reconstruction more accurate. However, the use of imaging priors bears the risk of over-constraining the FMT reconstruction.

7.2 2nd Generation FMT/MRI Setup

This section is adapted from:

F. Stuker, K. Dikaiou, J. Ripoll and M. Rudin. Miniaturized Non-Contact Fluorescence Molecular Tomography System for Hybrid Optical and Magnetic Resonance Imaging. In preparation and intended for submission to *Review of Scientific Instruments*.

7.2.1 Aims and Objectives

In the previous section we have reported the design of a prototype FMT/MRI system and demonstrated feasibility of simultaneous *in vivo* fluorescence and MRI imaging of a subcutaneous colon cancer xenograft model in mice. Nevertheless the technical solution revealed several shortcomings: i) limited FOV and array resolution which impacted the three dimensional spatial and depth resolution ii) use of rigid split guiding tubes turned out impractical iii) setup restricted to reflection mode.
All these experiences from the first generation FMT/MRI setup were integrated in a second further developed FMT/MRI setup which bear the following improvements: First of all, the laborious handling of the first generation FMT/MRI setup was elim-

inated by a redesigned more stable sample platform guidance based on a rigid rail system. Furthermore, we could compensate for the restrictions of the small array size resulting in a small number of source/detector pairs by using a newly designed detector technology: complementary metal-oxide-semiconductor (CMOS) detector with 256×256 pixels (CSEM, Zurich, Switzerland). This large detector array offers an improved image resolution. The optimized objective lens results in an enlarged FOV allowing a larger area for the point source scanning. A newly designed side-scanning strategy compared to the previously described top-scanning strategy leads to further improvements in the FOV enlargement due to the achieved larger sample-detector distances. Furthermore, the new concept allows both reflection and transmission geometry measurements, the latter should improve the restricted depth resolution caused by the reflection geometry as seen in the old setup.

7.2.2 Material and Methods

Instrumentation

The experimental setup consisted of an illumination module located outside and a sample platform inside the magnet (Fig. 7.6).
The illumination module consists of a fiber coupled 670nm continuous wave laser (B&W Tek, Newark, USA) for excitation. The multimode fiber (core diameter 100μm, NA=0.22) was connected to a numerical aperture matched collimation lens (Thorlabs, Munich, Germany). Before the beam reaches a pinhole behind the lens a beam splitter was attached to measure the laser power with a power meter (Gentec-Eo, Lake Oswego, USA). The pinhole (diameter 0.5mm) was mapped with an anti-reflectance coated spherical singlet lens (f=1000mm, Melles Griot, Bensheim, Germany) by a 2f image on the subject. To achieve a focal length of 2000mm (required due to the dimensions of the MR magnet) the laser beam was folded several times before reaching the focal lens. The light traveled five times between two coated highly reflective front surface mirrors (Thorlabs, Munich, Germany) placed 400mm apart. The light was then guided to a scan head (Scanlab, Puchheim, Germany), where it was deflected by 2 galvanometric driven mirrors to allow scanning of sources on the sample surface. These mirrors deflected the beam by 90° from the input direction. The beam was then directed parallel to the bore to the side of the sample platform. All components were fixed on a xyz-adjustable home-built aluminum breadboard placed outside the bore of the magnet in a magnetic stray field <10mT to ensure the proper function of the illumination platform components.
The sample platform was mounted with four v-shaped wheels on a rail comprising two hollow carbon rods (Fig. 7.7a) of a outer diameter of 20mm and a length of 2000mm. This rail system allows a smooth movement of the platform to the position of the isocenter inside the magnet bore. The two rods building the rail system were separated by 70mm (center-to-center distance) and mounted without any contact at the bottom of the gradient bore (diameter 120mm). The rail system was rigidly fixed

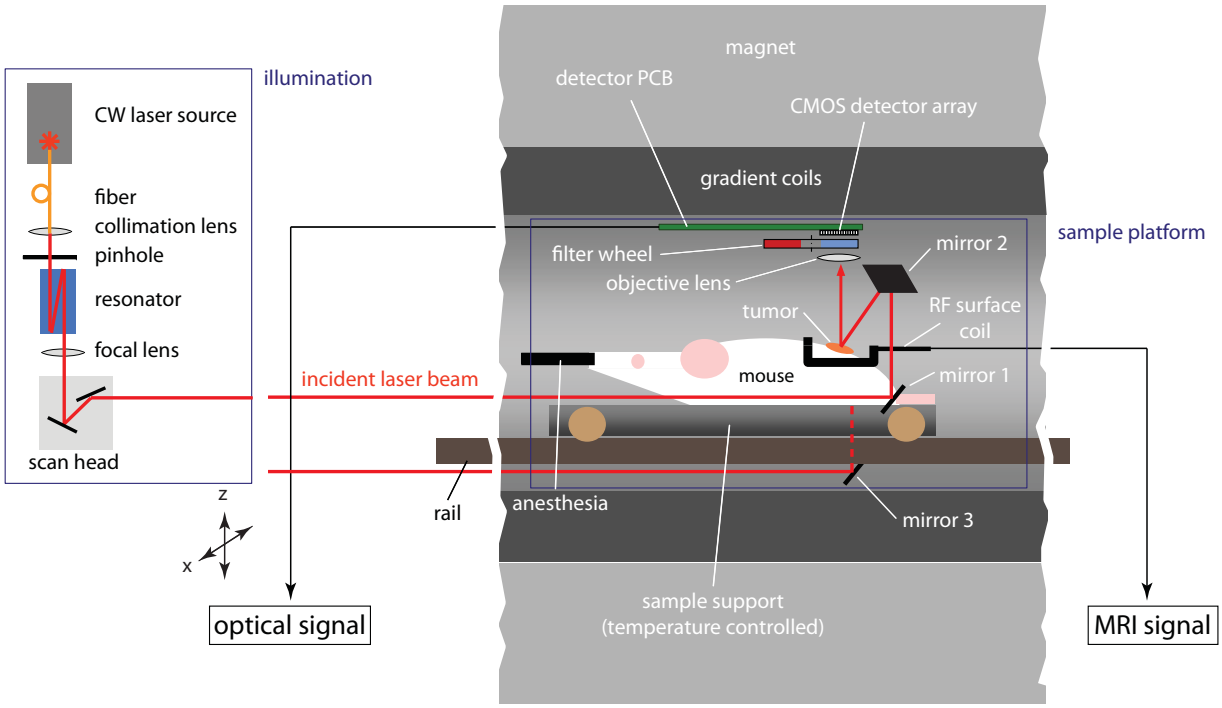

Figure 7.6: Experimental setup. Schematic of the FMT/MRI instrumentation. The illumination module comprises the laser source, a resonator and the scan head for deflecting the beam across the object. The sample platform comprises the detector, the focusing lens and the filter wheel used for selecting the wavelength for detection. A slightly bended RF coil is used in transceiver mode. The laser beam is deflected to the sample surface using two mirrors (reflection mode) or one mirror (transmission mode).

by two support frames mounted at both ends of the magnet. At the right side of the back plate of the sample platform a mirror was mounted (mirror 1) deflecting the incoming beam by 90° to a second mirror (mirror 2) mounted directly above the first one deflecting the beam by approximately 70° onto the sample surface. The beam deflected by the two coated front surface mirrors (Edmund Optics, Karlsruhe, Germany) is passing through the rectangular window of the MRI transceiver surface coil. This reflection geometry setup allowed the use of source intensity profiles for image reconstruction [107]. By moving the illumination platform in x and z direction the setup can also operate in transmission mode. For that, a coated front surface mirror (mirror 3) was mounted below the sample platform allowing an incoming beam deflection by 90° to illuminate the sample from below. The diffusive light patterns on the surface of the animal were recorded for each illumination point. Light emanating from the surface were selected according to their wavelength using filters placed in the filter wheel. High quality bandpass filters (Semrock, Rochester, USA) with peak wavelengths of 660nm and 720nm for measurements at the excitation and fluorescence

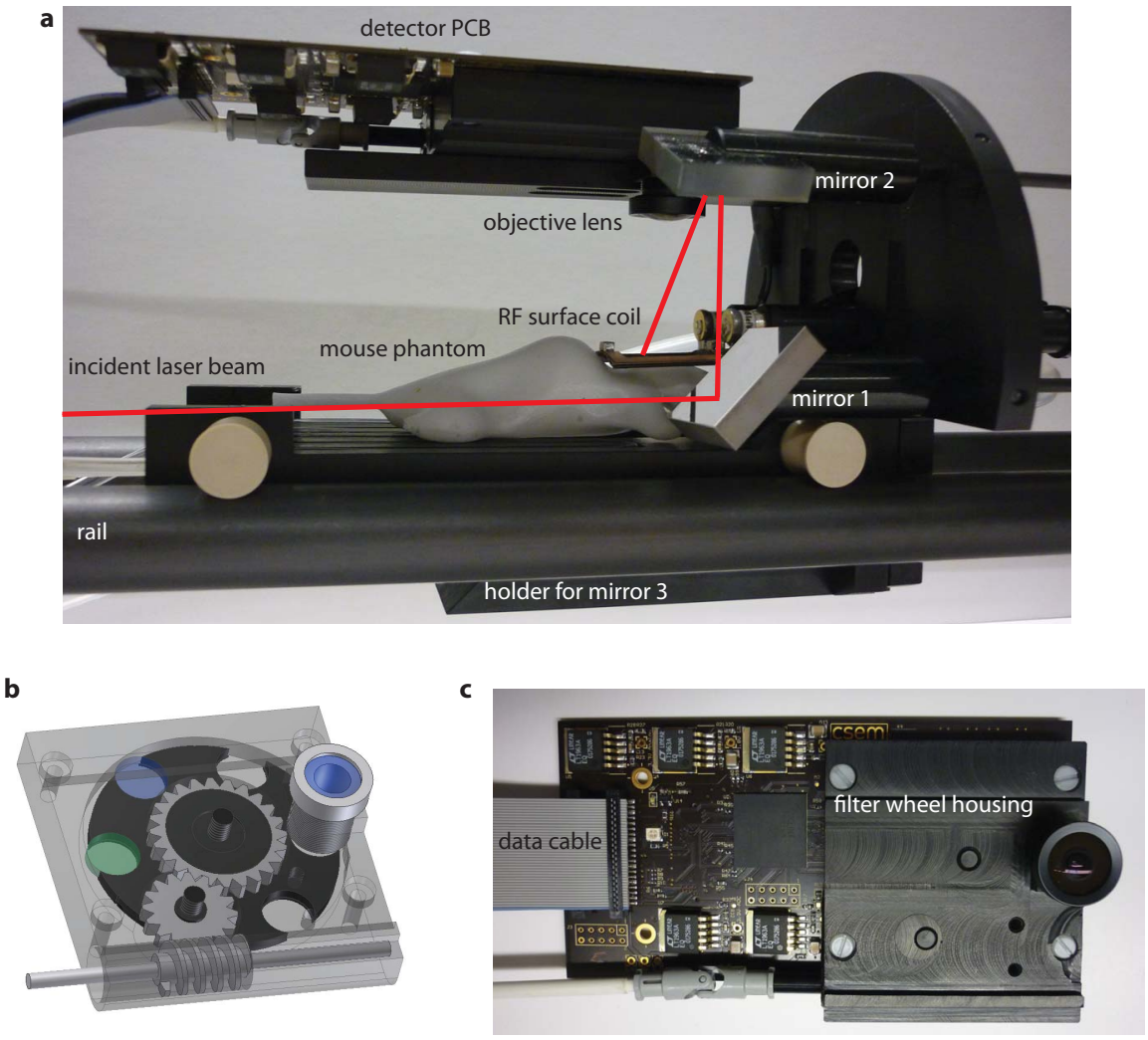

Figure 7.7: Sample platform. **a** Side view of the sample platform with the PCB, deflection mirrors (incoming light beam indicated in red), filter wheel housing and surface coil for the MRI acquirements. **b** Sketch of the filter wheel and the switching mechanism. **c** Bottom view of the PCB with mounted filter wheel housing.

wavelength have been used. Filters were characterized by >90% transmission over a range of ±13nm. An anti-reflection coated fixed focus glass lens (V-4301, FL=2.1mm BFL=5.6mm, Marshall Electronics, El Segundo, USA) was mounted by an M12 thread to a custom made light tight housing comprising the filter wheel and the filter switching mechanism (Fig. 7.7b). To account for the filter thickness which leads to a different focal length of the objective lens an antireflection coated glass slide was used in one filter wheel slot for precise focussing in the reference white light image. The whole assembly was screwed to the printed circuit board (PCB) in front of the detector array (Fig. 7.7c), yielding a FOV of $55\times55\text{mm}^2$ at a focal distance of 40mm. A custom made

256×256 CMOS array detector bonded on the PCB was used as photon detector. A small rectangular electroluminescent foil at the back flange was used for white light illumination during the acquisition of reference surface images. All parts used for the setup were made from materials compatible with operation in high magnetic fields.

MRI Details

All MR experiments were carried out on a Bruker BioSpec 94/30 (Bruker BioSpin MRI, Ettlingen, Germany) horizontal small animal MR system operating at 400MHz equipped with a gradient system capable of generating a maximum strength of 400mT/m with a minimum rise time of 80μs. A home-built rectangular surface coil (20×24mm) was used for RF signal transmission and reception. The coil made of a flexible PCB substrate with standard copper layer was designed for mouse imaging and therefore curved to a cylindrical radius. A slightly enlarged window of 16×20mm compared to the first generation setup was cut out of this single loop coil to allow for optical measurement (illumination and detection) in reflectance mode from the top[2]. First

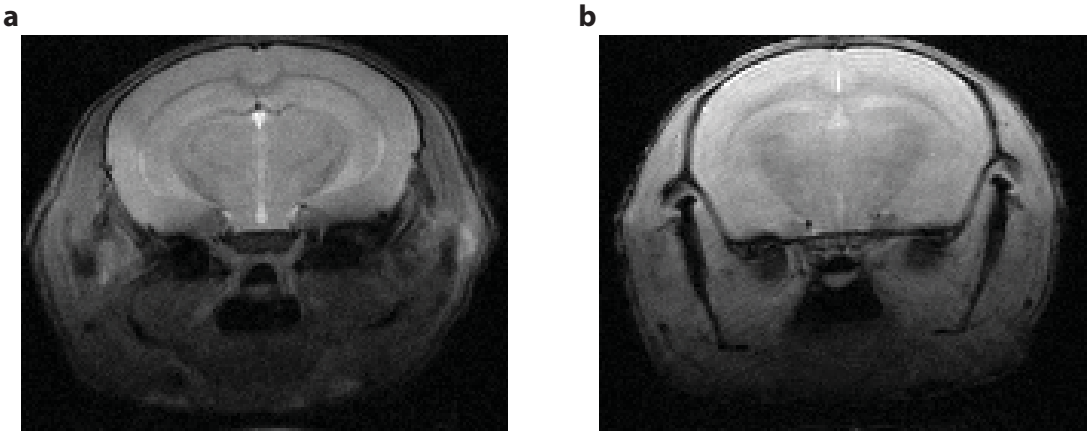

Figure 7.8: Different MR sequences. **a** Slice representation of a brain image recorded with the newly developed transceive surface coil with a spin echo sequence. **b** Slice representation of a brain image recorded with a gradient echo sequence.

in vivo experiments to test the coil performance were carried out on the head of a nude mouse with multislice spin echo and gradient echo sequences. The spin echo sequence has the following parameters: 14 slices of 790μm thickness; FOV=16×13mm^2; MTX=160×130; pixel dimension PIX=100×100μm^2; TE/TR=10.7/3000ms; NA=2, yielding a total acquisition time of 3min12s. The gradient echo sequence has the following parameters: 10 slices of 1000μm thickness; FOV=16×13mm^2; MTX=160×130; pixel dimension PIX=100×100μm^2; TE/TR=2.6/500ms; NA=4, yielding a total acquisition time of 4min20s. For the simultaneous acquired FMT/MRI experiments *in*

[2]A detailed description of the coil design can be found in Appendix B

vivo in an Alzheimer's disease mouse model the following MRI parameters where used for a gradient echo sequence: 29 slices (no slice gap) of 700μm thickness; FOV=20×22mm^2; MTX=200×200; pixel dimension PIX=100×110μm^2; TE/TR=5/383ms; NA=8, yielding a total acquisition time of 10min12s.

CMOS Detector Details

A so-called CMOS detector is an image sensor consisting of an integrated circuit which is produced by CMOS technology and contains an array of pixel sensors. The basic operation principle is the same as in a CCD camera where an image is projected through an objective lens onto the pixel array which causes an electrical charge in each pixel proportional to the light intensity at that location. The charge is then converted into a voltage which is measured electronically and is therefore producing the gray value of a certain pixel. Compared to CCD, CMOS detectors have a lower power consumption and lower fabrication costs and are therefore widely used as camera sensors in mobile phones.
Nevertheless we use a high end scientific CMOS detector which was fabricated with a 0.18μm technology and provides 256×256 pixels with a size of 11×11μm^2 and a fill factor of 63% [135]. The applied low-noise readout architecture [136] allowing even the detection of single photons. By having the possibility to transform the charges into a measurable current a logarithmic sensitivity and therefore a high dynamic range of 140dB was achieved.

	SPAD	CMOS	Unit
Array size	32×32	256×256	
Pixel size	30×30	11×11	μm^2
Detector size	0.96×0.96	5×5	mm^2
Field of view	8×8	55×55	mm^2
Fill factor	3.15	63	%
Dynamic range	90	140	dB
Frame rate @ 15bit	12	60	Hz
Technology	0.35	0.18	μm

Table 7.1: Parameter comparison of the 32×32 SPAD and the 256×256 CMOS array detector.

Phantom Preparation

For the phantom experiments three tissue-mimicking silicone-based phantoms were prepared (see section 6.2.4) with a thickness of 13mm: Phantom (A) was used to characterize spatial resolution and concentration accuracy of the optical system. It comprised holes for dye administration separated with center-to-center distances of 2, 3 and 4mm in a plane parallel to the surface at a depth of 1mm. Phantom (B) was

similar to Phantom (A) but having the holes for the dye administration in a depth of 2mm. Finally, phantom (C) was used for depth analysis and comprised holes parallel to the surface at depths of 1, 2, 3, 4 and 5mm with respect to the surface with an in-plane separation of 5mm.

Animal Model

For this study 18month old transgenic APP23 mice were used and housed in a controlled environment (23°C, 12h/12h light/dark cycle) with unlimited access to water and food (Kliba Nafag, Kaiseraugst, Switzerland). All experiments were performed in accordance to the Swiss Veterinary law. Prior to the FMT/MRI experiments, mice were shaved on their head under isofluorane anaesthesia. After that the animals were transferred to the heated platform and placed in a prone position with an initial dose of 3% isoflurane in an air/oxygen mixture (2:1). The body temperature was controlled and stabilized and the isoflurane level was reduced to 1.75%.
The head was fixed in a face mask for anaesthesia under the RF surface coil in the window allowing for optical imaging. For intravenous infusion, the tail vein was cannulated with a 30G needle (0.3mm×13mm, BD Microlance, Drogheda, Ireland). After baseline measurements prior dye administration, AOI987 (0.1mg/kg, 0.01mg/ml) was intravenously injected as a bolus.

Fluorescent Agent

As a fluorescent probe an oxazine derivative dye AOI987 was used which has been shown in a previously published study by Hintersteiner et al. [122] to bind to Aβ deposits in the brain of APP23 mice. The emission and excitation spectra peak at 650nm and 670nm respectively. AOI987 was synthesized by our collaborators (Laboratory of Prof. K.-H. Altmann, Institute of Pharmaceutical Sciences, ETH Zurich, Switzerland) according to previously established protocols [122]. A stock solution of 0.1mg/ml AOI987 in distilled water was prepared and a portion of AOI987 was diluted in saline to receive 0.01mg/ml solution.
For phantom experiments the near-infrared fluorescent cyanine dye Cy5.5 was used. This dye has a similar absorption and emission spectra as AOI987, therefore no changes in the equipment was necessary.

Fluorescence Data Acquisition

The silicone-based phantoms were used for characterizing the performance of the FMT/MRI system. For each measurement, one or two fluorescent sources consisting of an aqueous solution of Cy5.5 at various concentrations were included at defined depths and with variable spacing. Initially the sample was placed on the imaging platform within the FOV of the optical system and under the RF surface coil of the MRI system. For excitation, the laser beam was scanned across a grid with 12×8 illumination spots with dimensions and the exact location of the grid adjusted operator-interactively in

order to match the ROI on the sample surface. We have chosen an integration time of 0.1 to 0.9s per source position depending on the fluorescent signal strength and the laser power. Between each acquisition at the different spot position a 500ms wait time was included for proper timing of the image acquisition. This results in a total acquisition time between 1 and 2.5min. For each source position an image was recorded resulting in a $N_x \times N_y \times N_s$ array of images, where N_x and N_y are the number of pixels in x and y and N_s the number of sources. For calibration purposes the sources were measured on a millimeter paper placed in the focal plane of the camera in order to get the center position of the sources and the pixel dimensions in centimeters. After that the optical acquisition was started and images were recorded at two wavelengths corresponding to the excitation (660nm) and emission (720nm) of AOI987 and Cy5.5. For *in vivo* measurements the illumination scheme and filter settings were kept the same.

Fluorescence Data Reconstruction

For image reconstruction the normalized Born approximation was used, which has been shown to yield robust data by considering the ratio of the measured emission and excitation images [108]. The values of this ratio were used in the forward model [112] accounting for the fluorescence signal on the sample surface. The reconstruction was performed by inverting this forward model using an ART method. This algorithm is an iterative method used in computed tomography [110] and adapted for imaging diffusive media with boundary restrictions [105]. An initial assumption for the fluorophore distribution is iteratively improved using a least square minimization procedure to minimize the difference between reconstructed and measured data. The reconstruction yielded a three dimensional map of the fluorescent source distribution within the subject.

7.2.3 Results

The accuracy of the in-plane and depth reconstruction was analyzed with tissue mimicking silicone phantoms outside the MR system. Moreover the linearity between the fluorescence intensity and the local dye concentration was investigated. Finally first experiments in an *in vivo* animal study were carried out, where simultaneous hybrid measurements with the combined system were performed.

Crosstalk

A major concern in hybrid imaging systems is the potential crosstalk between the modalities as the sensitivity might be compromised as compared to the sensitivity of stand-alone-devices. Furthermore, possible interferences might cause image artifacts or even image distortions. To analyze that, signal-to-noise ratios (SNR) on both modalities were calculated: For the optical system the SNR was calculated from the

raw data where all raw images of a fluorescence measurement were added up to one single image. The mean of a signal in a ROI incorporating a fluorescence source was divided by the standard deviation of a ROI at the edge of the image where no fluorescence signal was present. The SNR was evaluated using the previously described phantom prior ($SNR_{opt} = 263.18$) and during the MR image acquisition ($SNR_{opt} = 261.49$) and we did not observe any degradation in SNR_{opt} due to insertion of the optical setup into the MRI system. Similarly, the SNR of the MR measurements was evaluated with and without simultaneous optical measurement ($SNR_{MRI} = 34.37$ versus $SNR_{MRI} = 33.47$), which did not effect the MRI sensitivity. For MRI SNR calculations the mean signal intensity in a sample ROI located at a fixed location within the FOV was divided by the standard deviation of the intensity in a ROI comprising only contributions from noise. Even though we could not observe any degradation in the MR signal during simultaneously acquired optical measurements, a significant MR signal enhancement was noticed by unplugging the power and USB connection. Moreover, we did not observed any artifacts introduced by the optical detector in the MR images since the CMOS detector was positioned at at a distance of 40mm from the RF coil and outside the FOV of the MRI data acquisition. Nevertheless, a vertical line in the MR image (see Fig. 7.11a) was present which corresponds to a certain frequency which was present due to signal transfer from the PCB to the mother board. All MR sequences can be run by the setup, the only limitation is the inhomogeneous excitation by the surface coil. We therefore conclude that crosstalk between modalities in FMT/MRI system is negligible.

Spatial Resolution

An important parameter to characterize an imaging system is the spatial resolution which determines the quality of the modality. In optical imaging the voxel dimensions are typically of the order of 0.5 to 1mm whereas in MRI the resolution is typically 150 to 500μm isotropic depending on the acquisition parameters. The FMT spatial resolution in the second generation hybrid system was evaluated using phantom (A) (Fig. 7.9a) and (B) comprising two identical fluorescent tubes with variable spacing (2-4mm) at depths of 1 and 2mm. The experimental data revealed that the sources placed in 1mm depth could be clearly localized and separated even though they were placed in a minimal distance of 2mm apart (Fig. 7.9b,c). The minimal tube separation distance of 2mm in phantom (B) where the tubes were placed in a depth of 2mm with respect to the surface could still be determined (Fig. 7.9e,f). To measure the separation distance the line profiles in x direction of a slice in the xz-plane with the highest fluorescent signal was used. Drawing the line profile through the peak value of the embedded tubes, the spatial separation could be analyzed by measuring the peak separation of the two Gaussian fits applied to the profiles. If two clearly distinguishable peaks could be identified in the line profile the two signals were considered as spatially separable. The experimental tube separation was limited by the diameter and the wall thickness of the capillaries used. The small artifacts in Fig. 7.9e and f are a result of imperfect

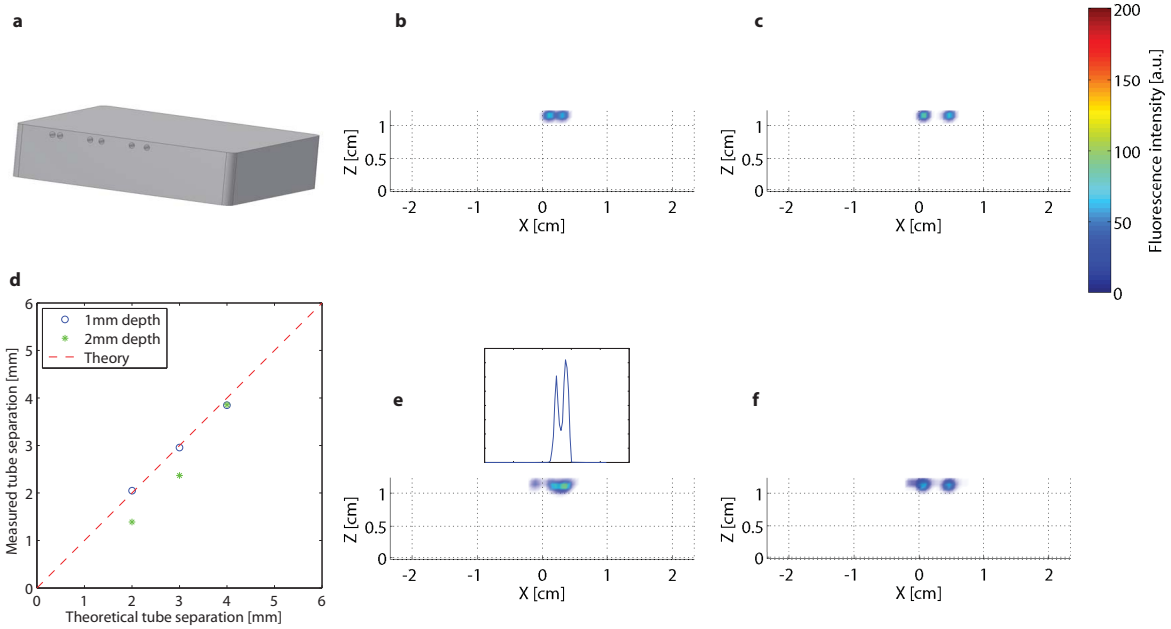

Figure 7.9: Spatial resolution analysis. **a** Sketch of the silicone phantom used for the spatial resolution measurements. **b,c** Reconstructed fluorescence intensity (arbitrary units) from experimental data in 1mm depth in xz-projection for 2mm **b** and 4mm **b** center-to-center tube separation. **d** Plot of the extracted tube separations for experimental data in 1mm depth (blue circles) and experimental data in 2mm depth (green stars) versus the theoretical separations (red dashed line). **e,f** Reconstructed fluorescence intensity (arbitrary units) from experimental data in 2mm depth in xz-projection for 2mm **e** and 4mm **f** center-to-center tube separation. The inset in **e** shows the line profile at z=1.1mm.

reconstruction due to deficiencies like the forward model (assuming a fluorescence point source embedded in an optically homogeneous medium), data collection (detector noise) and SNR which contributes to the uncertainty of the data. A comparison between the evaluated experimental separation and the theoretical separation revealed a good agreement for the extracted values in a depth of 1mm whereas a reduced accuracy of the tube separations in 2mm depth was found (Fig. 7.9d).

Depth Resolution

A prerequisite to derive quantitative readouts is an accurate depth reconstruction of the fluorescent source. For the experimental depth investigation the tissue phantom (C) was used for a depth range of 1 to 5mm (Fig. 7.10a). The depth accuracy was analyzed with a line profile which was drawn in z direction across the maximum intensity of the slice in xz-plane representing the highest fluorescent values. The distance between the phantom surface and the peak value of a fitted Gaussian line

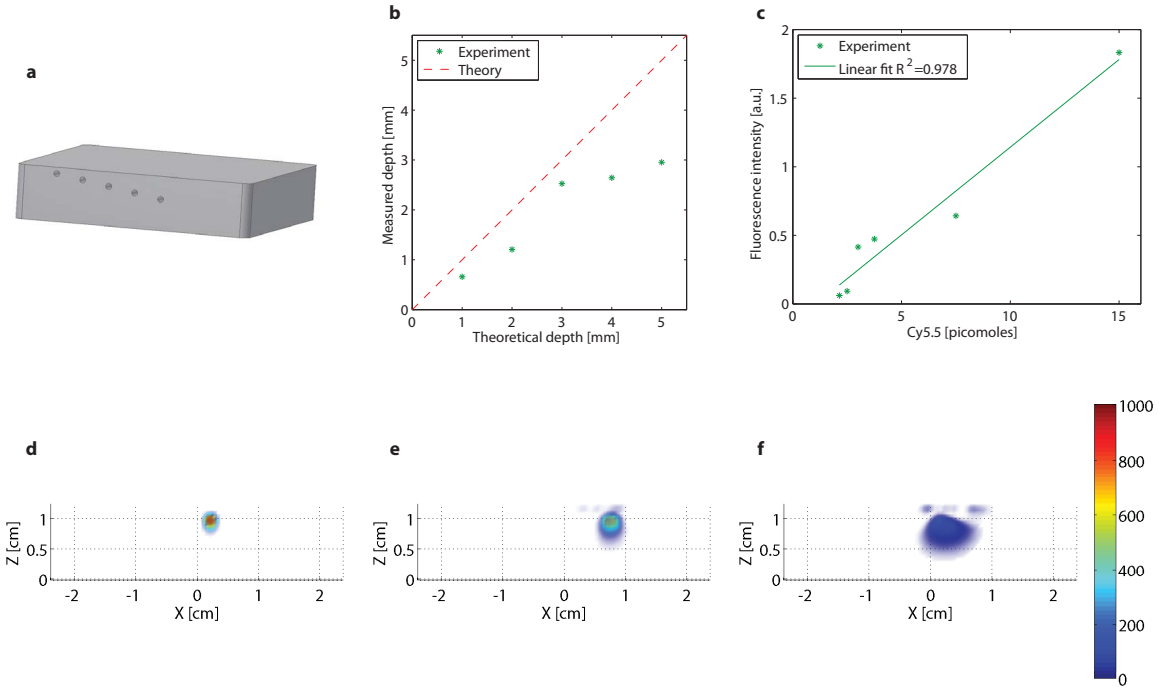

Figure 7.10: Depth resolution in a phantom. **a** Sketch of the silicone phantom used for the spatial resolution measurements. **b** Plot of the extracted tube depth for experimental data (green stars) versus theoretical depth (red dashed line). **c** Reconstructed mean fluorescence intensity versus Cy5.5 concentration in a tube of the phantom (A). **c-e** Reconstructed fluorescence intensity (arbitrary units) from experimental data in xz-projection for 3mm **d**, 4mm **e** and 5mm **f** below the surface.

was taken as a measure of depth. As light scattering scales with the path length through tissue, an increased dispersion of the fluorescence intensity with depth is observed (Figs. 7.10d-f). The fluorescent tube close to the surface is clearly localized and appears with a higher value compared to deeper located sources. Nevertheless, analyzing the integral over the volume of interest incorporating the fluorescent region should result in similar values for all depths. The small artifacts at the phantom surface in Fig. 7.10e and f are a result of imperfect reconstruction due to deficiencies like the forward model, detector noise and SNR which contributes to the uncertainty of the data. However, a good correlation between the reconstructed and the true depth could be observed (Fig. 7.10b) for depths <3mm. If the fluorescence source depth exceeds 3mm, the actual depth in the reconstructed data sets is underestimated. This can be attributed to reflection geometry setup, which emphasizes contributions from superficial structures.

Quantification Analysis

The benefit of FMT is the ability to derive quantitative information on the local dye concentrations compared to optical planar imaging. Therefore two aspects are of major interest: a) the minimal dye concentration that can be detected (detection limit), and b) the linearity of the relationship fluorescence intensity versus dye concentration. The experiments were carried out using the tissue phantom (A) allowing to embed fluorescent sources at a depth of 1mm. By extracting the fluorescence intensity values within a cubic volume of interest around the reconstructed fluorescent signal a correlation between the Cy5.5 concentration and the fluorescence intensity revealed a linear relation ship (R^2=0.978; Fig. 7.10c) for a range from 2.14 to 15picomoles dissolved in a volume of approximately 1.5μl.

Hybrid Imaging

For *in vivo* proof-of-principle feasibility study of simultaneous FMT/MRI measurements an Alzheimer's disease mouse model was used. A 18month old transgenic APP23 mouse was used for the first hybrid imaging experiment. These animals developed vasculature and parenchymal plaques in the brain. A concentration 0.1mg/ml of an oxazine derivative AOI987 dye which is known to bind to amyloid-β plaques was injected intravenously via the tail vein. All data were acquired simultaneously on both modalities with acquisition time on the same time scale allowing to measure time dependent processes simultaneously. A pre measurement before the dye injection was acquired followed by a measurement 15min after after the injection to investigate changes in fluorescence intensity. Representative MRI slices of the brain (Fig. 7.11a) showed the proper functioning of the MRI surface coil while acquiring optical images of the brain region in the rectangular field confined by the surface coil. In the white light images Fig. 7.11b and d the rectangular surface coil with its capacitors is clearly visible and references describing the animal orientation are indicated with yellow and green arrows for the position of the animals eyes and ears, respectively. As an overlay in Fig. 7.11b and d the reconstructed fluorescence intensity projected to the xy-plane is given for the two different time points prior (Fig. 7.11b) and 15min after (Fig. 7.11b) dye injection. Interestingly, the measured dye distribution in FMT was not homogeneous across the covered brain area. A different visualization of the data is given in Fig. 7.11c for the pre-measurement and in Fig. 7.11e for the 15min post measurement projected on the curved white light image, where the tilted view gives insight to the fluorophore distribution in depth. It revealed that the fluorescence signal originates from a layer which is located close to the surface of the animal head. The quantification analysis of the fluorescence signal covering the brain region in an area of 10×20mm revealed in a 3.2 fold increase in the fluorescence signal comparing to the pre measurement acquired 15min after the dye injection.

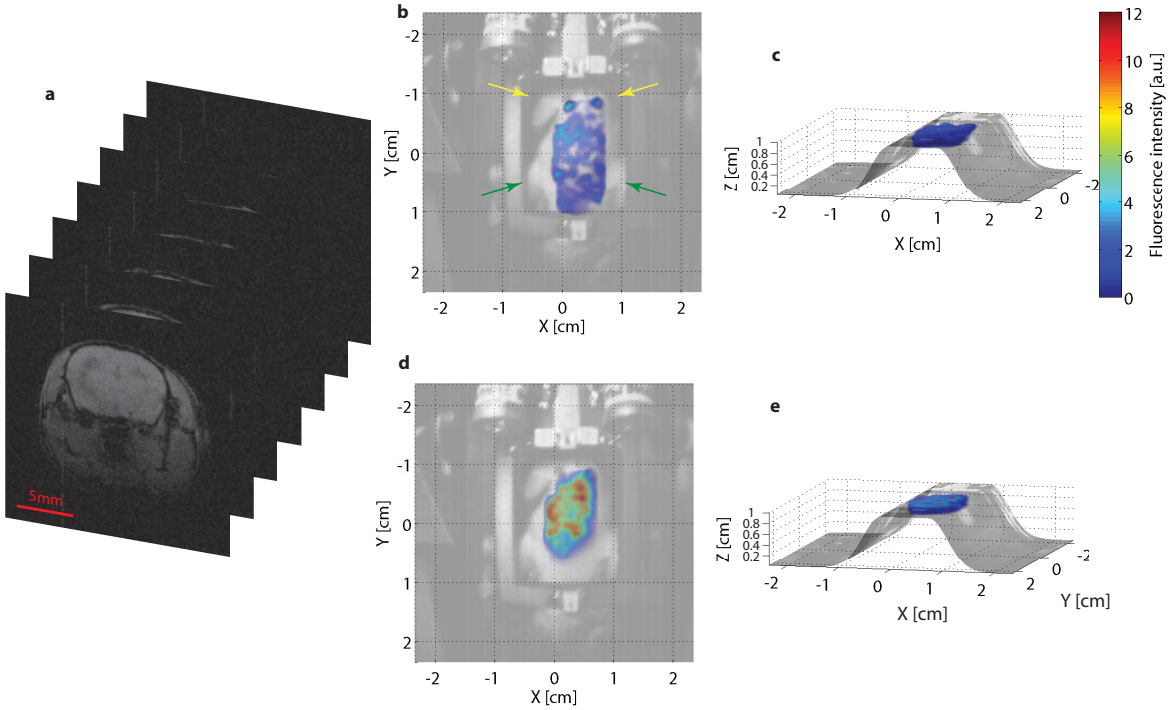

Figure 7.11: Simultaneous MRI and optical data acquisition. **a** Representative simultaneous acquired MRI data set from the middle of the brain towards the neck region. **b,c** Reconstructed fluorescence intensity acquired prior to the dye administration projected to the xy-plane **b** and in a tilted view **c**. The eyes and the ears of the animal are indicated with yellow and green arrows, respectively. **d,e** Reconstructed fluorescence intensity acquired 15min after the dye administration projected to the xy-plane **d** and in a tilted view **e**.

7.2.4 Discussion

For solving complex biological problems it is essential to combine different readouts providing complementary information of ongoing molecular and/or cellular processes. Especially in the field of molecular imaging it is of major importance to register the functional readout to an anatomical reference recorded with a different modality.
Therefore different strategies are proposed such as sequential imaging which makes use of the optimal performance of each stand-alone system without compromising image quality. The major problem of this concept is to find a solution for the animal translocation between the modalities without changing the physiological condition or moving the soft tissue which renders a later registration of both readouts difficult. In addition, for the investigation of fast concurrent processes with different modalities, sequential sampling is not feasible.
For biomedical research hybrid systems providing simultaneous multiplexed information in an inherently registered manner would be highly attractive. Due to the rigid configuration of both modalities the readout is inherently registered and concurrent

measurements on both modalities can be performed. A combination with MRI is beneficial as it provides high soft-tissue contrast which is requested for the investigation of biological processes and it is a well established modality in preclinical and clinical structural and functional imaging. The fully integration of optical imaging in an MR system is challenging due to the hostile environment of a high magnetic field.
As the few reported examples of hybrid optical imaging/MRI systems are fiber-based, they have a certain space requirements and are therefore built in a large clinical MRI system with a gradient bore of 50-60cm inner diameter. The lower field strengths and weak magnetic field gradients of clinical MR scanner compromise the achievable spatial resolution which makes such systems suboptimal for small rodent studies. Moreover in fiber-based systems the number of source/detector pairs is limited and due to the rigid arrangement the optical imaging geometry is fixed. In most examples only a few slices of the sample can be reconstructed as the fiber FOV is small and the space for fiber placement limited. Furthermore the fibers are typically brought in direct contact with the sample which complicates the experimental procedure by manually adjusting the individual fibers. In the previously described first generation setup (see section 7.1) it was shown that a non-contact optical system allows to overcome these limitations of the fibers as the excitation point grid can be varied by adjusting the scanning device outside the bore. The concept of placing the detector within the MR bore directly over the animal's body and the MR surface coil allows for a larger FOV compared to the fiber-based systems. Moreover the small size of the FMT platform allows the insertion into a preclinical MR scanner with a high magnetic field. Furthermore an improved experimental flexibility and an increased number of independent data generated for reconstruction could be achieved to render three-dimensional reconstructed volumes. The presented performance tests on tissue phantoms and the animal experiment were promising, showing the potential of such a system. However the setup handling and the SPAD detector FOV and its imaging quality had some limitations which makes routine measurements cumbersome and time consuming. Therefore an improved redesign of this concept with a new superior detector technology was implemented, which should help to establish the newly developed concept in biomedical research.
With the second generation FMT/MRI setup we succeeded to scale a stand-alone FMT system down to a size of 120mm with only minor performance losses. The CMOS detector adapted for these applications allowed for an enhanced imaging quality mainly due to higher detector resolution, larger FOV, increased number of pixels and sensitivity. The miniaturized FMT imaging platform can be placed on a rigid rail system which simplifies the experimental handling and the platform movement inside the MR bore.
In hybrid imaging systems combining two complementary imaging modalities, typically a degradation in both modalities with regard to their stand-alone performance is observed, which is in view of the benefits of the multimodality readouts acceptable. As the best of all cases, having the full performance of both systems, is hardly achievable for integrated systems, it would be a step forward if at least one modality has comparable readouts to state of the art systems. In combined FMT/MRI system, the MRI

setup defines the design of the integrated FMT system. It was shown, that mainly the optical system was limited by the fact that it has to operate in a high magnetic field and has to fit into the small bore. The improved imaging performance of the second generation construction leads to reconstructed fluorophore distributions which were comparable to stand alone FMT systems working with cooled CCD detectors.
The in-plane spatial resolution derived from phantom experiments where two fluorescent sources of equal strengths are embedded and separated by a certain distance revealed in a best resolution of 2mm center-to-center distance. The tubes were clearly separable in a depth of 1mm whereas the analysis of the line profile was needed to verify this separation distance in a depth of 2mm. The linear dependence of experimental and theoretical source separation for a range of 2 to 4mm in two different depths reflects the accuracy of the reconstruction algorithm. As already observed in the first FMT/MRI system the depth localization of a fluorescence source was found to be systematically smaller than the theoretical depth. Even though the detector can resolve deep located sources up to a depth of 5mm, the localization accuracy rapidly decreases for depths >3mm. The depth limitation is due to the diffusive light propagation as the intensity is reduced to a level that makes detection difficult (in particular in view of autofluorescence contributions from surface structures). Furthermore it is observed that the deeper the source the more spread the reconstructed fluorescence signal appears, which is due to the applied reconstruction technique ART. The algorithm tries to find a solution space for the illposed problem. As the illposness of the problem is increased the deeper a structure is embedded the larger the solution space and therefore the more spread the reconstructed result appears. Another effect of ART is that the signal of structures close to the surface appear in a much higher intensity than deeper located spread structures. The integration over a volume of interest at each depth should result in the same fluorescence intensity. The elimination of these limitations in representing the data is an ongoing project.
FMT as a molecular imaging modality should provide non-invasive quantitative information on molecular processes in intact organisms. This was proved with calibration experiments in a tissue phantom which revealed that the FMT/MRI system was capable of detecting 2 picomole amounts of dye. For *in vivo* applications typically similar amounts of dye are used. An important prerequisite for quantitative studies is a linear dependence of the reconstructed fluorescence intensity and the amount of fluorescent dye in the sample volume. By analyzing the results it revealed a correlation factor of 0.978 and therefore a high linearity.
The major advantage of an integrated hybrid imaging concept compared to other strategies is the annotation of molecular information to high resolution anatomical images. The *in vivo* study on Alzheimer mice allowed the identification of the fluorophore distribution in a sub-surface layer below the optical measurement window of the MR surface coil. This layer represents a functional information of the cortical area of the mouse brain as it can be annotated to the structural MR images acquired simultaneously. These results are in accordance to a previously reported study by Hyde et al. [121] where a combination of FMT and CT was used. Moreover the

measurement of two different time points before and after AOI987 injection showed an increase in reconstructed fluorescence intensity indicating that the FMT system is sensitive and *in vivo* quantification is possible during simultaneous system operations. Up to now the fluorescence distribution is not registered to the anatomical readout and both readouts need to be analyzed separately. The registration of both information is an ongoing project. Furthermore, structural MR information can be used in the forward and/or backward model of the FMT to improve the reconstruction [137, 134]. Besides appropriate allocation of the molecular readout to anatomy, a more attractive FMT/MRI application would be a correlation between physiological/functional MRI readouts (e.g. angiogenesis) with FMT derived molecular information which demand for simultaneous measurements.

Chapter 8

Conclusions and Outlook

The present thesis focused on the evaluation and development of non-contact FMT strategies and consists of two parts. As a first preparative part of the project a stand alone non-contact FMT system was constructed and evaluated with different *in vivo* applications. The experiences collected in this first part impaired the developments presented in the second part where a novel concept of combined fluorescence molecular tomography and magnetic resonance imaging was elaborated.

8.1 FMT

Non-contact FMT measurements are nowadays widely available in biomedical optic research laboratories and were used for selected studies on animal disease models where a fluorescent reporter strategy is available. However the routine use of FMT in biomedical research remains an issue due to the complexity of FMT compared to simple planar fluorescence and bioluminescence approaches. The latter methods provide a fast and more importantly immediately visible readout on the screen whereas for FMT the raw data need to be processed. The reconstruction procedure is time consuming due to the large data sets acquired in non-contact FMT and as multiple reconstruction parameters have to be adjusted sequentially for each study. Different parameter adjustments might lead to different results which need to be evaluated and might involve another round of reconstructions until the results are satisfactory.
In the here presented *in vivo* applications it was shown that a localization of the reconstructed fluorophore was precise as far as it can be evaluated according to the reference planar white light image. However, it is difficult to evaluate the precision of the depth localization of the reconstructed fluorophore distribution in the *in vivo* studies due to the absence of anatomical references. Therefore only conclusions related to a known default anatomy of the imaged structure can be drawn. As it was shown that the reconstructed fluorescence intensity of the imaged superficial structures such as lymph nodes and plaques deposits in the cortical region of the brain are located close to the surface, this allows the conclusion that the implemented reflection geometry and

the reconstruction parameters are well suited for this type of imaging targets. Nevertheless, the limited depth resolution performance of the reflectance geometry while imaging deep seated structures remains to be further evaluated. Another important parameter was the spatial resolution, which defines at which separation diestance objects can still be resolved. Not surprisingly it was observed that the auricularly lymph nodes are clearly distinguishable as they are separated by a large distance of 1cm. However, by resecting the lymph nodes it was observed that in few mice two nodes on one side are lying next to each other and could not be resolved by the FMT. The reconstruction of such a structure revealed a single spherical fluorophore distribution which lead to the conclusion that such structures which are assumed to have similar labeled antibody concentration are too close (less than 1mm) to be detected by the here presented method. The identical problem was observed by analyzing the tail bone data sets where a separation of the loaded from the adjacent vertebrae could not be achieved as they are separated by a few hundred microns and the difference between the fluorescence probe (OsteoSense 680) concentration in the different vertebrae might be minimal and not distinguishable.
Even though the spatial resolution of this method is limited it was shown that the readout is still sensitive and can be used for quantitative measurements by analyzing the reconstructed fluorescence intensities e.g. for distinguishing different lymph nodes or comparing tail vertebrae of different groups (loaded vs. non loaded). To verify the quantitative readout of FMT a comparison with results from other functional modalities such as PET might be useful [138].
The quantification for a single time point was further extended to follow either the clearance kinetic of an administered dye comparing a transgenic and a wild type control animal in the Alzheimer's study within three hours or to follow the load induced effect in vertebrae bone formation and resorption during a time span of four weeks. In the Alzheimer's study it could be visualized that the clearance in transgenic animals was slower which is due to the dye binding to the plaques compared to the control where the fluorescence intensity rapidly decreased.
For the tail bone study, as assumed, the group obtaining a loading showed a larger bone turn over (formation and resorption) whereas the non loaded group revealed reduced values. A validation of the molecular FMT readout in this bone study was performed by a correlation analysis with structural bone measurements from CT data, where a significant parameter agreement between the fluorescence intensity percentage difference and the bone formation rate and the mineral resorption rate was found by comparing the starting time point with the time point after two weeks. Therefore the FMT method described in this work can be seen as a tool to quantify biological processes, even though the values are not absolute but relative. Further attempts in the field are needed to achieve an absolute quantification of the FMT readout by accounting for the different optical properties in tissue which might make the FMT problem even more complex.
However, the improved non-contact FMT instrumentation compared to previously reported setups showed a proper functioning even though some manual handling is

needed for a correct measurement. With the here presented non-contact FMT setup no image quality loss was observed due to the concept of integrated standard size fluorescence filters positioned between the CCD chip and the camera objective. This design circumvents the use of expensive custom made large aperture fluorescence filters. Furthermore it simplifies the handling as the procedure of screwing filters in front of the objective for each measurement is redundant. Another convenience was brought by the fiber coupled light sources, which allow for a comfortable and fast excitation wavelength selection with help of a fiber switch. With precise fiber coupling and beam collimation minimal light loss and adequate beam shapes can be achieved.

8.2 FMT/MRI

In the second part of this thesis the experiences of the non-contact stand-alone FMT system was applied to a novel hybrid imaging strategy for simultaneous acquisition of FMT and MRI data in a small animal MRI system.
Based on that concept a first prototype FMT/MRI setup was developed using a SPAD array detector technology working at 9.4T and a free beam illumination from outside the MR bore. This free-beam and non-rigid imaging geometry was found to be superior to the existing fiber-based systems where only single slices can be acquired and reconstructed. With the here presented strategy it was shown that full three-dimensional volumetric tomography is feasible in combination with an MR acquisition. The interference between the two modalities was found negligible. Reconstruction of fluorescence data revealed an accurate localization of embedded fluorescent sources, whereas the spatial resolution was experimentally demonstrated to be in the order of 2mm (see Fig. 7.3) whereas based on the width of the individual profile of simulated data we estimated that sources separated by 0.9mm should be distinguishable. Limitations in depth resolution may be attributed to the inherent surface weighting of the reflectance geometry approach and to the limited array size (32×32 pixels) and the limited field of view of the current detector array. Improvements in depth reconstruction might therefore be achieved by using the setup in transmission mode, which would in addition reduce the interference by autofluorescence. The next generation detector arrays should have a significantly increased matrix dimensions and should due to the increased number of source/detector pairs improve the reconstruction accuracy. Hybrid FMT/MRI is sensitive and we determined a sub-picomole detection limit for sources embedded at a depth of 1mm below the surface (Fig. 7.4f). For this imaging domain the system performance was found to be quantitative, as reflected by the linear relationship of fluorescence signal versus dye concentration. With its potential for annotating structural/physiological with quantitative molecular information FMT/MRI constitutes an attractive hybrid modality for experimental biomedical researchers.
In the construction of a second generation FMT/MRI setup we tried to eliminated the major restrictions known from the first prototype. Therefore, the general concept of the combination of non-contact FMT and MRI was not changed but the setup was

completely redesigned and improved. The rail design which allows to move the imaging platform comprising the sample, the optical detector and MR components to the isocenter of the magnet was shown in experimental practice to be robust and reliable. The redesigned CMOS detector for the use in this application, was found to have a superior image quality compared to the previously used SPAD array as the number of pixels and the FOV could be enlarged. Overall, with this major improvements in the optical imaging system a miniaturization of an FMT system has been achieved which is providing a comparable performance to a stand-alone FMT system working with CCD detectors. The reconstructed data of the performance tests revealed an accurate depth localization of fluorescent sources up to a depth of 3mm whereas deeper located sources can still be recovered but with limited localization precision. This loss in localization accuracy is attributed to the chosen reflection geometry. The experimentally determined spatial resolution for a depth of 2mm was found to be in the order of 2mm center-to-center distance of two embedded fluorescent tubes. FMT sensitivity tests to determine the detection limit for sources embedded at a depth of 1mm below the surface was found in this first test to be in the order 2 picomoles. The good linear relation ship of the reconstructed fluorescence intensity versus dye concentration reflects the capacity for quantitative FMT readouts. The interference between the two modalities was found negligible. First hybrid *in vivo* experiments showed the proper functioning of both modalities while running simultaneous acquisitions. Considering both readouts separately, it is possible to localize the reconstructed signal with regard to the derived anatomical information form the MR. Further improvements could be achieved by correctly co-registered images of both modalities, which is an ongoing project. In summary, the potential of this miniaturized FMT system in combination with MRI was shown by several tests, but needs to be further validated with biological applications where complementary imaging information is needed to answer specific questions.

8.3 Outlook

The establishment of transmission measurement geometries on the FMT and on the hybrid FMT/MRI setup is certainly one of the next steps which should be followed. The transmission measurements would eliminate the restricted depth resolution of the now established reflection geometry [34], which was shown to work well for subsurface structures. As all systems are ready to be used in transmission mode, a comparison of both geometries in controlled phantom and in well established *in vivo* experiments should be straight forward. Nevertheless several questions concerning this geometry needs to be addressed such as the laser power and illumination light bleed through around the sample.
Efforts in the direction to a user friendly setup and reconstruction software should be undertaken that the developed systems find a broad acceptance in routinely biomedical research. This improvements would involve the software packages for image acquisition

and the reconstruction, which today needs a lot of expertise for a correct operation. For the image acquisition a faster illumination procedure and a fully automated FMT setup would further contribute to the acceptance as well as a "quasi" real time reconstruction procedure which would allow to subsequently analyze the measurements. Efforts in this directions are under way by using parallel computing by harnessing the graphical processor unit for fast reconstruction and using improved illumination patterns for the image acquisition. These are ongoing projects in the lab of our collaborator J. Ripoll.
Furthermore the use of multi spectral information should be stressed next. This would allow to address the issue of tissue autofluorescence which could be eliminated by using the spectral information for the reconstruction process. As different laser sources and bandpass filters are already implemented in the setup this point can be addressed immediately.
Another module which should be implemented in the future is the incorporation of the rendered sample surface for representation and interpretation purposes. The localized reconstructed fluorophores bounded by the surface e.g an animal surface would help to better interpret the data. The surface information is automatically obtained when using the hybrid setup whereas in the FMT setup an additional measurement with a point or line scanning of the object is needed. For this ongoing project in our lab we performed first tests but further evaluation is needed to finally implement this feature.

The most important next step for the hybrid imaging project is the incorporation of the MRI information into the optical image reconstruction. As it was shown by other groups this prior knowledge will have a big impact on the quality of the reconstructed fluorophore distribution. For state of the art hybrid FMT/MRI modalities only a small sample volume can be covered by the optical instrumentation. Therefore only resliced optical data matching the MR slice is used to demonstrate the beneficial incorporation of structural MR information improving the optical reconstruction. The presented optical design allows now to cover larger volumes such as a full mouse brain which renders the possibility to use the complete three dimensional information of the MR data for improving the optical reconstruction.
Related to that, software adaptations in the reconstruction part are needed and new tools e.g. tissue segmentation algorithms have to be implemented to combine the information of the two readouts. The incorporation of prior knowledge from segmented structural readouts need to be carefully applied as it is susceptible to over constrain the fluorescence reconstruction. Furthermore, the assignment of optical properties to different tissue types has the inherent problem that scattering and absorption values are highly dependent on the tissue condition and reported values varies within a wide range. Therefore, it has to be evaluated how the prior knowledge should be incorporated to not over constrain the optical readout. For the purpose of image co-registration of both systems a concept of placing fiducial marker which are visible in both modalities need to be further established. This points are addressed by an ongoing project in our lab.

A prerequisite to derive prior information is a correct tissue segmentation based on high quality MR images which would allow a segmentation according to the gray values of the soft tissue contrast obtained from the MR images. The image quality is related to the coil design and a proper parameter adjustment for the MR acquisition. Therefore a first step in this direction would be a modified coil design, which would allow a homogeneous sensitivity of the imaged volume compared to the implemented transceive surface coils which have a specific depth sensitivity. This issue would be mostly important while resolving deep seated structures which is problematic for surface coils as the image contrast decreases with increasing distance from the coil. Possible designs could be a saddle coil (combining two surface coils), an Alderman-Grant coil or a birdcage coil where all would allow a better MR field of view coverage. Since the coil design is now more complex and therefore not straight forward to implement, calculations of the electromagnetic fields and the coil characteristic might be investigated by simulations. A new coil design would be accompanied by the design of appropriate windows for the laser scanning and optical signal detection. With the new improved second generation FMT/MRI setup where the optical FOV was enlarged by a factor of eight, the coil lies within the FOV and therefore restricts the scan area and leads to blocking and dispersing light which is emitting from the sample. The scan region within the window of the RF coil is well suited for small ROI such as tumors and mouse head, but for larger ROI new strategies has to be found to eliminate these limitations for optical data acquisitions without affecting the MR image quality.
The SNR evaluation of the MR images revealed a decreased image quality in the second generation system compared to the first prototype which was caused by the data transfer from the detector to the motherboard. However, the image quality is still sufficient for structural imaging but needs to be improved if functional MR information is needed. Therefore the effect on image quality using shielded cables or a new concept based on optical data transfer needs to be evaluated.
A further issue which should be addressed in the future is the distortion caused by the objective lens in the newly developed FMT/MRI device. The distortion appears towards the edges of the image if the object distance is very short compared to the normal working distance of the objective lens. A post processing correction routine with help of a reference pattern should be elaborated to allow for undistorted image acquisitions.
As a last point it has to be mentioned that the full power of combining the two readouts was not yet achieved because only structural MR information was used, which could be obtained by simple sequential imaging approaches. Therefore a future development of a protocol where a simultaneous readout is necessary for conclusive findings would help to further characterize the presented hybrid imaging approach.
Finally, examples of stand alone FMT systems and combined FMT/XCT setups which acquires images of the animal at more than one angle showed an improved reconstructed fluorescent distribution due to fewer number of source detector pairs which helps to reduce the degree of the ill-conditioned inverse problem [139]. In principle the coverage of more than a single projection of the animal in a combined FMT/MRI

setup should be possible by using more than one detector array. By positioning several detectors around the animal in combination with a sophisticated non-contact illumination techniques with more than one deflection mirror, a full 360° detection and illumination would be conceivable. If it is worth to have a full angular coverage might be easily tested on the optical bench with the detectors available by adapting the current setups and the software used. If this fully integrated whole body hybrid imaging approach could be implemented it would certainly be the future of imaging in the field of combined FMT/MR instrumentations.

Appendix A

Photon Transport Theory

A.1 Transport Equations

Some parts of the following derivations can be found in the following books [75],[71] or [140].

A.1.1 Wave Propagation and Scattering in Random Media

Chapter 7 section 7-3 in [75] describes the fundamental characteristic of the specific intensity in a medium containing random particles. The particles scatter and absorb the wave energy and this characteristic should be included in a differential equation to be satisfied by the specific intensity. This equation is then called the equation of transfer in radiative transfer theory.

First: We consider a specific intensity $I(\mathbf{r}, \hat{\mathbf{s}})$ incident upon cylindrical elementary volume with unit cross section and length ds. The volume ds contains ρds particles where ρ is the number of particles in a unit volume and is called the number density. Each particle absorbs the power $\sigma_a I$ and scatters the power $\sigma_s I$ and therefore a decrease of the specific intensity $dI(\mathbf{r}, \hat{\mathbf{s}})$ for the volume ds is observed

$$\begin{aligned} dI(\mathbf{r}, \hat{\mathbf{s}}) &= -ds(\sigma_a + \sigma_s) I(\mathbf{r}, \hat{\mathbf{s}}) \\ &= -\rho \; ds \; \sigma_t \; I(\mathbf{r}, \hat{\mathbf{s}}) \end{aligned} \tag{A.1}$$

Second: In the same time the specific intensity increases because a portion of the specific intensity incident on this volume from other directions $\hat{\mathbf{s}}'$ is scattered into the direction $\hat{\mathbf{s}}$ and is added to the intensity $I(\mathbf{r}, \hat{\mathbf{s}})$. Let us consider a wave incident in the direction $\hat{\mathbf{s}}'$ on a particle. The

incident flux density through a small solid angle $d\omega'$ is given by $S_i = I(\mathbf{r}, \hat{\mathbf{s}}')d\omega'$. This flux is incident on particles in the volume ds. The power flux density S_r of the wave scattered by a single particle in the direction $\hat{\mathbf{s}}$ at a distance R from the particle is then given by $S_r = [|f(\hat{\mathbf{s}}, \hat{\mathbf{s}}')|^2/R^2]S_i$ where $f(\hat{\mathbf{s}}, \hat{\mathbf{s}}')$ is the scattering amplitude. The scattered specific intensity in the direction $\hat{\mathbf{s}}$ due to S_i is therefore

$$\begin{aligned} S_r\ R^2 &= |f(\hat{\mathbf{s}}, \hat{\mathbf{s}}')|^2\ S_i \\ &= |f(\hat{\mathbf{s}}, \hat{\mathbf{s}}')|^2\ I(\mathbf{r}, \hat{\mathbf{s}}')\ d\omega' \end{aligned} \tag{A.2}$$

Adding the incident flux from all directions $\hat{\mathbf{s}}'$ the specific intensity scattered into the direction $\hat{\mathbf{s}}$ by $\rho\ ds$ particles in the volume ds is given by

$$\int_{4\pi} \rho\ ds\ |f(\hat{\mathbf{s}}, \hat{\mathbf{s}}')|^2\ I(\mathbf{r}, \hat{\mathbf{s}}')\ d\omega' \tag{A.3}$$

where the integration over all ω' is taken to include the contribution from all directions $\hat{\mathbf{s}}'$. We can express A.3 using the phase function $p(\hat{\mathbf{s}}, \hat{\mathbf{s}}')$:

$$p(\hat{\mathbf{s}}, \hat{\mathbf{s}}') = \frac{4\pi}{\sigma_t}|f(\hat{\mathbf{s}}, \hat{\mathbf{s}}')|^2 \tag{A.4}$$

and therefore

$$\int_{4\pi} \rho\ ds\ \frac{\sigma_t}{4\pi}\ p(\hat{\mathbf{s}}, \hat{\mathbf{s}}')\ I(\mathbf{r}, \hat{\mathbf{s}}')\ d\omega' \tag{A.5}$$

Third: The specific intensity may also increase due to the emission from the volume ds. Denoting by $\varepsilon(\mathbf{r}, \hat{\mathbf{s}})$ the power radiation per unit volume per unit solid angle in the direction $\hat{\mathbf{s}}$ the increase of the specific intensity is given by

$$ds\ \varepsilon(\mathbf{r}, \hat{\mathbf{s}}) \tag{A.6}$$

Adding the contributions (A.1), (A.5) and (A.6) we get the equation of transfer in radiative transfer theory

$$\begin{aligned} \frac{dI(\mathbf{r}, \hat{\mathbf{s}})}{ds} &= -\rho\sigma_t I(\mathbf{r}, \hat{\mathbf{s}}) + \frac{\rho\sigma_t}{4\pi}\int_{4\pi} p(\hat{\mathbf{s}}, \hat{\mathbf{s}}')I(\mathbf{r}, \hat{\mathbf{s}}')d\omega' + \varepsilon(\mathbf{r}, \hat{\mathbf{s}}) \\ \hat{\mathbf{s}} \cdot \nabla I(\mathbf{r}, \hat{\mathbf{s}}) &= -\rho\sigma_t I(\mathbf{r}, \hat{\mathbf{s}}) + \frac{\rho\sigma_t}{4\pi}\int_{4\pi} p(\hat{\mathbf{s}}, \hat{\mathbf{s}}')I(\mathbf{r}, \hat{\mathbf{s}}')d\omega' + \varepsilon(\mathbf{r}, \hat{\mathbf{s}}) \end{aligned} \tag{A.7}$$

$I(\mathbf{r}, \hat{\mathbf{s}})$: specific intensity (also radiance or brightness) measured in W m^{-2} sr^{-1} Hz^{-1}

A.1.2 Linear Transport Theory

In [71] we can find in Chapter 1 the following equation (3) and its derivation. Equation (3) is the fundamental transport equation for neutrons

$$\frac{\delta\psi(\mathbf{r},\mathbf{v},t)}{\delta t} + \mathbf{v}\cdot\nabla\psi(\mathbf{r},\mathbf{v},t) + \upsilon\sigma(\mathbf{r},\mathbf{v})\psi(\mathbf{r},\mathbf{v},t) \quad = \quad q(\mathbf{r},\mathbf{v},t) + \int d^3\upsilon'\sigma(\mathbf{v}'\rightarrow\mathbf{v}\mathbf{r})\upsilon'\psi(\mathbf{r},\mathbf{v},t) \tag{A.8}$$

In chapter 2 (2.2 The one-speed approximation) we can find finally

$$\frac{\partial\psi(\mathbf{r},\mathbf{v},t)}{\partial t} + \upsilon\boldsymbol{\Omega}\cdot\nabla\psi(\mathbf{r},\mathbf{v},t) + \upsilon\sigma(\mathbf{r},\upsilon)\psi(\mathbf{r},\mathbf{v},t) \quad = \quad q(\mathbf{r},\mathbf{v},t) + \upsilon\sigma(\mathbf{r},\upsilon)c(\mathbf{r},\upsilon)\int\psi(\mathbf{r},\boldsymbol{\Omega}',t)f(\boldsymbol{\Omega}'\cdot\boldsymbol{\Omega},\mathbf{r},\upsilon)d\boldsymbol{\Omega}' \tag{A.9}$$

υ is the speed of the neutron and $c(\mathbf{r},\upsilon)$ can be written as

$$c(\mathbf{r},\upsilon) = \frac{\sigma_s(\mathbf{r},\upsilon)+\sigma_{in}(\mathbf{r},\upsilon)}{\sigma(\mathbf{r},\upsilon)} \tag{A.10}$$

$$\frac{\partial\psi(\mathbf{r},\mathbf{v},t)}{\partial t} + \upsilon\boldsymbol{\Omega}\cdot\nabla\psi(\mathbf{r},\mathbf{v},t) + \upsilon\sigma(\mathbf{r},\upsilon)\psi(\mathbf{r},\mathbf{v},t) \quad = \quad q(\mathbf{r},\mathbf{v},t) + \upsilon(\sigma_s(\mathbf{r},\upsilon)+\sigma_{in}(\mathbf{r},\upsilon))\int\psi(\mathbf{r},\boldsymbol{\Omega}',t)f(\boldsymbol{\Omega}'\cdot\boldsymbol{\Omega},\mathbf{r},\upsilon)d\boldsymbol{\Omega}' \tag{A.11}$$

A.1.3 Neutron Transport Theory

In [140] we can find in Chapter 2 the following equation (2.4) and its derivation. The equation is the so-called transport equation or Boltzmann equation, which forms the basis of the entire theory of neutron transport.

$$\frac{\partial N}{\partial t} + \upsilon\boldsymbol{\Omega}\cdot\nabla N + \frac{\upsilon N}{l_{tot}(\upsilon)} \quad = \quad \int\frac{\upsilon' d\upsilon'}{l_{tot}(\upsilon')}\int\int\int N(\mathbf{r},\upsilon'\boldsymbol{\Omega}',t-t')c_{t'}f(\upsilon'\boldsymbol{\Omega}'\rightarrow\upsilon\boldsymbol{\Omega};t')dt'd\Omega' + S$$

Boltzmann equation for a stationary problem

$$\upsilon\boldsymbol{\Omega}\cdot\nabla N + \frac{\upsilon N}{l_{tot}(\upsilon)} \quad = \quad \int\frac{\upsilon' c(\upsilon')d\upsilon'}{l_{tot}(\upsilon')}\int\int N(\mathbf{r},\upsilon'\boldsymbol{\Omega}')f(\upsilon'\boldsymbol{\Omega}'\rightarrow\upsilon\boldsymbol{\Omega})d\Omega' + S$$

A.2 P_N Approximation

Due to the fact that analytic solutions of the transport equation are difficult to obtain and numerical calculations requires a tremendous computational power approximative solutions are used. One of the usually used standard approximation method is the so-called P_N approximation. The method expands the radiance, phase function and the source in spherical harmonics $Y_{l,m}$ which is then stopped for the radiance at $l = N$. An outline to the following calculations can be found in [141].

The spherical harmonics for $l = 0, 1$:

$$Y_{0,0}(\vartheta, \varphi) = \frac{1}{\sqrt{4\pi}} \tag{A.12}$$

$$Y_{1,-1}(\vartheta, \varphi) = \sqrt{\frac{3}{8\pi}} \sin\vartheta \, e^{-i\varphi} \tag{A.13}$$

$$Y_{1,0}(\vartheta, \varphi) = \sqrt{\frac{3}{4\pi}} \cos\vartheta \tag{A.14}$$

$$Y_{1,1}(\vartheta, \varphi) = -\sqrt{\frac{3}{8\pi}} \sin\vartheta \, e^{i\varphi} \tag{A.15}$$

For the unit direction vector we get:

$$\begin{aligned} \hat{\mathbf{s}} &= (\hat{\mathbf{s}}_x, \hat{\mathbf{s}}_y, \hat{\mathbf{s}}_z) \\ &= (\sin\vartheta \cos\varphi, \ \sin\vartheta \sin\varphi, \ \cos\vartheta) \\ &= \sqrt{\frac{4\pi}{3}} \left(\frac{1}{\sqrt{2}} [Y_{1,-1}(\hat{\mathbf{s}}) - Y_{1,1}(\hat{\mathbf{s}})], \ \frac{i}{\sqrt{2}} [Y_{1,-1}(\hat{\mathbf{s}}) + Y_{1,1}(\hat{\mathbf{s}})], Y_{1,0}(\hat{\mathbf{s}}) \right) \end{aligned} \tag{A.16}$$

The radiance and the source term are the terms to be expanded

$$L(\mathbf{r}, \hat{\mathbf{s}}, t) = \sum_{l=0}^{N} \sum_{m=-l}^{l} \psi_{l,m}(\mathbf{r}, t) \, Y_{l,m}(\hat{\mathbf{s}}) \tag{A.17}$$

$$S(\mathbf{r}, \hat{\mathbf{s}}, t) = \sum_{l=0}^{N} \sum_{m=-l}^{l} q_{l,m}(\mathbf{r}, t) \, Y_{l,m}(\hat{\mathbf{s}}) \tag{A.18}$$

The term $q_{l,m}(\mathbf{r}, t)$ is the amplitude of the different angular moments of the source at position $\mathbf{r}$ and time t.

Substituting now equation (A.17) into equation (2.3) it can be seen that $\psi_{0,0}$ is proportional to the radiance (specific intensity)

$$\begin{aligned} U(\mathbf{r},t) &= \int d\hat{\mathbf{s}}\, L(\mathbf{r},\hat{\mathbf{s}},t) \\ &= \int d\hat{\mathbf{s}} \sum_{l=0}^{N} \sum_{m=-l}^{l} \psi_{l,m}(\mathbf{r},t)\, Y_{l,m}(\hat{\mathbf{s}}) \\ &= \sum_{l=0}^{N} \sum_{m=-l}^{l} \psi_{l,m}(\mathbf{r},t) \int d\hat{\mathbf{s}}\, Y_{l,m}(\hat{\mathbf{s}}) \end{aligned} \tag{A.19}$$

The only integral that does not disappear upon integration over all directions is for $l = m = 0$

$$\int d\hat{\mathbf{s}}\, Y_{0,0} = \frac{1}{\sqrt{4\pi}} \int d\hat{\mathbf{s}} = \frac{1}{\sqrt{4\pi}}\, 4\pi \tag{A.20}$$

The average intensity is written as

$$U(\mathbf{r},t) = \sqrt{4\pi}\, \psi_{0,0}(\mathbf{r},t) \tag{A.21}$$

Correspondingly substituting equation (A.17) into equation (2.4) we find that $\psi_{1,m}$ are the components of the flux density

$$\begin{aligned} \mathbf{J}(\mathbf{r},t) &= \int d\hat{\mathbf{s}}\, \hat{\mathbf{s}}\, L(\mathbf{r},\hat{\mathbf{s}},t) \\ &= \int d\hat{\mathbf{s}}\, \hat{\mathbf{s}} \sum_{l=0}^{N} \sum_{m=-l}^{l} \psi_{l,m}(\mathbf{r},t)\, Y_{l,m}(\hat{\mathbf{s}}) \\ &= \sum_{l=0}^{N} \sum_{m=-l}^{l} \psi_{l,m}(\mathbf{r},t) \int d\hat{\mathbf{s}}\ \hat{\mathbf{s}}\, Y_{l,m}(\hat{\mathbf{s}}) \\ &= \sum_{l=0}^{N} \sum_{m=-l}^{l} \psi_{l,m}(\mathbf{r},t) \int d\hat{\mathbf{s}}\, [\sin\vartheta\, \cos\varphi\ \hat{x} + \sin\vartheta\, \sin\varphi\ \hat{y} + \cos\vartheta\ \hat{z}]\, Y_{l,m}(\hat{\mathbf{s}}) \\ &= \sqrt{\frac{4\pi}{3}} \sum_{l=0}^{N} \sum_{m=-l}^{l} \psi_{l,m}(\mathbf{r},t) \int d\hat{\mathbf{s}} \left[\frac{1}{\sqrt{2}} \left(Y^*_{1,-1}(\hat{\mathbf{s}}) - Y^*_{1,1}(\hat{\mathbf{s}}) \right)\ \hat{x} - \frac{i}{\sqrt{2}} \left(Y^*_{1,-1}(\hat{\mathbf{s}}) + Y^*_{1,1}(\hat{\mathbf{s}}) \right) \hat{y} + Y^*_{1,0}(\hat{\mathbf{s}})\ \hat{z} \right] Y_{l,m}(\hat{\mathbf{s}}) \\ &= \sqrt{\frac{4\pi}{3}} \left[\frac{1}{\sqrt{2}} \left(\psi_{1,-1}(\mathbf{r},t) - \psi_{1,1}(\mathbf{r},t) \right)\ \hat{x} - \frac{i}{\sqrt{2}} \left(\psi_{1,-1}(\mathbf{r},t) + \psi_{1,1}(\mathbf{r},t) \right) \hat{y} + \psi_{1,0}(\mathbf{r},t)\ \hat{z} \right] \end{aligned}$$

$$= \sqrt{\frac{4\pi}{3}}\left(\frac{1}{\sqrt{2}}\left(\psi_{1,-1}(\mathbf{r},t)-\psi_{1,1}(\mathbf{r},t)\right)\ ,\ \frac{-i}{\sqrt{2}}\left(\psi_{1,-1}(\mathbf{r},t)+\psi_{1,1}(\mathbf{r},t)\right)\ ,\ \psi_{1,0}(\mathbf{r},t)\right) \tag{A.22}$$

$$= \sqrt{\frac{4\pi}{3}}\,(\qquad J_x \qquad ,\qquad J_y \qquad ,\quad J_z \quad)$$

For the phase function it is assumed that the probability amplitude is only dependent on the change in direction of the photons and thus

$$\begin{aligned} f(\hat{\mathbf{s}}\cdot\hat{\mathbf{s}}') &= \sum_{l=0}^{\infty}\frac{2l+1}{4\pi}\,g_l\,P_l(\hat{\mathbf{s}}\cdot\hat{\mathbf{s}}') \\ &= \sum_{l=0}^{\infty}\sum_{m=-l}^{l} g_l\,Y^*_{l,m}(\hat{\mathbf{s}}')\,Y_{l,m}(\hat{\mathbf{s}}) \end{aligned} \tag{A.23}$$

$P_l(x)$ is a Legendre polynomial and the second line is obtained using the angular addition theorem (see [142]). The phase function is normalized so that $g_0 = 1$ and g_1 is the average cosine of the scattering angle.

Inserting the equations (A.17), (A.18) and (A.23) into the original equation (2.8) yields to

$$\sum_{l=0}^{N}\sum_{m=-l}^{l}\left[\left(\frac{1}{\upsilon}\frac{\partial}{\partial t}+\hat{\mathbf{s}}\,\nabla+\mu_t\right)\psi_{l,m}(\mathbf{r},t)\,Y_{l,m}(\hat{\mathbf{s}})-q_{l,m}\,Y_{l,m}(\hat{\mathbf{s}})-\mu_s\int d\hat{\mathbf{s}}'\,\psi_{l,m}(\mathbf{r},t)\,Y_{l,m}(\hat{\mathbf{s}}')\sum_{l'=0}^{\infty}\sum_{m'=-l}^{l} g_{l'}\,Y^*_{l',m'}(\hat{\mathbf{s}}')\,Y_{l',m'}(\hat{\mathbf{s}})\right]=0 \tag{A.24}$$

The integral over $\hat{\mathbf{s}}'$ is calculated using the orthogonality relation for spherical harmonics

$$\int d\hat{\mathbf{s}}'\,Y_{l,m}(\hat{\mathbf{s}}')\,Y^*_{l',m'}(\hat{\mathbf{s}}')=\delta_{l,l'}\,\delta_{m,m'} \tag{A.25}$$

Rearranging equation (A.24) we get

$$\sum_{l=0}^{N}\sum_{m=-l}^{l}\left[\left(\frac{1}{\upsilon}\frac{\partial}{\partial t}+\hat{\mathbf{s}}\cdot\nabla+\mu_t\right)\psi_{l,m}(\mathbf{r},t)\,Y_{l,m}(\hat{\mathbf{s}})-q_{l,m}\,Y_{l,m}(\hat{\mathbf{s}})-\mu_s\,\psi_{l,m}(\mathbf{r},t)\sum_{l'=0}^{\infty}\sum_{m'=-l}^{l} g_{l'}\,Y_{l',m'}(\hat{\mathbf{s}})\int d\hat{\mathbf{s}}'\,Y_{l,m}(\hat{\mathbf{s}}')\,Y^*_{l',m'}(\hat{\mathbf{s}}')\right]=0 \tag{A.26}$$

For l=0, m=0 we get the following terms:

$$A\psi_{0,0}Y_{0,0}-q_{0,0}Y_{0,0}-\mu_s\psi_{0,0}(g_0Y_{0,0}\underbrace{\delta_{0,0}\delta_{0,0}}_{=1}+g_1Y_{1,0}\delta_{0,1}\delta_{0,0}+g_2Y_{2,0}\delta_{0,2}\delta_{0,0}+...) \tag{A.27}$$

For l=1, m=-1 we get the following terms:

$$\begin{aligned} A\psi_{1,-1}Y_{1,-1} - q_{1,-1}Y_{1,-1} - \mu_s\psi_{1,-1} \quad (\quad & g_0Y_{0,-1}\delta_{1,0}\delta_{-1,-1} + g_0Y_{0,0}\delta_{1,0}\delta_{-1,0} + g_0Y_{0,1}\delta_{1,0}\delta_{-1,1} + ... \\ & g_1Y_{1,-1}\underbrace{\delta_{1,1}\delta_{-1,-1}}_{=1} + g_1Y_{1,0}\delta_{1,1}\delta_{-1,0} + g_1Y_{1,1}\delta_{1,1}\delta_{-1,1} + ... \\ & g_2Y_{2,-1}\delta_{1,2}\delta_{-1,-1} + g_2Y_{2,0}\delta_{1,2}\delta_{-1,0} + g_2Y_{2,1}\delta_{1,2}\delta_{-1,1} + ...) \\ & \vdots \end{aligned} \tag{A.28}$$

For l=1, m=0 we get the following terms:

$$\begin{aligned} A\psi_{1,0}Y_{1,0} - q_{1,0}Y_{1,0} - \mu_s\psi_{1,0} \quad (\quad & g_0Y_{0,-1}\delta_{1,0}\delta_{0,-1} + g_0Y_{0,0}\delta_{1,0}\delta_{0,0} + g_0Y_{0,1}\delta_{1,0}\delta_{0,1} + ... \\ & g_1Y_{1,-1}\delta_{1,1}\delta_{0,-1} + g_1Y_{1,0}\underbrace{\delta_{1,1}\delta_{0,0}}_{=1} + g_1Y_{1,1}\delta_{1,1}\delta_{0,1} + ... \\ & g_2Y_{2,-1}\delta_{1,2}\delta_{0,-1} + g_2Y_{2,0}\delta_{1,2}\delta_{0,0} + g_2Y_{2,1}\delta_{1,2}\delta_{0,1} + ...) \\ & \vdots \end{aligned} \tag{A.29}$$

For l=1, m=1 we get the following terms:

$$\begin{aligned} A\psi_{1,1}Y_{1,1} - q_{1,1}Y_{1,1} - \mu_s\psi_{1,1} \quad (\quad & g_0Y_{0,-1}\delta_{1,0}\delta_{1,-1} + g_0Y_{0,0}\delta_{1,0}\delta_{1,0} + g_0Y_{0,1}\delta_{1,0}\delta_{1,1} + ... \\ & g_1Y_{1,-1}\delta_{1,1}\delta_{1,-1} + g_1Y_{1,0}\delta_{1,1}\delta_{1,0} + g_1Y_{1,1}\underbrace{\delta_{1,1}\delta_{1,1}}_{=1} + ... \\ & g_2Y_{2,-1}\delta_{1,2}\delta_{1,-1} + g_2Y_{2,0}\delta_{1,2}\delta_{1,0} + g_2Y_{2,1}\delta_{1,2}\delta_{1,1} + ...) \\ & \vdots \end{aligned} \tag{A.30}$$

For N=1 we get the following equation

$$\begin{aligned} & A\psi_{0,0}Y_{0,0} - q_{0,0}Y_{0,0} - \mu_s\psi_{0,0}g_0Y_{0,0} + A\psi_{1,-1}Y_{1,-1} - q_{1,-1}Y_{1,-1} - \mu_s\psi_{1,-1}g_1Y_{1,-1} + \\ & A\psi_{1,0}Y_{1,0} - q_{1,0}Y_{1,0} - \mu_s\psi_{1,0}g_1Y_{1,0} + A\psi_{1,1}Y_{1,1} - q_{1,1}Y_{1,1} - \mu_s\psi_{1,1}g_1Y_{1,1} = 0 \end{aligned} \tag{A.31}$$

By analyzing equation (A.31) we get a new formulation of (A.24)

$$\sum_{l=0}^{N}\sum_{m=-l}^{l}\left[\left(\frac{1}{\upsilon}\frac{\partial}{\partial t} + \hat{\mathbf{s}}\cdot\nabla + \mu_t\right)\psi_{l,m}(\mathbf{r},t)Y_{l,m}(\hat{\mathbf{s}}) - q_{l,m}Y_{l,m}(\hat{\mathbf{s}}) - \mu_s\psi_{l,m}(\mathbf{r},t)g_lY_{l,m}(\hat{\mathbf{s}})\right] = 0 \tag{A.32}$$

After a simplification we get

$$\begin{aligned}
\sum_{l=0}^{N}\sum_{m=-l}^{l}\left[\left(\frac{1}{\upsilon}\frac{\partial}{\partial t}+\hat{\mathbf{s}}\cdot\nabla+\mu_t\right)\psi_{l,m}(\mathbf{r},t)-\mu_s\psi_{l,m}(\mathbf{r},t)g_l-q_{l,m}\right]Y_{l,m}(\hat{\mathbf{s}}) &= 0\\
\sum_{l=0}^{N}\sum_{m=-l}^{l}\left[\left(\frac{1}{\upsilon}\frac{\partial}{\partial t}+\hat{\mathbf{s}}\cdot\nabla+\mu_t-\mu_s g_l\right)\psi_{l,m}(\mathbf{r},t)-q_{l,m}\right]Y_{l,m}(\hat{\mathbf{s}}) &= 0\\
\sum_{l=0}^{N}\sum_{m=-l}^{l}\left[\left(\frac{1}{\upsilon}\frac{\partial}{\partial t}+\hat{\mathbf{s}}\cdot\nabla+\mu_t^{(l)}\right)\psi_{l,m}(\mathbf{r},t)-q_{l,m}\right]Y_{l,m}(\hat{\mathbf{s}}) &= 0
\end{aligned} \tag{A.33}$$

where $\mu_t^{(l)}=\mu_s(1-g_l)+\mu_a$ is the reduced transport coefficient.

Next we multiply (A.33) with $Y^*_{l,m}(\hat{\mathbf{s}})$ and integrate over the directional space $\hat{\mathbf{s}}$. We obtain the following equation where we used the orthogonality relation for spherical harmonics on all terms except the term with $\hat{\mathbf{s}}\cdot\nabla\psi_{l,m}(\mathbf{r},t)$

$$\sum_{l=0}^{N}\sum_{m=l}^{l}\left[\frac{1}{\upsilon}\frac{\partial}{\partial t}\psi_{l,m}(\mathbf{r},t)+\mu_t^{(l)}\psi_{l,m}(\mathbf{r},t)+\sum_{l'=0}^{N}\sum_{m'=-l'}^{l'}\int d\hat{\mathbf{s}}\;\hat{\mathbf{s}}\cdot\nabla\psi_{l',m'}(\mathbf{r},t)Y_{l',m'}(\hat{\mathbf{s}})Y^*_{l,m}(\hat{\mathbf{s}})-q_{l,m}\right]=0 \tag{A.34}$$

We now analyze the product

$$\hat{\mathbf{s}}\cdot\nabla\psi_{l',m'}(\mathbf{r},t)Y_{l',m'}(\hat{\mathbf{s}}) \tag{A.35}$$

which leads to

$$\begin{aligned}
\hat{\mathbf{s}}\cdot\nabla\psi_{l',m'}(\mathbf{r},t)Y_{l,m}(\hat{\mathbf{s}}) &= \left[\sin\vartheta\cos\varphi\frac{\partial}{\partial x}+\sin\vartheta\sin\varphi\frac{\partial}{\partial y}+\cos\vartheta\frac{\partial}{\partial z}\right]\psi_{l',m'}(\mathbf{r},t)Y_{l',m'}(\hat{\mathbf{s}})\\
&= [\frac{1}{2}\sin\vartheta(\cos\varphi+i\sin\varphi)(\frac{\partial}{\partial x}-i\frac{\partial}{\partial y})+\frac{1}{2}\sin\vartheta(\cos\varphi-i\sin\varphi)(\frac{\partial}{\partial x}+i\frac{\partial}{\partial y})+\cos\vartheta\frac{\partial}{\partial z}]\psi_{l',m'}(\mathbf{r},t)Y_{l',m'}(\hat{\mathbf{s}})\\
&= \frac{1}{2}\sin\vartheta e^{i\varphi}Y_{l',m'}(\hat{\mathbf{s}})(\frac{\partial}{\partial x}-i\frac{\partial}{\partial y})\psi_{l',m'}(\mathbf{r},t)+\\
&\quad \frac{1}{2}\sin\vartheta e^{-i\varphi}Y_{l',m'}(\hat{\mathbf{s}})(\frac{\partial}{\partial x}+i\frac{\partial}{\partial y})\psi_{l',m'}(\mathbf{r},t)+\\
&\quad \cos\vartheta Y_{l',m'}(\hat{\mathbf{s}})\frac{\partial}{\partial z}\psi_{l',m'}(\mathbf{r},t)
\end{aligned} \tag{A.36}$$

For the following recurrence relations for associated Legendre polynomials we refer to section 12.9 of [143]:

$$\begin{aligned}
\cos\vartheta\ Y_{l',m'} &= \left(\frac{(l'+m')(l'-m')}{(2l'+1)(2l'-1)}\right)^{1/2} Y_{l'-1,m'} + \left(\frac{(l'+m'+1)(l'-m'+1)}{(2l'+1)(2l'+3)}\right)^{1/2} Y_{l'+1,m'} \\
\sin\vartheta e^{i\varphi} Y_{l,m} &= \left(\frac{(l'-m')(l'-m'-1)}{(2l'+1)(2l'-1)}\right)^{1/2} Y_{l'-1,m'+1} - \left(\frac{(l'+m'+1)(l'+m'+2)}{(2l'+1)(2l'+3)}\right)^{1/2} Y_{l'+1,m'+1} \\
\sin\vartheta e^{-i\varphi} Y_{l',m'} &= -\left(\frac{(l'+m')(l'+m'-1)}{(2l'+1)(2l'-1)}\right)^{1/2} Y_{l'-1,m'-1} + \left(\frac{(l'-m'+1)(l'-m'+2)}{(2l'+1)(2l'+3)}\right)^{1/2} Y_{l'+1,m'-1}
\end{aligned} \tag{A.37}$$

Now the recurrence relation is set in and the following equation is obtained

$$\begin{aligned}
\hat{\mathbf{s}}\cdot\nabla\psi_{l',m'}Y_{l',m'} &= \frac{1}{2}\left[\left(\frac{(l'-m')(l'-m'-1)}{(2l'+1)(2l'-1)}\right)^{1/2} Y_{l'-1,m'+1} - \left(\frac{(l'+m'+1)(l'+m'+2)}{(2l'+1)(2l'+3)}\right)^{1/2} Y_{l'+1,m'+1}\right](\frac{\partial}{\partial x} - i\frac{\partial}{\partial y})\psi_{l',m'} + \\
&\quad \frac{1}{2}\left[-\left(\frac{(l'+m')(l'+m'-1)}{(2l'+1)(2l'-1)}\right)^{1/2} Y_{l'-1,m'-1} + \left(\frac{(l'-m'+1)(l'-m'+2)}{(2l'+1)(2l'+3)}\right)^{1/2} Y_{l'+1,m'-1}\right](\frac{\partial}{\partial x} + i\frac{\partial}{\partial y})\psi_{l',m'} + \\
&\quad \left[\left(\frac{(l'+m')(l'-m')}{(2l'+1)(2l'-1)}\right)^{1/2} Y_{l'-1,m'} + \left(\frac{(l'+m'+1)(l'-m'+1)}{(2l'+1)(2l'+3)}\right)^{1/2} Y_{l'+1,m'}\right]\frac{\partial}{\partial z}\psi_{l',m'}
\end{aligned} \tag{A.38}$$

Multiplication with $Y^*_{l,m}(\hat{\mathbf{s}})$ and integration over the directional space $\hat{\mathbf{s}}$ yields for the $\mathbf{1^{st}}$ **term** of equation (A.38)

$$\begin{aligned}
\int d\hat{\mathbf{s}} Y^*_{l,m}(\hat{\mathbf{s}}) \quad & \sum_{l'=0}^{N}\sum_{m'=l'}^{l'} \frac{1}{2}\left[\left(\frac{(l'-m')(l'-m'-1)}{(2l'+1)(2l'-1)}\right)^{1/2} Y_{l'-1,m'+1} - \left(\frac{(l'+m'+1)(l'+m'+2)}{(2l'+1)(2l'+3)}\right)^{1/2} Y_{l'+1,m'+1}\right](\frac{\partial}{\partial x} - i\frac{\partial}{\partial y})\psi_{l',m'} \\
= & \sum_{l'=0}^{N}\sum_{m'=l'}^{l'} \frac{1}{2}(\frac{\partial}{\partial x} - i\frac{\partial}{\partial y})\psi_{l',m'}\left(\frac{(l'-m')(l'-m'-1)}{(2l'+1)(2l'-1)}\right)^{1/2}\delta_{l,l'-1}\delta_{m,m'+1} - \\
& \sum_{l'=0}^{N}\sum_{m'=l'}^{l'} \frac{1}{2}(\frac{\partial}{\partial x} - i\frac{\partial}{\partial y})\psi_{l',m'}\left(\frac{(l'+m'+1)(l'+m'+2)}{(2l'+1)(2l'+3)}\right)^{1/2}\delta_{l,l'+1}\delta_{m,m'+1}
\end{aligned} \tag{A.39}$$

The first addend gives only contributions for $l=1$ $m=-1$ $l'=2$ $m'=-2$, $l=1$ $m=0$ $l'=2$ $m'=-1$, $l=1$ $m=1$ $l'=2$ $m'=0$ etc. It can be seen that $m'=m-1$ and $l'=l+1$.
The second addend gives only contributions for $m'=m-1$ and $l'=l-1$.
This leads to

$$\mathbf{1^{st}\ term} = \frac{1}{2}(\frac{\partial}{\partial x} - i\frac{\partial}{\partial y})\psi_{l+1,m-1}\left(\frac{(l-m+2)(l-m+1)}{(2l+3)(2l+1)}\right)^{1/2} - \frac{1}{2}(\frac{\partial}{\partial x} - i\frac{\partial}{\partial y})\psi_{l-1,m-1}\left(\frac{(l+m-1)(l+m)}{(2l-1)(2l+1)}\right)^{1/2} \tag{A.40}$$

Multiplication with $Y^*_{l,m}(\hat{\mathbf{s}})$ and integration over the directional space $\hat{\mathbf{s}}$ yields for the $\mathbf{2^{nd}}$ **term** of equation (A.38)

$$\begin{aligned}
\int d\hat{\mathbf{s}} Y^*_{l,m}(\hat{\mathbf{s}}) \qquad & \sum_{l'=0}^{N}\sum_{m'=l'}^{l'}\frac{1}{2}\left[-\left(\frac{(l'+m')(l'+m'-1)}{(2l'+1)(2l'-1)}\right)^{1/2} Y_{l'-1,m'-1} + \left(\frac{(l'-m'+1)(l'-m'+2)}{(2l'+1)(2l'+3)}\right)^{1/2} Y_{l'+1,m'-1}\right](\frac{\partial}{\partial x}+i\frac{\partial}{\partial y})\psi_{l',m'} \\
= & \sum_{l'=0}^{N}\sum_{m'=l'}^{l'} -\frac{1}{2}(\frac{\partial}{\partial x}+i\frac{\partial}{\partial y})\psi_{l',m'}\left(\frac{(l'-m')(l'-m'-1)}{(2l'+1)(2l'-1)}\right)^{1/2}\delta_{l,l'-1}\delta_{m,m'-1} + \\
& \sum_{l'=0}^{N}\sum_{m'=l'}^{l'} \frac{1}{2}(\frac{\partial}{\partial x}+i\frac{\partial}{\partial y})\psi_{l',m'}\left(\frac{(l'-m'+1)(l'-m'+2)}{(2l'+1)(2l'+3)}\right)^{1/2}\delta_{l,l'+1}\delta_{m,m'-1} \\
\mathbf{2^{nd}\ term} = & -\frac{1}{2}(\frac{\partial}{\partial x}+i\frac{\partial}{\partial y})\psi_{l+1,m+1}\left(\frac{(l+m+2)(l+m+1)}{(2l+3)(2l+1)}\right)^{1/2} + \frac{1}{2}(\frac{\partial}{\partial x}+i\frac{\partial}{\partial y})\psi_{l-1,m+1}\left(\frac{(l-m-1)(l-m)}{(2l-1)(2l+1)}\right)^{1/2}
\end{aligned} \tag{A.41}$$

Multiplication with $Y^*_{l,m}(\hat{\mathbf{s}})$ and integration over the directional space $\hat{\mathbf{s}}$ yields for the $\mathbf{3^{rd}}$ **term** of equation (A.38)

$$\begin{aligned}
\int d\hat{\mathbf{s}} Y^*_{l,m}(\hat{\mathbf{s}}) \qquad & \sum_{l'=0}^{N}\sum_{m'=l'}^{l'}\left[\left(\frac{(l+m)(l-m)}{(2l+1)(2l-1)}\right)^{1/2} Y_{l-1,m} + \left(\frac{(l+m+1)(l-m+1)}{(2l+1)(2l+3)}\right)^{1/2} Y_{l+1,m}\right]\frac{\partial}{\partial z}\psi_{l,m} \\
= & \sum_{l'=0}^{N}\sum_{m'=l'}^{l'}\frac{\partial}{\partial z}\psi_{l',m'}\left(\frac{(l'+m')(l'-m')}{(2l'+1)(2l'-1)}\right)^{1/2}\delta_{l,l'-1}\delta_{m,m'} + \\
& \sum_{l'=0}^{N}\sum_{m'=l'}^{l'}\frac{\partial}{\partial z}\psi_{l',m'}\left(\frac{(l'+m'+1)(l'-m'+1)}{(2l'+1)(2l'+3)}\right)^{1/2}\delta_{l,l'+1}\delta_{m,m'} \\
\mathbf{3^{rd}\ term} = & \frac{\partial}{\partial z}\psi_{l+1,m}\left(\frac{(l+m+1)(l-m+1)}{(2l+3)(2l+1)}\right)^{1/2} + \frac{\partial}{\partial z}\psi_{l-1,m}\left(\frac{(l+m)(l-m)}{(2l-1)(2l+1)}\right)^{1/2}
\end{aligned} \tag{A.42}$$

By putting in the first, second and third term in (A.34) we obtain

$$\sum_{l=0}^{N}\sum_{m=l}^{l}\left[\frac{1}{v}\frac{\partial}{\partial t}\psi_{l,m}(\mathbf{r},t) + \mu_t^{(l)}\psi_{l,m}(\mathbf{r},t) + \mathbf{1^{st}\ term} + \mathbf{2^{nd}\ term} + \mathbf{3^{rd}\ term} - q_{l,m}\right] = 0 \tag{A.43}$$

The so-called P_N approximations are obtained by setting $\psi_{l,m} = 0$ for all values of $l > N$. This gives rise to $(N+1)^2$ coupled first-order partial differential equations.

A.3 P_1 Approximation

An outline to the following calculations can be found in [141].
For N=1 we will obtain four equations with $(l,m) = (0,0),\ (1,-1),\ (1,0),\ (1,1)$

$l = 0, m = 0$:

$$\frac{1}{\upsilon}\frac{\partial}{\partial t}\psi_{0,0} + \mu_t^{(0)}\psi_{0,0} + \frac{1}{2}\left(\frac{\partial}{\partial x} - i\frac{\partial}{\partial y}\right)\psi_{1,-1}\left(\frac{2}{3}\right)^{1/2} - \frac{1}{2}\left(\frac{\partial}{\partial x} + i\frac{\partial}{\partial y}\right)\psi_{1,1}\left(\frac{2}{3}\right)^{1/2} + \frac{\partial}{\partial z}\psi_{1,0}\left(\frac{1}{3}\right)^{1/2} - q_{0,0} = 0 \tag{A.44}$$

$l = 1, m = -1$:

$$\frac{1}{\upsilon}\frac{\partial}{\partial t}\psi_{1,-1} + \mu_t^{(1)}\psi_{1,-1} + \frac{1}{2}\left(\frac{\partial}{\partial x} + i\frac{\partial}{\partial y}\right)\psi_{0,0}\left(\frac{2}{3}\right)^{1/2} - q_{1,-1} = 0 \tag{A.45}$$

$l = 1, m = 0$:

$$\frac{1}{\upsilon}\frac{\partial}{\partial t}\psi_{1,0} + \mu_t^{(1)}\psi_{1,0} + \frac{\partial}{\partial z}\psi_{0,0}\left(\frac{1}{3}\right)^{1/2} - q_{1,0} = 0 \tag{A.46}$$

$l = 1, m = 1$:

$$\frac{1}{\upsilon}\frac{\partial}{\partial t}\psi_{1,1} + \mu_t^{(1)}\psi_{1,1} - \frac{1}{2}\left(\frac{\partial}{\partial x} - i\frac{\partial}{\partial y}\right)\psi_{0,0}\left(\frac{2}{3}\right)^{1/2} - q_{1,1} = 0 \tag{A.47}$$

We now replace the radial functions $\psi_{l,m}(\mathbf{r},t)$ by the parameters average intensity $U(\mathbf{r},t)$ (see equation (A.21)) and flux density $\mathbf{J}(\mathbf{r},t)$ (see equation (A.22))

For $l = 0$ we obtain the first differential equation:

$$\begin{aligned}
\frac{1}{\upsilon}\frac{\partial}{\partial t}\psi_{0,0} + \mu_t^{(0)}\psi_{0,0} + \frac{1}{2}\left(\frac{2}{3}\right)^{1/2}\frac{\partial}{\partial x}(\psi_{1,-1} - \psi_{1,1}) - \frac{1}{2}\left(\frac{2}{3}\right)^{1/2} i\frac{\partial}{\partial y}(\psi_{1,-1} + \psi_{1,1}) + \left(\frac{1}{3}\right)^{1/2}\frac{\partial}{\partial z}\psi_{1,0} &= q_{0,0} \\
\frac{1}{\upsilon}\frac{\partial}{\partial t}\frac{1}{\sqrt{4\pi}}U(\mathbf{r},t) + \mu_t^{(0)}\frac{1}{\sqrt{4\pi}}U(\mathbf{r},t) + \frac{1}{2}\left(\frac{2}{3}\right)^{1/2}\frac{\partial}{\partial x}\left(\sqrt{\frac{3}{4\pi}}\sqrt{2}J_x\right) - \frac{1}{2}\left(\frac{2}{3}\right)^{1/2} i\frac{\partial}{\partial y}\left(\sqrt{\frac{3}{4\pi}}\sqrt{2}iJ_y\right) + \left(\frac{1}{3}\right)^{1/2}\frac{\partial}{\partial z}J_z &= q_{0,0}
\end{aligned}$$

$$\begin{aligned}
\frac{1}{\upsilon}\frac{\partial}{\partial t}\frac{1}{\sqrt{4\pi}}U(\mathbf{r},t)+\mu_t^{(0)}\frac{1}{\sqrt{4\pi}}U(\mathbf{r},t)+\frac{1}{\sqrt{4\pi}}\left(\frac{\partial}{\partial x}J_x+\frac{\partial}{\partial y}J_y+\frac{\partial}{\partial z}J_z\right) &= q_{0,0}\\
\frac{1}{\sqrt{4\pi}}\left[\frac{1}{\upsilon}\frac{\partial}{\partial t}U(\mathbf{r},t)+\mu_t^{(0)}U(\mathbf{r},t)+\nabla\ \mathbf{J}(\mathbf{r},t)\right] &= q_{0,0}
\end{aligned} \tag{A.48}$$

For $l=1$ we obtain the second differential equation:
For the x-coordinate we subtract the equation (A.47) where $l=1,\ m=1$ from equation (A.45) where $l=1,\ m=-1$:

$$\begin{aligned}
\frac{1}{\upsilon}\frac{\partial}{\partial t}\psi_{1,-1}-\frac{1}{\upsilon}\frac{\partial}{\partial t}\psi_{1,1}+\mu_t^{(1)}\psi_{1,-1}-\mu_t^{(1)}\psi_{1,1}+\frac{1}{2}\left(\frac{\partial}{\partial x}+i\frac{\partial}{\partial y}\right)\psi_{0,0}\left(\frac{2}{3}\right)^{1/2}+\frac{1}{2}\left(\frac{\partial}{\partial x}-i\frac{\partial}{\partial y}\right)\psi_{0,0}\left(\frac{2}{3}\right)^{1/2} &= q_{1,-1}-q_{1,1}\\
\frac{1}{\upsilon}\frac{\partial}{\partial t}(\psi_{1,-1}-\psi_{1,1})+\mu_t^{(1)}(\psi_{1,-1}-\psi_{1,1})+\frac{1}{2}\left(\frac{\partial}{\partial x}+i\frac{\partial}{\partial y}\right)\psi_{0,0}\left(\frac{2}{3}\right)^{1/2}+\frac{1}{2}\left(\frac{\partial}{\partial x}-i\frac{\partial}{\partial y}\right)\psi_{0,0}\left(\frac{2}{3}\right)^{1/2} &= q_{1,-1}-q_{1,1}\\
\frac{1}{\upsilon}\frac{\partial}{\partial t}(\psi_{1,-1}-\psi_{1,1})+\mu_t^{(1)}(\psi_{1,-1}-\psi_{1,1})+\frac{\partial}{\partial x}\psi_{0,0}\left(\frac{2}{3}\right)^{1/2} &= q_{1,-1}-q_{1,1}\\
\frac{1}{\upsilon}\frac{\partial}{\partial t}\sqrt{\frac{3}{4\pi}}\sqrt{2}J_x+\mu_t^{(1)}\sqrt{\frac{3}{4\pi}}\sqrt{2}J_x+\frac{\partial}{\partial x}\frac{1}{\sqrt{4\pi}}U(\mathbf{r},t)\left(\frac{2}{3}\right)^{1/2} &= q_{1,-1}-q_{1,1}\\
\frac{1}{\upsilon}\frac{\partial}{\partial t}\sqrt{\frac{3}{4\pi}}J_x+\mu_t^{(1)}\sqrt{\frac{3}{4\pi}}J_x+\frac{\partial}{\partial x}\frac{1}{\sqrt{4\pi}}U(\mathbf{r},t)\left(\frac{1}{3}\right)^{1/2} &= \frac{1}{\sqrt{2}}(q_{1,-1}-q_{1,1})\\
\sqrt{\frac{3}{4\pi}}\left[\frac{1}{\upsilon}\frac{\partial}{\partial t}J_x+\mu_t^{(1)}J_x+\frac{1}{3}\frac{\partial}{\partial x}U(\mathbf{r},t)\right] &= \frac{1}{\sqrt{2}}(q_{1,-1}-q_{1,1})
\end{aligned} \tag{A.49}$$

For the y-coordinate we add the equation (A.47) where $l=1,\ m=1$ to equation (A.45) where $l=1,\ m=-1$:

$$\begin{aligned}
\frac{1}{\upsilon}\frac{\partial}{\partial t}\psi_{1,-1}+\frac{1}{\upsilon}\frac{\partial}{\partial t}\psi_{1,1}+\mu_t^{(1)}\psi_{1,-1}+\mu_t^{(1)}\psi_{1,1}+\frac{1}{2}\left(\frac{\partial}{\partial x}+i\frac{\partial}{\partial y}\right)\psi_{0,0}\left(\frac{2}{3}\right)^{1/2}-\frac{1}{2}\left(\frac{\partial}{\partial x}-i\frac{\partial}{\partial y}\right)\psi_{0,0}\left(\frac{2}{3}\right)^{1/2} &= q_{1,-1}+q_{1,1}\\
\frac{1}{\upsilon}\frac{\partial}{\partial t}(\psi_{1,-1}+\psi_{1,1})+\mu_t^{(1)}(\psi_{1,-1}+\psi_{1,1})+\frac{1}{2}\left(\frac{\partial}{\partial x}+i\frac{\partial}{\partial y}\right)\psi_{0,0}\left(\frac{2}{3}\right)^{1/2}-\frac{1}{2}\left(\frac{\partial}{\partial x}-i\frac{\partial}{\partial y}\right)\psi_{0,0}\left(\frac{2}{3}\right)^{1/2} &= q_{1,-1}+q_{1,1}\\
\frac{1}{\upsilon}\frac{\partial}{\partial t}(\psi_{1,-1}+\psi_{1,1})+\mu_t^{(1)}(\psi_{1,-1}+\psi_{1,1})+\frac{\partial}{\partial y}i\psi_{0,0}\left(\frac{2}{3}\right)^{1/2} &= q_{1,-1}+q_{1,1}\\
\frac{1}{\upsilon}\frac{\partial}{\partial t}\sqrt{\frac{3}{4\pi}}\sqrt{2}iJ_y+\mu_t^{(1)}\sqrt{\frac{3}{4\pi}}\sqrt{2}iJ_y+\frac{\partial}{\partial y}i\frac{1}{\sqrt{4\pi}}U(\mathbf{r},t)\left(\frac{2}{3}\right)^{1/2} &= q_{1,-1}+q_{1,1}
\end{aligned}$$

$$\begin{aligned}
\frac{1}{\upsilon}\frac{\partial}{\partial t}\sqrt{\frac{3}{4\pi}}iJ_y + \mu_t^{(1)}\sqrt{\frac{3}{4\pi}}iJ_y + \frac{\partial}{\partial y}i\frac{1}{\sqrt{4\pi}}U(\mathbf{r},t)\left(\frac{1}{3}\right)^{1/2} &= \frac{1}{\sqrt{2}}(q_{1,-1}+q_{1,1}) \\
i\sqrt{\frac{3}{4\pi}}\left[\frac{1}{\upsilon}\frac{\partial}{\partial t}J_y + \mu_t^{(1)}J_y + \frac{1}{3}\frac{\partial}{\partial y}U(\mathbf{r},t)\right] &= \frac{1}{\sqrt{2}}(q_{1,-1}+q_{1,1}) \\
\sqrt{\frac{3}{4\pi}}\left[\frac{1}{\upsilon}\frac{\partial}{\partial t}J_y + \mu_t^{(1)}J_y + \frac{1}{3}\frac{\partial}{\partial y}U(\mathbf{r},t)\right] &= \frac{-i}{\sqrt{2}}(q_{1,-1}+q_{1,1})
\end{aligned} \tag{A.50}$$

For the z-coordinate we use equation (A.46) where $l = 1,\ m = 0$:

$$\begin{aligned}
\frac{1}{\upsilon}\frac{\partial}{\partial t}\,\psi_{1,0} + \mu_t^{(1)}\psi_{1,0} + \frac{\partial}{\partial z}\,\psi_{0,0}\left(\frac{1}{3}\right)^{1/2} &= q_{1,0} \\
\frac{1}{\upsilon}\frac{\partial}{\partial t}\sqrt{\frac{3}{4\pi}}\,J_z + \mu_t^{(1)}\sqrt{\frac{3}{4\pi}}J_z + \left(\frac{1}{3}\right)^{1/2}\frac{\partial}{\partial z}\frac{1}{\sqrt{4\pi}}\,U(\mathbf{r},t) &= q_{1,0} \\
\sqrt{\frac{3}{4\pi}}\frac{1}{\upsilon}\frac{\partial}{\partial t}\,J_z + \sqrt{\frac{3}{4\pi}}\mu_t^{(1)}J_z + \sqrt{\frac{3}{4\pi}}\frac{1}{3}\frac{\partial}{\partial z}\,U(\mathbf{r},t) &= q_{1,0} \\
\sqrt{\frac{3}{4\pi}}\left[\frac{1}{\upsilon}\frac{\partial}{\partial t}\,J_z + \mu_t^{(1)}J_z + \frac{1}{3}\frac{\partial}{\partial z}\,U(\mathbf{r},t)\right] &= q_{1,0}
\end{aligned} \tag{A.51}$$

The second differential equation is

$$\sqrt{\frac{3}{4\pi}}\left[\frac{1}{\upsilon}\frac{\partial}{\partial t}\,\mathbf{J}(\mathbf{r},t) + \mu_t^{(1)}\mathbf{J}(\mathbf{r},t) + \frac{1}{3}\nabla U(\mathbf{r},t)\right] = \mathbf{q}_1(\mathbf{r},t) \tag{A.52}$$

where

$$\mathbf{q}_1(\mathbf{r},t) = \left(\frac{1}{\sqrt{2}}\left[q_{1,-1}(\mathbf{r},t) - q_{1,1}(\mathbf{r},t)\right],\ \frac{-i}{\sqrt{2}}\left[q_{1,-1}(\mathbf{r},t) + q_{1,1}(\mathbf{r},t)\right],\ q_{1,0}(\mathbf{r},t)\right) \tag{A.53}$$

We end up with the two coupled partial differential equations for the photon density and the photon flux

$$\frac{1}{\sqrt{4\pi}}\left[\frac{1}{\upsilon}\frac{\partial}{\partial t}\,U(\mathbf{r},t) + \mu_t^{(0)}U(\mathbf{r},t) + \nabla\cdot\mathbf{J}(\mathbf{r},t)\right] = q_{0,0}(\mathbf{r},\mathbf{t}) \tag{A.54}$$

$$\sqrt{\frac{3}{4\pi}}\left[\frac{1}{\upsilon}\frac{\partial}{\partial t}\,\mathbf{J}(\mathbf{r},t) + \mu_t^{(1)}\mathbf{J}(\mathbf{r},t) + \frac{1}{3}\nabla U(\mathbf{r},t)\right] = \mathbf{q}_1(\mathbf{r},t) \tag{A.55}$$

$$\frac{1}{\sqrt{4\pi}}\left[\frac{1}{\upsilon}\frac{\partial}{\partial t}U(\mathbf{r},t)+[\mu_s(\mathbf{r})(1-g_0)+\mu_a(\mathbf{r}))]U(\mathbf{r},t)+\nabla\,\mathbf{J}(\mathbf{r},t)\right] = q_{0,0}(\mathbf{r},t) \tag{A.56}$$

$$\sqrt{\frac{3}{4\pi}}\left[\frac{1}{\upsilon}\frac{\partial}{\partial t}\,\mathbf{J}(\mathbf{r},t)+[\mu_s(\mathbf{r})(1-g_1)+\mu_a(\mathbf{r})]\mathbf{J}(\mathbf{r},t)+\frac{1}{3}\nabla U(\mathbf{r},t)\right] = \mathbf{q}_1(\mathbf{r},t) \tag{A.57}$$

We now define the following terms:

$$\text{isotropic source}: \ \frac{1}{\sqrt{4\pi}}\,S_0(\mathbf{r},t)=q_{0,0}(\mathbf{r},t) \tag{A.58}$$

$$\text{transport coefficient}: \ \mu_{tr}(\mathbf{r})=\mu_s(\mathbf{r})+\mu_a(\mathbf{r}) \tag{A.59}$$

$$\text{reduced scattering coefficient}: \ \mu_s'(\mathbf{r})=\mu_s(\mathbf{r})(1-g_1)=\mu_s(\mathbf{r})(1-g) \tag{A.60}$$

$$\text{diffusion coefficient}: \ D(\mathbf{r})=\frac{1}{3[\mu_s'(\mathbf{r})+\mu_a(\mathbf{r})]} \tag{A.61}$$

Insertion in the first partial differential equation leads to

$$\frac{1}{\sqrt{4\pi}}\left[\frac{1}{\upsilon}\frac{\partial}{\partial t}\,U(\mathbf{r},t)+\mu_s(\mathbf{r})(1-g_0)\,U(\mathbf{r},t)+\mu_a(\mathbf{r})\,U(\mathbf{r},t)+\nabla\,\mathbf{J}(\mathbf{r},t)\right] = \frac{1}{\sqrt{4\pi}}S_0(\mathbf{r},t) \tag{A.62}$$

Finally making use of the fact that $g_0=1$ we obtain

$$\frac{1}{\upsilon}\frac{\partial}{\partial t}\,U(\mathbf{r},t)+\mu_a(\mathbf{r})\,U(\mathbf{r},t)+\nabla\,\mathbf{J}(\mathbf{r},t) = S_0(\mathbf{r},t) \tag{A.63}$$

Insertion in the second partial differential equation leads to

$$\begin{aligned}
\sqrt{\frac{3}{4\pi}}\left[\frac{1}{\upsilon}\frac{\partial}{\partial t}\mathbf{J}(\mathbf{r},t)+\mu_s(\mathbf{r})(1-g_1)\mathbf{J}(\mathbf{r},t)+\mu_a(\mathbf{r})\mathbf{J}(\mathbf{r},t)+\frac{1}{3}\nabla U(\mathbf{r},t)\right] &= \sqrt{\frac{3}{4\pi}}\mathbf{S}_1(\mathbf{r},t)\\
\frac{1}{\upsilon}\frac{\partial}{\partial t}\mathbf{J}(\mathbf{r},t)+\mu_s'(\mathbf{r})\mathbf{J}(\mathbf{r},t)+\mu_a(\mathbf{r})\mathbf{J}(\mathbf{r},t)+\frac{1}{3}\nabla U(\mathbf{r},t) &= \mathbf{S}_1(\mathbf{r},t)\\
\frac{1}{\upsilon}\frac{\partial}{\partial t}\mathbf{J}(\mathbf{r},t)+(\mu_s'(\mathbf{r})+\mu_a(\mathbf{r}))\mathbf{J}(\mathbf{r},t)+\frac{1}{3}\nabla U(\mathbf{r},t) &= \mathbf{S}_1(\mathbf{r},t)\\
\frac{1}{\upsilon}\frac{\partial}{\partial t}\mathbf{J}(\mathbf{r},t)+\frac{1}{3D(\mathbf{r})}\mathbf{J}(\mathbf{r},t)+\frac{1}{3}\nabla U(\mathbf{r},t) &= \mathbf{S}_1(\mathbf{r},t)
\end{aligned} \tag{A.64}$$

The reformulated coupled differential equations are now obtained as

$$\frac{1}{\upsilon}\frac{\partial}{\partial t}\,U(\mathbf{r},t)+\mu_a(\mathbf{r})\,U(\mathbf{r},t)+\nabla\,\mathbf{J}(\mathbf{r},t) = S_0(\mathbf{r},t) \tag{A.65}$$

$$\frac{1}{\upsilon}\frac{\partial}{\partial t}\,\mathbf{J}(\mathbf{r},t)+\frac{1}{3D(\mathbf{r})}\,\mathbf{J}(\mathbf{r},t)+\frac{1}{3}\,\nabla U(\mathbf{r},t) = \mathbf{S}_1(\mathbf{r},t) \tag{A.66}$$

A.4 Diffusion Equation

The diffusion equation can be written in time or frequency domain for homogeneous and heterogeneous media. To change between frequency and time domain we make use of the relation

$$\frac{\partial}{\partial t} \Longleftrightarrow i\,\omega \tag{A.67}$$

The **diffusion equation in the time domain for a homogeneous media**

$$\frac{1}{v}\frac{\partial}{\partial t}\,U(\mathbf{r},t) + \mu_a\,U(\mathbf{r},t) - D\,\nabla^2\,U(\mathbf{r},t) \quad = \quad S_0(\mathbf{r},t) \tag{A.68}$$

The **diffusion equation in the frequency domain for a homogeneous media**

$$\frac{i\omega}{v}\,U(\mathbf{r},\omega) + \mu_a(\mathbf{r})\,U(\mathbf{r},\omega) - D\,\nabla^2\,U(\mathbf{r},\omega) \quad = \quad S_0(\mathbf{r},\omega) \tag{A.69}$$

In heterogeneous media the optical properties (μ_s and μ_a) are dependent on the position $\mathbf{r}$ as well as the diffusion coefficient D.

The **diffusion equation in the time domain for a heterogenous media**

$$\frac{1}{v}\frac{\partial}{\partial t}\,U(\mathbf{r},t) + \mu_a(\mathbf{r})\,U(\mathbf{r},t) - \nabla\cdot[D(\mathbf{r})\,\nabla\,U(\mathbf{r},t)] \quad = \quad S_0(\mathbf{r},t) \tag{A.70}$$

The **diffusion equation in the frequency domain for a heterogenous media**

$$\frac{i\omega}{v}\,U(\mathbf{r},\omega) + \mu_a\,U(\mathbf{r},\omega) - \nabla\cdot[D(\mathbf{r})\,\nabla\,U(\mathbf{r},\omega)] \quad = \quad S_0(\mathbf{r},\omega) \tag{A.71}$$

Appendix B

Coil Design

The rectangular surface coil (20×24mm) was used for RF signal transmission and reception. The coil made of a flexible PCB substrate with standard copper layer was designed for mouse imaging and therefore curved to a cylinder. A window was cut out of this single loop coil to allow for optical measurement (illumination and detection) in reflectance mode from the top.
The rectangular coil was split in two symmetrical parts as it would otherwise violate the law that each coil element should not be bigger than $\lambda/20$. To evaluate the capacitors used for the surface coil operating at 400.33MHz which is exactly the Larmor frequency ω_0 at a magnetic field B_0=9.4T we make use of Kirchhoff's circuit law and could derive the following set of equations:

$$\frac{1}{C_2 + C_4} + \frac{1}{C_3} = \frac{1}{C_1} \tag{B.1}$$

$$\frac{1}{C_2 + C_4} = \frac{1}{C_3} \tag{B.2}$$

$$\frac{1}{C_2 + C_4} + \frac{1}{C_3} + \frac{1}{C_1} = \frac{1}{C_{tot}} \tag{B.3}$$

where C_1, C_2, C_3 are the static capacitors, C_4 is a trimmer capacitor and C_{tot} accounts for the total capacitance.
Choosing a first set of capacitors obeying the above mentioned equations we can experimentally evaluate (with the loaded and unloaded coil) if the frequency ω of the designed circuit is tunable to ω_0. If this is the case the coil is ready for measuring.
If we cannot tune the coil with help of the trimmer capacitor to the desired frequency ω_0 (which is usually the case and the potentiometer of the tuning capacitor reached a stopping point) we can use the closest reachable frequency ω to ω_0 for recalculating the capacitor values. Therefore we make use of the equation

$$\omega = \frac{1}{\sqrt{L\, C_{tot}}} \tag{B.4}$$

and find the relation

$$\left(\frac{\omega}{\omega_0}\right)^2 = \frac{C_{tot,0}}{C_{tot}} \tag{B.5}$$

Knowing now the value of $C_{tot,0}$ allows the recalculation of the capacitor values with help of the above mentioned equations.
For our coils we used the following capacitor values C_1 = 7.5pF, C_2 = 3pF and C_3 = 13pF (ATC Europe, Kungens Kurva, Sweden) and for the trimmer capacitors (Voltronics Corporation, Denville, USA) for matching C_4 and tuning C_5, we used adjustable capacitors ranging from 1 to 19pF.

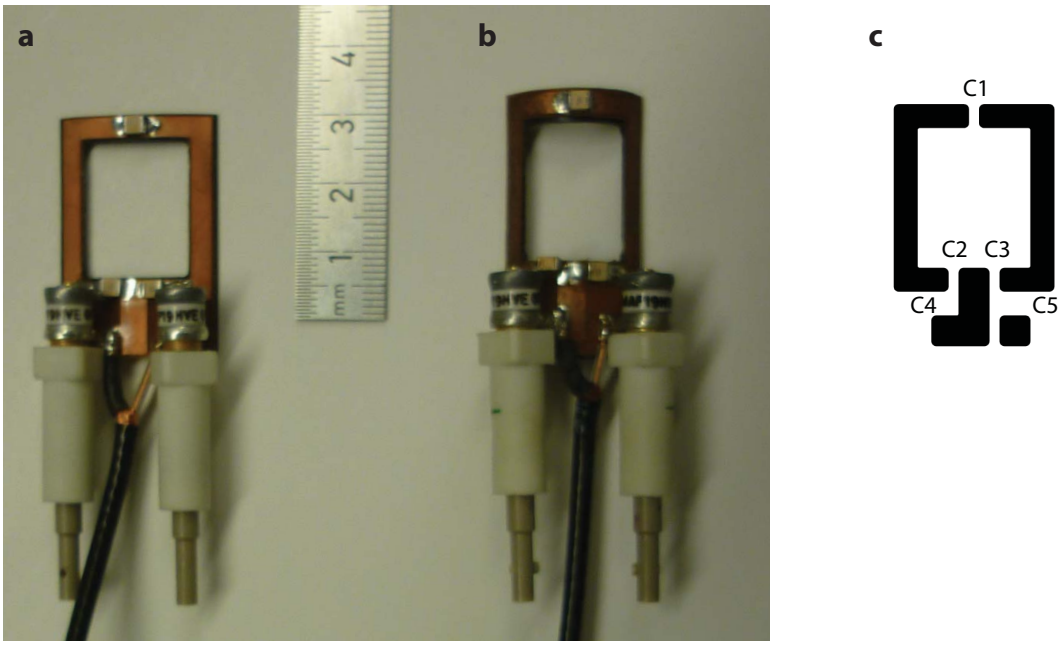

Figure B.1: MR coils. **a** MR transceive coil used in the 2nd generation setup. **b** MR transceive coil used in the 1st generation setup. **c** Schematic of the coil design with the corresponding labels for the capacitors.

Appendix C

A Setup to derive the optical properties of samples

C.1 Introduction

Diagnostic and therapeutic optical systems require the use of tissue mimicking phantoms that simulate the optical characteristic of human and animal tissue. The use of phantoms is on one hand driven by the application of light in medicine for diagnostic (near infrared spectroscopy), therapy (laser surgery) and on the other hand for preclinical research such as fluorescence molecular tomography and optical coherence tomography among other applications. These phantoms are often used for testing and calibrating system designs, for reference measurements and for routine performance tests of and between systems. To produce a stable phantom that matches tissue properties a profound knowledge of parameters which describes the light-tissue interaction is essential. Therefore it is important to match the absorption coefficient μ_a, the scattering coefficient μ_s and the average cosine of the scattering angle called anisotropy coefficient g. All these parameters depend on the wavelength. For some applications it is sufficient to account for the reduced scattering coefficient μ_s' which is defined as $\mu_s' = (1-g)\mu_s$. A summary of optical properties of several tissue types can be found in [144, 145].
In literature different types of phantom materials mimicking the optical properties of biological tissue are proposed including liquid phantoms composed of aqueous suspensions, jellies such as gelatine/agar or room temperature vulcanizing (RTV) silicone [115, 113] and solid materials like epoxy resin and polyurethane resin [146, 147]. One of the major benefits of silicone phantoms is the material stability over years and that arbitrary shapes with inclusions can be produced. Furthermore the material is pliable and therefore closely matches the stiffness of living tissue.
To match the optical properties of a phantom scattering and absorbing agents are necessary to account for light tissue interaction. There exist a variety of scattering agents which can be used in combination with a silicone material. Among those titanium dioxide (TiO_2) and aluminum oxide (Al_2O_3) powder are the cheapest and most frequently used agents. TiO_2 particles are also used as the main pigment in common white paint.
A comprehensive list of phantom materials, absorbers and scatterers is given in [148].
The large variation of the optical properties of living tissue found in literature is due to different radiative transfer models, different tissue preparation procedures and due to differences in the measuring techniques. New established techniques are photoacoustic spectroscopy [149], time of flight measurements [150] and pulsed photothermal radiometry [151, 152] whereas the most established and studied techniques are photometric measurements of transmission and reflection based on measurements with integrating spheres. A number of publication describes the integrating sphere theory for

measurements with either one or two integrating spheres with intervening samples [153, 154]. The double sphere assembly, in which the sample is placed between the two spheres is more convenient and allows simultaneous measurement of the optical properties. This can be of importance when the optical properties are changing during the measurement time e. g. by heating up the sample due to radiation.
However, photometric measurement techniques of optical properties can be separated into direct and indirect methods. In direct techniques the optical parameters are measured directly without using any model of light propagation in tissue. On the contrary in indirect measurements the transmission and reflection are measured and from those measurements the optical coefficients are calculated by solving a so called inverse problem. The optical properties are fed into a light propagation model and values for reflection and transmission are calculated by approximation of an analytic model or by Monte Carlo simulations [155]. The optical properties are then iteratively adjusted until the computed values for reflection and transmission match the measured values. In this work we used an inverse adding-doubling (IAD) algorithm provided by S. Prahl [156], for which the optical properties were obtained by iterating an adding-doubling solution of the radiative transport equation until the calculated values of the reflection and transmission match the measurements within error limits.
The aim of this work was to build a double integrating sphere setup allowing a variable illumination input for laser sources. Furthermore a template to produce samples with different thicknesses was built and a standardized phantom production procedure was established for RTV silicone samples. First samples with different thicknesses and concentration of scattering agent were measured with the setup at a fixed wavelength. The measurements were then evaluated with S. Prahl's inverse adding-doubling code, which allows to quantify the optical properties of the measured samples. First findings and experiences with the setup and the measurement procedure were elaborated.

C.2 Theory

C.2.1 Measurement of Optical Properties

There are a number of methods/techniques proposed for measuring the optical properties of tissues with photometric means. They are obtained by using solutions of the RTE that express the optical properties in terms of measurable quantities. These solutions are either exact or approximated and can be separated in two classes: direct and indirect methods (see Fig. C.1) [157].
Direct techniques are independent of a specific model to obtain the optical parameter from measurements. Unscattered (also known as collimated) transmission measurements can be used for calculations of the total attenuation coefficient using thin samples where multiple scattering can be ignored [158]. The effective attenuation coefficient μ_{eff} is estimated from fluence rate measurements by interstitial detectors describing the exponential attenuation of scattered light with depth in tissue.
A theoretical model of light scattering is used to measure the optical properties in indirect techniques. Furthermore the indirect techniques can be subdivided into iterative and non-iterative methods. A non-iterative approach uses expressions which relates the optical properties directly to the measured transmission and reflection in the experiment which is e.g. implemented in the Kubelka-Munk theory [159, 160]. A further development of the Kubelka-Munk approach was derived in [161] where the Kubelka-Munk coefficients are transformed into transport coefficients to calculate the optical properties.
The most sophisticated but tedious techniques to derive optical properties are the indirect iterative methods where the values for the optical properties are iterated until the calculated reflection and transmission match the measured values. Examples for this methods are diffusion theory, adding-doubling models [156], and Monte Carlo simulations [155]. Depending on which parameters are experimentally measured a full set of optical parameters can be derived or only a part of it: The measurement of the total reflectance M_R and the total transmittance M_T allow the determination of the absorption coefficient μ_{a} and the reduced scattering coefficient μ'_{s} which is defined as $\mu'_{\text{s}} = \mu_{\text{s}}(1-g)$.

The total reflectance accounts for all light light specularly reflected and backscattered by the sample whereas the total transmittance accounts for all light passing through the sample. An additional third measurement of the collimated (unscattered) transmission M_U accounting for unscattered light passing directly through the sample or the phase function allows the separation of the reduced scattering coefficient in μ_s and g. M_R, M_T and M_U account for the properties of the integrating sphere setup and are therefore normalized values (see Section C.3.3).

C.2.2 Indirect Measurements of Optical Properties

The diffuse reflectance M_R and the diffuse transmittance M_T, which are needed to determine the tissue optical properties by the model chosen can be measured with an integrating sphere (also known as Ulbricht sphere). A generalized sphere theory is given in [162]. The interior of this hollow sphere cavity has a white coating which is associated with high diffuse reflectivity. We can think of either a single sphere or a double sphere configuration with the detector situated on the inner sphere surface. In a single sphere setup the reflected and transmitted light from the sample is measured by placing the sample either at the exit or at the entrance port of the sphere [154]. In the double sphere assembly the sample is placed between the spheres allowing a simultaneous measurement of the optical properties (see Fig. C.2). The sample is then placed at the exit port of the first sphere measuring reflectance (called the reflectance sphere) and at the entrance port of the second sphere measuring transmittance (called the transmittance sphere). It is only required that both spheres have the same sample port size. A portion of the light which is irradiating the sample in the reflectance sphere will be transmitted through the sample to the transmittance sphere. Some of the light within the transmittance sphere will irradiate the back of the sample and some of this light will be transmitted back into the reflectance

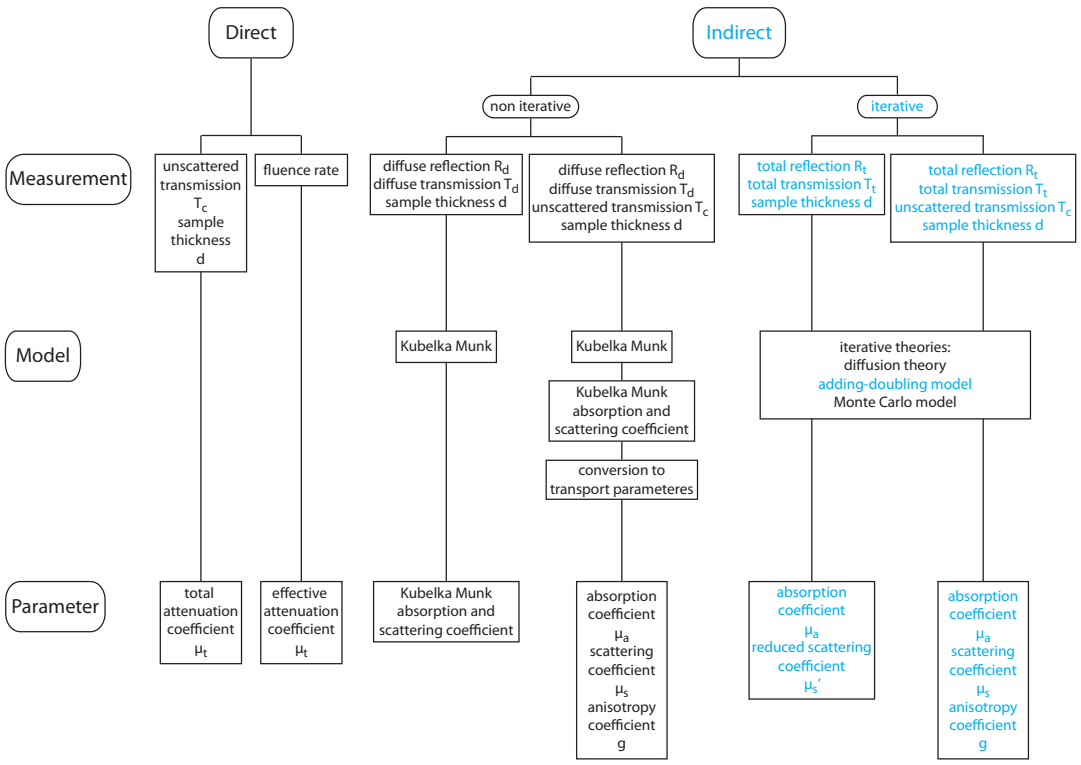

Figure C.1: Photometric methods to measure optical tissue properties. Light blue indicates the method used for this work.

sphere resulting in an increased signal in the reflectance sphere. A portion of this additional light is then retransmitted to the transmittance sphere and leads to a signal increase. This process of light transmittance forth and back continues until all light has been absorbed or lost from the spheres, which leads then to a net effect of increased signal in both spheres compared to the single sphere case. In all cases a baffle is placed between sample and detector to prevent detection of specularly reflected light.
Furthermore the sample illumination scheme can either be diffuse or collimated for both sphere configurations. For the reflectance configuration in the single sphere case and for the reflectance sphere in the double sphere the light incident upon the side of the wall and therefore diffusely irradiated the sample. When using a diffuse illumination scheme in single sphere configuration an increased uncertainty in the diffuse reflectance was discovered compared to collimated illumination [153]. Even if the effect is not that strong in a double sphere setup the measurements tend to be more accurate when using collimated illumination.

C.2.3 Adding-Doubling Method

Optical tissue properties are mostly derived by the well established iterative indirect method based on a diffusion approximation for a solution for the RTE. Such a diffusion approximation computing the expected reflection and transmission measurements was published in [163]. The method is simple to use and the sample constraints are minor. However diffusion approximations are based on the assumption that internal radiance is isotropic, which is in most samples not the case. Therefore a general, numerical method to solve the RTE in a slab geometry was proposed by van de Hulst [164]. The so-called adding-doubling (AD) method [165] provides a fast iterative solution and can be adapted to anisotropic scattering and is valid for all angles of incidence used in the integrations and internal reflections at the boundaries of turbid media can be implemented. A prerequisite of this method is a uniform sample illumination, a sample consisting of uniform layers with homogeneous optical properties and layers of finite thickness and infinite extension in direction perpendicular to the input beam. Further assumptions has to be made before the calculation starts: For this algorithm it is assumed that the light is time-independent and that the sample geometry is an infinite plane-parallel slab of finite thickness and uniform index of refraction. Fresnel's law describes the internal reflection at the boundaries of the unpolarized light. Furthermore the algorithm can handle a non-absorbing layer with different index of refraction added to the boundaries of the sample (such as glass slides covering a tissue sample). The doubling method assumes that the reflection and transmission is known for a single layer for light entering at one angle and exiting at an other angle. The reflection and transmission of a slab that is twice as thick is obtained by putting two identical slabs together and adding the reflection and transmission contributions from each slab. Therefore the reflection and transmission for an arbitrary thick slab is first calculated for a thin slab with the same optical properties and is then obtained by doubling until the desired thickness is reached. Thus samples consisting of layers with different index of refractions can be analyzed with this algorithm.
The inverse adding-doubling (IAD) method works in brief as followed: A set of optical properties is assumed as a starting point then the reflection and transmission values are calculated by the adding-doubling method. The calculated values are then compared with the measured reflection and transmission values from the experiment. If they do not match the procedure is repeated until the values are identical within error limits. The reflection and transmission values found are then further used to calculated the optical properties of the sample. The IAD method can be made arbitrarily precise but it increases the computation time due to more approximation steps. Details about the adding-doubling algorithm implemented in Prahl's code can be found in [156] and on the internet `http://omlc.ogi.edu/software/iad/`.

C.3 Material and Methods

C.3.1 Measurement Setup

For the measurement setup we used a double-integrating sphere approach. In this approach the spheres were placed as such that the exit port of the reflectance sphere (where the reflectance is measured) and the entry port of the transmittance sphere (where the transmittance is measured) were adjacent with only a sample intervening (Fig. C.2). We used two spectralon coated integrating-spheres (Newport Spectra-Physics GmbH, Darmstadt, Germany) with an inner diameter of 83.82mm (3.3in) and each mounted on a xyz-stage. The spectralon coating offered a high reflectivity of $> 95\%$ over a wavelength region of 250 to 2100nm allowing measurements in the ultra violet up to near infrared. Each sphere had 4 measurement ports where the 0° port had a diameter of 38.1mm (1.5in) and the others 25.4mm (1in). The setup was constructed that the two 0° ports are adjacent and connected via a fixed custom made sample holder i.e. placed along the joined axis of the two-sphere setup. The holder allowed to bring samples into the light path of the setup without interfering with the alinement. A removable cassette allows a fast sample replacement. The cassette holds the sample in the right position and can be adapted to hold different samples (tissue samples, silicone phantoms) of different shapes and thicknesses (see Fig. C.3). Even a cuvette filled with liquid could be hold and measured with that design. As it was found that the entrance and exit ports of each sphere are slightly misplaced in terms of parallelism (p) and misalignment (m) with respect to the center points (Sphere Nr. X737 (p) 0.1mm and (m) 0.3mm and sphere Nr. X736 (p) 0.3mm and (m) 1.1mm) a pitch and yaw platform was used for each sphere to ensure a proper alignment.
Both north poles were covered with a plug whereas a detector was attached to both 90° ports. The detector attached to the reflectance sphere (detector 1) measured the diffuse reflected light from the sample and the detector attached to the transmittance sphere (detector 2) collected the diffuse scattered light. A baffle was used between the sample and the detector to ensure that all light leaving the sample hits first the white sphere coating of the sphere walls. In the absence of a baffle it might happen that light from the sample is transmitted directly to the detector and disturbs the measurement. The sphere diameter determined the maximum sample port size. A rule of thumb is that the sample port area should not be bigger than 10% of the sphere wall area. A short calculation for our sphere resulted in sphere wall area (without the port area) of 18810mm^2 and a sample port area of $\pi r^2 = 1140$mm^2. Hence, this rule was fulfilled for our setup: 1140mm^2 <1881mm^2.
A custom made plug at the 180° port of the reflectance sphere allowed the attachment of a small kinematic mount (Thorlabs, Munich, Germany) and therefore the adjustment of a collimation lens (Thorlabs, Munich, Germany) which was screwed onto the end of an SMA fiber connector which was linked with the laser source in our case a 671nm continuous wave (CW) laser (B&W Tek, Newark, USA). Thus a collimated sample illumination was achieved. The 180° port in the transmittance sphere was covered with a iris diaphragm (opening diameter 6mm) allowing the direct transmitted light leaving the sphere. The light was then measured at a distance of 280mm from the sphere by a third detector (detector 3). All detectors in use were low-power silicon (Si) photo-detectors (Newport, Spectra-Physics GmbH, Darmstadt, Germany) with a spectral range of 400-1100nm and an active area of 100mm^2 (diameter of the active area 11.3mm) which were calibrated depending on where they were placed in the setup. For detector read out we used a one channel (Newport 1835-C, Newport Spectra-Physics GmbH, Darmstadt, Germany) and a two channel powermeter (Newport 2835-C, Newport Spectra-Physics GmbH, Darmstadt, Germany) which were connected to a PC and controlled by a home built LabVIEW (National Instruments, Austin, USA) program. This program allowed a simultaneous read out of all detectors (see Fig. C.2).
To assure a proper alignment, each component (spheres, detector 3) was mounted on xyz-stage which was attached to a rail mounted on a small breadboard. A black box was used to avoid interference by ambient light.

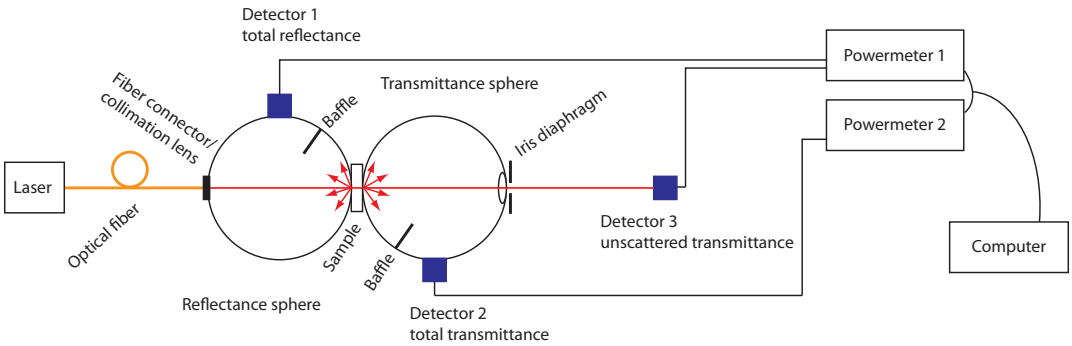

Figure C.2: Schematic of the setup.

C.3.2 Sample Preparation

Three series of samples were produced: A first series was made of pure silicone material without any scattering or absorbing agent added. These samples were then used for the calibration described in the following section. The second series was prepared from a silicone batch with a scattering agent concentration of 0.1717g/l TiO_2. On the contrary a third series was produced with a seven times higher concentration of TiO_2 (1.2269g/l).
Four different phantom templates (see Fig. C.4a) were prepared to produce sample thicknesses of 0.5, 1, 2 and 4mm. The samples Fig. C.4b where produced as such that they could be fixed in a cassette and measured in the setup.
Before the template for the phantom production was designed the size and thickness of the samples had to be considered: On one side the size of the sphere dictates the largest sample size but on the other side the size of the illumination beam determines the smallest sample size. The entire beam should illuminate the sample and no light should miss the sample otherwise the transmittance measurements were not correct. Moreover light loss through the sides of the sample will result in a erroneously increased calculated absorption coefficient. It was shown in [153] that a large sample port compared to the sample thickness lead to no light loss over a broad range of optical depth. Small sample ports were only acceptable if the optical depth was large enough and therefore the scattering was sufficient to prevent a transport to the side of the sample. It is suggested to use a large aspect ratio e.g. sample port should be ten times the sample thickness. Hence with a sample port diameter of 38.1mm a maximal sample thickness of 3.8mm should be possible to measure.

C.3.3 Measurement Procedures

The determination of the tissue optical parameter μ_a, μ_s and g required three independent measurements: The total reflectance M_R, the total transmittance M_T and the collimated transmittance M_U. These parameters need to be accurately measured and serve as a set of values which are used for an inverse adding doubling algorithm providing the actual optical properties of the samples measured. For the measurements we proceeded as described in [166].

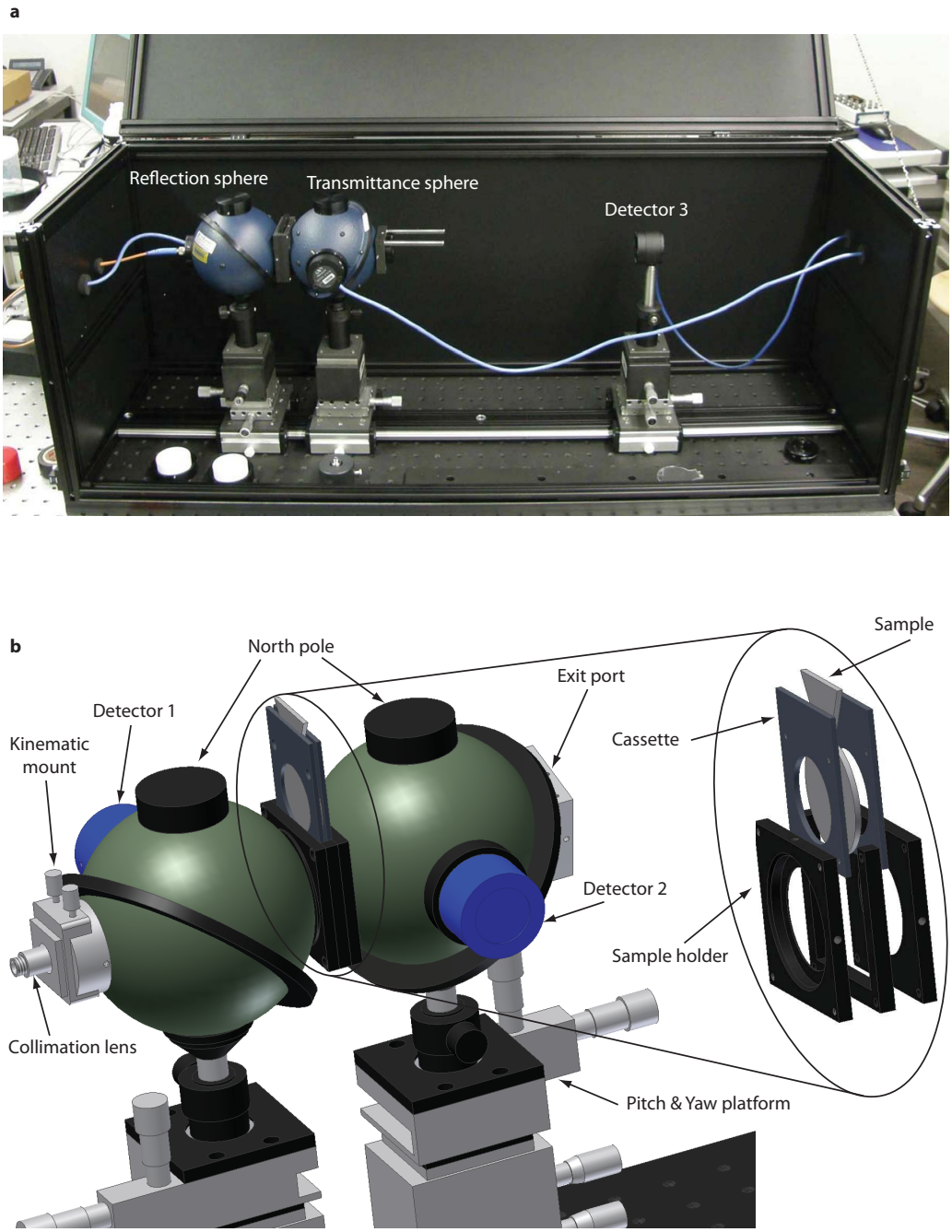

Figure C.3: Experimental setup. **a** Photograph of the setup inside the black box. **b** Enlarged sketch of the two spheres and the sample holder (at the left). The sample holder with a cassette and a sample on the right.

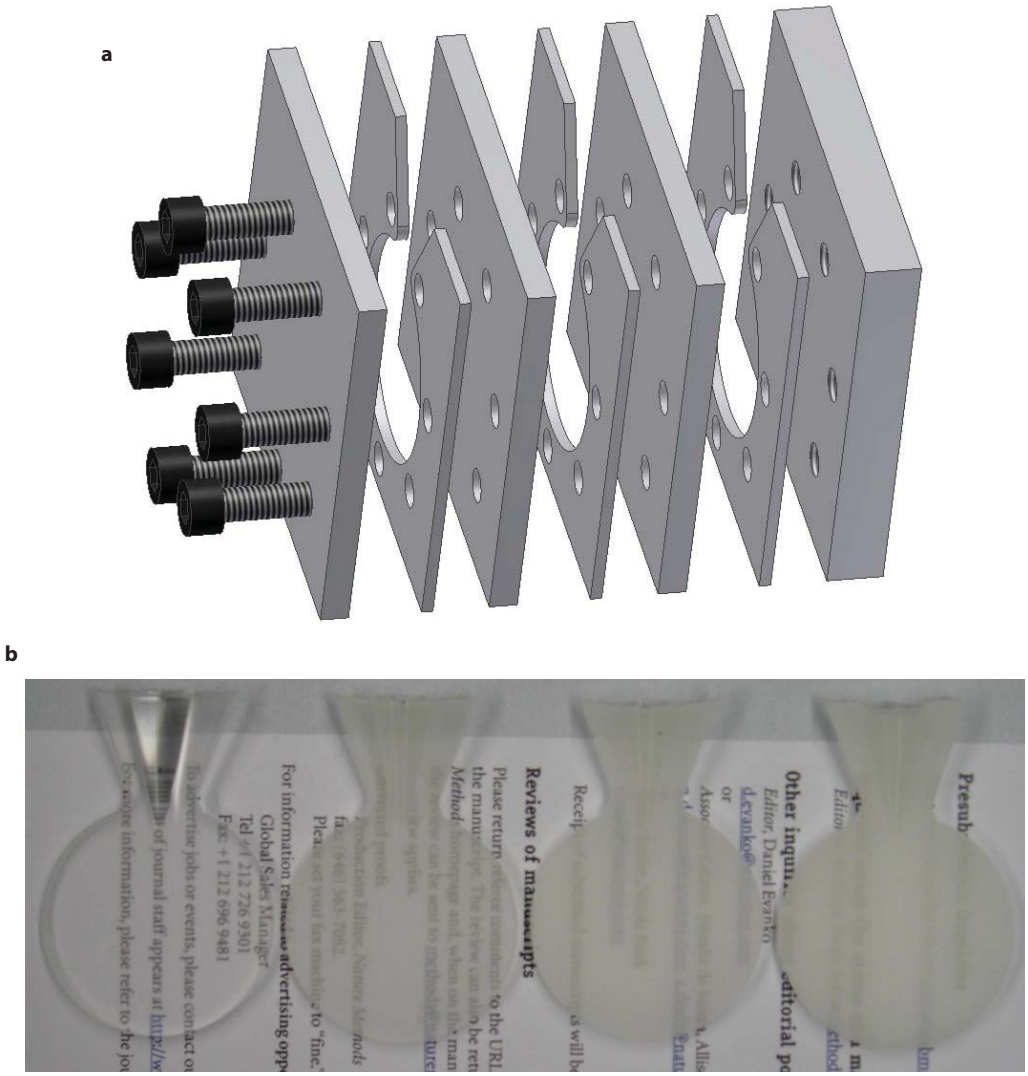

Figure C.4: Sketch of silicone sample template and a sample series. **a** Template for sample production. **b** Samples with increasing TiO_2 concentration from left to right.

Sphere Calibration

First an integrating sphere calibration measurements was performed. These measurements yielded information on the sphere wall reflectance r_w, which could influence the calculation of the optical properties [166]

$$\frac{1}{r_w} = a_w + a_d r_d (1 - a_e) + a_s r_{std} (1 - a_e) \frac{R_{std}^{diffuse}}{R_{std}^{diffuse} - R_0^{diffuse}} \tag{C.1}$$

Where a_w is the relative area of the sphere wall (ports excluded), a_d the relative area of the detector port, a_e the relative area of the entrance port and a_s the relative area of the sample port whereas r_d and r_{std} ar the true reflectance of the detector and the true reflectance of the reflectance standard, respectively. The two diffuse reflectance measurements $R_{std}^{diffuse}$ and $R_0^{diffuse}$ are the power measured with either a transparent silicon sample or a reflectance standard sample at the probe position as

shown in Fig. C.5a,b. Due to the fact that we did not possess a calibrated reflectance standard which differ from the sphere wall coating we skipped this measurement and read the value for r_w from the spectralon data sheet for 671nm which was set at 0.99. However for sake of completeness this calibration step was mentioned here and should be used for future measurements.

Total Reflectance M_R and Total Transmittance M_T

The experimental sphere configurations to measure the individual sphere parameters $R_2(w,x,y,z)$, $T_2(w,x,y,z)$ which are used to calculated the parameters M_R and M_T are shown in Fig. C.6. The normalized values for the total reflectance and the total transmittance are calculated as [166]

$$M_R = r_{std} \cdot \frac{R_2(r_s^{direct}, r_s, t_s direct, t_s) - R_2(0,0,0,0)}{R_2(r_{std}, r_{std}, 0, 0) - R_2(0,0,0,0)} \tag{C.2}$$

$$M_T = \frac{T_2(r_s^{direct}, r_s, t_s direct, t_s) - T_2(0,0,0,0)}{T_2(0,0,1,1) - T_2(0,0,0,0)}. \tag{C.3}$$

Unscattered/Collimated Transmittance M_U

Finally the third measurement accounts for the amount of light which passes through a sample without being scattered or absorbed which is called the unscattered transmittance (or collimated transmittance) M_U (see Fig. C.7) [166]:

$$M_U = \frac{U_S - U_0}{U_{100} - U_0} \tag{C.4}$$

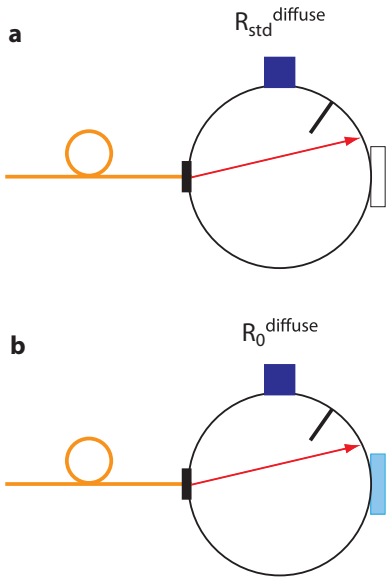

Figure C.5: Sphere calibration measurements. **a** Reflectance standard present at the exit port. **b** Transparent silicone sample present at the exit port.

U_S represents the unscattered sample transmission, U_0 the background measurement when the beam is blocked and U_{100} refers to the unscattered transmission measurement when no sample is in the light path.
Detector 3 which measures the collimated transmitted light is placed behind the exit port of the transmittance sphere. If the detector is too close to the port it will detect also light which is slightly scattered and possibly some of the diffuse light lost through the port. It is therefore advisable to put the detector far from the port to collect as little scattering light as possible. For an optical depth < 10, a detector distance larger than 600mm and an active area of the photodiode of 3mm^2 the error of the measured power was found to be lower than 5% [153].

C.4 Results

First preliminary measurements on the setup were recorded and some tests of intersample reproducibility and the general measurement reproducibility at different time points were analyzed. Further analysis of unscattered transmission measurements were compared with theory. Lastly optical properties of measured reflectance and transmittance parameters were computed with the IAD algorithm.

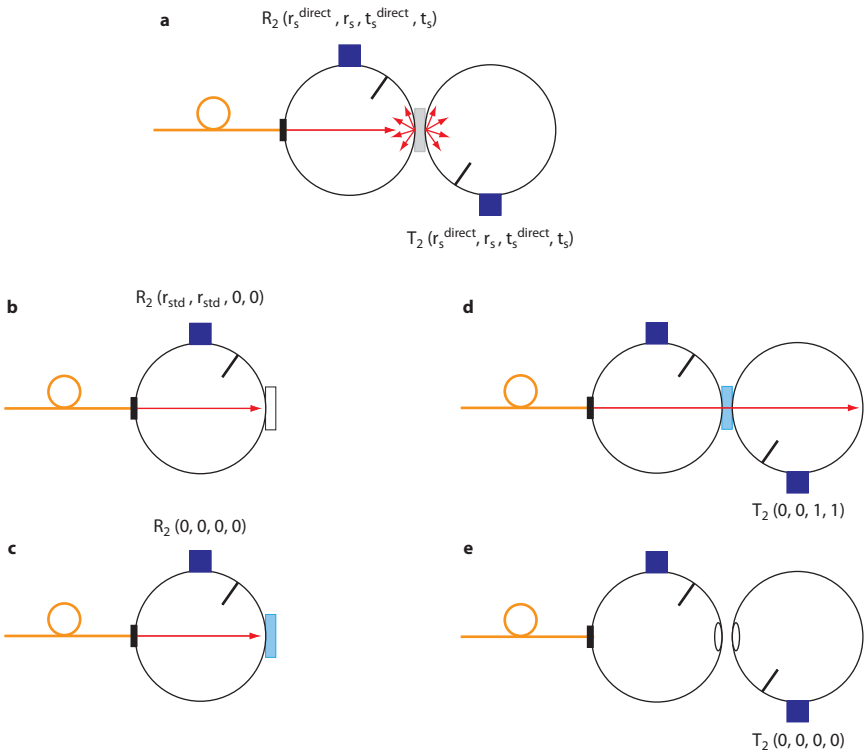

Figure C.6: Reflectance and transmittance measurements needed for a two integrating sphere assembly. **a** Sample measurement with both spheres. **b** Reflectance standard measurement with the reflectance sphere. **c** Reference measurement with the reflectance sphere on a transparent silicone sample. **d** Reference measurement with the transmittance sphere on a transparent silicone sample. **e** Background measurement with no illumination on the transmittance sphere.

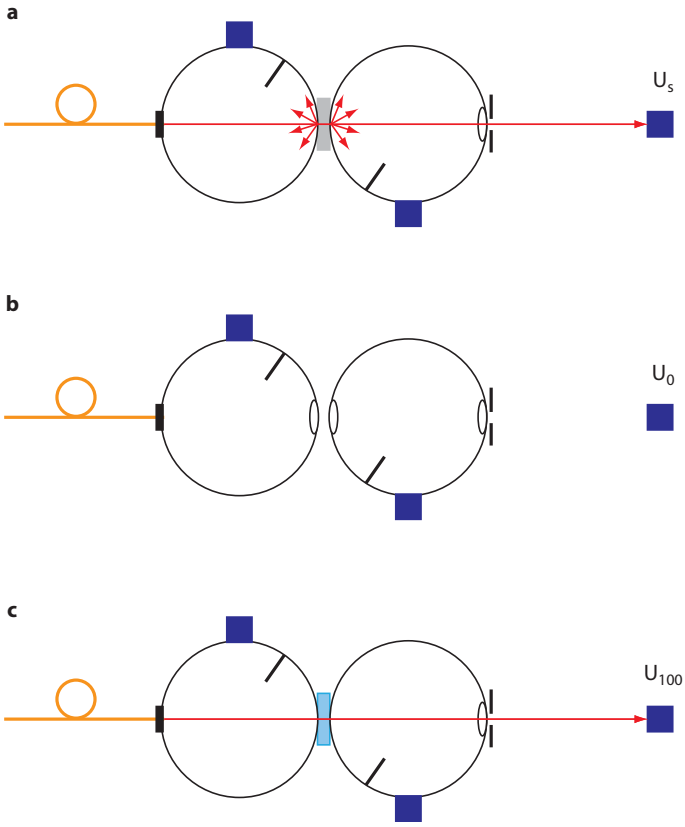

Figure C.7: Collimated transmission measurements. **a** Measurement with the sample. **b** Background measurement with no illumination. **c** Reference measurement with a transparent silicone sample.

C.4.1 Intersample Reproducibility

From one silicone batch with added scattering agent three samples were produced for each thickness. The measurements of M_R showed increased values with increasing sample thickness where as M_T and M_U showed lower values for thicker samples. The measured values of M_R, M_T and M_U for each sample of the same thickness (see Table C.1) showed no significant difference and indicated a reproducible sample preparation.

C.4.2 Measurement Reproducibility

Comparing the values from two measurement series taken at different time points should show the robustness of the measurement setup. Two measurements of the three samples of thickness 2mm were taken at two different time points. Table C.2 clearly shows the high reproducibility of the measurements.

#	thickness [mm]	M_R	M_T	M_U
1		0.11063	0.76347	0.42686
2	0.5	0.10961	0.76327	0.43057
3		0.11004	0.76160	0.43215
4		0.13749	0.63162	0.20341
5	1	0.13711	0.63069	0.19911
6		0.13852	0.62874	0.19796
7		0.18586	0.47002	0.04322
8	2	0.18586	0.47168	0.04280
9		0.18586	0.47354	0.04289
10		0.23610	0.36260	0.00184
11	4	0.23645	0.36414	0.00184
12		0.23791	0.36174	0.00181

Table C.1: Measurement reproducibility between samples.

#	timepoint	M_R	M_T	M_U
7		0.18586	0.47002	0.04322
8	1	0.18586	0.47168	0.04280
9		0.18586	0.47354	0.04289
7		0.18349	0.48408	0.04388
8	2	0.18349	0.48518	0.04358
9		0.18349	0.48574	0.04370

Table C.2: Reproducibility of measurements at different timepoints.

C.4.3 Unscattered Transmittance

As mentioned in [166] the unscattered transmittance M_U is the most difficult measurement to take. Therefore it is worthwile to check if this measurement is no source of error. The measured values for unscattered transmittance at detector 3 were plotted versus the sample thickness for the sample series with the highest TiO_2 concentration. It is shown in Fig. C.8 that the values decreases exponentially with increased sample thickness as expected from theory. A linear data fit in the semi-logarithmic plot with a correlation factor of 0.99996 confirmed the expected result described by the theory.

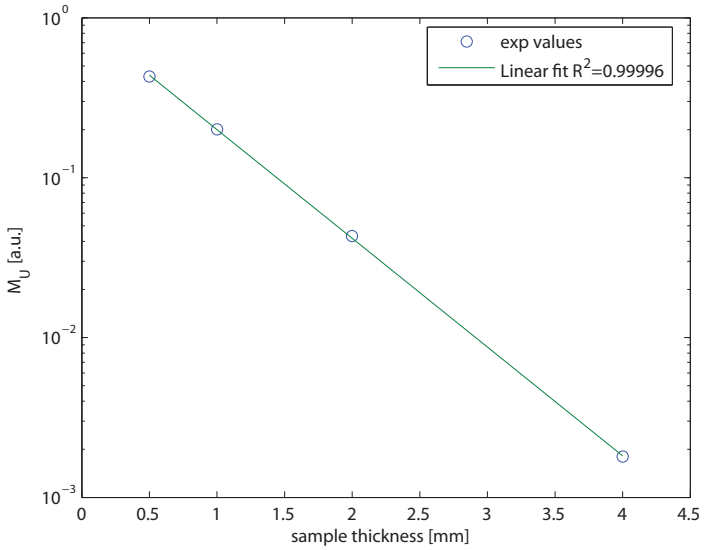

Figure C.8: Unscattered transmittance for sample thickness 0.5, 1, 2, and 4mm.

C.4.4 Calculation of the Optical Properties

For calculation of the optical properties of samples the IAD algorithm provided by S. Prahl was used [166]. A set of setup dependent parameters are required as an input for the algorithm such as the different sample port diameters, the size of the sphere, sphere wall reflectivity and the laser beam diameter. Necessary sample dependent input parameters are the sample thickness and the three measurements M_R, M_T and M_U.
For example for a sample thickness of 2mm and the highest TiO_2 concentration we extracted a μ_a of 0.0685mm^{-1}, a μ_s of 0.406mm^{-1} and a g of 0.723. The algorithm is able to treat the input parameters and to generate a set of optical properties. Whether these optical properties are correct needs to be evaluated and further measurement are needed in order to confirm the correctness of the calculated optical properties by the IAD algorithm.

C.5 Discussion

Integrating spheres are very sensitive devices, reacting on small changes in the illumination or in the setup alignment. These changes can influence the measured parameters, which are used for the

calculation of the optical properties and can lead to inaccurate representation of those. Therefore we put some effort in building up a robust and stable setup, which allows us to measure several sample series in a row without changing the setup for every individual sample. The mechanism with sliding in and out the sample fixed in a so-called cassette was shown to be robust and handy through out a measurement series. The variabilities observed at the detectors (mainly at detector 3) during preliminary setup tests was due to ambient light disturbing the measurements. This influence was then eliminated by enveloping the setup in a black box. Finally a small program to control the detector read outs facilitated the measurement procedure by having a simultaneous power detection of all detectors at the time saved in a log file which was then used for further data analysis. By acquiring for all three detectors 500 measurements for each sample we are able to account for possible small light source instabilities.
The mechanical stability and the user friendliness is one important issue if we consider to measure large sample numbers. Another issue is the measurement reproducibility of stable samples at different time points. Such measurement series were performed at different dates with an additional new set of sphere calibration measurements. It could be shown that there were no significant differences between the measured parameters of the time points. This indicates that the basic measurement procedure described by S. Prahl [166] including our modifications is very stable.
For first setup tests it was important to have standardized and stable samples available. These samples were then measured one after the other to test the system performance. The design of a phantom production procedure which allows the development of silicone phantoms with added scattering agents and/or absorbing agents is fundamental for future sample designs. It was found that with the phantom production procedure described the measurement reproducibility among different samples of the same thickness made of the same silicone batch is very high. Therefore it can be concluded that an establishment of a standardized phantom production procedure has been achieved. It was also found that thicker samples lead to an increased M_R values which is due to higher scattering of thick samples. The inverse effect also caused by increased scattering could be observed for the measured values of M_T and M_U.
So far the basic setup tests showed that the values for the scattered reflectance, scattered transmittance and unscattered transmittance seemed to be consistent. A further test of the unscattered transmittance is needed to quantify the obtained measurement values. Therefore the values for different sample thicknesses were evaluated. With increased sample thickness or scattering agent concentration the measured value at detector 3 (unscattered transmission) should follow an exponential law. This was successfully verified for a measurement series and showed that the measured values from the setup are in good agreement with the theory (correlation coefficient of 0.99996) and can therefore be used as an input for the IAD algorithm.
For optical properties calculation the IAD algorithm described by S. Prahl [156] was used with input arguments concerning the setup configuration and dimensions adapted for our measurement setup. It was demonstrated for one sample as an example that the measured values from the setup can be treated by the algorithm. The calculated value for the anisotropy factor g of 0.723 was in good agreement with values between 0.7 and 0.9 reported for living tissue [167]. This indicates that the produced samples can mimic the forward scattering of living tissue. Even though the measured values from our setup are very stable and reproducible we observed that the calculated values for μ_a of 0.0685mm^{-1} and μ_s of 0.406mm^{-1} are too low compared to literature values. The low absorption coefficient might be explained by the absence of an absorbing agent but no explanation is found for the scattering coefficient mismatch.
From this preliminary setup tests we conclude that we have built a robust setup for measuring standardized silicone phantoms. The measurement reproducibility with the setup was high and furthermore it could be shown that a phantom production procedure was established with small variation within the different samples. Finally a quantification of the optical sample properties by the IAD algorithm could only be partly achieved. Further experiments need to be performed to address the mismatch of μ_a and μ_s.

C.6 Outlook

The first evaluation steps of the setup were performed but the open questions need to be answered and addressed in the future.
Due to a large variety of optical properties of living tissue an investigation is required of the upper and lower limit of scattering agent concentration in the samples, which can be still treated by the double sphere system and the algorithm. It is possible that the measured values from the setup are too small and can not be treated anymore neither by the detectors itself nor by the algorithm.
As further tests of the system with standardized samples the consistency of the calculated values from the IAD algorithm needs to be evaluated for different sample thickness and scattering concentrations. One analysis could be focused on the absorption coefficient, which should not change through out the samples of different thickness produced from the same silicone batch having the same TiO_2 particle concentration.
Another focus should be set on the relation between the scattering and the anisotropy coefficient. Depending on the number of input measurements (M_R, M_T, M_U) the IAD algorithm can calculate a full set of optical properties (μ_a, μ_s and g) or it only calculates μ_a and μ_s' if the input consists only of M_R and M_T. The relation $\mu_s' = (1-g)\mu_s$ should then be consistent through out the calculation performed for two or three input arguments.
A further evaluation with other wavelengths can give a deeper insight in the system performances. By spectrally resolving the different standard silicone samples it may be possible to derive a formulation for silicone samples with specified optical properties. This would be very helpful for researchers for system performance tests to have a formulation by hand which allows them to prepare a phantom with a pre-defined set of optical properties valid for a specific wavelength of interest.
The last and most important issue is the procedure extension to real tissues and liquid samples which based on our own experience with the standardized silicone samples appears to be a very challenging step!

Bibliography

[1] V. Ntziachristos, J. Ripoll, L. V. Wang, and R. Weissleder. Looking and listening to light: the evolution of whole-body photonic imaging. *Nature Biotechnology*, 23(3):313–320, March 2005.

[2] R. Weissleder and U. Mahmood. Molecular imaging. *Radiology*, 219:316–333, May 2001.

[3] R. Weissleder. A clearer vision for *in vivo* imaging. *Nature Biotechnology*, 19:316–317, April 2001.

[4] T. F. Massoud and S. S. Gambhir. Molecular imaging in living subjects: seeing fundamental biological processes in a new light. *Genes and Development*, 17:545–580, 2003.

[5] R. Weissleder and M. J. Pittet. Imaging in the area of molecular oncology. *Nature*, 452:580–589, 2008.

[6] R. Weissleder and V. Ntziachristos. Shedding light onto live molecular targets. *Nature Medicine*, 9(1):123–128, January 2003.

[7] F. Leblond, S. C. Davis, P. A. Valdés, and B. W. Pogue. Pre-clinical whole-body fluorescence imaging: Review of instruments, methods and applications. *Journal of Photochemistry and Photobiology B: Biology*, 98(1):77–94, January 2010.

[8] M. Rudin, M. Rausch, and M. Stoeckli. Molecular imaging in drug discovery and development: potential and limitations of nonnuclear methods. *Molecular Imaging and Biology*, 7:5–13, December 2005.

[9] M. Rudin and R. Weissleder. Molecular imaging in drug discovery and development. *Nature Reviews Drug Discovery*, 2:123–131, February 2003.

[10] V. Ntziachristos. Fluorescence molecular imaging. *Annual Review of Biomedical Engineering*, 8:1–33, 2006.

[11] J. V. Frangioni. *In vivo* near-infrared fluorescence imaging. *Curr*, 7(5):626–634, October 2003.

[12] V. Ntziachristos, C. Bremer, and R. Weissleder. Fluorescence imaging with near-infrared light: new technological advances that enable *in vivo* molecular imaging. *European Radiology*, 13:195–208, 2003.

[13] A. H. Hielscher. Optical tomographic imaging of small animals. *Current Opinion in Biotechnology*, 16(1):79–88, February 2005.

[14] S. A. Hildebrand and R. Weissleder. Near-infrared fluorescence: application to *in vivo* molecular imaging. *Current Opinion in Biotechnology*, 14(1):71–91, February 2010.

[15] V. Ntziachristos, J. Ripoll, and R. Weissleder. Would near-infrared fluorescence signals propagate through large human organs for clinical studies? *Optics Letters*, 27(5):333–335, March 2002.

[16] S. R. Cherry. Multimodality *in vivo* imaging systems: twice the power or double the trouble? *Annual Review in Biomedical Engineering*, 8:35–62, February 2006.

[17] M. Niedre and V. Ntziachristos. Elucidating structure and function *in vivo* with hybrid fluorescence and magnetic resonance imaging. *Proceedings of the IEEE*, 96(3):382–396, March 2008.

[18] U. Mahmood, C.-H. Tung, A. Bogdanov, and R. Weissleder. Near-infrared optical imaging of protease activity for tumor detection. *Radiology*, 213:866–870, 1999.

[19] S. Ke, X. Wen, M. Gurfinkel, C. Charnsangavej, S. Wallace, E. M. Sevick-Muraca, and C. Li. Near-infrared optical imaging of epidermal growth factor receptor in breast cancer xenografts. *Cancer Research*, 63:7870–7875, November 2003.

[20] R. Weissleder, C.-H. Tung, U. Mahmood, and A. Bogdanov. *In vivo* imaging of tumors with protease-activated near-infrared fluorescent probes. *Nature Biotechnology*, 17:375–378, April 1999.

[21] A. Wunder, C.-H. Tung, U. Müller-Ladner, R. Weissleder, and U. Mahmood. *In vivo* imaging of protease activity in arthritis: A novel approach for monitoring treatment response. *Arthritis and Rheumatism*, 50(8):2459–2465, August 2004.

[22] A. Zaheer, R. E. Lenkinski, A. Mahmood, A. G. Jones, L. C. Cantley, and J. V. Frangioni. *In vivo* near-infrared fluorescence imaging of osteoblastic activity. *Nature Biotechnology*, 19:1148–1154, December 2001.

[23] M. Yang, E. Baranov, P. Jiang, F.-X. Sun, X.-M. Li, S. Hasegawa, M. Bouvet, M. Al-Tuwaijri, T. Chishima, H. Shimada, A. R. Moossa, S. Penman, and R. M. Hoffman. Whole-body optical imaging of green fluorescent protein-expressing

tumors and metastases. *Proceedings of the National Academy of Sciences of the United States of America*, 97(3):1206–1211, February 2000.

[24] M. Cutler. Transillumination as an aid in the diagnosis of breast lesions. *Surgery, Gynecology and Obstetrics*, pages 721–729, 1929.

[25] V. Ntziachristos, G. Turner, J. Dunham, S. Windsor, A. Soubret, J. Ripoll, and H. A. Shih. Planar fluorescence imaging using normalized data. *Journal of Biomedical Optics*, 10(6):064007, November/December 2005.

[26] D. L. Farkas, C. Du, G. W. Fisher, C. Lau, W. Niu, E. S. Wachman, and R. M. Levenson. Non-invasive image acquisition and advanced processing in optical and bioimaging. *Computerized Medical Imaging and Graphics*, 22:89–102, 1998.

[27] X. Gao, Y. Cui, R. M. Levenson, L. W. K. Chung, and S. Nie. *In vivo* cancer targeting and imaging with semiconductor quantum dots. *Nature Biotechnology*, 22(8):969–976, August 2004.

[28] V. Ntziachristos, C.-H. Tung, C. Bremer, and R. Weissleder. Fluorescence molecular tomography resolves protease activity *in vivo*. *Nature Medicine*, 8(7):757–760, July 2002.

[29] G. M. Turner, G. Zacharakis, A. Soubret, J. Ripoll, and V. Ntziachristos. Complete-angle diffuse optical tomography by use of early photons. *Optics Letters*, 30(4):409–411, February 2005.

[30] M. J. Niedre, R. H. de Kleine, E. Aikawa, D. G. Kirsch, R. Weissleder, and V. Ntziachristos. Early photon tomography allows fluorescence detection of lung carcinomas and disease progression in mice *in vivo*. *Proceedings of the National Academy of Sciences of the United States of America*, 105(49):19126–19131, December 2008.

[31] V. Ntziachristos, X. Ma, and B. Chance. Time-correlated single photon counting imager for simultaneous magnetic resonance and near-infrared mammography. *Review of Scientific Instruments*, 69(12):4221–4233, December 1998.

[32] Vasilis Ntziachristos, A. G. Yodh, Mitchell Schnall, and Britton Chance. Concurrent MRI and diffuse optical tomography of breast after indocyanine green enhancement. *Proceedings of the National Academy of Sciences of the United States of America*, 97(6):276–2772, March 2000.

[33] V. Ntziachristos and R. Weissleder. Charge-coupled-device based scanner for tomography of fluorescent near-infrared probes in turbid media. *Medical Physics*, 29(5):803–809, May 2002.

[34] J. P. Culver, V. Ntziachristos, M. J. Holboke, and A. G. Yodh. Optimization of optode arrangements for diffuse optical tomography: A singular-value analysis. *Optics Letters*, 26(10):701–703, May 2001.

[35] J. P. Culver, R. Choe, M. J. Holboke, L. Zubkov, T. Durduran, A. Slemp, V. Ntziachristos, B. Chance, and A. G. Yodh. Three-dimensional diffuse optical tomography in the parallel plane transmission geometry: Evaluation of a hybrid frequency domain/continuous wave clinical system for breast imaging. *Medical Physics*, 30(2):235–247, February 2003.

[36] A. Corlu, R. Choe, T. Durduran, M. A. Rosen, M. Schweiger, S. R. Arridge, M. D. Schnall, and A. G. Yodh. Three-dimensional *in vivo* fluorescence diffuse optical tomography of breast cancer in humans. *Optics Express*, 15(11):6696–6716, May 2007.

[37] Edward E. Graves, Jorge Ripoll, Ralph Weissleder, and Vasilis Ntziachristos. A submilimeter resolution fluorescence molecular imaging system for small animal imaging. *Medical Physics*, 30(5):901–911, May 2003.

[38] G. Zacharakis, J. Ripoll, R. Weissleder, and V. Ntziachristos. Fluorescent protein tomography scanner for small animal imaging. *IEEE Transactions on Medical Imaging*, 24(7):878–886, July 2005.

[39] R. B. Schulz, J. Ripoll, and V. Ntziachristos. Experimental fluorescence tomography of tissues with noncontact measurements. *IEEE Transactions on Medical Imaging*, 23(4):492–500, April 2004.

[40] J. Ripoll, R. B. Schulz, and V. Ntziachristos. Free-space propagation of diffuse light: Theory and experiments. *Physical Review Letters*, 91(10):103901, September 2003.

[41] R. B. Schulz, J. Ripoll, and V. Ntziachristos. Noncontact optical tomography of turbid media. *Optics Letters*, 28(18):1701–1703, September 2003.

[42] A. Martin, J. Aguirre, A. Sarasa-Renedo, D. Tsoukatou, A. Garofalakis, H. Meyer, J. Ripoll, and A. M. Planas. Imaging changes in lymphoid organs *in vivo* after brain ischemia with three-dimensional fluorescence molecular tomography in transgenic mice expressing green fluorescent protein in t lymphocytes. *Molecular Imaging*, 7(4):1–11, July/August 2008.

[43] A. Koenig, L. Hervé, V. Josserand, M. Berger, J. Boutet, A. Da Silva, J.-M. Dinten, and P. Peltié. *In vivo* mice lung tumor follow-up with fluorescence diffuse optical tomography. *Journal of Biomedical Optics*, 13(1):011008, January/February 2008.

[44] H. Meyer, A. Garofalakis, G. Zacharakis, S. Psycharakis, C. Mamalaki, D. Kioussis, E. N. Economou, V. Ntziachristos, and J. Ripoll. Non-contact optical imaging in mice with full angular coverage and automatic surface extraction. *Applied Optics*, 46(17):3617–27, June 2007.

[45] N. Deliolanis, T. Lasser, D. Hyde, A. Soubret, J. Ripoll, and V. Ntziachristos. Free-space fluorescence molecular tomography utilizing 360° geometry projections. *Optics Letters*, 32(4):382–384, February 2007.

[46] T. Lasser, A. Soubret, J. Ripoll, and V. Ntziachristos. Surface reconstruction for free-space 360^{circ} fluorescence molecular tomography and the effects of animal motion. *IEEE Transactions on Medical Imaging*, 27(2):188–194, February 2008.

[47] C. Li, G. S. Mitchell, J. Dutta, S. Ahn, R. M. Leahy, and S. R. Cherry. A three-dimensional multispectral fluorescence optical tomography imaging system for small animals based on a conical mirror design. *Optics Express*, 17(9):7571–7578, April 2099.

[48] D. W. Townsend, J. P. J. Carney, J. T. Yap, and N. Hall. PET/CT today and tomorrow. *The Journal of Nuclear Medicine*, 45(1):4S–14S, January 2004.

[49] M. S. Judenhofer, C. C. Catana, B. K. Swann, S. B. Siegel, W.-I. Jung, R. E. Nutt, S. R. Cherry, C. D. Claussen, and B. J. Pichler. PET/MR images acquired with a compact MR-compatible PET detector in a 7-T magnet. *Radiology*, 224(3):807–814, September 2007.

[50] B. J. Tromberg, B. W. Pogue, K. D. Paulsen, A. G. Yodh, D. A. Boas, and A. E. Cerussi. Assessing the future of diffuse optical imaging technologies for breast cancer managment. *Medical Physics*, 35(6):2443–2451, June 2008.

[51] Fred S. Azar and X. Intes, editors. *MRI-guided fluorescence tomography of the breast: A phantom study*, volume 7171 of *Multimodel Biomedical Imaging IV*. Proceedings of SPIE, 2009.

[52] S. C. Davis, H. Dehghani, J. Wang, S. Jiang, B. W. Pogue, and K. D. Paulsen. Image-guided diffuse optical fluorescence tomography implemented with Laplacian-type regularization. *Optics Express*, 15(7):4066–4082, April 2007.

[53] X. Zhang, V. Y. Toronov, and A. G. Webb. Simultaneous integrated diffuse optical tomography and functional magnetic resonance imaging of the human brain. *Optics Express*, 13(14):5513–5521, July 2005.

[54] T. J. Huppert, S. G. Diamond, and D. A. Boas. Direct estimation of evoked hemoglobin changes by multimodality fusion imaging. *Journal of Biomedical Optics*, 13(5):054031, 2008.

[55] C. M. McCann, P. Waterman, J.-L. Figueiredo, E. Aikawa, R. Weissleder, and J. W. Chen. Combined magnetic resonance and fluorescence imaging of the living mouse brain reveals glioma response to chemotherapy. *Neuroimage*, 45:360–369, 2009.

[56] M. Allard, D. Côté, L. Davidson, J. Dazai, and R. M. Henkelman. Combined magnetic resonance and bioluminescence imaging of live mice. *Journal of Biomedical Optics*, 12(3):034018, May/June 2007.

[57] S. C. Davis, B. W. Pogue, R. Springett, C. Leussler, P. Mazurkewitz, S. B. Tuttle, S. L. Gibbs-Strauss, S. S. Jiang, H. Dehghani, and K. D. Paulsen. Magnetic resonance-coupled tomography scanner for molecular imaging of tissue. *Review of Scientific Instruments*, 79(6):064302, 2008.

[58] Andrew M. Siegel, Joseph B. Mandeville, and David A. Boas. Temporal comparison of functional brain imaging with optical tomography and fmri during rat forepaw stimulation. *Physics in Medicine and Biology*, 48(10):1391–1403, 2003.

[59] F. S. Azar and X. Intes, editors. *MRI-coupled spectrally-resolved fluorescence tomography for* in vivo *imaging*, volume 6850. Proceedings of SPIE, 2008.

[60] S. C. Davis, K. S. Samkoe, J. A. O'Hara, S. L. Gibbs-Strauss, H. L. Payne, J. Hoopes, K. D. Paulsen, and B. W. Pogue. MRI-coupled fluorescence tomography quantifies EGFR activity in brain tumor. *Academic Radiology*, 17(3):271–276, March 2010.

[61] Heng Xu, Roger Springet, Hamid Dehghani, Brian W. Pogue, Keith D. Paulsen, and Jeff F. Dunn. Magentic-resonance-imaging-coupled broadband near-infrared tomography system for small animal brain studies. *Applied Optics*, 44(11):2177–2188, April 2005.

[62] Gultekin Gulsen, Ozlem Birgul, Mehmet Burcin Unlu, Roshanak Shafiiha, and Orhan Nalcioglu. Combined diffuse optical tomography (DOT) and MRI system for cancer imaging in small animals. *Technology in Cancer Research and Treatment*, 5(4):351–363, August 2006.

[63] N. C. Shaner, P. A. Steinbach, and R. Y. Tsien. A guide to choosing fluorescent proteins. *Nature Methods*, 2(12):905–909, December 2005.

[64] R. Y. Tsien. Building and breeding molecules to spy on cells and tumors. *FEBS Letters*, 579(4):927–932, 2005.

[65] C.-H. Tung, U. Mahmood, S. Bredow, and R. Weissleder. *In vivo* imaging of proteolytic enzyme activity using a novel molecular reporter. *Cancer Research*, 60:4953–4958, September 2000.

[66] D. K. Chatterjeea, A. J. Rufaihaha, and Yong Zhanga. Upconversion fluorescence imaging of cells and small animals using lanthanide doped nanocrystals. *Biomaterials*, 29(7):937–943, March 2008.

[67] J. Zhou, Y. sun, X. Du, L. Xiong, H. Hu, and F. Liuzzi. Dual-modality *in vivo* imaging using rare-earth nanocrystals with near-infrared to near-infrared (nir-to-nir) upconversion luminescence and magnetic resonance properties. *Biomaterials*, 31(12):3287–3295, April 2010.

[68] M. Nyk, R. Kumar, T. Y. Ohulchanskyy, E. J. Bergey, and P. N. Prasad. High contrast *in vitro* and *in vivo* photoluminescence bioimaging using near infrared to near infrared up-conversion in tm^{3+} and yb^{3+} doped fluoride nanophosphors. *Nano Letters*, 8(11):3834–3838, October 2008.

[69] Y. Tian, W.-H. Cao, X.-X. Luo, and Y. Fu. Preparation and luminescence property of gd_2o_2s:tb x-ray nano-phosphors using the complex precipitation method. *Journal of Alloys and Compounds*, 433(1-2):313–317, May 2007.

[70] H. Wang, R. Wang, X. Sun, R. Yan, and Y. Li. Synthesis of red-luminescent eu3+ doped lanthanides compounds hollow spheres. *Materials Research Bulletin*, 40(6):911–919, June 2005.

[71] K. M. Case and P. F. Zweifel. *Linear Transport Theory*. Addison-Wesley Publishing Group, 1967.

[72] B. Davison and J. B. Sykes. *Neutron Transport Theory*. Oxford and the Claredon Press, 1957.

[73] S. Chandrasekhar. *Radiative Transfer*. Dover Publications, 1960.

[74] A. Ishimaru. Theory and application of wave propagation and scattering in random media. *Proceedings of the IEEE*, 65(7):1030–1061, July 1977.

[75] Akira Ishimaru. *Wave Propagation and Scattering in Random Media*. Oxford University Press, 1997.

[76] A. Ishimaru. Diffusion of light in turbid material. *Applied Optics*, 28(12):2210–2215, June 1989.

[77] A. Ishimaru. Diffusion of a pulse in densely distributed scatterers. *Journal of the Optical Society of America A*, 68(8):1045–1050, August 1978.

[78] K. Furutsu. Diffusion equation derived from space-time transport equation. *Journal of the Optical Society of America A*, 70(4):360–366, April 1980.

[79] M. S. Patterson, B. Chance, and B. C. Wilson. Time resolved reflectance and transmittance for the noninvasive measurement of tissue optical properties. *Applied Optics*, 28(12):2331–2336, June 1989.

[80] R. Aronson and N. Corngold. Photon diffusion coefficient in an absorbing medium. *Journal of the Optical Society of America A*, 16(5):1066–1071, May 1999.

[81] J. F. Beek, P. Blokland, P. Posthumus, M. Aalders, J. W. Pickering, H. J. C. M. Sterenborg, and M. J. C. van Gemert. *In vitro* double-integrating-sphere optical properties of tissues between 630 and 1064 nm. *Physics in Medicine and Biology*, 42(11):2255–2261, November 1997.

[82] J. Ripoll, D. Yessayan, G. Zacharakis, and V. Ntziachristos. Experimental determination of photon propagation in highly absorbing and scattering media. *Journal of the Optical Society of America A*, 22(3):546551, March 2005.

[83] A. Garofalakis, G. Zacharakis, G. Filippidis, E. sanidas, D. D. Tsiftsis, V. Ntziachristos, T. G. Papazoglou, and J. Ripoll. Characterization of the reduced scattering coefficient of optically thin samples: theory and experiments. *Journal of Optics A: Pure and Applied Optics*, 6(7):725–735, 2004.

[84] V. A. Markel and J. C. Schotland. Inverse problem in optical diffusion tomography. i. fourier laplace inversion formulas. *Journal of the Optical Society of America A*, 18(6):1336–1347, June 2001.

[85] B. Chance and R. R. Alfano, editors. *Tumor Localization Using Fluorescence of Indocynanine Green (ICG) in Rat Models*, volume 2389 of *Optical Tomography, Photon Migration, and Spectroscopy of Tissue and Model Media: Theory, Human Studies, and Instrumentation*. SPIE, 1995.

[86] X. D. Li, M. A. O'Leary, D. A. Boas, B. Chance, and A. G. Yodh. Fluorescent diffuse photon density waves in homogeneous and heterogeneous turbid media: Analytic solutions and applications. *Applied Optics*, 35(19):3746–3758, July 1996.

[87] *Frequency-domain photon propagation in turbid media*, volume 21 of *OSA Proceedings on Advances in Optical Imaging and Photon Migration*. OSA, 1994.

[88] M.A. O'Leary, D.A. Boas, X.D. Li, B. Chance, and A.G. Yodh. Fluorescence lifetime imaging in turbid media. *Optics Letters*, 21(2):158–160, January 1996.

[89] J. Ripoll and M. Nieto-Vesperinas. Scattering integral equation for diffusive waves: detection of objects buried in diffusive media in the presence of rough interfaces. *Journal of the Optical Society of America A*, 16(6):1453–1465, June 1999.

[90] J. Ripoll and M. Nieto-Vesperinas. Index mismatch for diffuse photon density waves at both flat and rough diffuse-diffuse interfaces. *Journal of the Optical Society of America A*, 16(8):1947–1957, August 1999.

[91] A. H. Hielscher, S. L. Jacques, L. Wang, and F. K. Tittelt. The influence of boundary conditions on the accuracy of diffusion theory in time-resolved reflectance spectroscopy of biological tissues. *Physics in Medicine and Biology*, 40:1957–1975, June 1995.

[92] R. C. Haskell, L. O. Svaasand, T.-T. Tsay, T.-C. Feng, M. S. McAdams, and B. J. Tromberg. Boundary conditions for the diffusion equation in radiative transfer. *Journal of the Optical Society of America A*, 11(10):2727–2741, October 1994.

[93] R. Aronson. Boundary conditions for diffusion of light. *Journal of the Optical Society of America A*, 12(11):2531–2538, May 1995.

[94] G. Popescu, C. Mujat, and A. Dogariu. Evidence of scattering anisotropy effects on boundary conditions of the diffusion equation. *Physical Review E*, 61(4):4523–4529, April 2000.

[95] R. Schulze, D. D. Bruellmann, F. Roeder, and B. d'Hoedt. Determination of projection geometry from quantitative assessment of the distortion of spherical references in single-view projection radiography. *Medical Physics*, 31(10):2849–2854, 2004.

[96] M. Baba, K. Ohtani, M. Imai, and T. Konishi. New laser rangefinder for three-dimensional shape measurement of specular objects. *Optical Engineering*, 40:53–60, 2001.

[97] A. Koenig, L. Hervé, G. Gonon, V. Josserand, M. Berger, J.-M. Dinten, J. Boutet, P. Peltié, J.-L. Coll, and P. Rizo. Fluorescence diffuse optical tomography for free-space and multifluorophore studies. *Journal of Biomedical Optics*, 15(1):016016, January/February 2010.

[98] F. Chen, F. M. Brown, and M. Song. Overview of three-dimensional shape measurement using optical methods. *Optical Engineering*, 39(1), January 2000.

[99] J. Sikora, A. Zacharopoulos, A. Douiri, M. Schweiger, L. Horesh, S. A. Arridge, and J. Ripoll. Diffuse photon propagation in multilayered geom. *Physics in Medicine and Biology*, 51(3):497–516, January 2006.

[100] J. Ripoll, V. Ntziachristos, R. Carminati, and M. Nieto-Vesperinas. Kirchhoff approximation for diffusive waves. *Physical Review E*, 64(5):051917, 2001.

[101] J. Ripoll, M. Nieto-Vesperinas, R. Weissleder, and V. Ntziachristos. Fast analytical approximation for arbitrary geometries in diffuse optical tomography. *Optics Letters*, 27(7):527–529, April 2002.

[102] J. Ripoll and V. Ntziachristos. Interative boundary method for diffuse optical tomography. *Journal of the Optical Society of America A*, 20(6):1103–1110, June 2003.

[103] S. R. Arridge, M. Schweiger, M. Hiraoka, and D. T. Delpy. A finite element approach for modeling photon transport in tissue. *Medical Physics*, 20(2):299–309, April/March 1993.

[104] M. Schweiger, S. R. Arridge, M. Hiraoka, and D. T. Delpy. The finite element method for propagation of light in scattering media: boundary and source conditions. *Medical Physics*, 22(11):1779–1792, November 1995.

[105] J. Ripoll and V. Ntziachristos. From finite to infinite volumes: removal of boundaries in diffuse wave imaging. *Physical Review Letters*, 96:173903, May 2006.

[106] V. A. Markel and J. C. Schotland. Symmetries, inversion formulas, and image reconstruction for optical tomography. *Physical Review E*, 70:056616, 2004.

[107] A. Sarasa-Renedo, R. Favicchio, U. Birk, G. Zacharakis, C. Malamaki, and J. Ripoll. Source intensity profile in noncontact optical tomography. *Optics Letters*, 35(1):34–36, January 2010.

[108] V. Ntziachristos and R. Weissleder. Experimental three-dimensional fluorescence reconstruction of diffuse media by use of a normalized born approximation. *Optics Letters*, 26(12):893–895, June 2001.

[109] A. Soubret, J. Ripoll, and V. Ntziachristos. Accuracy of fluorescent tomography in the presence of heterogeneities: Study of the normalized born ratio. *IEEE Transactions on Medical Imaging*, 24(10):1377–1386, October 2005.

[110] Avinash C. Kak and Malcolm Slaney. *Principles of computerized tomographic imaging*. Society of Industrial and Applied Mathematics, 2001.

[111] Maureen A. O'Leary. *Imaging with diffuse photon density waves*. PhD thesis, University of Pennsylvania, 1996.

[112] J. Ripoll and V. Ntziachristos. Imaging scattering media from a distance: theory and applications of noncontact optical tomography. *Modern Physice Letters B*, 18(28 and 29):1403–1431, May 2004.

[113] R. Bays, G. Wagnieres, D. Robert, J. F. Theumann, I. A. Vitkin, J. F. Savary, P. Monnier, and H. van den Bergh. Three-dimensional optical phantom and its application in photodynamic therapy. *Lasers in Surgery and Medicine*, 21:227–234, 1997.

[114] G. C. Beck, N. Akgun, A. Ruck, and R. Steiner. Design and characterisation of a tissue phantom system for optical diagnostics. *Lasers in Medical Sicence*, 13(3):160–171, 1998.

[115] M. Lualdi, A. Colombo, A. Mari, S. Tomatis, and R. Marchesini. A phantom with tissue-like optical properties in the visible and near infrared for use in photomedicine. *Lasers in Surgery and Medicine*, 28:237–243, 2001.

[116] M. Firbank and D. T. Delpy. A design for a stable and reproducible phantom for use in near infrared imaging and spectroscopy. *Physics in Medicine and Biology*, 38:847–853, 1993.

[117] D. J. Webster, P. L. Morley, G. H. van Lenthe, and R. Müller. A novel *in vivo* mouse model for mechnaically stimulated bone adaptation - a combined experimental and computational validation study. *Computer Methods in Biomechanics and Biomedical Engineering*, 11(5):435–441, October 2008.

[118] V. Mumprecht, M. Honer, B. Vigl, S. T. Proulx, E. Trachsel, M. Kaspar, N. E. Banziger-Tobler, R. Schibli, D. Neri, and M. Detmar. *In vivo* imaging of inflammation- and tumor-induced lymph node lymphangiogenesis by immuno-positron emission tomography. *Cancer Research*, 70(21):8842–8851, November 2010.

[119] A. Garofalakis, G. Zacharakis, H. Meyer, E. N. Economou, C. Mamalaki, J. Papamatheakis, D. Kioussis, V. Ntziachristos, and J. Ripoll. Three-dimensional *in vivo* imaging of green fluorescent protein-expressing T cells in mice with non-contact fluorescence molecular tomography. *Molecular Imaging*, 6(2):96–107, March/April 2007.

[120] S. B. Raymond, A. T. N. Kumar, D. A. Boas, and B. J. Bacskai. Optimal parameters for near infrared fluorescence imaging of amyloid plaques in alzheimer's disease mouse models. *Physics in Medicine and Biology*, 54:6201–6216, 2009.

[121] D. Hyde, R. de Kleine, S. A. MacLaurin, E. Miller, D. H. Brooks, T. Krucker, and V. Ntziachristos. Hybrid FMT-CT imaging of amyloid-β plaques in a murine Alzheimer's disease model. *Neuroimage*, 44(4):1304–1311, February 2009.

[122] M. Hintersteiner, A. Enz, P. Frey, A.-L. Jaton, W. Kinzy, R. Kneuer, U. Neumann, M. Rudin, M. Staufenbiel, M. Stoeckli, K.-H. Wiederhold, and H.-U. Gremlich. *In vivo* detection of amyloid-β deposits by near-infrared imaging using an oxazine-derivative probe. *Nature Biotechnology*, 23(5):577–583, May 2005.

[123] B. J. Pichler, M. S. Judenhofer, C. Catana, J. H. Walton, M. Kneilling, R. E. Nutt, S. B. Siegel, C. D. Claussen, and S. R. Cherry. Performance test of an LSO-APD detector in a 7-T MRI scanner for simultaneous PET/MRI. *Journal of Nuclear Medicine*, 47:639–647, 2006.

[124] E. Grigoriev, A. Akindinov, M. Breitenmoser, S. Buono, E. Charbon, C. Niclass, I. Desforges, and R. Rocca. Silicon photomultipliers and their bio-medical applications. *Nuclear Instruments and Methods in Physics Research Section A*, 571:130–133, 2007.

[125] L. Carrara, C. Niclass, N. Scheidegger, H. Shea, and E. Charbon. A gamma, X-ray and high energy proton radiation-tolerant cis for space applications. In *IEEE Solid-State Circuits Conference*, 2009.

[126] F. Stuker, K. Dikaiou, C. Baltes, and M. Rudin. Optical MRI device, November 2010.

[127] F. Stuker, K. Dikaiou, C. Baltes, and M. Rudin. Mri device with fluorescence molecular tomography system, November 2010.

[128] C. Niclass, A. Rochas, A. Besse, and E. Charbon. Design and characterization of a cmos 3-D image sensor based on single photon avalanche diodes. *IEEE Journal of Solid-State Circuits*, 40(9):1847–1854, September 2005.

[129] M. M. Mohamed and B. F. Sloane. Cystein cathepsins: Multifunctional enzymes in cancer. *Nature Reviews Cancer*, 6:764–775, 2006.

[130] C. Knoess, S. Siegel, A. Smith, and D. Newport. Performance evaluation of the micropet r4 pet scanner for rodents. *European Journal of Nuclear Medicine and Molecular Imaging*, 30(5):737–747, 2003.

[131] Y. C. Tai, A. Chatziioannou, S. Siegel, J. Young, D. Newport, R. E. Nutt, and S. R. Cherry. Performance evaluation of the microPET P4: a PET system dedicated to animal imaging. *Physics in Medicine and Biology*, 46(7):1845–1862, 2001.

[132] M. Rudin, P. M. J. McSheehy, P. R. Allegrini, M. Rausch, D. Baumann, M. Becquet, K. Brecht, J. Brueggen, S. Ferretti, F. Schaeffer, C. Schnella, and J. Wood. PTK787/ZK222584, a tyrosine kinase inhibitor of vascular endothelial growth factor receptor, reduces uptake of the contrast agent GdDOTA by murine orthotopic B16/BL6 melanoma tumours and inhibits their growth *in vivo*. *NMR in Biomedicine*, 18(5):308–321, August 2005.

[133] P. E. Kinahan, B. H. Hasegawa, and T. Beyer. X-ray-based attenuation correction for positron emission tomography/computed tomography scanners. *Seminars in Nuclear Medicine*, 33(3):166–179, July 2003.

[134] D. Hyde, E. L. Miller, D. H. Brooks, and V. Ntziachristos. Data specific spatially varying regularization for multimodal fluorescence molecular tomography. *IEEE Transactions on Medical Imaging*, 29(2):365–374, February 2010.

[135] Simon Neukom and Thomas Baechler. A low-noise CMOS imager with 1.2e- readout noise, 2.5e- overall noise and over 140dB dynamic range at 60fps. In *Frontiers in Electronic Imaging*, 2009.

[136] Christian Lotto and Peter Seitz. Synchronous and asynchronous detection of ultra-low light levels. In *International image sensor workshop*, 2009.

[137] A. Ale, R. B. Schulz, A. Sarantopoulos, and V. Ntziachristos. Imaging performance of a hybrid X-ray computed tomography-fluorescence tomography system using priors. *Medical Physics*, 37(5):1976–1986, May 2010.

[138] A. Garofalakis, A. Dubois, B. Kühnast, D. M. Dupont, I. Janssens, N. Mackiewicz, F. Dollé, B. Tavitian, and F. Ducongé. *In vivo* validation of free-space fluorescence tomography using nuclear imaging. *Optics Letters*, 35(18):3024–3026, September 2010.

[139] T. Lasser and V. Ntziachristos. Optimization of 360° projection fluorescence molecular tomography. *Medical Image Analysis*, 11(4):389–399, August 2007.

[140] B. Davison and J. B. Sykes. *Neutron Transport Theory*. Oxford and the Claredon Press, 1957.

[141] S. R. Arridge. Optical tomography in medical imaging. *Inverse Problems*, 15(2):R41–R93, 1999.

[142] J. D. Jackson. *Classical Electrodynamics*. John Wiley and Sons Ltd., 1999.

[143] G. B. Arfken and H. J. Weber. *Mathematical methods for physicists*. Academic Press, 5 edition, 2001.

[144] W. F. Cheong, S. A. Prahl, and A. J. Welch. A review of the optical properties of biological tissues. *IEEE Journal of Quantum Electronics*, 26(12):2166–2185, 1990.

[145] A. J. Welch and M. J. C. van Gemert, editors. *Optical-thermal response of laser-irradiated tissue*. Plenum Press, 1995.

[146] T. Moffitt, Y.C. Chen, and S. A. Prahl. Preparation and characterisation of polyurethane optical phantoms. *Journal of Biomedical Optics*, 11(4):041103, 2006.

[147] M. L. Vernon, J. Frechette, Y. Painchaud, S. Caron, and P. Beaudry. Fabrication and characterisation of a solid polyurethane phantom for optical imaging through scattering media. *Applied Optics*, 38:4247–4251, 1999.

[148] B. W. Pogue and M. S. Patterson. Review of tissue simulating phantoms for optical spectroscopy, imaging and dosimetry. *Journal of Biomedical Optics*, 11(4):041102, 2006.

[149] J. S. MacLeod, D. Blanc, and M. J. Colles. Measurement of the optical absorption coefficients at 1.06μm of various tissues using the photoacoustic effect. *Lasers in Surgery and Medicine*, 8:143, 1988.

[150] M. S. Patterson, B. Chance, and B. c. Wilson. Time resolved reflectance and transmittance for the non-invasive measurement of tissue optical properties. *Applied Optics*, 28:2331–2336, 1989.

[151] F. H. Long, N. S. Nishioka, and T. F. Deustch. Measurement of the optical and thermal properties of biliary calculi using pulsed photothermal radiometry. *Lasers in Surgery and Medicine*, 7:461–466, 1987.

[152] S. A. Prahl, I. A. Vitkin, B. C. Wilson, and R. R. Anderson. Determination of optical properties of turbid media using pulsed photothermal radiometry. *Physics in Medicine and Biology*, 37(6):1203–1217, 1992.

[153] J. W. Pickering, S. A. Prahl, N. van Wieringen, J. F. Beek, H. J. C. M. Sterenborg, and M. J. C. van Gemert. Double-integrating-sphere system for measuring the optical properties of tissue. *Applied Optics*, 32(4):399–409, 1993.

[154] J. W. Pickering, C. J. M. Moes, H. J. C. M. Sterenborg, S. A. Prahl, and M. J. C. van Gemert. Two integrating spheres with an intervening scattering sample. *Journal of the Optical Society of America A*, 9(4):621–631, 1992.

[155] B. C. Wilson and G. Adam. A monte carlo model for the absorption and flux distributions of light in tissue. *Medical Physics*, 10(6):824–830, 1983.

[156] S. A. Prahl, M. J. C. van Gemert, and A. J. Welch. Determining the optical properties of turbid media by using the adding-doubling method. *Applied Optics*, 32(4):559–568, 1993.

[157] B. C. Wilson, M. S. Patterson, and S. T. Flock. Indirect versus direct techniques for the measurement of the optical properties of tissues. *Photochemistry and Photobiology*, 46(5):601–608, 1987.

[158] S. T. Flock, B. C. Wilson, and M. S. Patterson. Total attenuation coefficients and scattering phase functions of tissues and phantom materials at 633nm. *Medical Physics*, 14(5):835–841, 1987.

[159] P. Kubelka. New contributions to the optics of intensely light-scattering materials. part i. *Journal of the Optical Society of America*, 38:448–457, 1948.

[160] P. Kubelka. New contributions to the optics of intensely light-scattering materials. part ii. *Journal of the Optical Society of America*, 44:330–335, 1954.

[161] M. J. C. van Gemert, A.J. Welch, W. M Star, M. Motamedi, and W. F. Cheong. Tissue optics for a slab geometry n the diffusion approximation. *Lasers in Medical Sicence*, 2:295–302, 1987.

[162] A. G. Goebel. Generalized integrating sphere theory. *Applied Optics*, 6(1):125–128, 1967.

[163] S. L. Jacques and S. A. Prahl. Modeling optical and thermal distributions in tissue during laser irradiation. *Lasers in Surgery and Medicine*, 6:494–503, 1987.

[164] H. C. van de Hulst. *Light scattering by small particles*. Dover Publication Inc., 1981.

[165] G. N. Plass, G. W. Kattawar, and F. E. Catchings. Matrix operator theory of radiative transfer. 1: Rayleigh scattering. *Applied Optics*, 12(2):314–329, 1973.

[166] S. A. Prahl. *Everything I think you should know about inverse adding-doubling*, February 2010.

[167] M. Keijzer, R. R. Richards-Kortum, S. L. Jacques, and M. S. Feld. Fluorescence spectroscopy of turbid media: Autofluorescence of the human aorta. *Applied Optics*, 28(20):4286–4292, 1989.

Acknowledgements

I would like to thank all those who have contributed to the success of my PhD thesis and everyone who helped and supported me during the past five years. My special thanks go to:

- Prof. Dr. Markus Rudin, group leader and my supervisor. Thank you for giving me the opportunity to perform this interesting PhD project. I appreciated the open door to your office at anytime and the scientific and personal support. With your enthusiasm and knowledge you always supported my ideas and projects which was highly motivating.
- Dr. Jorge Ripoll, co-referee. Thank you for all the support and answering to all my questions. I highly appreciated the collaboration and your scientific input to my work. I am still impressed by your experience and knowledge in the field and your programming speed, fantastic!
- Prof. Dr. Wilhelm Krek and Dr. Martin Wolf, co-referees. Thank you for your interest in my research and for taking the time to act as co-referees in my PhD committee. I appreciated your input during the committee meetings and the scientific discussions.
- Christof Baltes. I am very grateful for all our scientific discussions and your help at the MR scanner. I also appreciated the introduction to the running tracks in the forests around the campus.
- Thomas Müggler. Thank you for the perfect time we had at the beginning, when we started building up the optical lab. I also appreciated your biological teaching in the lab.
- Dr. Jürg Fröhlich, Dr. Dirk Baumann and Christoph Böcklin. Thank you for the scientific and non-scientific discussions and the fruitful collaboration elucidating the secrets of optical properties in phantom materials.
- Dr. Divya Vats. Thank you for being always ready to place an animal in one of the setups for one of my ad-hoc experiments.
- Katerina Dikaiou. Thank you for working together in the "opti team", for your great programming skills and the nice time we had in the lab.

- Dr. David Ratering. Thank you for your comments and answers to scientific and non-scientific questions and for being a big support at the MR scanner.
- Prof. Dr. Edoardo Charbon, Lucio Carrara, Yuki Maruyama. I appreciated the collaboration which helped to push our project forward.
- David Beyeler, Bächler Thomas, Edith Innerhofer. Thank you for the smooth collaboration and the help in designing a next generation hybrid setup.
- Dr. Viviane Mumprecht. Thank you for providing a very interesting application to test our developments.
- Floor Lambers. Thank you for providing another very interesting and challenging molecular imaging application to further characterize the implemented methods.
- Markus Küpfer, workshop. Thank you for the lively discussions we had on solving construction problems within our projects. I appreciated the time we spend at the machine to complete parts. It was always very exciting to see how the parts were processed from the beginning to the end.
- Bruno Willi, IT services. Thank you for your fast and competent IT support.
- AIC Group. I would like to thank all the members of the animal imaging center for the nice working atmosphere.

$ The project was financially supported by Swiss National Foundation under Grant SNF 3100-112835 and Grant 310030-126029.

⚣ Meinen Eltern für alles.

♡ Barbara für die Zuneigung und Ablenkung nach intensiven Arbeitstagen.

✷— Christoph für die angeregten Disskusionen und hilfreichen Tipps während unseren unzähligen Lauf- und Radkilometern.

⚷ Florian für die gegenseitige Motivation und die zahlreichen Abenden an den Wochenenden in Bern.

⚖ Sibylle für die zahlreichen Besuche in der Limmatstadt und die angeregten Diskussionen zu jeglichen Themen.

🚲 Simone für die zahlreichen Sportstunden und asiatischen Mittagessen.